AUTONOMOUS STRUCTURAL HEALTH MONITORING TECHNIQUE FOR INTERPLANETARY DRILLING APPLICATIONS USING LASER DOPPLER VELOCIMETERS

A Dissertation
Presented to
The Academic Faculty

by

Shannon M. Statham

In Partial Fulfillment
of the Requirements for the Degree
Doctor of Philosophy in the
School of Aerospace Engineering

Georgia Institute of Technology
May 2011

AUTONOMOUS STRUCTURAL HEALTH MONITORING TECHNIQUE FOR INTERPLANETARY DRILLING APPLICATIONS USING LASER DOPPLER VELOCIMETERS

Approved by:

Dr. Sathya Hanagud, Advisor
School of Aerospace Engineering
Georgia Institute of Technology

Dr. George Kardomateas
School of Aerospace Engineering
Georgia Institute of Technology

Dr. Brian Glass
Exploration Systems Division
NASA Ames Research Center

Dr. Vinod Sharma
Millennium Dynamics Corporation

Dr. Massimo Ruzzene
School of Aerospace Engineering
Georgia Institute of Technology

Date Approved: 17 December 2010

To my family and friends,

for their love and endless support throughout my education endeavors.

ACKNOWLEDGEMENTS

I would like to thank my advisor, Dr. Sathya Hanagud, for guiding me the last five years and sharing his insight, experiences, and endless wisdom. I am extremely grateful and appreciative for all the knowledge and know-how he has given me.

In addition, I would like to recognize individuals who have given me endless support and guidance throughout my Ph.D. work. Dr. Vinod Sharma for showing me the ropes, guiding me through countless experiments, and always being there for me through the good times and the bad. Dr. Brian Glass for his continuous support of my research efforts and for giving me the opportunity to work on such an amazing project and travel to remarkable sites. The NASA Ames team (specifically Howard Cannon and Sarah Thompson) for helping me understand the drill software and modify my code as necessary. The Honeybee Robotics team (specifically Gale Paulsen, Kris Zacney, and Joanna Cohen) for always being available to help me operate, assemble/dissemble, and fix the drill system. Dr. Massimo Ruzzene and Dr. Nicole Apetre for their guidance and assistance with a number of tasks and obstacles throughout my Ph.D.

Lastly, I'd like to acknowledge the incredible people I have met during my time at Georgia Tech. My loving boyfriend, mentor, and best friend, Sven Krasser. He has seen me at my best and my worst, and still supports and loves me every day. My partners in crime, Vincent Emanuele and Yannick Van Weddingen. Life, and salsa, would not have been the same without them. My roommate of five years, Stephanie Mma. I'm so fortunate to have had such an awesome roommate and doggie co-owner. Finally, my work-out buddies, Parisa Pooyan and Swati Rane. Thanks for keeping me motivated and fit!

TABLE OF CONTENTS

LIST OF TABLES

LIST OF FIGURES

SUMMARY

The research work presented in this thesis is devoted to the formulation and field testing of a dynamics-based structural health monitoring system for an interplanetary subsurface exploration drill system. Structural health monitoring is the process of detecting damage or other types of defects in structural and mechanical systems that have the potential to adversely affect the current or future performance of these systems. Interplanetary exploration missions, specifically to Mars, involve operations to search for water and other signs of extant or past life. Such missions require advanced robotic systems that are more susceptible to structural and mechanical failures, which motivates a need for structural health monitoring techniques relevant to interplanetary exploration systems.

Strict design requirements for interplanetary exploration missions create unique research problems and challenges compared with structural health monitoring procedures and techniques developed to date. These challenges include implementing sensors and devices that will not interfere with the drilling operation, producing "real-time" diagnostics of the drilling condition, and developing an automation procedure for complete autonomous operations.

The first research area involves modal analysis experiments to understand the dynamic characteristics of interplanetary drill structural systems in operation. These experiments also validate the use of Laser Doppler Velocimeter sensors in real-time structural health monitoring and prove the drill motor system adequately excites the drill for dynamic measurements and modal analysis while the drill is in operation. The second research area involves the development of modal analysis procedures for rotating structures using a Chebyshev signal filter to remove harmonic components

and other noise from the rotating drill signal. This filter is necessary to accurately analyze the condition of the rotating drill auger tube while in operation. The third research area involves the development of structural dynamic models to represent the drill system under nominal and expected drilling fault conditions. These models are compared with the modal analysis experimental results and provide theoretical means to analyze the drilling operation and predict fault conditions. The fourth research area involves the formulation of a complete autonomous system to collect and perform the dynamic analysis of the drill signal, identify fault-diagnostic results, and relay these results to the drill Executive computer. The formulated system includes the signal filter, trained Neural Networks, and an automation procedure. Trained Neural Networks are implemented to provide a rapid-response method of relating and comparing the current drill signal with the fault-based structural dynamic models developed in this thesis. Lastly, an automation procedure, and the corresponding software, is developed to interface the measurement equipment, signal filter, Neural Networks, and drill Executive computer to provide a complete hands-off operation of the structural health monitoring system. The fifth research area involves field testing and validation of the developed structural health monitoring system through three field campaigns. Two of these field campaigns were completed at a Mars-analog site in the Canadian Arctic.

The automated dynamics-based structural health monitoring technique developed in this thesis presents advanced research accomplishments leading to real-time, autonomous structural health monitoring, and it has been successfully demonstrated on an operating dynamic system. Other major contributions of this thesis work include the formulation and demonstration of real-time, autonomous structural health monitoring in rotating structures using Laser Doppler Velocimeter sensors.

CHAPTER I

INTRODUCTION

Initial stages of interplanetary exploration involve the collection and analysis of samples from the planet's subsurface region. As near-term planetary exploration missions also require unmanned operations, it is necessary to develop techniques to obtain subsurface samples through unmanned and automated processes. After exploring techniques such as mechanical excavation, explosives, and high speed projectiles, the operation of drilling has become the preferred means for collecting uncontaminated subsurface samples.

The available power is also a major consideration for interplanetary exploration. Interplanetary exploration missions and operations generally depend on solar power or radioisotope batteries, which greatly limits the available power for the exploratory drill and drilling operation compared to terrestrial drilling. With limited power and human involvement, drilling into unknown subsurface environments has the potential to result in conditions that hinder or stop the drilling operation and potentially damage the drill structure. It is therefore necessary to identify conditions that can negatively or catastrophically impact the drilling operation and produce diagnostics for these conditions. These limitations and concerns present unique design restrictions and requirements, compared to terrestrial drilling, that need to be solved [24].

Structural health monitoring (SHM) techniques are extensively used to detect and quantify damages and other defects of structural and mechanical systems [146]. When applied to drilling applications, SHM is useful in detecting complications with the drilling operation by examining the dynamic characteristics of the system. Changes in the drilling operation alter the dynamic characteristics of the system, which can

be quantified and used to produce diagnostics for the drill system and operation.

This thesis work combines SHM methods with the design restrictions of a low-power, unmanned, interplanetary subsurface drilling mission. Changes in the dynamic characteristics of the drill system are key indicators of changes in the drilling operation. Thus, using dynamics-based SHM techniques and theoretical models of the drill system under expected drilling faults, it is possible to identify and quantify the condition of the drilling operation. To comply with the unique restrictions of an interplanetary exploration mission, an automated SHM technique is developed using Laser Doppler Velocimeter sensors, a signal filter, and trained Neural Networks. Each of these is critical to provide a completely hands-off, rapid-response health monitoring of an interplanetary subsurface drill system.

The following chapters include background and literature reviews relevant to this thesis work, the formulated research and thesis objectives, and detailed descriptions of dynamic response experiments conducted on a prototype subsurface drill system, a procedure developed for modal analysis of rotating structures using Chebyshev filters, structural dynamic models formulated for the drill system under nominal and expected drilling fault conditions, the developed automation procedure including a signal analysis algorithm and trained Neural Networks for predicting the drilling condition with a measure of probability, and field tests completed to demonstrate and validate the integrated, autonomous SHM system. The final chapter also discusses concluding remarks, significant research contributions, and recommendations for future research.

CHAPTER II

BACKGROUND & LITERATURE REVIEWS

2.1 Subsurface Exploration by Autonomous Drilling

To search for evidence of extant or past microbial life, sources of water, and determine the geological make-up of Mars and other celestial objects, acquisition of core samples from subsurface depths estimated at tens to hundreds and thousands of meters is required [24,63]. Direct subsurface sampling is the most fundamental technique for exploring unaltered in-situ characteristics of any planetary subsurface, and drilling is necessary for subsurface exploration below a few meters [117]. Other options, such as mechanical excavation (scooping/scraping), explosives, and penetrators, have limitations with achievable depths, sample retrieval, and preservation of the subsurface region.

Interplanetary exploration drilling involves many restrictions compared to terrestrial drilling. Size, weight, and power consumption, for example, are major considerations in the design and operation of such drills. With limited to no direct human involvement, interplanetary exploration drills also require autonomous command and control of the drilling operation, which is beyond the scope of any terrestrial drilling operation to date. Blacic [24] provides a list of mission requirements for subsurface planetary exploration using drilling mechanisms. A fully robust planetary drill therefore requires developments of drilling hardware, automated control software, and automated on-board diagnostic modules and fault recovery procedures to operate it safely and effectively.

Another obstacle for interplanetary exploration drilling is the incorporation of robotic and human-tended operations. Terrestrial drilling is complex - an art form

more than an engineering discipline [64]. Human operators use the sound and vibrations of the drill system to identify the condition of the drilling operation, and brute-force methods to address system failures and other performance issues. Interplanetary subsurface drills, however, require intelligent and autonomous systems to perform these same tasks.

Near-term in-situ resource utilization will use lightweight, rover-deployable or standalone drills capable of penetration of one to five meters in depth [63]. These drills need to include autonomous sample handling, down-hole scientific instruments, and drill diagnostics [117].

Two "sister" projects have completed the first stage of developing a suitable prototype for near-term space drilling missions: MARTE (Mars Astrobiology Research and Technology Experiment) [152] and DAME (Drilling Automation for Mars Exploration) [63]. The MARTE objectives were to develop drilling and sample handling procedures and instrument technologies relevant to searching for life in the Martian subsurface [152]. The two primary goals for MARTE were to search for a subsurface biosphere in an environment of unique relevance to life in the Martian subsurface and demonstrate in a mission realistic field test the technical approach for drilling into the subsurface of Mars. The MARTE drill system was a dry, low-power prototype that was capable of reaching a 10 m depth and bring core segments to the surface. The drill system was also equipped with a remote sensing device and life detection instruments to analyze the core segments, and it was operated at or below 150 Watts of power. A photograph of the MARTE drill system is provided in Fig. 1. The accomplishments of the MARTE project included mission simulations, with science payload, at a Mars-analog site in Rio Tinto, Spain, and automated core handling and auger tube change-outs to a depth of 6 m [153].

Given lightspeed delays in communications between Earth and Mars, human oversight or control of the drilling operation is impractical. Complications involved with

Figure 1: MARTE Drill System.

drilling into unknown territories occur quickly and have critical impacts on the system and mission. Thus, the objective of the DAME project is to develop and field test a real-time automated and adaptive drilling system that has capabilities to identify and recover from the most common drilling obstructions, faults, and other complications and continue with the drilling operation [63]. Figure 2 provides a photograph of the DAME drill system.

The DAME system architecture consists of a Contingent Executive, Tiny Instrument Interface (TInI) dispatcher, drill server, diagnostic modules, diagnostic user interface, and drill controller, and the drilling operation operates at or below 100 Watts of power (the projected power availability from solar cells on Mars). The Contingent Executive, originally developed to control planetary rovers, executes the operating procedure for both the DAME and MARTE drill systems.

The diagnostic modules include a rule-based system, a model-based system, and the dynamics-based structural health monitoring system that forms this thesis work. These diagnostic modules individually predict the current condition of the drilling

Figure 2: DAME Drill System.

operation based on expected drilling faults. Drilling faults are any condition that hinders progress of the normal drilling procedure. If a drilling fault is not corrected in a timely matter, a catastrophic failure of the drilling operation is possible. A catastrophic event for the drill structure has the potential to prevent drilling and other mission objectives from being achieved as well. For example, if the drill is mounted to a planetary rover and it becomes frozen or otherwise immobile in the ground, the drill has essentially anchored the rover, resulting in a catastrophic event for the entire mission.

The DAME drill is also equipped with sensors above the surface and at the bit to collect drill telemetry. Sensors above the surface provide telemetry for the torque on the drill string, applied down-hole force, rotational speed, and rate of penetration. Sensors at the drill bit provide telemetry for the torque on the bit, force on the bit or Weight on Bit (WOB), and temperature at the bit location. This data is

useful for the drill plan and the three diagnostic modules and is helpful in subsurface material characterization [117]. Changes in drill telemetry also help identify changes in stratigraphy to flag regions of scientific interest.

The DAME project accomplishments included developing drilling automation and associated robotic technologies and field testing the DAME drill system at a Mars-analog site in the Canadian Arctic. In the final field test (2006), DAME demonstrated 44 hours of autonomous, hands-off drilling to a final drill depth of 3.2 m, and the identification and successful recovery from four expected drilling faults.

As a combined unit, the MARTE and DAME drill systems demonstrate the ability to drill successfully with low power and WOB (weight on bit), autonomously add and replace drill strings, collect and deliver core samples, and identify and recover from drilling faults [61]. Near-term in-situ missions, however, require a hybrid of these two drill systems that maintains the design requirements of a lightweight, low-powered, subsurface exploration drill. Glass [65] describes recent advancements to the infrastructure used in the DAME project, and Mukherjee [111] provides information on other interplanetary drill prototypes based on various goals and available technologies.

2.2 Dynamics-Based Structural Health Monitoring

Structural Health Monitoring (SHM) is the process of detecting damages or other defects in structural and mechanical systems that adversely affect the current or future performance of these systems [66, 146]. The foundation of SHM techniques is that any defects or faults in a structural or mechanical system alter the dynamic response of that system. There are two broad classifications of SHM: on-line and off-line. On-line SHM techniques monitor the health of a structure while in operation, and off-line SHM evaluates the structural health and any defects while the system is not in operation. The current practice of SHM for vehicles such as aircraft are off-line in

depot inspection facilities. This allows analysis of the whole system and completion of any recommended or required maintenance before the aircraft returns to flight. In the case of many space related operations, including interplanetary exploration with subsurface drilling, on-line SHM is the only choice for health monitoring and diagnostics.

One common approach to SHM considers that the modal parameters (natural frequencies, mode shapes, curvature, etc.) are functions of the physical properties (mass, stiffness, damping, etc.) of a structure [32, 58, 90, 121, 146]. Therefore, any changes in the physical properties of the system due to changes in boundary conditions, damage, or other defects cause changes to the modal parameters of a system [51].

The first step in such SHM is the identification of modal parameters from measured dynamic responses [130]. To acquire the dynamic response of a system, the system is excited using either external transducers (such as a piezoelectric actuator, shaker, and impact/impulse hammer) or ambient forces in the service environment. Sensors (such as strain gauges, accelerometers, and Laser Doppler Velocimeters) are used to capture the dynamic signal of the system. The recorded signal is then analyzed, with a linear, discrete system model, to identify the modal parameters and other information about the dynamic system. A detailed review of modal analysis techniques is in Section 2.3.

One of the most popular parameters used in modal- or dynamics- based SHM systems is the natural frequencies as they are easy to measure and require few sensors [7, 37, 49, 71, 92, 130]. As damage is a local property of the structure and frequencies are a global property, changes in natural frequencies are not always significant enough to identify and/or locate damage unless very precise measurements are obtained or large levels of damage have occurred [57]. Natural frequencies (specifically lower frequencies), however, are most affected by changes in boundary conditions [53]. As in systems such as an operating drill, different fault conditions uniquely alter the boundary conditions and, therefore, change the natural frequencies of the system.

Other common modal parameters used in SHM systems are mode shapes, mode shape curvatures, flexibility, and changes in strain energy distribution. Changes in the modal parameters are not the same for each mode since these changes depend on the nature, location, and severity of the damage [130]. Therefore, most of the mode shape based SHM techniques compare two sets of mode shapes to identify and locate damage in a structure. Measurement of the mode shapes requires either a single excitation point and many spatially located sensors or a roving exciter with one or more fixed sensors. This is a drawback compared to other methods [32]. However, with the advancement of sensor technology, specifically Laser-based sensors, this drawback is minimized [34,141]. Laser-based sensors are extensively used to measure the velocities of fluids and solid structural surfaces. A detailed review of Laser-based technologies and sensors is in Section 2.4.

Changes in the mode shape curvatures are shown to be highly localized and sensitive to the region of damage and thus more suitable for locating damage than changes in mode shapes [32]. In some papers, it is argued that higher modes are more sensitive to local damage compared with lower modes [130]; therefore, these techniques require access to higher modes, which require adequate equipment for exciting and identifying such modes.

Flexibility-based techniques use the inverse problem, relating the applied static force to the resulting structural displacement. The flexibility matrix is generally estimated using lower modes, which is suitable for this technique as the matrix is most sensitive to changes in lower modes. The literature, however, argues whether flexibility-based techniques are more successful than modal-based techniques [32].

Another common approach to SHM uses wave propagation measurements to discern the presence of damage in structures [12, 141, 146, 150]. These wave-based SHM methods assume the presence of damage distorts the wavefield by causing reflections and diffractions, and this distortion helps identify and quantify damage in plate-like

structures. Although many studies demonstrate the validity and accuracy of wave-based SHM, these methods are not currently practical for interplanetary drill systems.

Many of the state-of-the-art reviews on SHM techniques [32, 53, 57, 146] have similar critiques and conclusions for the field. Most of the methods require prior analytical models or prior test data to properly detect and locate damage, which are not practical or available in most scenarios. The number and location of sensors necessary for modal-based methods is also problematic for most practical applications. Finally, more tests on real structures in their operating environments should be completed, rather than laboratory tests on representative structures. Development of autonomous and prognostic techniques is also important for the advancement of the SHM field, specifically for real-time SHM methods.

2.3 Modal Analysis

Modal analysis is a technique for finding the dynamic characteristics, specifically the modes of vibration, of a machine or structure [134]. Modes are inherent properties of structures that are defined by natural frequencies, damping coefficients, and mode shapes. The modes of a structure are functions of the material properties, geometry, and boundary conditions of that structure, and any changes in these parameters inevitably alter the dynamic characteristics, which forms the basis of SHM methods.

Frequency Response Functions (FRF) are fundamental measurements that isolate the inherent dynamic properties of a mechanical structure so modal parameters are easily identified [134]. An FRF describes the relationship between the dynamic response of a structure due to an external dynamic input [154]. The current theory behind modal analysis techniques, using FRFs, assumes a linear, viscously damped, discrete, finite degree of freedom (DOF) system [154]. A complete theoretical derivation of the FRF for a finite DOF system is provided in Appendix C.

Modal parameters of a structure are often obtained by artificially exciting the

structure with an external actuator (such as impact hammer, shaker, piezo-actuator, etc.), measuring the displacement, velocity, or acceleration of the structure with sensors (such as accelerometers, strain gauges, Laser Doppler Velocimeters, etc.), a data acquisition device and Fast Fourier Transform (FFT) analyzer (such as SigLab, a data acquisition device and dynamic signal analyzer [147]), and post-processing software. The input and output signals are captured in the time domain, and the FFT analyzer filters noise and uses time domain techniques from foundation to obtain the FRF. The FRF defines the input-output relationship between two points of a structure (Fig. 3). The experimental FRF (H_{jk}) is a ratio between the output at the sensor location (X_j) and the input of the artificial excitation at another point (Y_k).

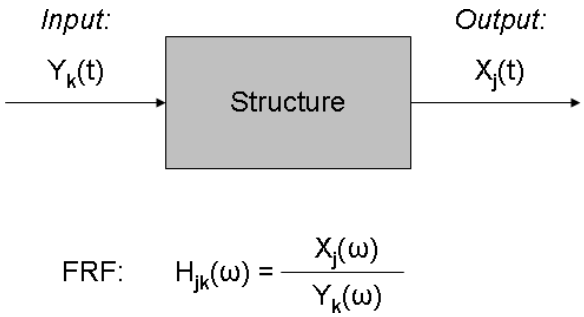

Figure 3: Description of Frequency Response Function [134].

To better define the modal parameters of a structure and eliminate noise in the measurement system, multiple FRF measurements are necessary. As time and costs are always major considerations, it is important that a sufficient number of FRF measurements are taken as possible to eliminate noise and ensure accurate results. Technological advancements in the modal analysis field improve measurement capabilities and modal analysis techniques. These advancements include non-contact sensors, such as the Laser Doppler Velocimeter (LDV, also commonly referred to as Laser Doppler Vibrometers), that allow measurements of structures where sensors cannot be attached and eliminate added mass effects on the structure.

Following the FRF measurements, post-processing procedures of the data are

needed to extract the dynamic characteristics and modal parameters of the structure. The Operation Deflection Shape (ODS) is defined as the motion of one point relative to another point for a specific frequency [135]. The identification of modal parameters is obtained by curve fitting a set of ODS data with the theoretical model derived in Appendix C using software packages such as STAR Modal from Spectral Dynamics and the Rational Fraction Polynomial (rfp) function available in MATLAB [124].

A common practice in the SHM field is to obtain the modal parameters of a structure and compare the results with theoretical models [7, 39, 58]. The theoretical models are usually altered, by adjusting either material properties or boundary conditions, to better represent the experimental results. These models help define health monitoring parameters for the given structure.

2.3.1 Modal Analysis of Rotating Structures

Many structural systems in today's world, such as cars, airplanes, and drills, contain rotating components. Understanding the dynamic characteristics and defining the modal parameters of rotating structures, however, is considerably more complex compared with ordinary, non-rotating structures. Rotary inertia, gyroscopic, and coriolis affects due to the rotating components need to be included and analyzed, which adds considerable complexity to the theoretical and experimental analysis of these types of structures.

Several studies are dedicated to the modal analysis and testing of rotating structures. Bucher and Ewins [29] provide a state of the art survey for modal testing techniques of rotating structures, including discussions of the advantages and limitations in current models and methods. Gladwell and Bishop [60] examine the dynamics of an axially symmetric system composed of a flexible shaft rotating in flexible bearings, and present an analytical approach for free and forced motions of rotating shafts with massive bearings. Bauer [20] and Sheu and Yang [143] examine the vibrational

behavior of a beam rotating with a constant angular velocity for different boundary conditions and different angular velocities. Sheu and Yang [143] also include rotary inertia and gyroscopic moment effects, and they investigate the whirl speed, critical speed, and mode shapes of the rotating beam for different angular velocities. Katz et al. [91] and Han and Zu [75] examine the dynamic behavior of a simply-supported beam rotating at a constant angular velocity and subject to an axially moving load using Euler-Bernoulli, Rayleigh, and Timoshenko beam theories. Both studies found that Euler-Bernoulli beam theory is appropriate when the angular velocity and slenderness ratio are small.

Choi et al. [44] formulate the governing differential equations for the lateral vibration in two orthogonal planes and the torsional vibration of a straight, non-symmetric, rotating Timoshenko beam subject to a compressive axial load. The derivation also includes gyroscopic moment effects. Similarly, Chen and Liao [40], Liao and Dang [98], and Lee [94] derive the equations of motion for the lateral vibrations of a rotating pre-twisted Rayleigh beam subject to an axial compressive load. These studies also investigate the structural stability of such beams for different angular velocities and axial loads, and all three conclude that beams with larger pre-twist angles can sustain larger axial loads (compared to smaller or no pre-twist angles) before buckling occurs.

Much consideration for the actuators and sensors used to excite and measure the dynamic response of rotating structures is also needed. Although it is more convenient to use artificial/forced excitation in a controlled laboratory environment, this may not be the most convenient or practical means for obtaining the dynamic response of a rotating structure. The ability to capture the dynamic response of a rotating structure in operation (and without artificial excitation) is, therefore, desirable. This type of excitation is commonly referred to as *ambient excitation*, and modal analysis using ambient responses is often called Operational Modal Analysis (OMA) [19]. Further discussion and details of OMA techniques is in Section 2.3.2.

Measuring the dynamic response of a rotating structure in operation is also challenging. Contact-based sensors, such as accelerometers, strain gauges, etc., are problematic in such applications because they are intrusive to the operation (most often require system installation) and create added mass effects that alter the dynamic response of the system [34]. It is also difficult to transfer the signal data from the rotating structure to the analysis equipment using contact-based sensors. Thus, optical sensors, specifically Laser-based sensors, are attractive alternatives. Reinhardt et al. [122] use Laser Doppler Vibrometers to measure the dynamic response of two rotating cantilevered blades, and Rantatalo et al. [120] investigate the dynamic measurements of a rotating tool in a milling machine spindle using a Laser Doppler Vibrometer.

Halliwell [74] describes the development and advantages of the Laser Torsional Vibrometer (LTV). LTV sensors allow *in situ* torsional measurements of rotating machinery. Bell and Rothberg [21] use a parallel Laser Torsional Vibrometer setup to measure torsional vibrations of the crank-shaft of a running diesel engine. From these torsional measurements, they derive the pitch and yaw vibrations of the crank-shaft and identify the first bending natural frequency. Each of these studies demonstrate the advantages of using laser technology to measure the dynamic response of rotating structures in operation. A detailed description and further discussion of Laser-based technology are in Section 2.4.

2.3.2 Modal Analysis using Ambient Excitation

Ambient excitation is defined as the excitation experienced by a structure under normal operating conditions [146]. In dynamic measurements, ambient excitations are generally not recorded and the results and analysis are based on output-only (i.e. response of the system) measurements. For the development of on-line, real-time

SHM, ambient excitation, however, provides an attractive means of exciting the structure [18, 146]. Ambient measurements are specifically attractive in systems that are consistently subject to ambient excitations while in operation. For example, bridge structures undergo ambient excitations from several sources while in operation: traffic, pedestrians, wind, etc. Drill systems also undergo much ambient excitation while in operation. The drill motor system, whether rotary, percussive, sonic, etc., in general provide enough ambient excitation to yield measurable dynamic characteristics of the drill.

As output-only measurements are obtained using ambient excitation, FRF measurements are not possible. Modal analysis of ambient responses (i.e. OMA) is possible, however, and there are several techniques for determining the modal parameters of a structure from output-only measurements. The classical frequency domain approach often referred to as the basic frequency domain (BFD) technique is based on simple signal processing using a discrete Fourier transform to obtain the measured system response in the frequency domain, most commonly in the form of auto- or power- spectrums. The BFD technique assumes well separated modes can be estimated directly from the power spectral density matrix at the peaks [22, 27].

The frequency domain decomposition (FDD) technique is an extension of BFD that decomposes the power spectral density function matrix into a set of single DOF systems, each corresponding to one individual mode [27]. The FDD technique is an improvement to the BFD technique in that it identifies closely spaced modes well, but it does not provide damping information. The Enhanced Frequency Domain Decomposition (EFDD) technique is similar to the FDD technique and provides damping information and enhanced estimates of the frequencies and mode shapes of a system [85]. Several methods using output-only time domain data are also available including the Ibrahim Time Domain (ITD) method [83, 84], the polyreference time-domain method [160], and the Eigen Realization Algorithm (ERA) [89].

Many research efforts have focused on using these and similar techniques to determine the modal parameters of real structures under ambient excitation. Huang [82] identifies the dynamic characteristics of a three-span highway bridge using the multivariate AR (ARV) model, and Hermans and Van Der Auweraer [79] extract the modal parameters of a concrete bridge and the rear suspension of a driving car using two correlation-driven stochastic subspace techniques and the polyreference LSCE method. Andersen et al. [10] compare four identification techniques for an operating highway bridge structure, and Alam et al. [9] uses stochastic subspace identification (SSI) to demonstrate Operational Modal Analysis for on-orbit satellite appendages. Basseville et al. [18] also use the SSI method, formulated for non-simultaneous measurements, to determine the modal parameters of the Ariane V launcher, a helicopter, and the Swiss Z24 bridge, and describes how this technique can be used in the design of damage detection algorithms. Doebling and Farrar [52] evaluate the results of a flexibility-based damage detection method using ambient modal test techniques for a decommissioned highway bridge. Jaishi and Ren [86] and Reynders et al. [123] use operational modal test results for operating bridges to update structural finite element models to create a better correlation between the theoretical models and the experimental results. Further discussion of the use of ambient excitation in modal analysis techniques and SHM methods is provided in Sohn et al. [146].

2.3.3 Modal Analysis with Harmonic Excitation

As rotating structures undergo continuous self-excitation while in operation, it is advantageous to use ambient excitation and operational modal analysis (OMA) in determining the dynamic characteristics of such structures. Harmonic excitations due to unbalanced rotors, bearings, gear mesh systems, etc. in rotating structures, however, appear in the signal response and interfere with the signal analysis [26, 29, 85, 110]. This leads to inaccurate identification of modal parameters, which is an

obstacle that needs to be resolved.

OMA research has been conducted to identify the modal parameters of harmonically excited structures. Mohanty and Rixen [110] introduce a modified single-reference least-square complex exponential (LSCE) method to identify the modal parameters in the presence of harmonic excitations, assuming the harmonic frequencies are known *a priori*. The technique accurately identifies the modal parameters of a pinned-pinned beam under harmonic loads. Brincker et al. [26] use a developed harmonic indicator with the Frequency Domain Decomposition (FDD) technique to separate the harmonic and structural modes in an output-only signal of a plate excited by engine rotations. Jacobsen et al. [85] describes a new method based on the Enhanced Frequency Domain Decomposition (EFDD) technique that first identifies and then removes the harmonic components in the signal of a plate structure under harmonic excitations.

Removing the harmonic components from the signal response is also an attractive option before analyzing the signal and identifying the modal parameters of a rotating structure. Groover et al. [70] present an order removal algorithm to separate and remove harmonic components from signal responses of rotating equipment and demonstrates the algorithm on a rotating shaft. Serviere and Fabry [136] develop a source separation technique to separate harmonic noise from the dynamic signal of rotating structures and demonstrates the technique with simulations and rotating machine vibration data.

Filtering techniques have also been developed to remove unwanted noise and other components from signal data. Ruzzene [129] presents a filtering technique for analyzing the signal response of an artificially excited structure using guided waves. The filtering technique removes the incident wave from the signal response, which highlights the presence of reflections associated with damage(s). This technique is demonstrated on analytical and numerically simulated data, damaged aluminum and

composite specimens, and an aluminum plate with artificially seeded slits [13, 129].

Other research efforts use the harmonic components as a source of information for diagnosing the health of a rotating structure. Sinou and Lees [145] use the change of frequencies and the harmonics of a rotating shaft to detect the presence of a transverse breathing cracks, and Samuel and Pines [131] provide a state-of-the-art review of vibration-based techniques that utilize the change in dynamic characteristics and harmonics for helicopter transmission diagnostics.

2.4 Laser Doppler Velocimeter Sensors

Laser Doppler Velocimetry (LDV), first introduced by Y. Yeh and H.Z. Cummins in 1964 [164], is a technique for measuring the dynamic response of moving objects (fluids, solid structural surfaces, etc.) by measuring the component of velocity along the laser line-of-sight [54]. This measurement is based on the Doppler effect that occurs when the laser beam is scattered from a moving surface, creating a shift in the laser beam frequency.

As the velocities of a moving object are much smaller than the velocity of light, the frequency shifts in the laser beam cannot be measured directly [104]. Thus a reference beam is used, and the interference (interferometry technique [77]) between the measured and reference beam frequencies is used to measure the Doppler frequency shift. To determine the direction of the moving object, an acoustic-optic modulator is used to shift the reference beam frequency by 40 MHz [5, 104]. Thus, a modulation frequency of 40 MHz is observed if the object is at rest, and a value smaller or greater than 40 MHz is observed if the object is moving toward or away from the LDV sensor, respectively. A basic schematic of an LDV system is provided in Fig. 4, and a description of the Doppler effect and how it is used to measure the velocity of a moving object is provided in Appendix D.

LDV technology allows measurement capabilities and opportunities beyond what

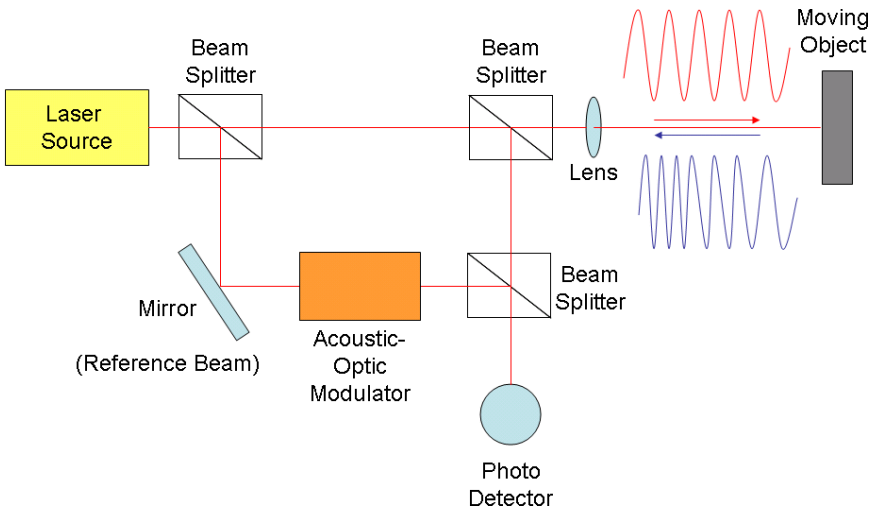

Figure 4: Schematic of Laser Doppler Velocimeter System [5, 141].

is available with more traditionally used contact-based sensors (such as accelerometers, strain gauges, etc.) [34]. LDV sensors provide a "remote" non-intrusive measurement technique as they do not require direct contact with the object or surface of interest. The moving object must only be optically visible. Therefore, objects that could not be measured using contact-based sensors because of their orientation, operating conditions or environment, or other conditions, such as extreme temperatures, can now be measured by LDV sensors. Added mass effects due to sensor attachment are also eliminated with LDV sensors, which allows for more accurate comparisons between theoretical and experimental results. This is especially important when analyzing small structures, such as MEMS.

Advancements in technology and various research efforts have made significant developments using LDV technology. P. Sriram and S. Hanagud [148, 149] present a capability for measuring distributed velocities by continuously oscillating an LDV sensor. Laser Doppler Vibrometers (also commonly referred to as LDVs) are fixed-point, Laser Doppler Velocimeter sensors that are generally very portable and user-friendly. Scanning Laser Doppler Vibrometers (SLDV), a commercially available sensor, can

collect rapid and precise point by point measurements over a specified grid, allowing for large surfaces to be measured with high spatial resolution and low testing time [34]. LDV technology is also used to produce sensors for measuring vibrations orthogonal to the optical axis (in-plane vibrations), torsional vibrations of a rotating surface, and three-dimensional measurements using three SLDV sensors [5].

LDV sensors are growing in popularity for use in the SHM field because of their value in many applications where more traditional sensors are problematic or infeasible [34]. For large civil structures, fixed-point LDV sensors and SLDV sensors are used to measure the ambient vibration response and detect damages [41,59]. SLDV sensors are also widely used in research efforts to estimate damage [12, 133, 139, 140] and detect fatigue cracks in beams and plates [97,150] as well as delaminations in composite materials [36]. To measure the rotational response of rotating objects, such as shafts and rotors, various methods using LDV technology are investigated and implemented. These include using two parallel LDV sensors [21,128] and a Laser Torsional Vibrometer (LTV) [108] to measure the rotational and translational vibrations of a rotating object, and a Tracking Laser Vibrometer (TLV) to track and measure the vibrations of a specific point or grid of points on a moving object [35]. As three-dimensional SLDV units are currently very expensive and cumbersome, research efforts are also conducted to capture measurements in multiple directions using either three fixed-point LDV sensors [109] or three measurements from one SLDV sensor [133, 139]. A state-of-the-art review of LDV technology through 2006 is in P. Castellini et al. [34].

2.5 Neural Networks

Inspired by biological nervous systems, artificial Neural Networks (NN) are composed of simple elements (neurons) operating in parallel, which are commonly adjusted, or trained, so that a particular input leads to a specific target output [48]. Neural Networks have been trained to perform complex functions in various fields of application

including pattern recognition, identification, and control systems.

Although Neural Networks appear to be a recent development and research interest, the first artificial neuron is traced back to 1943 by neurophysiologist Warren McCulloch and logician Walter Pits. Important advancements in technology and the NN field over the years have increased the capabilities and enthusiasm for Neural Networks. A detailed breakdown of the history and basic concepts of Neural Networks are provided in Stergiou et al. [151] and Widrow et al. [162].

Neural Networks, like people, learn from example [151]. A diagram of a simple neuron is in Fig. 5. Unlike conventional computers, NNs are not trained to perform a specific task. They are trained to solve a specific problem, and the network solves the problem on its own with the user-set parameters. Therefore, the training process is unpredictable and not unique.

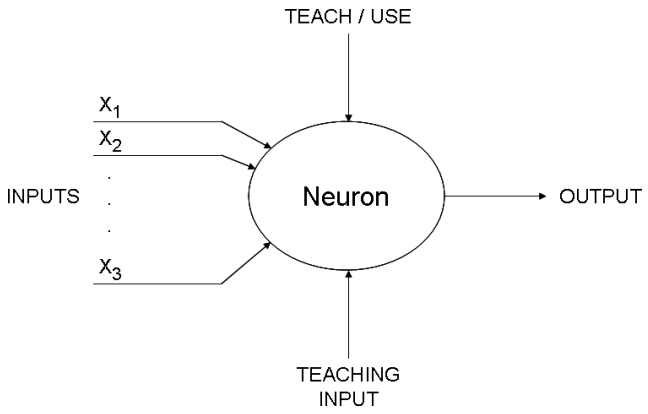

Figure 5: Diagram of Simple Neuron [151].

The most common type of Neural Networks consists of three groups, or layers: the input layer, one or more hidden layers, and the output layer. Figure 6 is a diagram of a feed-forward multi-layer Neural Network. Feed-forward NNs allow signals to travel from input to output only (i.e. there are no feedback loops). These NNs are straight forward and are extensively used in pattern recognition [23, 33, 126]. Pattern recognition is the scientific discipline of taking raw data and classifying the data into

a number of categories [56, 157], and it is useful in a number of fields including computer science, artificial intelligence, and medicine. Pattern recognition is also useful in SHM because it provides a probabilistic means of identifying and characterizing defects and damages of a structure based on changes in the dynamic response. Many SHM techniques use pattern recognition via Neural Networks to detect, localize, and quantify damage in structural systems [38, 43, 102, 146, 158].

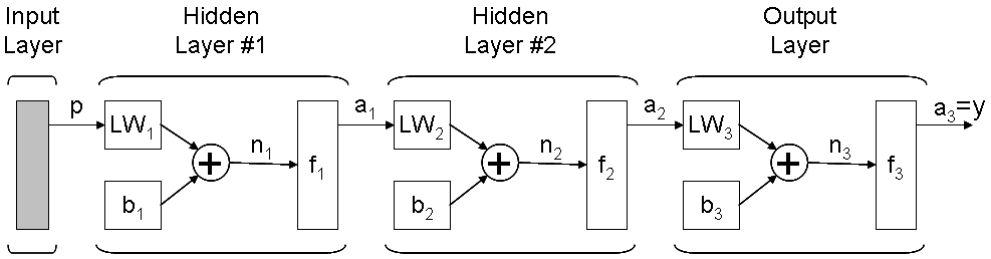

Figure 6: Feed-Forward Multi-Layer Neural Network [48] (p=input values, LW_i=weights for layer i, b_i=biases, n_i=net input vector, f_i=transfer function, a_i=layer outputs, y=network output).

There are a number of parameters to consider when training NNs: fixed or adaptive learning, supervised or unsupervised training, layer transfer functions, etc. Neural Networks are trained using a fixed or adaptive learning process. Fixed learning processes use fixed weights and biases for training while adaptive learning processes change/update the weights and biases throughout the training process. For more involved data sets, the adaptive learning process is preferred.

The training process of NNs can be supervised or unsupervised. Supervised learning compares the target output with the NN output and computes the error convergence. The Mean Square Error (MSE) is a common method used to determine the convergence error. MSE is calculated as

$$MSE = \frac{1}{N}\sum_{j=1}^{N} e(j)^2 = [t(j) - a(j)]^2 \tag{1}$$

where N is the size of the training data, and t and a are the target and NN outputs, respectively [48]. The ultimate goal is to minimize the MSE during the training

process. Supervised learning is most commonly conducted off-line where unsupervised learning, which only uses local information for training, is conducted on-line.

The most common transfer functions used in training Neural Networks are the hard-limit, linear, and sigmoid transfer functions. The hard-limit transfer function limits the neuron outputs to either 0 or 1, the linear transfer function computes a linear approximation for the neuron outputs, and the sigmoid transfer function computes a continuous, non-linear approximation (often between -1 and 1) for the neuron outputs. Figure 7 provides diagrams of these three types of transfer functions. The italicized labels are the respective function names in MATLAB.

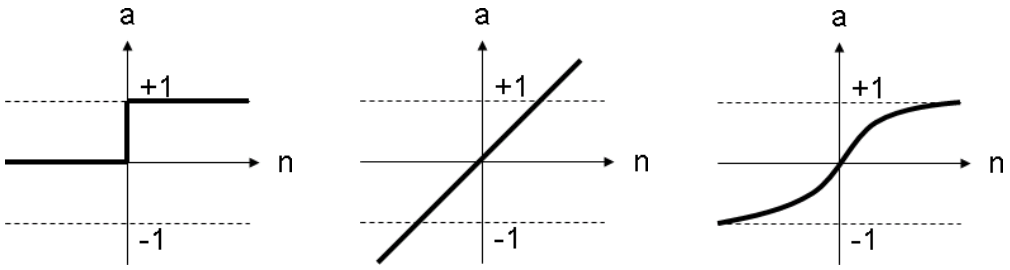

(a) Hard-Limit *hardlim* (b) Linear *purelin* (c) Sigmoid *tansig*

Figure 7: Three Common Transfer Functions for Training Neural Networks [48].

The backpropagation algorithm is a supervised, adaptive learning technique developed in 1986. According to Widrow et al. [162], the backpropagation technique is unquestionably the most influential development in the NN field during the 1980s. The backpropagation technique presents an input pattern to the network, completes one iteration to produce an output, and then computes the error between the target and NN output values (most commonly using the MSE). The technique then sweeps backward through the network to compute error gradients for each output and finally updates the training weights and biases based on these error gradients. This process is continued for a set number of iterations or until a minimum MSE is met. The backpropagation technique is a convergent method for the training process of Neural Networks, and the training accuracy depends on the complexity of the training data,

the desired MSE, and the available computing power. Figure 8 is a flow chart of the backpropagation training process.

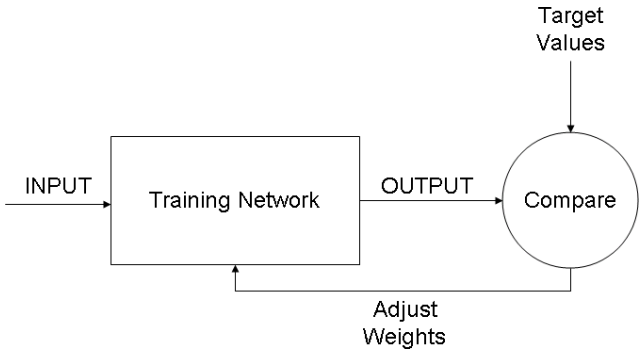

Figure 8: Backpropagation Training Process for Neural Networks.

Several SHM studies implement feed-forward, backpropagation NNs to detect the existence, location, and size of damages in structural systems. Tsou and Shen [158] use feed-forward, backpropagation NNs to identify the location(s) and severity of damages of discrete structural systems for a real-time, on-line SHM device. Luo and Hanagud [102] use an improved training method for feed-forward, backpropagation NNs to detect delaminations and impact damage of composite structures in real-time. Jenq and Lee [88] and Sanders et al. [132] study the use of feed-forward, backpropagation NNs to predict the size and location of delamination within composite plates and beams. These studies demonstrate the advantages of feed-forward, backpropagation Neural Networks in SHM as an on-line, adaptive tool for detecting damage and other defects in structural systems.

CHAPTER III

RESEARCH OBJECTIVES & DESIGN APPROACH

3.1 Objectives

The objective of this thesis work is to conduct basic research that leads to the formulation of a structural health monitoring method for rotating structures, specifically automated drill systems used for interplanetary subsurface exploration. The formulation of such an SHM method involves strict and unique restrictions compared with most SHM techniques developed to date. These restrictions motivate the following research issues and objectives:

1. Unlike most current SHM procedures for aerospace systems (such as aircraft) that remove the system from service to complete inspections and maintenance in depot environments, structural and mechanical systems, such as interplanetary subsurface drills, require SHM while the system is in full operation. Thus, the first objective is to formulate an SHM method with "real-time" capabilities.

2. In "real-time" SHM capabilities, the common practice of using external actuators (such as impact hammers, shaker devices, piezo-electric transducers, etc.) is impractical. Thus, the second objective is to use the rotating mechanism (e.g. drill motor system) as an internal actuator.

3. Use of more common contact-based sensors (such as accelerometers, strain gauges, etc.) for dynamic measurements of rotating structures is intrusive and problematic. In the operating drill system, there are also considerable limitations for transmitting SHM sensor data to the appropriate analysis and diagnostic equipment. The third objective is therefore to formulate a "real-time"

SHM method using non-contact sensors.

4. Due to the limited available power for drilling operations (e.g. 100 Watts for the DAME drill), drilling performance parameters (rotation speed, rate of penetration, etc.) are greatly restricted compared to terrestrial drilling, which makes interplanetary drilling operations more susceptible to fault and failure conditions. Thus, the fourth objective is to identify fault or failure conditions that have the potential to halt or stop the drilling operation or cause failures in the drill structure.

5. Due to the unpredictable and varying subsurface conditions of Mars and other celestial objects, the fifth thesis objective is to update the expected fault conditions from learning experience.

6. To compare the current dynamic response of the operating drill structure with theoretical models, the sixth objective is to formulate structural dynamic models for the drill system under damage or various fault conditions. The formulation of structural dynamic models also provides a means to predict various fault conditions in terms of probabilities before they occur.

7. Because real-time dynamic measurements and SHM are needed, the sensor data contains rotation harmonics due to the drill's gear mesh system. The seventh objective is therefore to formulate an SHM procedure for rotating structures that include rotation harmonics in the signal data.

8. In practice, the operation of the interplanetary exploration drill requires rapid SHM data to identify drilling fault conditions before any failures occur, initiate appropriate corrective actions, and allow for a continuous drilling operation. Thus, the eighth objective is to implement trained Neural Networks to rapidly analyze the dynamic signal of the drill structure and provide SHM results.

9. As the dynamic response and boundary conditions of the drill auger tube include the drilling parameters (rotation speed, rate of penetration, down-hole force, etc.), the ninth objective is to use the current drilling parameters (i.e. drill telemetry provided by the on-board sensors) to better define the dynamics of the drill auger tube and predict the health of the drilling operation.

10. To provide complete autonomous operations of the interplanetary subsurface drill system, the final research objective is to automate the entire SHM procedure.

3.2 Thesis Approach & Outline

To meet the thesis objectives, an SHM technique that utilizes dynamic analysis of rotating structures and the associated structural dynamic models are needed. The foundation for such an SHM is that each drilling fault uniquely alters the dynamic response and characteristics of the drill system (specifically the boundary conditions), which is identified using modal analysis techniques. Thus, the thesis approach and outline are as follows.

- To validate a procedure for measurements of rotating structures and understand the dynamic characteristics of the prototype subsurface drill system, modal analysis experiments were conducted and the dynamic response analyzed. These modal analysis experiments validated the use and advantages of LDV sensors for space-related SHM measurements. As the SHM technique must monitor the drill system while in operation, a signal filter to identify and remove the harmonic components (due to the gear mesh system) has been designed and implemented. Multi-dimensional experiments were also conducted to measure the dynamic response in two orthogonal directions and validate a procedure for using one fixed-point LDV sensor to capture the dynamic response in multiple

directions. A detailed description of the completed modal analysis experiments is provided in Chapter 4.

- In parallel with the modal analysis experiments, theoretical models to represent the drill under nominal and drilling fault conditions were formulated. Baseline and nominal drilling models were developed and analyzed to determine what drilling parameters were negligible, and these models were compared with the results from the experiments. Structural dynamic models for the six identified and expected drilling faults were then developed. Each drilling fault condition was thoroughly analyzed to establish how the fault will alter the boundary conditions of the drill auger tube and determine the best model to represent this change. The natural frequency shifts due to each drilling fault were then evaluated. A detailed description of the development and analysis of these structural dynamic models is provided in Chapter 5.

- To automate the signal analysis and produce diagnostics, automation algorithms and procedures, and the corresponding software, were developed. To analyze the signal response of the drill, a peak-picking algorithm has been developed to decipher the (filtered) drill signal and determine the natural frequencies of the auger tube. The selected frequencies are then compared with the developed structural dynamic models through trained Neural Networks, and the Neural Network results and additional dynamic drilling variables (from the drill telemetry) are used to identify the fault-diagnostics. Finally, to automate the complete SHM technique, from collecting the dynamic signal to producing the SHM diagnostics to relaying these diagnostics to the drill Executive computer, an automation procedure and the corresponding software have been developed. Detailed descriptions of the design and development of this automation procedure and the individual components are provided in Chapter 6.

- To test and validate the completed autonomous SHM technique, three field tests have been completed. Two of the field tests were completed at a remote Mars-analog site, which provided a more practical testing environment (approximately similar to environments expected for interplanetary subsurface exploration) for the drill hardware and software compared with laboratory experiments. The third field test was a two-week "blind" test and demonstration. From these field tests, the autonomous SHM technique accurately predicted all six expected drilling faults and proved to be a valuable part of the interplanetary subsurface drill system. A detailed description of these field tests is provided in Chapter 7.

- Lastly, concluding remarks and research contributions are provided in Chapter 8. The significant research contributions from this thesis work include the formulation of an autonomous, on-line, "real-time" SHM method that has been demonstrated on a real structural system in its operating environment with minimal sensors, a complete analysis of complex structural dynamic models, and demonstration of automated SHM techniques for rotating flexible structures requiring real-time controls. Recommendations for future research efforts are also listed.

CHAPTER IV

MODAL ANALYSIS OF ROTATING STRUCTURES

One of the objectives of this thesis work focuses on modal analysis of rotating structures with specific applications to an interplanetary subsurface drill system. The following sections describe preliminary findings regarding the dynamic characteristics of the drill prototype, laboratory experiments conducted on the drill, a developed signal filter to remove harmonic components from the signal of the rotating drill structure, two-dimensional experiments conducted on a cantilevered aluminum beam and the drill prototype, and finally discussions on the bounds for using LDV sensors in subsurface exploration applications.

4.1 Preliminary Findings

The SHM procedure formulated for interplanetary subsurface drills used the DAME drill system as the primary test vehicle for laboratory and field tests and analysis. The DAME drill system is comprised of an aluminum platform, drill column for axial motion, drill head for casing the motor system and securing the auger tube, and auger tubes (also referred to as drill strings) 87.5 to 100 cm in length. The drill system was relatively simple in its design as the focus of the DAME project was to develop automated drilling operations and procedures. Automated drill string and sample handling was the primary focus for the sister project, MARTE. Thus, adding, replacing, and removing drill strings was done manually. A picture of this drill system is provided in Fig. 9.

Two preliminary field tests on this drill system were conducted at the Haughton Crater Research Station (HCRS) [63] in 2004 and 2005. The goals of these preliminary field campaigns were to test the drill hardware, construct a procedure for the drilling

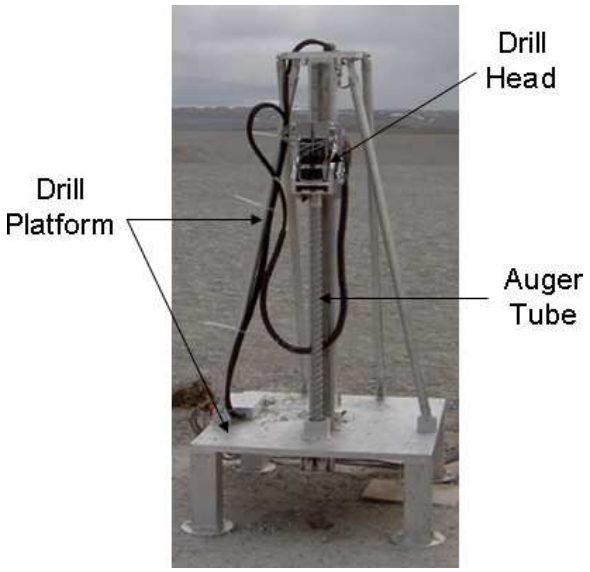

Figure 9: Space Drill Prototype for DAME Project.

operations and automation software, and identify the expected drilling faults. Drilling faults were defined as any condition that hinders progress with the normal drilling procedure and, if not dealt with in a timely manner, had the potential to result in a catastrophic event for the drill structure and mission. The drilling operation included recovery procedures if any drilling fault was encountered (or was expected to occur) to ensure the safety of the drill and continuation of the drilling operation and objectives. Six drilling faults were identified and classified during the preliminary field tests. A detailed description of these drilling faults is provided in Chapter 5.

Other findings during the preliminary field tests include the following:

- The dynamic response of the drill auger tube is sufficient for determining the dynamic characteristics of the drill structure and analyzing the drill condition.
- Under nominal drilling conditions, given the restricted power consumption, the rotational speed, rate of penetration, and down-hole force have negligible effects on the dynamic response of the drill auger tube.
- The vibrations created by the drilling operation adequately excite the dynamic

response of the drill auger tube for dynamic measurements.

- The drill's gear mesh system produces incremental frequencies in the signal response of the drill that interfere with the signal analysis and diagnostics.

These preliminary findings helped formulate the objectives of the SHM technique for interplanetary exploration drills and also provided more insight to the dynamic characteristics of the drill system. Using the auger tube as the primary source for understanding and predicting the behavior of the drill allowed the use of simple structural dynamic models.

4.2 Modal Analysis Experiments & LDV Validation

To understand the dynamic characteristics of the drill system, numerous modal analysis experiments have been completed. These experiments also provided validation for using LDV sensors to capture the signal response of the auger tube and the drill motor system as an internal actuator.

The use of LDV sensors in this thesis work has many benefits compared with accelerometers and other contact-based sensors. To measure the dynamic response of the drill auger tube, each accelerometer needs to be installed in the auger tube and will only measure the response at the installed location. Each installed accelerometer also requires a bus-line in the auger tube to transfer the data, which complicates manufacturing, installation, and system setup of the drill and auger tube. LDV sensors can be positioned practically anywhere, which provides much flexibility in the location of the sensor and the measuring points. They also do not require any of the bus-lines in the auger tube.

Wireless sensors and wireless sensor networks (WSN) offer a means of transferring the dynamic drill signal without the limited auger tube bus-lines, and several studies have investigated the benefits of using wireless sensors in structural health monitoring

techniques [15, 93, 103, 116, 163]. A considerable limitation to wireless sensors, however, is the battery life, which is significantly more problematic with interplanetary exploration missions. The transmission of the signal data through the auger tube(s) is also a concern as the auger tubes are not completely hollow and may block the transmitting data. Therefore, wireless sensors are not investigated further in this thesis work.

Lastly, as the auger tube is a slender tube and portability of any applied sensors is important, SLDV sensors are not feasible for this application. Thus, fixed-point LDV sensors are the ideal sensor type for space drilling applications and is used throughout this thesis work.

4.2.1 Experimental Equipment & Set-Up

This section details the tools and equipment used throughout the modal analysis laboratory experiments. Table 1 provides a list of the actuator and sensor equipment used. When the drill system was stationary, an impulse hammer (086B01 from PCB Piezotronics, Inc.) was used to excite the auger tube. When the drill system was in operation, the drill motor system was used as an internal actuator (i.e. an external actuator was not used). The drill motor system was a 90-tooth gear mesh system comprised of two electronically commutated DC minimotors (from Maxon Motors).

To capture the signal, two types of sensors were used: an accelerometer and LDV sensor. The accelerometer was a shear accelerometer (352C23 from PCB Piezotronics, Inc.), which has a 2 Hz to 10 kHz frequency range. The accelerometer was only used for stationary experiments. The LDV sensor was a fixed-point vibrometer (PDV-100 from Polytec [118]), which has a 0 to 22 kHz frequency range and a working distance for accurate measurements of 0.2 to 30!m. The LDV sensor was used for all the experiments positioned approximately 1.5 m from the auger tube.

A SigLab Data Acquisition system (from Spectral Dynamics [147]) was used to

Table 1: Actuator & Sensor Equipment for Drill Experiments

Device	Specifications		Experiments		
	Sensitivity	Voltage Range	Stationary	Rotating	Drilling
Impulse Hammer	1000 lb/V	± 5 V	✓		
Drill Motor	NA	NA		✓	✓
Accelerometer	197.6 G/V	± 2.5 V	✓		
LDV	25 mm/s/V	± 5 V	✓	✓	✓

record the signal from the sensors and any external actuators. The SigLab unit included four input channels and two output channels. For the input channels, SigLab is equipped with a dynamic signal analyzer (VNA) that is capable of measuring multi-channel time histories, power spectrums, transfer functions, impulse responses, fast-fourier transforms, etc. For the output channels, SigLab is equipped with a virtual function generator (VFG), which is a general purpose signal source featuring periodic functions (sine, square, impulse, etc.), chirp functions, random noise, etc. The virtual function generator is useful when external actuators such as shakers and piezoelectric transducers are used.

The dynamic signal analyzer allows the user to define a number of settings for the measurement data and individual input channels. The measurement settings include the frequency bandwidth and record length, trigger source, FFT analysis window (boxcar, hanning, etc.), and number of averaging samples. The input channel settings include the sensitivity and voltage range for each actuator and sensor used. The measurement parameters used for these experiments are provided in Table 2 and a diagram of the experimental setup is provided in Fig. 10.

For the completed experiments, the dynamic signal analyzer in SigLab was used to measure and process the signal from the impulse hammer, accelerometer, and LDV sensor, and MATLAB was used for post-processing the data and analyzing the results. The dynamic signal analyzer completed a fast Fourier transform (FFT) of the incoming signals, which was averaged over the specified number of measurement

Table 2: SigLab Settings for Drill Experiments

Experiment	Stationary	Rotating	Drilling
Frequency Settings:			
Bandwidth	1.0 kHz	1.0 kHz	1.0 kHz
Anti-Alias Filter	On	On	On
Record Length	2048	2048	2048
Resolution	1.25 Hz	1.25 Hz	1.25 Hz
Sample Processing:			
Mode	Add	Add	Add
Zero Padding	Off	Off	Off
Average Count	10	25	25
Overload Reject	On	On	On
Overlap Range	0%	50%	50%
FFT Analysis Window	Boxcar	Hanning	Hanning
Sample Trigger:			
Mode	Every Frame	Off (Free Run)	Off (Free Run)
Threshold	9%	NA	NA
Filter Button	NoFilt	NA	NA
Slope	Positive	NA	NA
Delay	-0.5	NA	NA

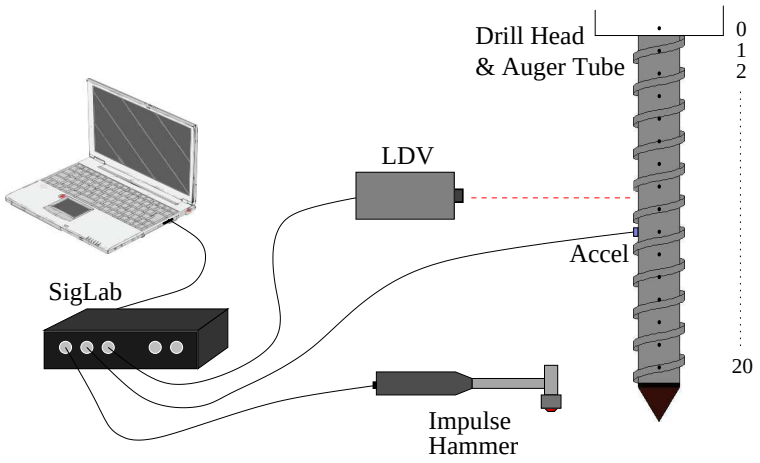

Figure 10: Diagram of Equipment Setup for Laboratory Experiments.

samples, and estimated cross-channel measurements (such as the frequency response function) using a broad-band FFT analyzer. When using the impulse hammer, the drill response in the form of a frequency response function (FRF) was analyzed. When using the drill motor system as an internal actuator, the drill response in the form of an auto-spectrum (squared magnitude of the frequency spectrum) was analyzed.

4.2.2 Stationary Tests

The first set of experiments were conducted while the auger tube was free-standing and stationary. A photograph of the drill system is provided in Fig. 11. The dynamic response was captured at 21 equally spaced points along the auger tube to determine the natural frequencies and mode shapes of the auger tube. The magnitude of a sample frequency response function from these experiments is provided in Fig. 12. The dynamic response was captured by the accelerometer and LDV sensor, and the first two natural frequencies of the auger tube were identified (highlighted with asterisks). These experiments and results also validated the use of the LDV sensors compared with the more traditionally used accelerometer.

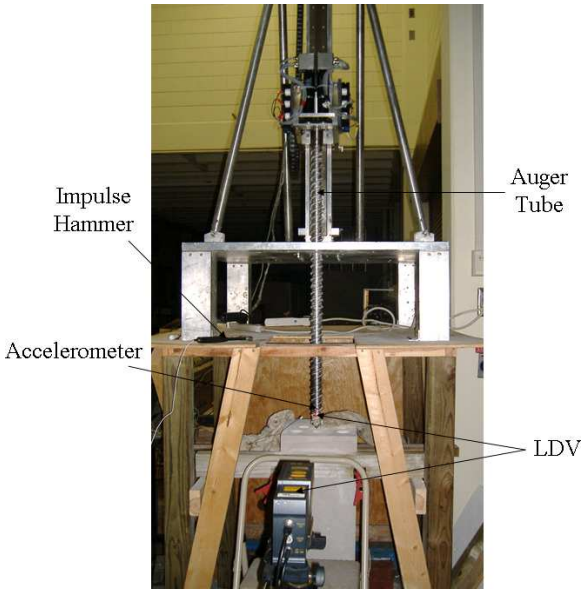

Figure 11: Drill System Set-Up for Stationary Experiments.

From these experiments, the first two frequencies of the auger tube were found to be 9 Hz and 95 Hz. For simplification, it is assumed that the damping coefficient is small (see Appendix C). Thus, the natural frequencies of the auger tube are selected as the peaks in the dynamic response, and the mode shapes are the operational deflection shapes at these peaks [7, 135]. The first two mode shapes of the stationary auger tube and a polyfit curve for each were as shown in Fig. 13. The points along

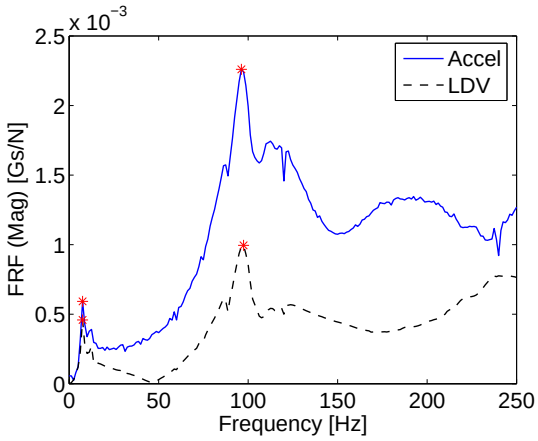

Figure 12: Impulse Hammer Dynamic Response of Stationary Drill Auger Tube.

the auger were in ascending order with point 0 at the fixed end and point 20 at the free end (Fig. 10). From these plots, it is seen that the free-standing, stationary auger tube had similar mode shapes to a fixed-free beam.

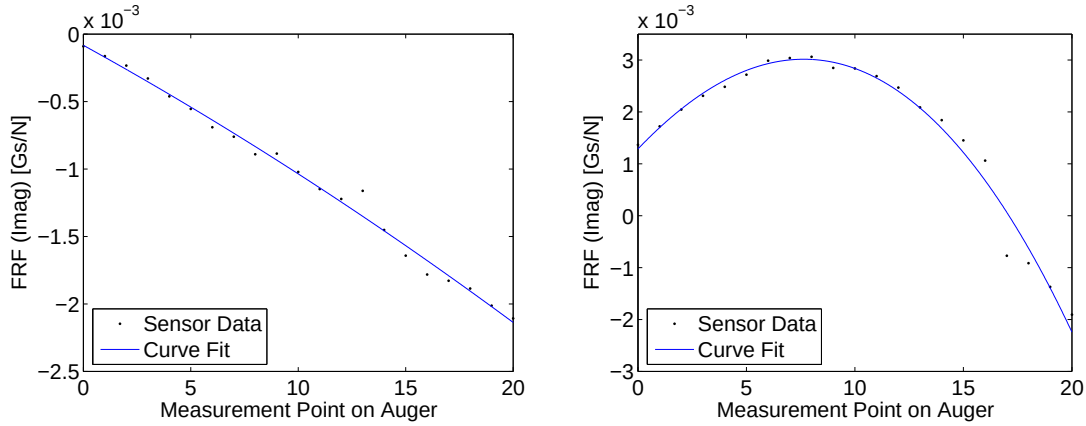

(a) First Mode (b) Second Mode

Figure 13: First Two Mode Shapes of Free-Standing, Stationary Auger Tube.

4.2.3 Rotating Tests

Experiments while the auger tube was rotating in place were conducted. The dynamic response of the drill rotating at 10 RPM and 45 RPM were as shown in Fig. 4. The first two natural frequencies of the auger tube were present in the dynamic response (peaks indicated by asterisks), and they have not altered from the frequencies

found in the stationary experiments. Therefore, these experiments confirmed the drill motors adequately excited the auger tube for dynamic response measurements and the rotational speed conditions had negligible effects on the dynamic characteristics of the auger tube.

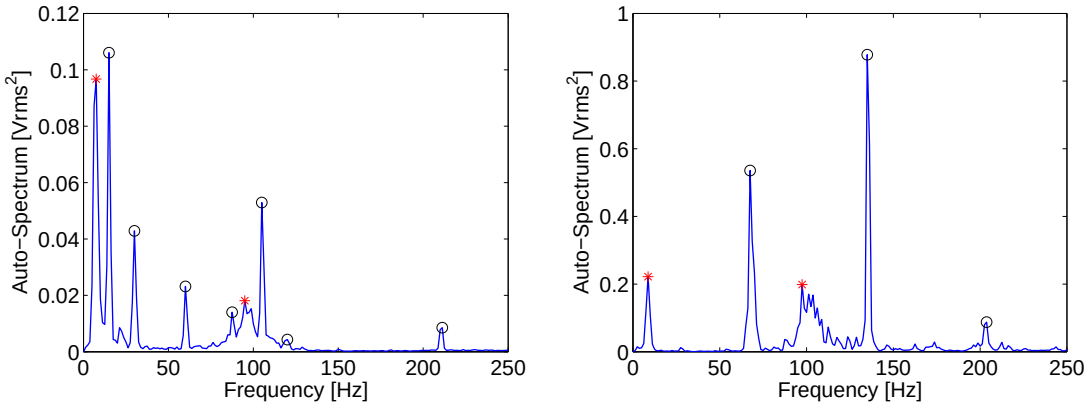

(a) 10 RPM (b) 45 RPM

Figure 14: Rotating Dynamic Response of Drill Auger Tube.

It was also important to note the incremental (harmonic) frequencies present in the dynamic response of the rotating auger tube (peaks indicated by circles). These frequencies were created by the drill's gear mesh system and are present whenever the drill motors are in operation.

4.2.4 Drilling Tests

Drilling tests were conducted to study the dynamic response of the auger tube under nominal drilling conditions and to validate theoretical models. Nominal drilling conditions were based on the expected drilling parameters (rotation speed, rate of penetration, down-hole force, etc.) for nominal drilling operations, and these parameters were defined from the preliminary field tests in Devon Island, Canada, and the restrictions on the drilling operation due to the limited available power (100 Watts). The drilling parameters for these experiments were therefore set to a maximum rate of penetration (ROP) of 0.3 cm/min, maximum down-hole force of 500 N, and 45 RPM

auger speed.

These tests were completed by drilling into a fixed limestone column (11 in × 11 in × 3 ft). Limestone was chosen because it is a softer sedimentary rock that is similar to materials encountered in the preliminary field tests and can test the drill system under nominal drilling conditions. A photograph of the experimental set-up is provided in Fig. 15.

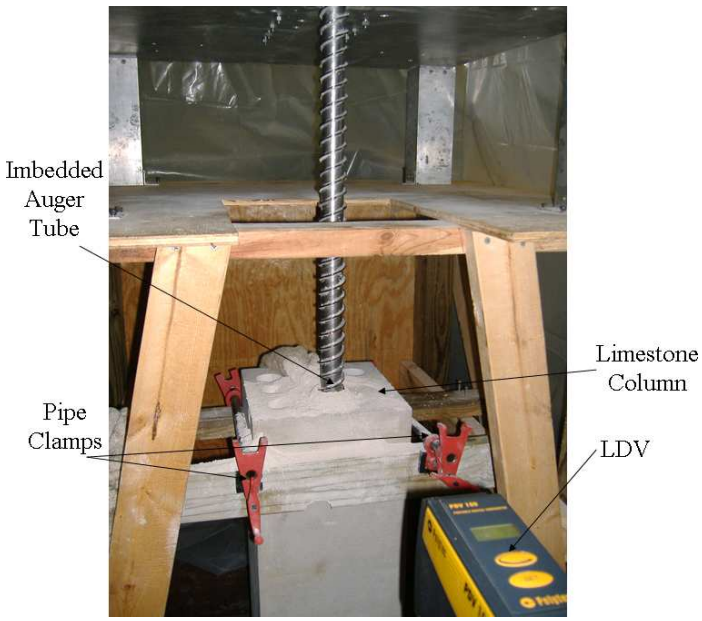

Figure 15: Drill System Set-Up for Drilling Experiments.

A final depth of 70 cm was reached, and dynamic measurements via the LDV sensor were collected continuously throughout the drilling operation. Two auto-spectrum samples of the nominally drilling auger tube are provided in Fig. 16. The determined natural frequencies are indicated with asterisks and the harmonic frequencies due to the gear mesh system are indicated with circles.

Stationary tests were also completed at 10 cm drill depth increments to analyze the changes in the dynamic characteristics of the embedded auger tube. The magnitude of two frequency response samples of the embedded 2 m auger tube (30 cm and 70 cm drill depths) are provided in Fig. 17, and the first two mode shapes for each are provided in Fig. 18. The natural frequencies for the stationary embedded auger tube

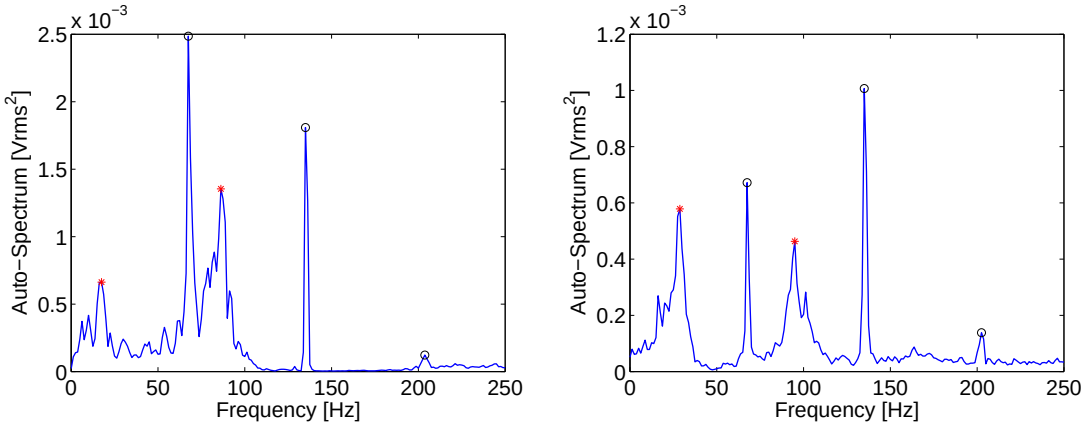

(a) 1m Auger, 14cm Depth (b) 2m Auger, 43cm Depth

Figure 16: Nominal Drilling Dynamic Response of Auger Tube.

were determined and are listed in Table 3. From these results, it was concluded that the natural frequencies of the auger tube increased with increasing drill depths, which was a result of the bore-hole wall creating frictional side supports on the partially embedded auger tube.

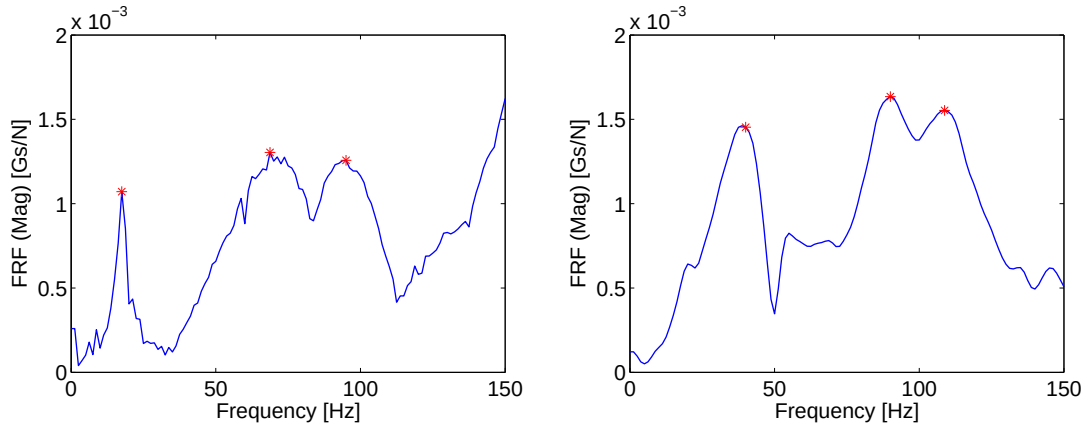

(a) 30cm Depth (b) 70cm Depth

Figure 17: Impulse Hammer Dynamic Response of Embedded 2m Auger Tube.

4.3 Harmonic Excitation Signal Filter

Rotating structures experience harmonic excitation while in operation, and this harmonic excitation creates harmonic components in the measured dynamic response of

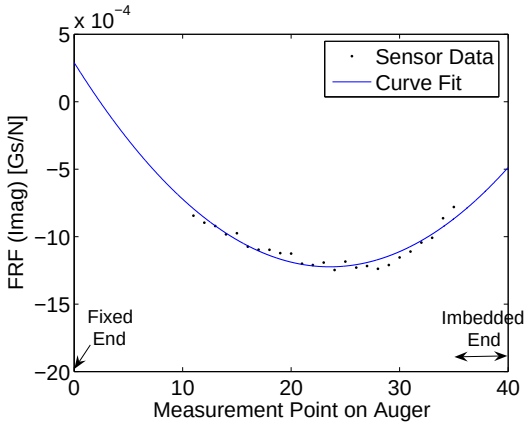

(a) 1st Mode: 30 cm Depth

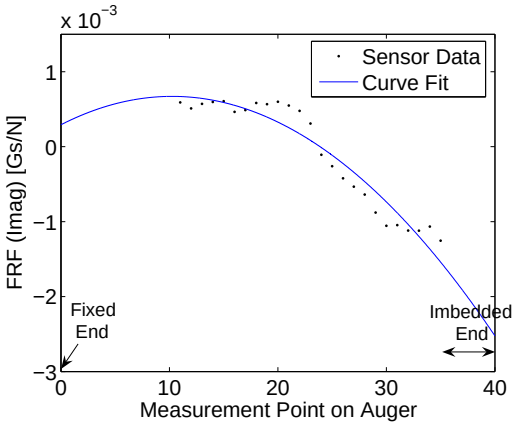

(b) 2nd Mode: 30 cm Depth

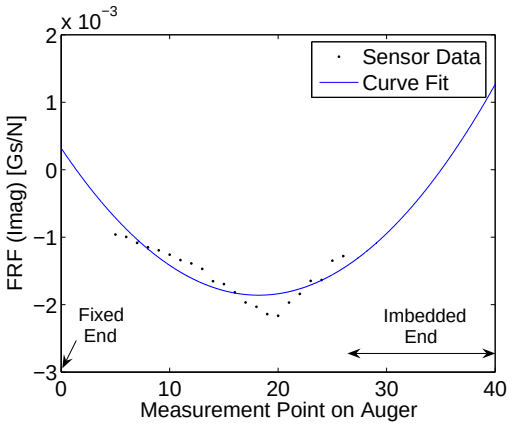

(c) 1st Mode: 70 cm Depth

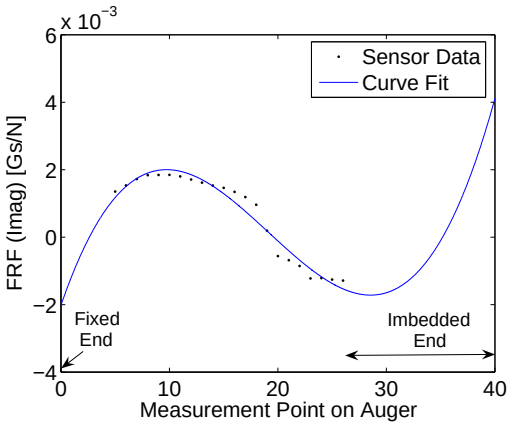

(d) 2nd Mode: 70 cm Depth

Figure 18: Mode Shapes of Embedded 2m Auger Tube.

Table 3: Auger Tube Natural Frequencies

Auger Length (m)	Drill Depth (cm)	Embedded Auger (%)	1st Mode (Hz)	2nd Mode (Hz)
1	0	0	9	95
1	10	10	41	111
1	20	20	58	119
1	30	30	71	131
2	30	15	17	60
2	40	20	20	61
2	50	25	23	62
2	60	30	36	81
2	70	35	42	94

the rotating structure and interferes with the signal analysis and modal identification [26,29,85,110]. As described from the preliminary field tests and presented in the laboratory experiments, the drill gear mesh system produces harmonic frequencies in the dynamic response of the drill auger tube. (Note the incrementing 67.5 Hz peaks in Fig. 14(b).) These incremental frequencies often dominate the signal and can interfere with the signal analysis and diagnostics. Therefore, a signal filter is needed to remove the incremental frequencies before the drill signal is analyzed.

4.3.1 Signal Filters

A filter is a signal processing system that modifies the characteristics of a signal [42]. The subject of signal processing and filter design is very extensive. Orfanidis [113] and Chirlian [42] provide an overview of this field and common design methods. Signal filters are divided into analog (continuous) and digital (discrete) filters, and infinite impulse response (IIR) and finite impulse response (FIR) filters. There are advantages and disadvantages to each filter type, and the optimal filter type is dependent on the specific application, the number of necessary filters, and the facilities available to the designer [14].

For all filter types, the passband is the region of interest, and the stopband, or rejection band, is the region to be filtered. The four most common types of filters are low-pass, high-pass, bandpass, and bandstop. Low-pass filters are designed to pass low frequencies and attenuate the signal beyond a cut-off frequency (ω_c). High-pass filters are the opposite of low-pass filters where they attenuate the signal up to a cut-off frequency (ω_c) and pass frequencies beyond the cut-off frequency. Bandpass filters are a combination of low-pass and high-pass filters where they pass the signal for a specified frequency domain ($\omega_1 \leq \omega \leq \omega_2$) and attenuate the signal outside of this domain. Bandstop filters are the opposite of bandpass filters where the signal is attenuated for a specified frequency domain ($\omega_1 \leq \omega \leq \omega_2$) and all other frequencies

are passed. Figure 19 provides the magnitude of the transfer function for these four filter types [113]. These graphs are ideal representations (no tolerances) of each filter type. In practice, filter characteristics are specified with tolerances.

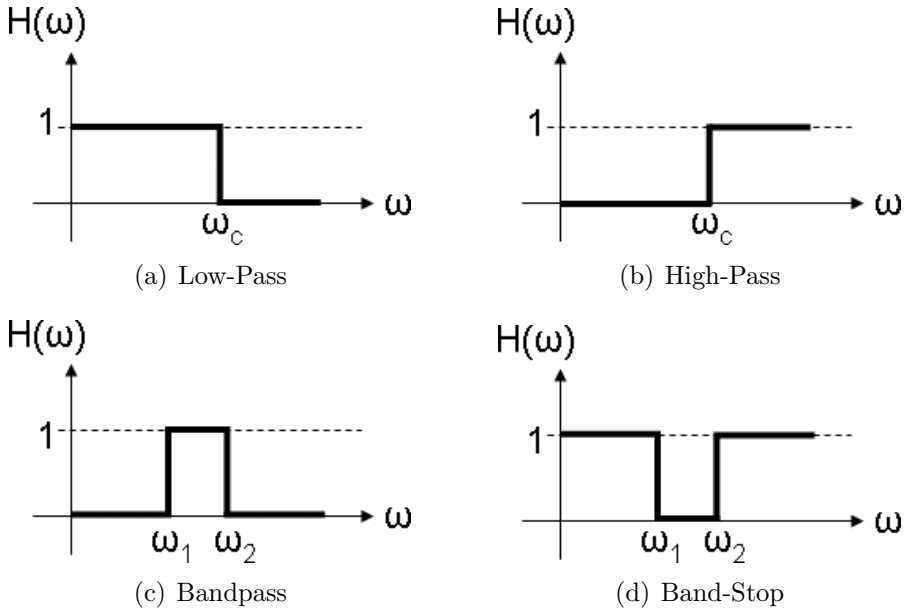

(a) Low-Pass (b) High-Pass

(c) Bandpass (d) Band-Stop

Figure 19: Magnitude of Ideal Transfer Function for Four Common Filter Types.

A key advantage to using infinite impulse response (IIR) filters is smaller implementation costs when compared to finite impulse response (FIR) filter counterparts [101]. The most common IIR filters are Butterworth, Chebyshev (Type I and II), and Elliptic. Figure 20 provides an example of these four IIR filters for fifth order low-pass and bandstop filter designs. From Fig. 20(a), it is seen that the Chebyshev filters are sharper than the Butterworth filter with less equiripple than the Elliptic filter. Equiripple refers to the oscillatory response of the filter in the passband and/or stopband. From the bandstop example (Fig. 20(b)), it is also seen that the Chebyshev Type I filter is sharper than the Butterworth and Chebyshev Type II filters and, unlike the Chebyshev Type II and Elliptic filters, has no equirriple in the bandstop region. This is an important distinction as the bandstop filter is necessary for filtering the harmonic components of the rotating drill signal.

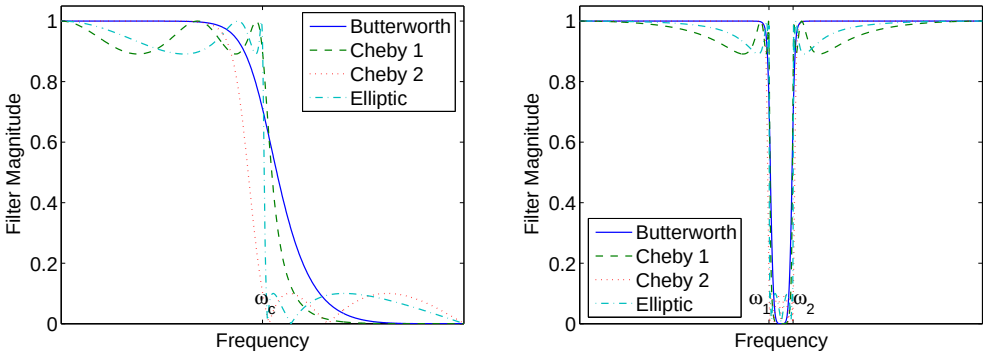

(a) Low-Pass (b) Bandstop

Figure 20: Example of Common IIR Filters ($n = 5$).

This thesis work focuses on the Chebyshev filter design, which is available in MATLAB software [101]. Chebyshev filters are higher-order IIR filters based on the Chebyshev polynomial. These filters are advantageous because they minimize the error between the ideal and actual filter characteristics over the range of the filter, and they are commonly used in noise filtering processes [101, 115]. Pahk et al. [115] also demonstrate the advantages of Chebyshev filters to improve the positional accuracy and remove the noise components of motion of the ultra precision positioning technique for precision machining. Thus, Chebyshev filters provide accurate means of removing harmonic components and other noise from the signal response of a rotating structure while retaining the useful structural dynamic data.

The Chebyshev filter produces an n^{th} order frequency domain function [28, 105] in the form

$$H(z) = \frac{B(z)}{A(z)} = \frac{b_1 + b_2 z^{-1} + ... + b_{n+1} z^{-n}}{1 + a_2 z^{-1} + ... + a_{n+1} z^{-n}} \tag{2}$$

using the specified bandstop information, which can then be used to filter the signal response. There are two types of Chebyshev filters: Chebyshev Type I and Chebyshev Type II. Type I has an equiripple passband and monotonic stopband and Type II has a monotonic passband and equiripple stopband. Figure 21 provides the low-pass

magnitude response of these two filters.

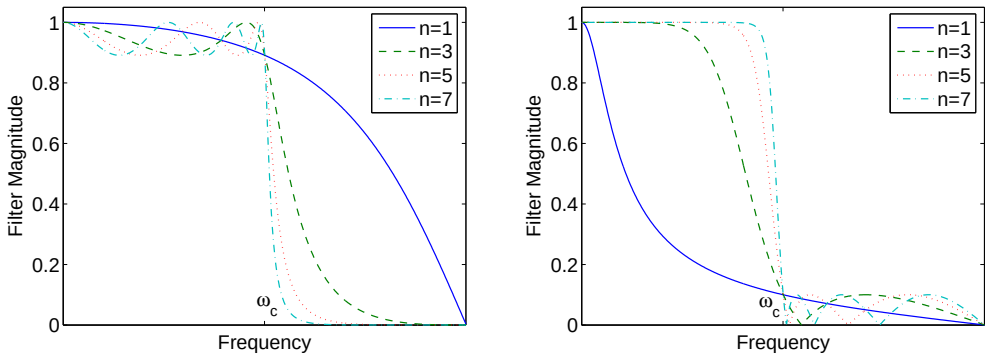

(a) Type I (b) Type II

Figure 21: Magnitude of Chebyshev Low-Pass Filters (n = polynomial order).

Type I is the more commonly used Chebyshev filter because the passband equiripple property allows for a narrower transition from the passband and stopband compared with Type II and also requires less filter characteristics to be defined. The *cheby1* function, available in MATLAB, creates a Chebyshev Type I digital filter with the following user-specified parameters: filter order, magnitude of filter response, cut-off frequency (or cut-off frequencies for the bandstop filter), and filter type. Figure 22 provides examples of a bandstop Chebyshev Type I digital filter created in MATLAB, which is the filter type used in this research work.

4.3.2 Harmonic Frequency Filter

A frequency filter is developed to determine the location of the harmonic gear mesh frequencies in the dynamic response of the operating drill system and filter these frequencies before the signal is analyzed further. The equation used for determining the incremental frequencies is based on a mathematical model formulated for the rotorcraft transmission vibration signal by McFadden [106] in 1986. Assuming a

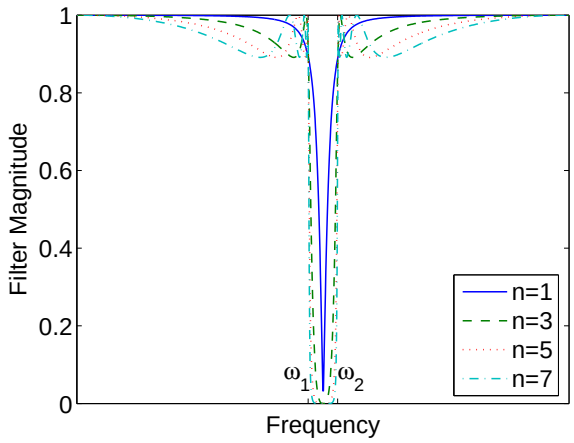

Figure 22: Magnitude of Chebyshev Type I Bandstop Filters (n = polynomial order).

perfect gear system, the tooth meshing vibration is approximated by:

$$\xi_{\text{perfect}}(t) = \sum_{n=0}^{\infty} \Xi_n \cos(n\omega t + \Phi_n) + w(t) \tag{3}$$

where Ξ_n is the amplitude of the n^{th} harmonic, ω is the mesh frequency given by $\omega{=}2\pi f_r Q$, f_r is the gear rotation frequency, Q is the number of teeth, Φ_n is the phase angle of the n^{th} harmonic, and $w(t)$ is noise often represented as Gaussian white noise [131]. According to this model, the harmonic components occur in increments related to the rotational speed of the motor and the number of gear teeth. Thus, the following formula is used to determine the harmonic frequencies (f_n):

$$f_n = Q f_r n, \quad n = 1, 2, 3, ... \tag{4}$$

Therefore, with the drill system of interest using a 90-gear tooth motor, the harmonic frequencies of the drill rotating at 45 RPM (revolutions per minute) or 0.75 Hz, occur at 67.5 Hz, 135 Hz, 202.5 Hz, etc. These values match the harmonic peaks found in Fig. 14(b) and, from experiments, Eq. 4 has proven to be an accurate model for predicting the gear mesh frequencies of the rotating drill.

Modifications to the tooth meshing vibration model (Eq. 3) accommodate for time-dependent modulations in the amplitude and phase in the gear mesh signal

[46, 106, 131]:

$$\xi_{\text{perfect}}(t) = \sum_{n=0}^{\infty} \Xi_n[1 + a_n(t)]\cos[n\omega t + \Phi_n + b_n(t)] + w(t) \tag{5}$$

where $a_n(t)$ and $b_n(t)$ are the amplitude and phase modulations, respectively. These modulations are due to manufacturing and assembly imperfections that cause non-uniform meshing of the gear system. In this research work, it is assumed that these manufacturing imperfections are not present, the vibrations of the drill gear mesh system follow Eq. 3, and the harmonic frequencies are determined using Eq. 4. The updated model (Eq. 5), however, is useful in predicting complications and failures within the drill gear mesh system, which is a recommendation for future work in Section 8.2.

To filter the harmonic frequencies from the signal response, a Chebyshev Type I digital bandstop filter of order three is used. The frequency response of a third-order Chebyshev Type I digital filter, applying a bandstop between ω_1 and ω_2, is provided in Fig. 23. Order $n = 3$ was used for this filter because it provided a wide enough bandpass to filter the harmonic frequencies with minimal passband ripple. The plots in Fig. 24 apply this filter to a simulated frequency response function (FRF) containing harmonic frequencies at every 30 Hz. The left and right plots are the original and filtered FRF, respectively.

From Fig. 24, it is evident that the harmonic frequencies are filtered from the signal response using Eq. 4 to determine the location of the frequencies and the Chebyshev filter to eliminate, or minimize, these peaks. Figure 25 provides the filtered response of the auger tube rotating in place at 45 RPM. It is seen that the harmonic frequencies have been filtered appropriately and the first two natural frequencies of the auger tube are clearly visible and detectable in the filtered signal response.

It is important to note that the auger tube frequencies can be unintentionally filtered if they occur close enough to the harmonic frequencies. This is a constraint on operations of the drill as it is desirable to use rotational speeds that do not conflict

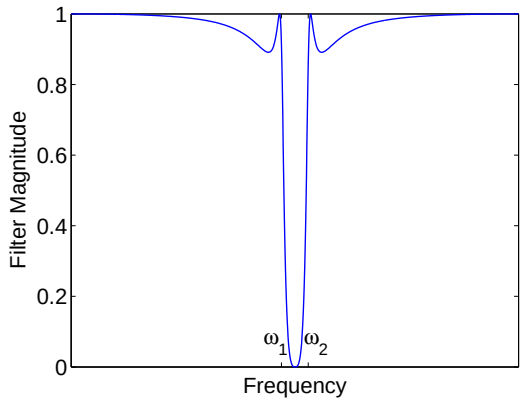

Figure 23: Frequency Response of Third-Order Chebyshev Type I Digital Filter.

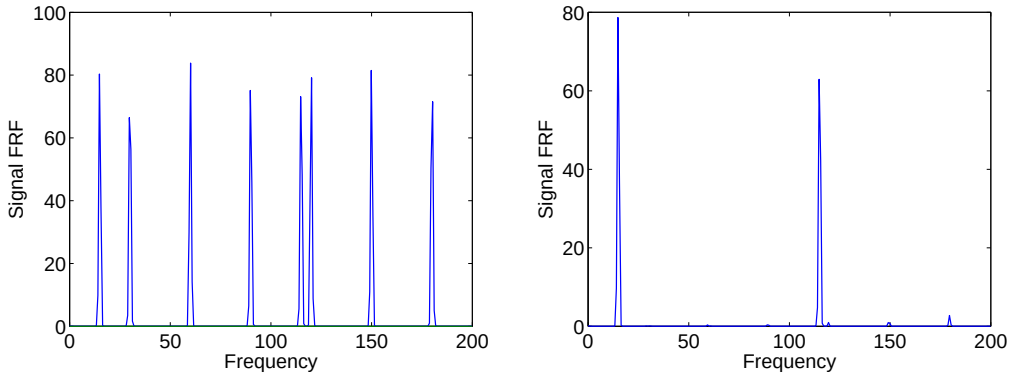

(a) Original (b) Filtered

Figure 24: Simulated FRF with 30 Hz Harmonic Frequencies.

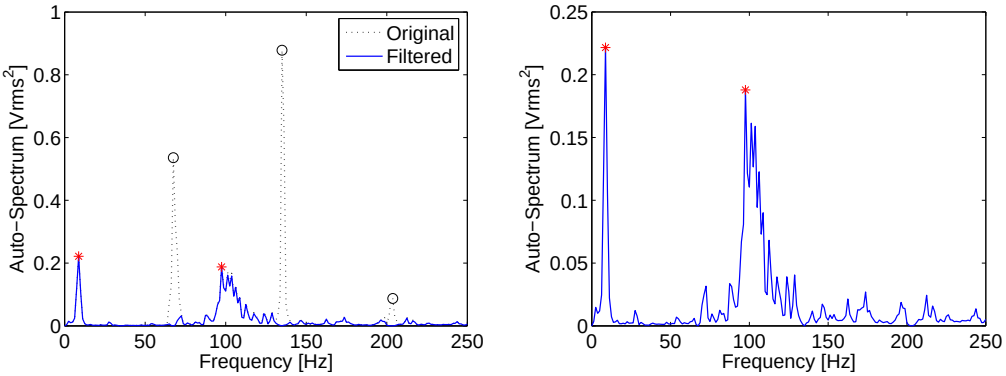

Figure 25: Filtered Rotating Dynamic Response of Drill System at 45 RPM.

with the auger tube frequencies. Higher rotational speeds also correspond to more disperse harmonic frequencies in the signal response (e.g. 20 RPM corresponds to 30 Hz increments where 45 RPM corresponds to 67.5 Hz increments), which limits the interference of these frequencies with the auger tube frequencies. Therefore, throughout the signal analysis procedures (before and after filtering), it is critical to note the expected location of the auger and harmonic gear mesh frequencies and to resolve the signal as best as possible to ultimately provide accurate signal analysis and diagnostic results. This topic is further discussed in Chapter 6 as part of the signal analysis algorithm.

4.4 Two-Dimensional Measurements using LDV

The modal analysis experiments conducted thus far have focused on one-dimensional lateral vibrations of the auger tube measured from the *front* of the drill system. The *front* and *side* views/planes of the drill system are represented in Fig. 26. The lateral vibrations orthogonal to the *front* and *side* planes are the lateral vibrations in the y- and x- directions, respectively.

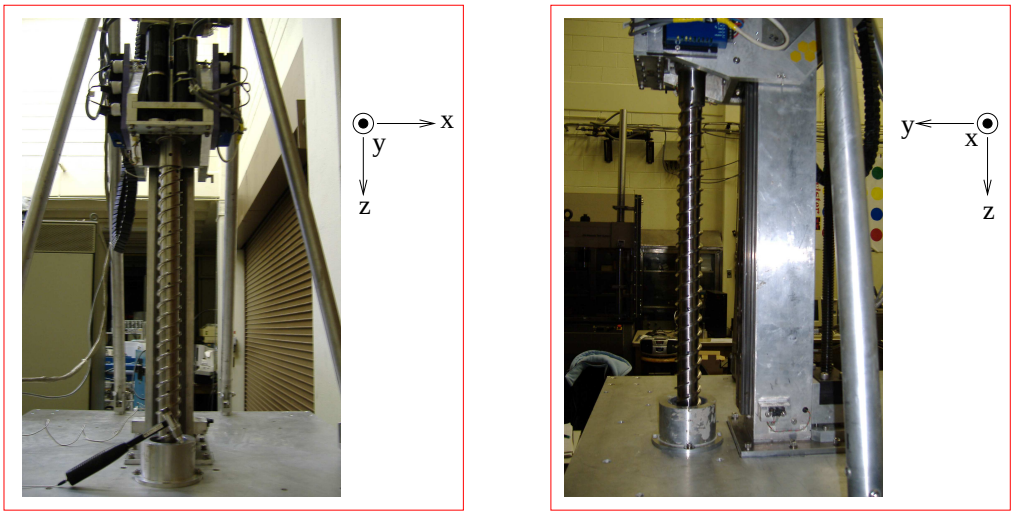

(a) Front (b) Side

Figure 26: *Front* and *Side* of Drill System.

Understanding the dynamic response of the auger tube in two and three dimensions, however, provides more information regarding the drill dynamics and operating condition. The motivations and implications of multi-dimensional measurements, a theoretical analysis for using LDV sensors to complete these measurements, and two-dimensional experiments conducted on a cantilevered beam and the drill system are provided in the following sections.

4.4.1 Motivations

In practice, systems do not incur only uniaxial loading and will experience structural deformation and damage in multiple directions. Most published research efforts focus on identifying structural damage using sensor data from a single direction [31, 45, 119, 146]. Without *a priori* knowledge of the structure and damage, dynamic measurements from a single direction, however, may not be sufficient to determine the existence and severity of all defects. Therefore, the ability to capture and extract the dynamic response of a structure in two or three dimensions is very valuable for modal analysis and structural health monitoring.

Schubert et al. [133], Staszewski et al. [150] and Sharma et al. [139] study two- and three- dimensional analysis of plate-like structures under high frequency Lamb wave excitations for the purpose of improving detection of crack-like damages. These research efforts use Scanning Laser Doppler Vibrometer (SLDV) sensors for measuring the signal response. Staszewski et al. [150] use three separate scanning LDV sensors working simultaneously to measure the response of the plate-like structure in three dimensions. A simpler and less expensive option of using one scanning LDV sensor positioned for multi-dimensional measurements is used by Schubert et al. [133] and Sharma et al. [139]. Another three-dimensional set-up is demonstrated by Miyashita and Fujino [109] where three single-point LDV sensors are used to measure the dynamic signal of a plate in three directions. Other multi-dimensional research include

measurements of translational and rotational vibration for rotating shafts using parallel measurements from LDV sensors [128].

As the cost, size, and required number of sensors are important factors, specifically for interplanetary exploration missions, this research work focuses on demonstrating accurate measurements in multiple dimensions using one fixed-point LDV sensor. Although superior in many ways, the fixed-point LDV sensor is preferred to the commercially available, bulky, scanning LDV for this application because it is more compact and less expensive.

4.4.2 Theoretical Analysis

For most structures, it is a difficult task to attain isolated responses of the system in multiple dimensions. Depending on the equipment setup and structure (dynamic measurements of a fixed-free beam for example), it is difficult to capture the isolated signal response of both the bending and axial vibrations. It is therefore beneficial to collect measurements at an off-set position and resolve the response into bending and axial directions. To achieve this, the LDV sensor captures the response of the system for the same point from two different positions (Fig. 27(b)) [133].

The magnitude of the response for the two positions is written as:

$$V_{L1} = U_2\cos(\theta_1) + U_3\sin(\theta_1), \tag{6}$$

$$V_{L2} = U_2\cos(\theta_2) + U_3\sin(\theta_2) \tag{7}$$

where V_{L1} corresponds to the LDV positioned at θ_1, V_{L2} corresponds to the LDV positioned at θ_2, and U_2 and U_3 are the magnitudes of the response along the u_2-axis and u_3-axis (Fig. 27) [139]. The angles (θ_1 and θ_2) are measured from the u_2-axis where positive and negative angles relate to the sensor being above and below the point of interest, respectively. Thus in Fig. 27(b), θ_1 is a positive angle and θ_2 is a negative angle. The response along the u_2-axis and u_3-axis are found by solving for

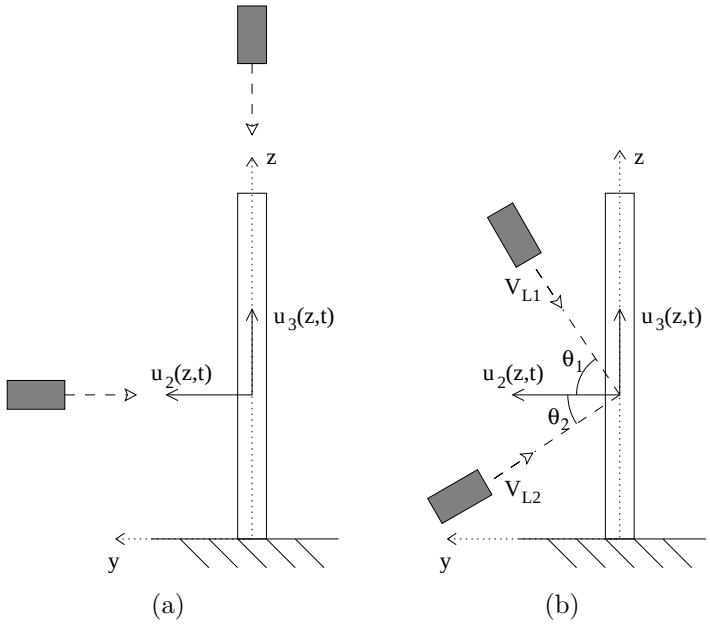

Figure 27: LDV Sensor Positioning versus Fixed-Free Beam.

U_2 and U_3 in Eq. 8.

$$\begin{Bmatrix} U_2 \\ U_3 \end{Bmatrix} = \begin{bmatrix} \cos(\theta_1) & \sin(\theta_1) \\ \cos(\theta_2) & \sin(\theta_2) \end{bmatrix}^{-1} \begin{Bmatrix} V_{L1} \\ V_{L2} \end{Bmatrix} \tag{8}$$

Expanding this concept to three directions, the signal response of a structure is captured in three dimensions using three LDV measurements (Fig. 28) and resolving the signal using the following equation [139]:

$$\begin{Bmatrix} U_1 \\ U_2 \\ U_3 \end{Bmatrix} = \begin{bmatrix} \cos(\theta_1)\sin(\varphi_1) & \cos(\theta_1)\cos(\varphi_1) & \sin(\theta_1) \\ \cos(\theta_2)\sin(\varphi_2) & \cos(\theta_2)\cos(\varphi_2) & \sin(\theta_2) \\ \cos(\theta_3)\sin(\varphi_3) & \cos(\theta_3)\cos(\varphi_3) & \sin(\theta_3) \end{bmatrix}^{-1} \begin{Bmatrix} V_{L1} \\ V_{L2} \\ V_{L3} \end{Bmatrix} \tag{9}$$

where

$$V_{Li} = U_1\cos(\theta_i)\sin(\varphi_i) + U_2\cos(\theta_i)\cos(\varphi_i) + U_3\sin(\theta_i), \tag{10}$$

$i = 1, 2, 3$, and U_1, U_2, and U_3 are the magnitudes of the response along the x-axis, y-axis, and z-axis, respectively. To ensure three unique directions, three measurements for two to three unique values for both θ and φ are required.

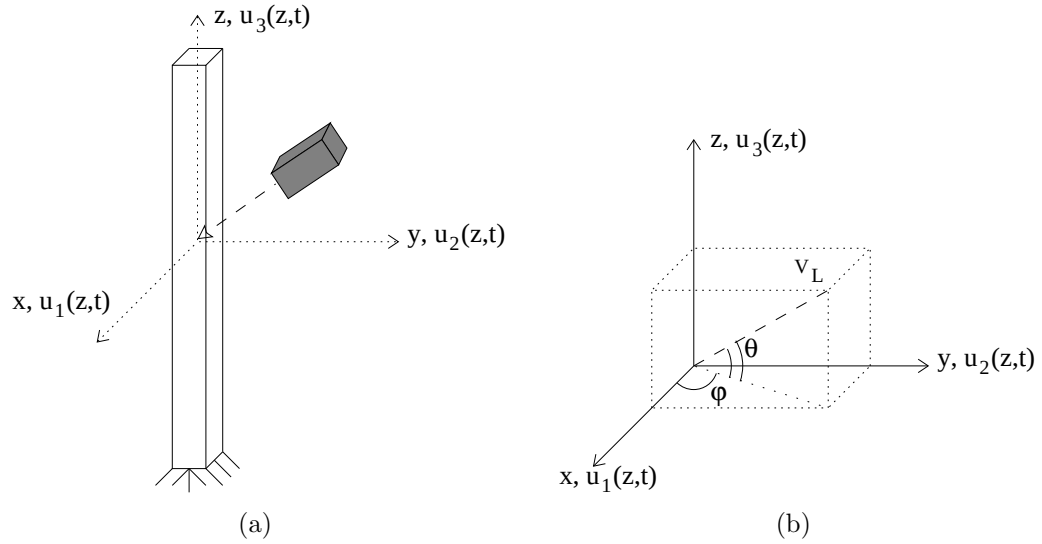

Figure 28: Three-Dimensional LDV Set-Up.

4.4.3 Cantilevered Beam Analysis & Experiments

An experiment involving a fixed-free aluminum beam with an added tip mass validates the presented theoretical and experimental multi-dimensional measurement approach. The beam is of length L, mass per unit length m, axial rigidity EA, and bending stiffness EI. The added mass is an actuator attached at the tip of the beam used to excite the response in the axial direction. This actuator has total mass M and mass moment of inertia I_M. A diagram of this dynamic structure is in Fig. 29, and Table 4 lists the relevant geometric and material properties.

4.4.3.1 Theoretical Analysis of Cantilevered Beam

The governing differential equations for axial and bending motions (assuming Euler-Bernoulli beam theory) are as follows:

$$EI\frac{\partial^4 u_2}{\partial z^4}(z,t) + m\frac{\partial^2 u_2}{\partial t^2}(z,t) = 0, \tag{11}$$

$$EA\frac{\partial^2 u_3}{\partial z^2}(z,t) - m\frac{\partial^2 u_3}{\partial t^2}(z,t) = 0, \tag{12}$$

where $u_2(z,t)$ and $u_3(z,t)$ represent the bending and axial deflections, respectively, at location z and time t [107]. Equations 11 and 12 include Euler-Bernoulli assumptions,

Table 4: Geometric & Material Properties of Aluminum Beam with Added Tip Mass

Property	Symbol	Value	Units
Cross-section base	b	38.1	mm
Cross-section height	h	4.83	mm
Cross-section area	$A = bh$	183.8	mm^2
Area moment of inertia	$I = bh^3/12$	356.9	mm^4
Length	L	266.7	mm
Density	ρ	2700	kg/m^3
Mass per unit length	$m = \rho A$	0.496	kg/m
Modulus of Elasticity	E	74.5e9	Pa
Added mass	M	0.0399	kg
Diameter of added mass	d	19.17	mm
Mass moment of inertia of added mass	$I_M = Md^2/4$	3.665	kg mm^2

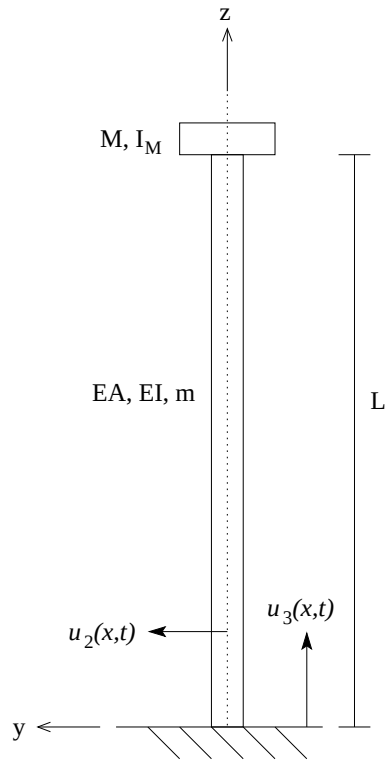

Figure 29: Diagram of Fixed-Free Beam with Added Tip Mass.

and coupling effects between axial and bending deformations are not considered.

The boundary conditions for a fixed-free beam with an added tip mass (approximated as a rigid body) [72, 73] are

$z = 0$:

$$u_2(z,t) = 0,$$
$$\frac{\partial u_2}{\partial z}(z,t) = 0, \tag{13}$$
$$u_3(z,t) = 0,$$

(14)

and $z = L$:

$$EI\frac{\partial^2 u_2}{\partial z^2}(z,t) + I_M\frac{\partial^3 u_2}{\partial z \partial t^2}(z,t) = 0,$$
$$EI\frac{\partial^3 u_2}{\partial z^3}(z,t) - M\frac{\partial^2 u_2}{\partial t^2}(z,t) = 0, \tag{15}$$
$$EA\frac{\partial u_3}{\partial z}(z,t) + M\frac{\partial^2 u_3}{\partial t^2}(z,t) = 0.$$

(16)

Applying the non-dimensional variable $\eta = z/L$, the equations of motion become

$$EIu_2^{IV}(\eta,t) + m\ddot{u}_2(\eta,t) = 0, \tag{17}$$

$$EAu_3''(\eta,t) - m\ddot{u}_3(\eta,t) = 0, \tag{18}$$

where

$$()' = \frac{\partial}{\partial \eta},\ \dot{()} = \frac{\partial}{\partial t},\ \eta = \frac{z}{L},\ 0 < \eta < 1.$$

Assuming a simple harmonic motion and applying separation of variables, the bending and axial deflections can be written as:

$$u_2(\eta,t) = U_2(\eta)e^{i\omega t}, \tag{19}$$

$$u_3(\eta,t) = U_3(\eta)e^{i\omega_A t}. \tag{20}$$

Therefore, one obtains the following solutions:

$$U_2(\eta) = B_1\cosh(\alpha\eta) + B_2\sinh(\alpha\eta) + B_3\cos(\alpha\eta) + B_4\sin(\alpha\eta) \tag{21}$$

$$U_3(\eta) = B_5\cos(\beta\eta) + B_6\sin(\beta\eta), \tag{22}$$

where

$$\alpha^4 = \omega^2\frac{mL^4}{EI},\ \beta^2 = \omega_A^2\frac{mL^2}{EA},$$

B_1 through B_6 are constants, and ω_A and ω are the axial and bending frequencies, respectively.

Non-dimensionalizing the boundary conditions and applying the solution forms in Equations 19 and 20, the boundary conditions are rewritten as

$\eta = 0$:

$$\begin{aligned} U_2(\eta) &= 0, \\ U_2'(\eta) &= 0, \\ U_3(\eta) &= 0, \end{aligned} \tag{23}$$

$$\tag{24}$$

and $\eta = 1$:

$$\begin{aligned} U_2''(\eta) + \chi\alpha^4 U_2'(\eta) &= 0, \\ U_2'''(\eta) - \mu\alpha^4 U_2(\eta) &= 0, \\ U_3'(\eta) + \mu\beta^2 U_3(\eta) &= 0, \end{aligned} \tag{25}$$

$$\tag{26}$$

where

$$\chi = \frac{I_M}{mL^2}\,,\ \mu = \frac{M}{mL^2}\,.$$

Applying Equations 21 and 22 to these boundary conditions, the natural frequencies for the axial and bending motions of the beam are found. Table 5 provides the axial and bending natural frequencies of this beam structure through 22 kHz.

The mode shape equations for axial and bending motion are the following:

$$U_{2n}(\eta) = B_1\left[\cosh(\alpha_n\eta) - \cos(\alpha_n\eta) - K_n(\sinh(\alpha_n\eta) - \sin(\alpha_n\eta))\right], \tag{27}$$

Table 5: Natural Frequencies of Fixed-Free Beam with Added Tip Mass

n	Axial (Hz)	Bending (Hz)
1	3820.6	38.562
2	12077	284.69
3	21130	837.26
4		1651.9
5		2667.1
6		3855.9
7		5323.6
8		7156.8
9		9854.7
10		11900
11		14783
12		17995
13		21539

$$U_{3n}(\eta) = B_6 \sin(\beta_n \eta) \tag{28}$$

where

$$K_n = \frac{\sinh(\alpha_n) - \sin(\alpha_n) + \mu\alpha_n \cosh(\alpha_n) - \mu\alpha_n \cos(\alpha_n)}{\cosh(\alpha_n) + \cos(\alpha_n) + \mu\alpha_n \sinh(\alpha_n) - \mu\alpha_n \sin(\alpha_n)}, \tag{29}$$

and $n = 1, 2, ...$ The first three axial mode shapes and first four bending mode shapes are in Fig. 30. The mode shapes are normalized by setting $B_1 = 1$ and $B_6 = 1$, and the bending mode shapes are further normalized to a maximum amplitude of ± 1.

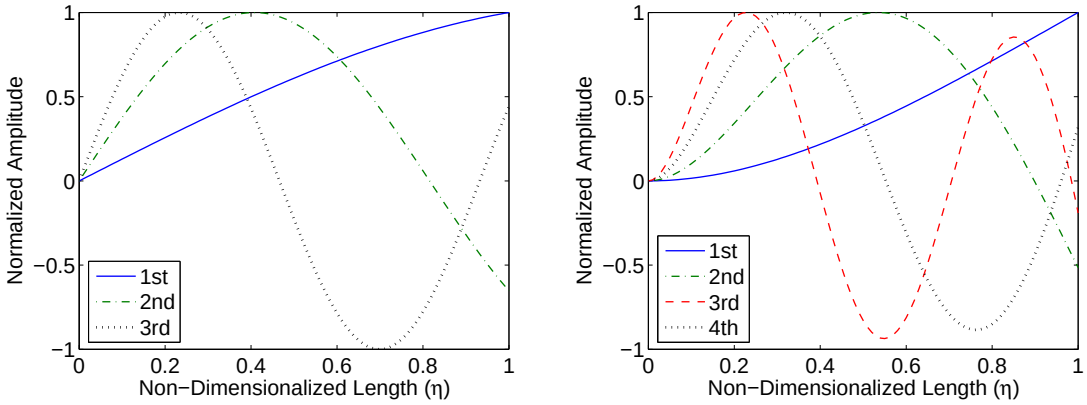

(a) Axial (b) Bending

Figure 30: Mode Shapes for Fixed-Free Beam with Added Tip Mass.

4.4.3.2 Experimental Analysis of Cantilevered Beam

Experiments have been conducted on the fixed-free aluminum beam using one fixed-point LDV sensor (PDV-100 from Polytec) [118]. As the reflected beam from the moving surface was critical for the LDV sensor to measure and compute the velocity, the angular positions of the LDV sensor were limited to ensure adequate signals and reception of the reflected beam. For these experiments, the LDV sensor was positioned at a maximum angle of $\pm 25^{o}$.

Two actuators were used to excite the beam in the bending and axial directions. The first actuator was a piezoelectric transducer disc, which had a diameter of 15 mm and thickness of 2.1 mm. This actuator was bonded to the back side of the beam, along the length of the beam, to excite the bending motion. The second actuator was a piezoelectric transducer ring, which had an outer diameter of 24 mm, inner diameter of 12 mm, and thickness of 8 mm. This actuator was bonded with an additional solid metal cylinder at the tip of the beam, hence the added tip mass. The additional solid metal cylinder had a diameter of 19.17 mm and 8.12 mm thickness, and it was used to secure the actuator onto the tip of the beam and ensure adequate transfer of the excitation to the beam structure.

SigLab (a commercially available data acquisition device and signal processor [147]) was used to generate the signal for the actuators and record the signal from the LDV sensor. The SigLab virtual function generator (VFG) was used to generate a random output signal with 2 V RMS, 0 V offset, and 20 kHz bandwidth, and this signal was transferred to the actuators via an external amplifier. The SigLab dynamic signal analyzer (referred to as VNA) was used to capture the time histories of the LDV sensor and actuators and provide cross-channel measurements, specifically the frequency response function (FRF). The parameters of the LDV signal included a 20 kHz bandwidth with a 6.25 Hz measurement resolution, ± 5 V range, and 5 mm/s/V measurement sensitivity. Finally, each data set was collected over 50

measurement averages. A diagram of the experimental setup is provided in Fig. 31.

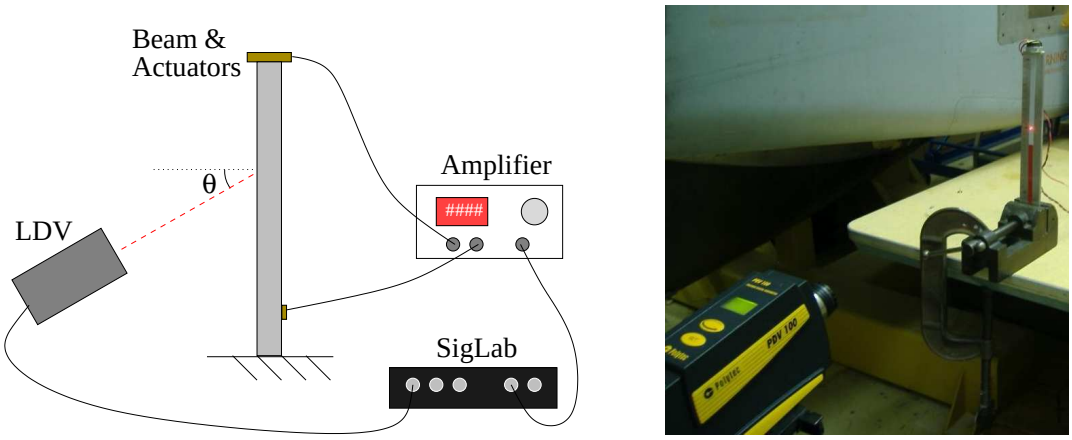

Figure 31: Experimental Setup of Fixed-Free Beam Measurements.

Various experimental conditions were used to capture and analyze the beam signal. The two actuators were used individually to isolate the bending and axial components and used simultaneously (referred here after as BA excitation) to excite both bending and axial vibrations. The LDV sensor was positioned at five different angles: 25°, 15°, 0°, −10°, −15°. For each condition, the signal for ten points along the beam was captured. The position along the beam for each point (measured from the free end of the beam) were as shown in Table 6 and Fig. 32. Finally, for each unique experimental condition, three data sets were collected to ensure adequate measurements and an accurate analysis of the system.

Table 6: Position of Points Along Beam Measured from Free End

Point	1	2	3	4	5	6	7	8	9	10
Position (cm)	0.5	2.5	5.5	7.5	10.5	12.5	15.5	17.5	20.5	22.5

The response for point 5 in various experimental conditions is provided. Figure 33 is the frequency response of point 5 with bending excitation only and the LDV positioned at 0°, and the frequency response with axial excitation only and the LDV positioned at 15° is provided in Fig. 34. Comparison plots of the bending and axial excitations with the BA (bending and axial) excitation are provided in Figures 35

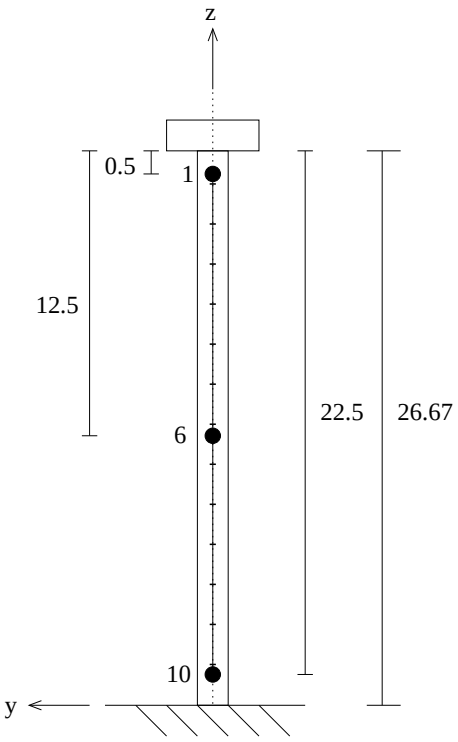

Figure 32: Position of Points Along Beam (distance in cm).

and 36, respectively. Analyzing the bending versus BA excitation responses, three peaks were identified as the axial frequencies. These frequencies are indicated with asterisks in Fig. 35.

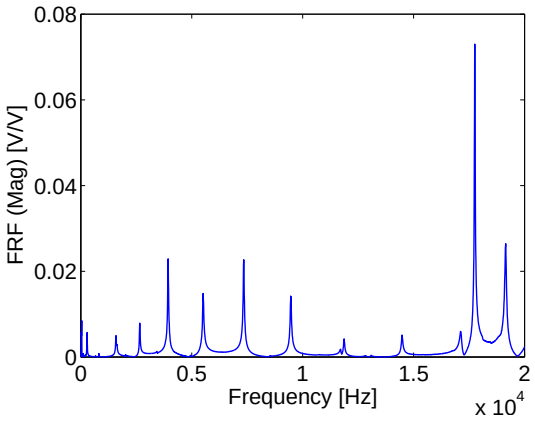

Figure 33: Point 5 Frequency Response with Bending Excitation and LDV at 0°.

Applying Eq. 8 to the experimental data, the frequency response is resolved into axial and bending components. This is only applicable for the BA excitation condition

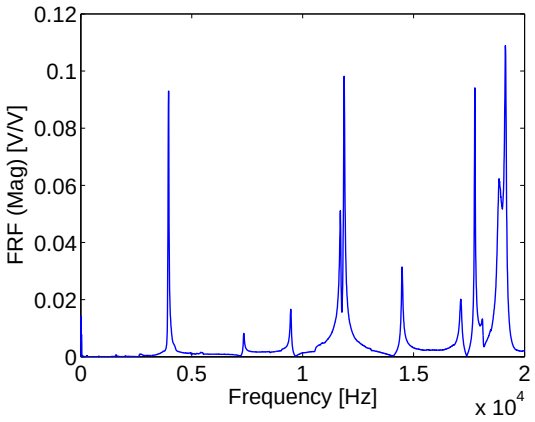

Figure 34: Point 5 Frequency Response with Axial Excitation and LDV at 15°.

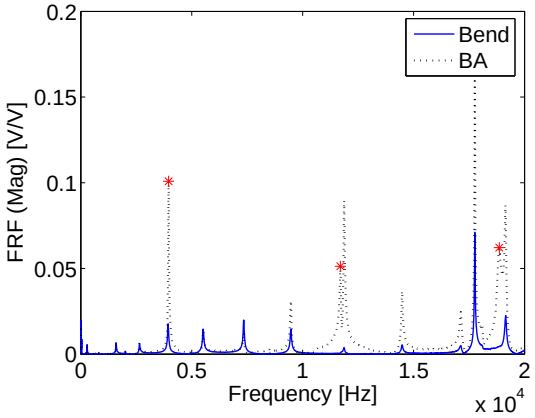

Figure 35: Point 5 Frequency Response Comparison (Bending vs BA) with LDV at 15°.

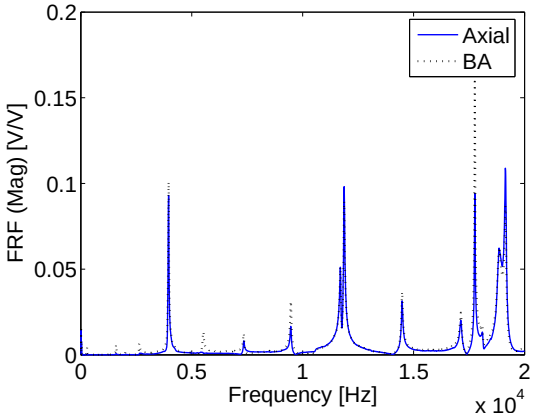

Figure 36: Point 5 Frequency Response Comparison (Axial vs BA) with LDV at 15°.

to ensure both bending and axial responses are excited. The original response for point 1 at LDV angles 25° and 0° and the resolved components are provided in Fig. 37. Similar plots are provided for point 4 at angles 25° and −15° (Fig. 38), point 7 at angles 15° and −15° (Fig. 39), and point 10 at angles 25° and 15° (Fig. 40). From these experimental results, the peaks for each data set were identified, compared, and averaged to determine the bending and axial frequencies of the beam structure. For simplification, it is assumed the damping coefficient is small. Thus, the natural frequencies of the cantilever beam are the peaks in the dynamic response, and the mode shapes are the operational deflection shapes at these peaks. The experimental frequencies and a comparison with the evaluated theoretical frequencies are provided in Table 7. The error measurement used to compare these frequencies is evaluated as

$$\% \,\text{error} = \left| \frac{\omega_t - \omega_e}{\omega_e} \right| \cdot 100\%, \tag{30}$$

where 't' and 'e' stand for the *theoretical* and *experimental* frequencies, respectively.

Table 7: Theoretical & Experimental Frequencies of Fixed-Free Beam with Tip Mass

	Axial			Bending		
n	Theory (Hz)	Exp (Hz)	Error (%)	Theory (Hz)	Exp (Hz)	Error (%)
1	3820.6	3956.25	3.55	38.562	37.5	2.75
2	12077	11725.0	2.91	284.69	287.5	0.99
3	21130	18862.5	10.73	837.26	818.75	2.21
4				1651.9	1600.0	3.14
5				2667.1	2656.25	0.41
6				3855.9	3931.25	1.95
7				5323.6	5512.5	3.55
8				7156.8	7343.75	2.61
9				9354.7	9468.75	1.22
10				11900	11875.0	0.21
11				14783	14481.25	2.04
12				17995	17756.25	1.33
13				21539	19150.0	11.09

The experimental mode shapes are determined by resolving the system response

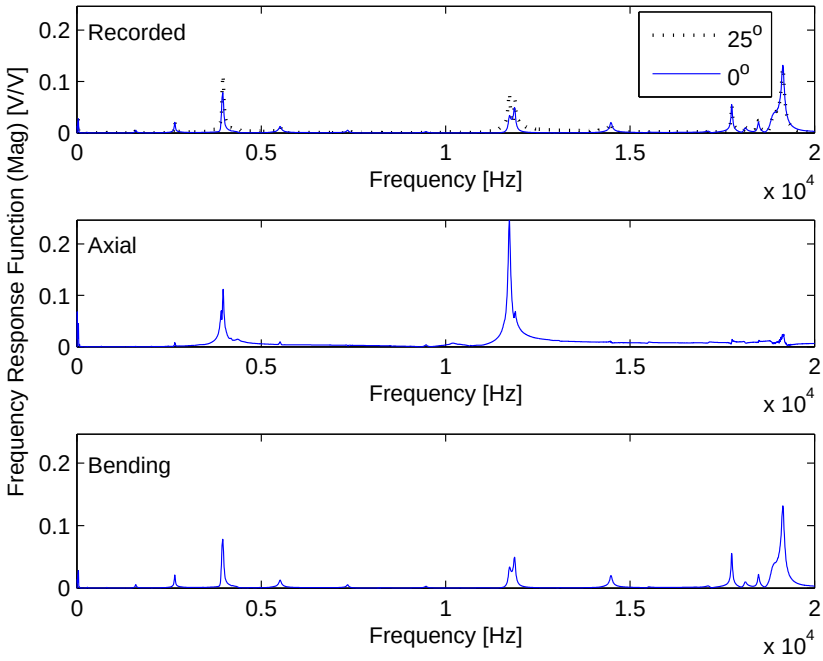

Figure 37: Original and Resolved Axial and Bending Response for Point 1.

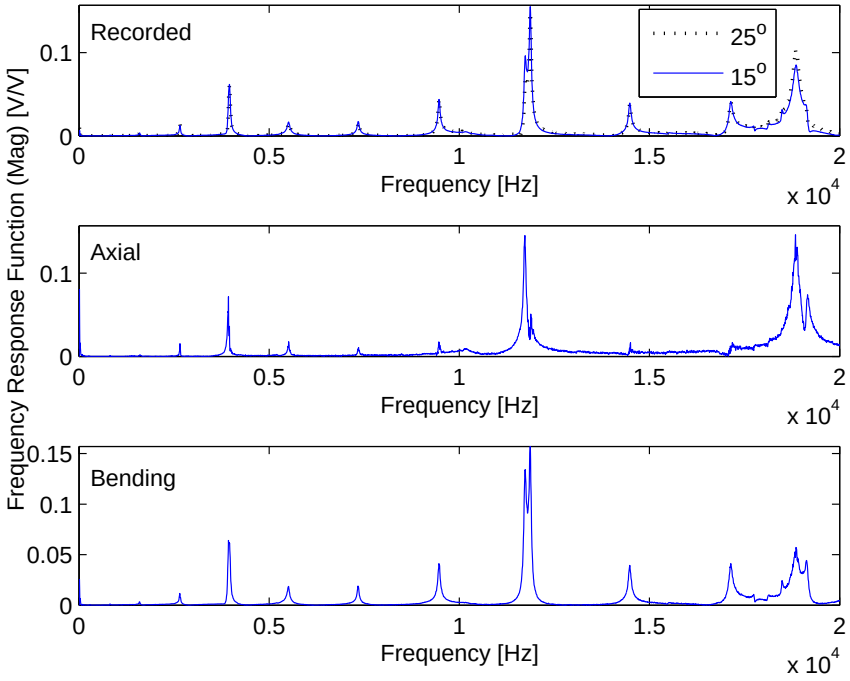

Figure 38: Original and Resolved Axial and Bending Response for Point 4.

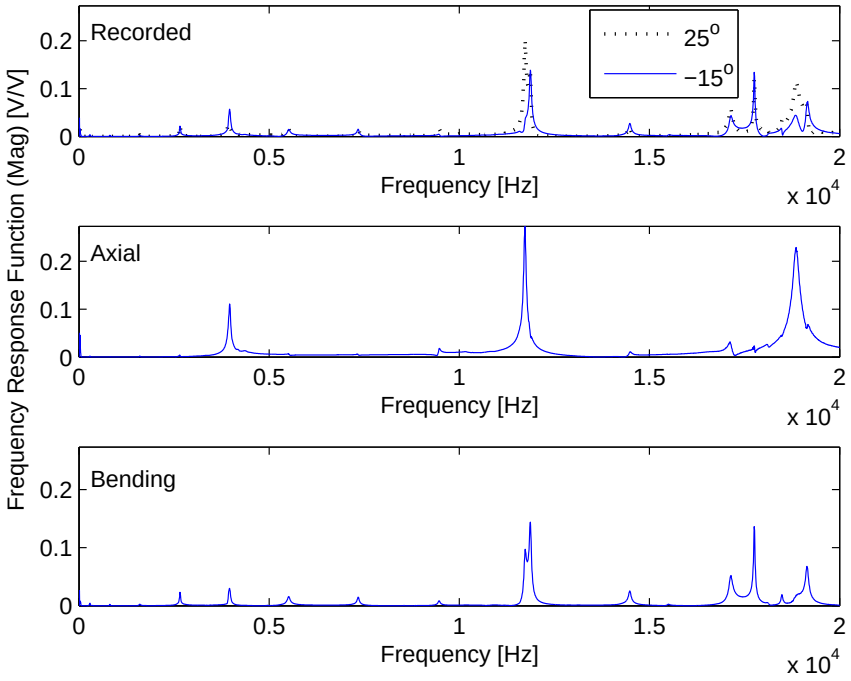

Figure 39: Original and Resolved Axial and Bending Response for Point 7.

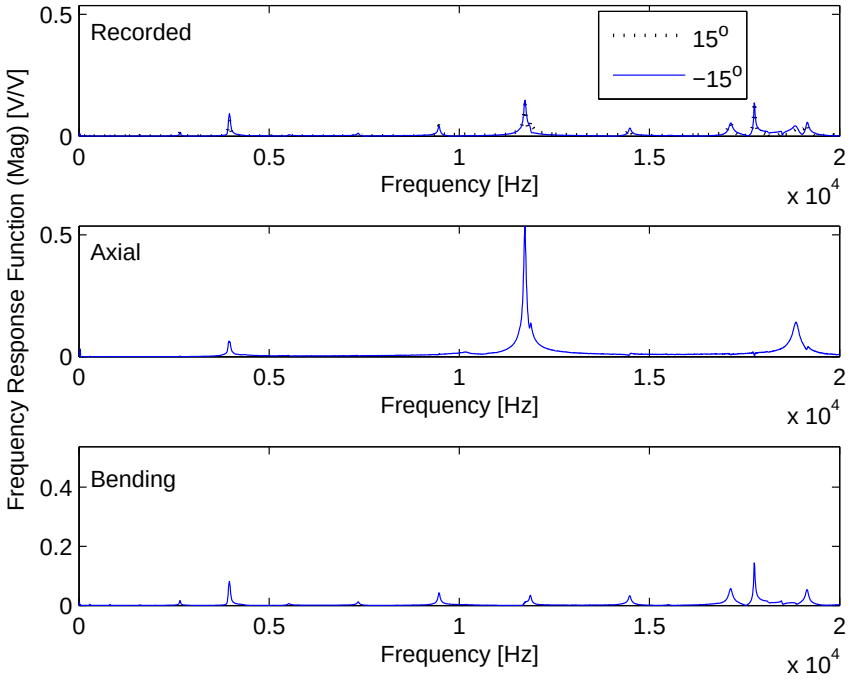

Figure 40: Original and Resolved Axial and Bending Response for Point 10.

into isolated bending and axial modes for each point along the beam. The resolved mode shapes, evaluated from the BA excited response at 25° and 0° for each of the ten points, are provided. Figure 41 is the first three axial mode shapes and Fig. 42 is the first four bending mode shapes. For each experimental mode shape, a basic curve fit is provided. Figures 43 and 44 compare these basic curve fits with its corresponding theoretical mode shape. The mode shapes are normalized for a maximum magnitude of 1, and the response at $\eta = 0$ is set to zero for the fixed boundary condition. The "Curve Fit (q)" in the legend of these plots represents the degree of the polynomial used for the curve fit.

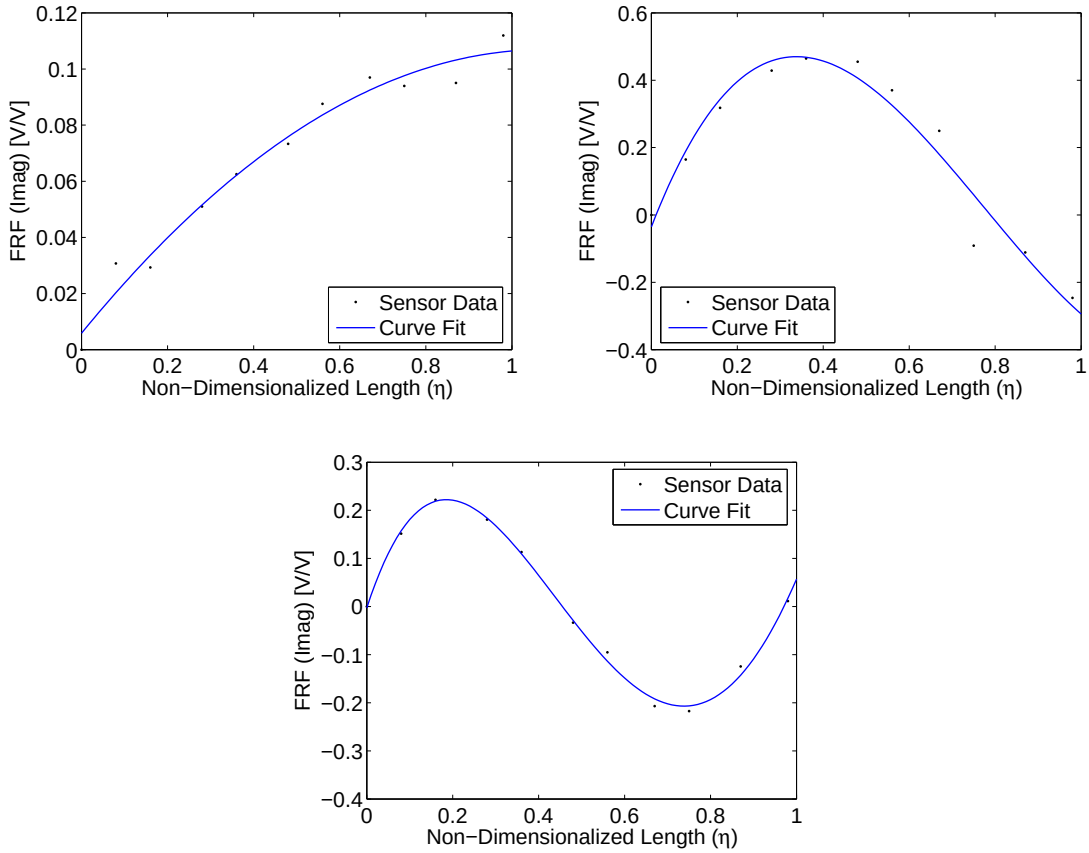

Figure 41: Basic Curve Fitting of Experimental Axial Mode Shapes.

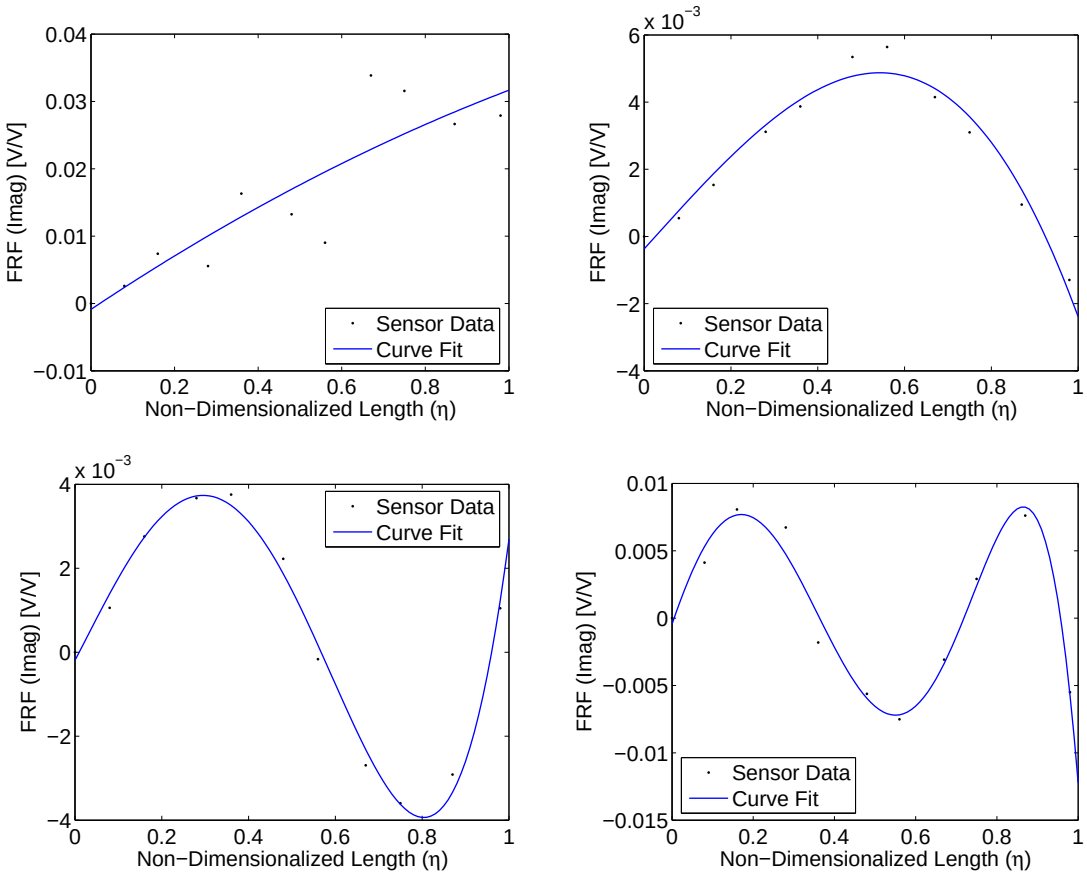

Figure 42: Basic Curve Fitting of Experimental Bending Mode Shapes.

4.4.3.3 Observations from Analysis of Cantilevered Beam

Examining the theoretical and experimental analysis of the beam structure, many observations and comparisons are made. From the frequency response plots provided in Figs. 33 through 36, the following conditions are observed:

1. The axial actuator with the bending actuator (i.e. BA excitation) excites some bending modes more effectively than the bending actuator alone while other modes are not affected by the additional excitation. This is most likely due to the positioning of both actuators, which can influence the response of the individual modes and cause coupling effects.

2. Comparing the bending and BA signal responses, the three axial modes are clearly identifiable.

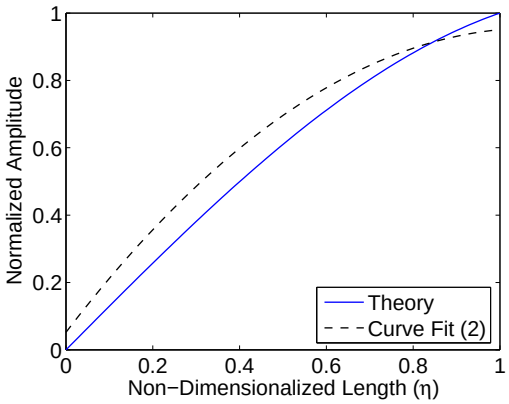

(a) Mode 1

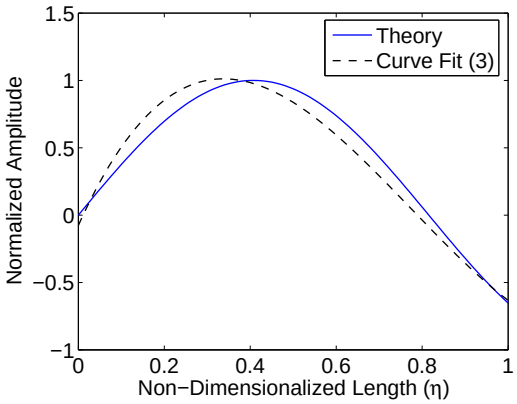

(b) Mode 2

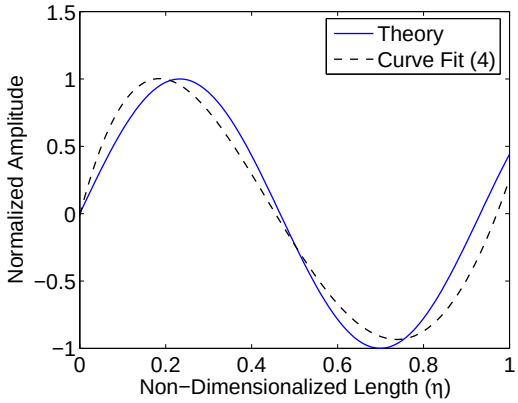

(c) Mode 3

Figure 43: Comparison of Theoretical and Experimental Axial Mode Shapes.

3. For the bending and axial natural frequencies that are similar along the frequency domain, the frequency of only one is identifiable in the signal response. This is most evident in Fig. 35 for the first axial mode and sixth bending mode. As these two modes are very close and the first axial mode has a greater magnitude, the axial mode consumes the sixth bending mode in the signal response for the BA excitation. This is not the case for any other modes observed.

4. In most of the plots provided (Fig. 33 through 40), an extra peak is visible at approximately 17144 Hz. This is most likely a torsional frequency that is being excited by one or both of the actuators.

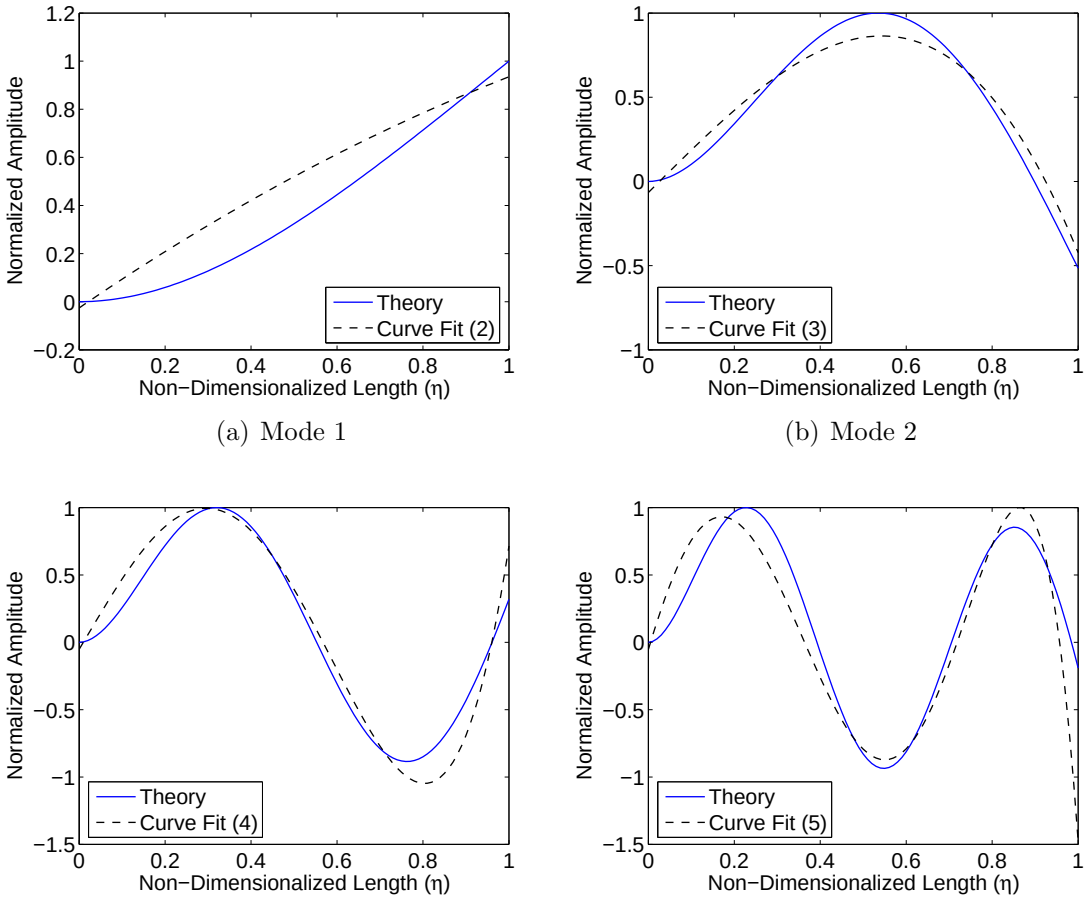

(a) Mode 1

(b) Mode 2

(c) Mode 3

(d) Mode 4

Figure 44: Comparison of Theoretical and Experimental Bending Mode Shapes.

From the original and resolved frequency response plots provided in Figs. 37 through 40, the following observations are made:

1. For most cases, applying Eq. 8 to the experimental signal responses accurately resolves the response into axial and bending motion.

2. As coupling between modes always occur in experimentation and practice, the modes can never be completely isolated. This is evident in Fig. 37, as axial modes are still present when the LDV is positioned at 0°. Further evidence of this is in Fig. 36 where bending modes are present in the axial response even though the bending actuator wasn't used. This does affect the process of resolving the axial and bending components, and more sophisticated modal

analysis methods, available in the literature [47, 55, 78], are needed.

3. The angular distance between the two LDV positions used to capture the signal response of the system is important. This is most evident in Fig. 40 where the two angles used are too similar to accurately resolve the signal response into axial and bending motion. Reviewing Eq. 8, the determinant of the matrix is:

$$\det \begin{bmatrix} \sin(\theta_1) & \cos(\theta_1) \\ \sin(\theta_2) & \cos(\theta_2) \end{bmatrix} = \sin(\theta_1)\cos(\theta_2) - \sin(\theta_2)\cos(\theta_1)$$

$$= \sin(\theta_1 - \theta_2).$$

Therefore, if $\theta_1 \simeq \theta_2$, the inverse of this matrix approaches infinity. This indicates that the two angular positions chosen for the LDV must be far enough apart to accurately resolve the frequency response.

Comparing the theoretical and experimental frequencies (Table 7), the maximum percentage error is 3.6% for the first twelve bending modes and first two axial modes. The percentage error for the thirteenth bending mode and third axial mode for this investigation is 11%. This leap in error is most likely due to the higher modes being more sensitive to rotational inertia and shearing effects, which can be resolved by using a higher order beam theory such as Timoshenko Beam Theory.

Comparing the theoretical and experimental mode shapes (Figs. 43 and 44), there are small deviations from the experimental results and the theoretical analysis, which can be resolved by using a higher order beam theory and using more experimental points along the beam. Each experimental mode shape, however, follows the basic curvature of the corresponding theoretical mode shape. Therefore, the mode shapes and frequencies are correctly identified using the experimental approach presented in this research work.

4.4.4 Two-Dimensional Drill Experiments

Modal analysis experiments to capture the dynamic response of the drill system in two orthogonal directions have been completed. Specifically, these experiments measured the lateral motion of the drill auger tube in the directions perpendicular to the front and side views/planes of the drill (Fig. 26), which represented the lateral motions in the y- and x- directions, respectively.

The observations from the cantilever beam experiments were taken into account for the drill experiments, and the same process was used to analyze dynamic measurements. The key differences between these experiments were the excitation devices used and the deflections measured. The cantilever beam measurements identified the lateral motion (y-direction) and axial motion where the drill measurements identified the lateral motions in two orthogonal directions (x and y). For excitation, the drill motors were used in the drill experiments, and piezoelectric actuators were used in the cantilever beam experiments. The details and results of the two-dimensional experiments completed on the drill system are presented in the following sections.

4.4.4.1 Two-Dimensional Stationary Tests

Two-dimensional stationary tests were completed to measure the lateral motion and identify the dynamic characteristics of the drill auger tube in two orthogonal directions (x and y) using artificial excitation from an impulse hammer. To isolate the dynamic response in the two directions, the lateral motion in the y-direction was first captured with the LDV sensor positioned directly in front of the drill (same measurements provided in Section 4.2). Then, the lateral motion in the x-direction was captured with the same LDV positioned directly to the side of the drill (Fig. 26). For both tests, an impulse hammer was used to excite the drill auger tube only in the direction of interest. The specifications for these experiments were the same as the stationary auger tube experiments described in detail in Section 4.2.

Figure 45 provides the magnitude of sample frequency response functions for the same measurement point on the auger tube from the two orthogonal positions. These two FRF measurements show the first three natural frequencies of the two lateral directions (front and side), and some signal noise is present at increments of 60 Hz. The first two mode shapes of the side measurements are in Fig. 46 and Table 8 provides the determined frequencies for the front and side positions of the auger tube. Although similar, there are distinct differences between the front and side auger frequencies, which shows a dependence of the dynamic response to the position of the sensors. These findings motivate a two-dimensional and three-dimensional analysis of the drill system to provide more information about the dynamics of the drill and to better diagnose the condition of the drilling operation.

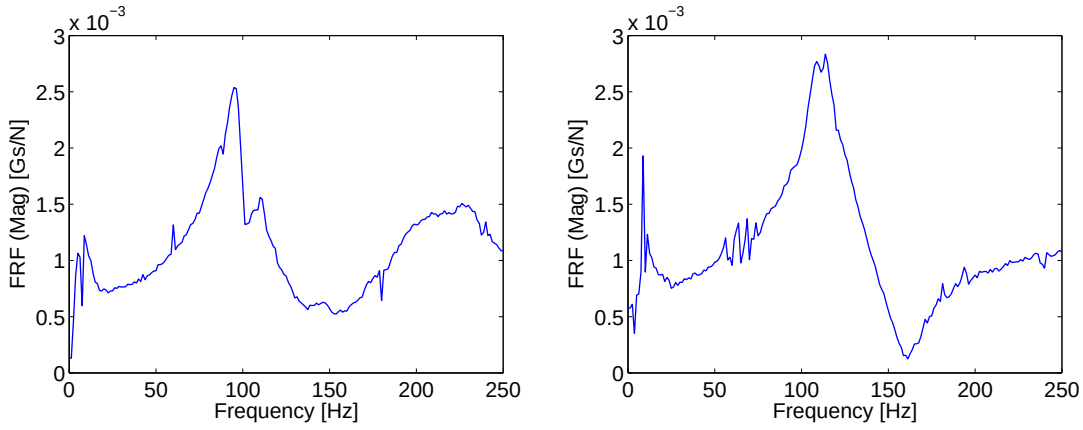

(a) Front (b) Side

Figure 45: Impulse Hammer Dynamic Response of Same Position on Auger Tube from Two Orthogonal Directions.

Table 8: Auger Frequencies Captured from Two Orthogonal Positions

Mode	Front (Hz)	Side (Hz)
1	9	8
2	95	113
3	250	319
4	486	497

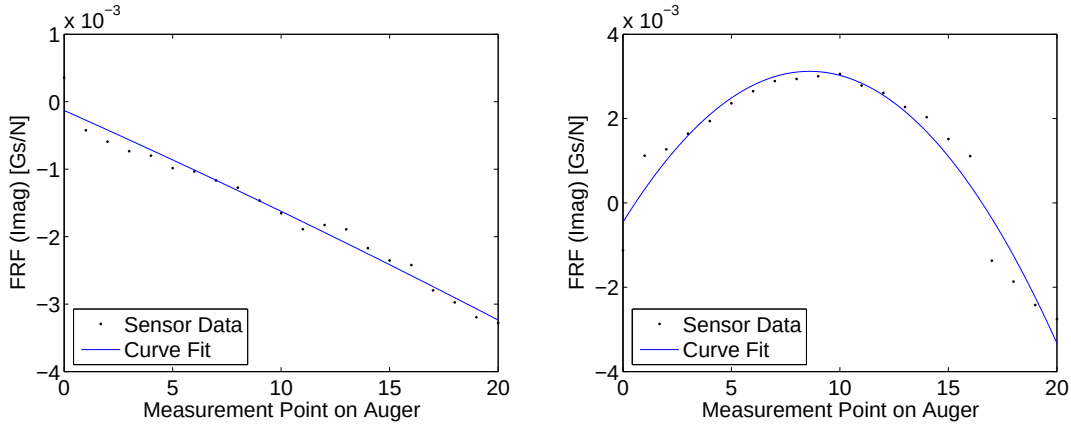

(a) First Mode (b) Second Mode

Figure 46: Mode Shapes of Free-Standing, Stationary Auger Tube Captured from Side Position.

4.4.4.2 Two-Dimensional Drilling Tests

For the two-dimensional drilling experiments, two LDV sensors (both PDV-100 units from Polytec) were used simultaneously while the auger tube was drilling under nominal conditions (maximum ROP of 0.3 cm/min, maximum down-hole force of 500 N, and 45 RPM auger speed) into the limestone column. Specifications for nominal drilling and the limestone column are provided in detail in Section 4.2. One LDV sensor (LDV #1) was positioned directly in front of the drill system and the second LDV sensor (LDV #2) was positioned at 25° from the axis aligned with LDV #1 (Fig. 47). This set-up was chosen to capture the signal response in one lateral direction (i.e. front of auger tube, y-direction) with LDV #1 and a combined signal response of the two lateral directions (i.e. front and side of auger tube, y- and x-directions) with LDV #2. This provided measurements from two angles to resolve the signal into the front and side lateral vibrations.

Figures 48 and 49 provide the measured and resolved/analyzed signals of a 1 m auger tube at 10.5 cm depth and a 2 m auger tube at 40 cm depth, respectively. Equation 8 with $\theta_1 = 0°$ and $\theta_2 = 25°$ was used to resolve the signals into the two lateral directions. The determined natural frequencies are indicated with asterisks

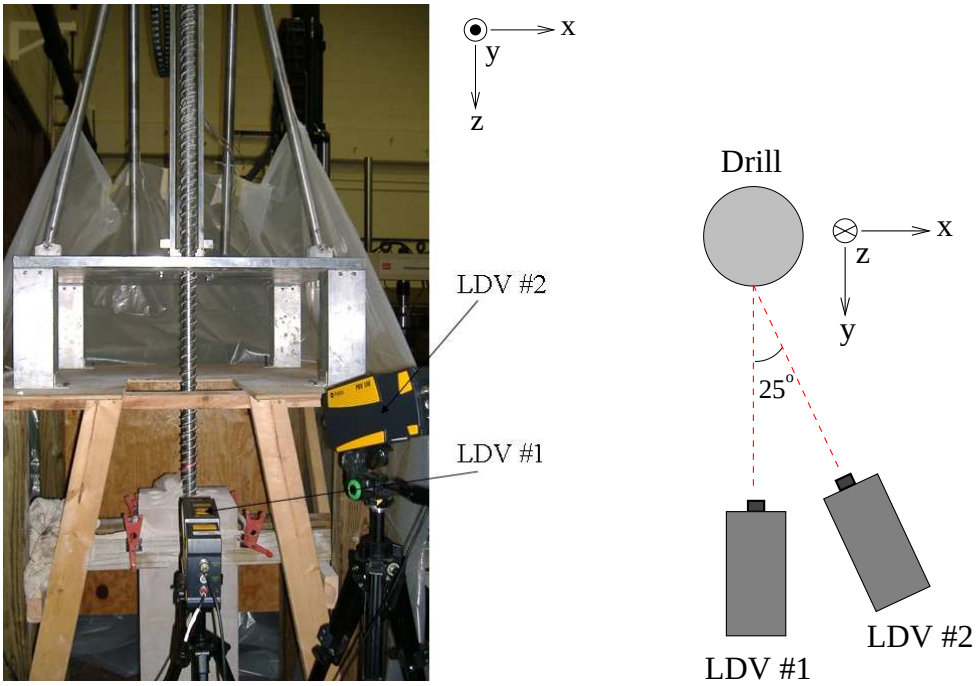

(a) Front View (b) Top View

Figure 47: Drill System Setup for Two-Dimensional Experiments.

and the gear mesh frequencies are indicated with circles.

From these experiments, similar and additional observations are made regarding two-dimensional measurements and its application to drill systems. As in the cantilevered beam experiments, mode coupling is always present: the lateral (y-direction) and axial (z-direction) motions of the cantilever beam, and the two lateral (x- and y- directions) motions of the drill system. This is most evident in Fig. 49 for the resolved side frequency response. It is also possible to have slight discrepancies between the two LDV sensors, as no two sensors are identical. Ideally the two- (and three-) dimensional measurements should be captured by the same sensor within a short time span.

For interplanetary exploration applications, accurate and reliable measurements are critical. As the cost and number of sensors are also important factors, capturing the dynamic response of the drill in two (and three) dimensions using one LDV sensor is very valuable. With the real-time drilling experiments and no available

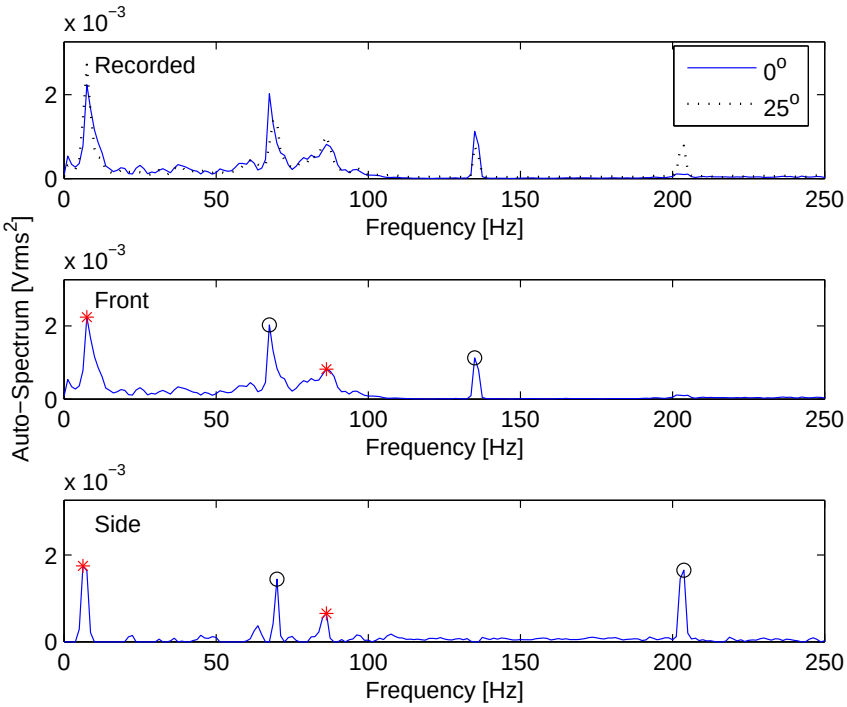

Figure 48: Recorded and Resolved Signal Response of 1m Auger Tube at 10cm Depth.

sensor position mechanism, however, two LDV sensors were used. These experiments, however, have demonstrated the two-dimensional measurement application to drill systems, and the cantilevered beam experiments have demonstrated the use of one fixed-point LDV sensor for two-dimensional measurements. Therefore, given proper positioning devices for an LDV sensor, two- and three- dimensional measurements using a single LDV sensor is possible and provides additional information regarding the drill structural dynamic characteristics.

4.4.5 Formulated Measurement Procedure for Two- and Three- Dimensional Measurements using LDV Sensor

Without *a priori* knowledge of the structure and damage, uniaxial dynamic measurements may not be sufficient to determine all damages and defects. Understanding the dynamic response of the drill auger tube in two and three dimensions also provides more information regarding the drill dynamics and operating condition. Therefore,

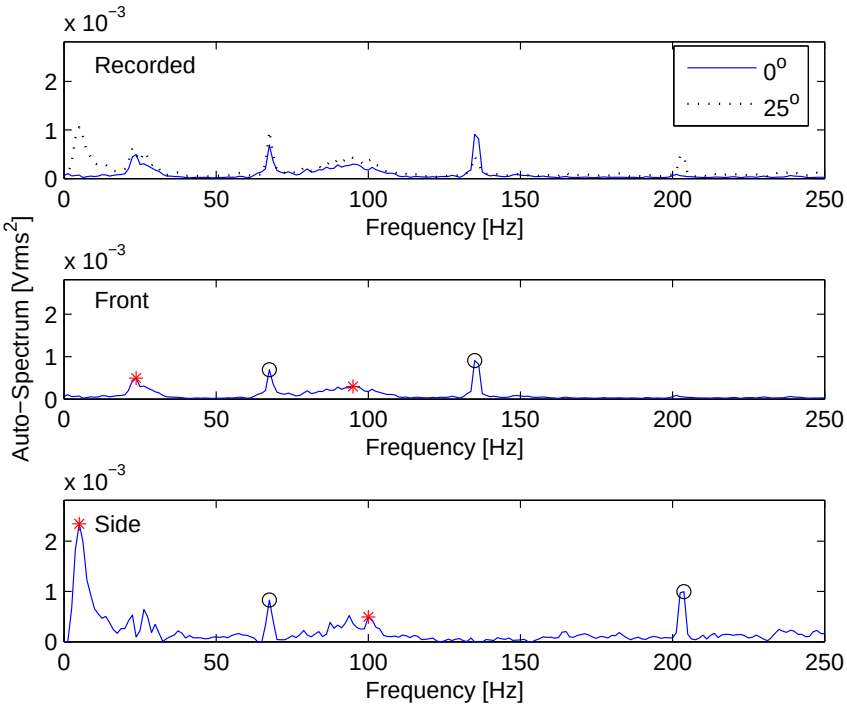

Figure 49: Recorded and Resolved Signal Response of 2m Auger Tube at 40cm Depth.

the ability to capture and extract the dynamic response of a structure in two or three dimensions is very valuable for modal analysis and structural health monitoring. From the theoretical and experimental analysis presented, a procedure for determining multi-dimensional components of a dynamic structure using a single LDV sensor is formulated.

1. Using two (or three) unique angular positions of the LDV sensor, capture the signal response of the dynamic structure.

    - Verify the angular positions do not exceed the limitations of the LDV sensor to capture a sufficient signal from the structure. The maximum angles used for this investigation were $\pm 25^{o}$.
    - Verify the different angular positions are far enough apart to accurately resolve the signal into the desired components. The adequate distance

between any two angles used in this investigation was $\pm 25^{o}$.

- Verify the excitation technique used is exciting all desired modes.

2. Resolve the collected signal response into the desired components using Eq. 8 for two-dimensional or Eq. 9 for three-dimensional measurements.

    - The value of θ for Eq. 8 is the angle measured between the laser beam and the normal vector to the surface of the measured structure. For the cantilevered beam investigation, 0^{o} was parallel to the y-axis (bending direction) and 90^{o} was parallel to the z-axis (axial direction). For the drilling experiments, 0^{o} was parallel to the front lateral direction and 90^{o} was parallel to the side lateral direction.

    - If more than the desired modes are being excited, the additional modes will likely be present in the captured signal response. To resolve this, more measurements or a signal filter are needed.

4.5 Measurement Limitations

Although position flexibility is one of the advantages of using LDV sensors for rotating structures and interplanetary exploration applications, there are measurement limitations that need to be considered. Accelerometers or other contact-based sensors can be installed in the drill auger tube at various strategic locations, including at or near the drill bit. The difficulties with this installation and collecting measurements from contact-based sensors were major considerations for using the LDV sensors. Whether the LDV sensors are part of the drill system or isolated from the drill system (as in the completed laboratory experiments), measurements using these sensors are limited to only parts of the drill and drill auger tube that are optically visible (i.e. at or above the surface). Therefore, as the drill depth increases, more of the auger tube becomes embedded in the subsurface and the surface measurements may not adequately reflect

the conditions of the drill below the surface beyond a certain depth. To clarify, these are not limitations of the LDV sensors but of the signal response at the surface to adequately represent the condition of the entire drill auger tube.

To investigate these depth limitations with the use of LDV sensors, the nominal drilling measurements have been further analyzed. After each 10 cm nominal drilling segment, stationary (impulse hammer excitation) and rotating experiments were conducted. The signal strength of these measurements have been compared for the different drill depths. Data for both the one meter and two meter auger lengths were obtained, and the maximum amplitude of the first two modes as a function of drill depth for the stationary measurements are provided in Fig. 50. The sharp corners in these plots were due to a limited number of data points available for this analysis.

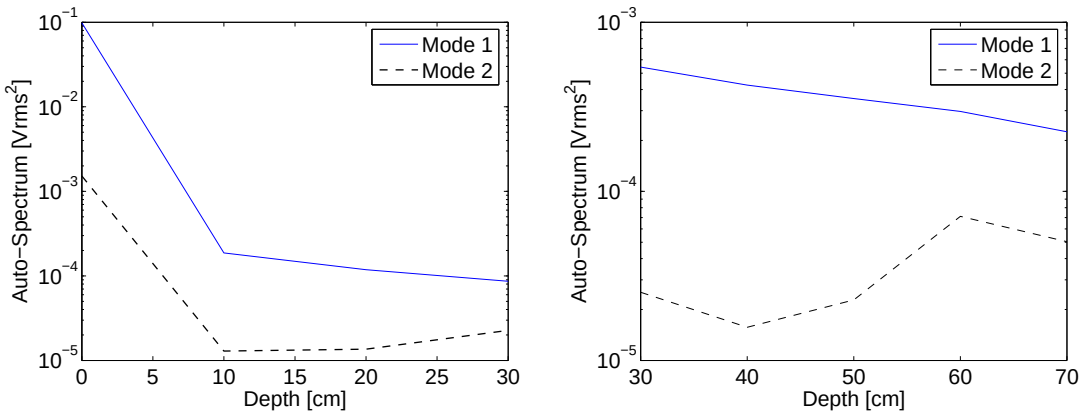

(a) 1m Auger (b) 2m Auger

Figure 50: Maximum Impulse Hammer Amplitude of First Two Auger Frequencies.

From these plots, it is evident that the amplitude of the first natural frequency decreases with increasing depth. The same, however, cannot be positively said about the second natural frequency. As discussed in Section 4.2 for the drilling experiments, the natural frequencies of the drill auger tube increase and the mode shapes (and nodal locations) change as the drill depth increases. This is due to the bore-hole wall

creating frictional side supports on the partially embedded auger tube. With increasing depths, less of the auger tube is measurable, which also affects the information that can be obtained about the individual mode shapes. Although inconclusive from the obtained data (Fig. 50), it is assumed that the magnitude of the second natural frequency decreases with increasing depth.

To further examine the signal strength as a function of drill depth, the measurements of the auger tube rotating in place are analyzed. Figure 51 provides the maximum amplitude of the first natural frequency for the one meter auger tube at various drill depths. The amplitudes are normalized by the maximum peak in the respective signal. The maximum peak in each signal was a gear mesh frequency. An example of the two meter auger tube rotating in place at 45 RPM for two different drilling depths is provided in Fig. 52 (first two natural frequencies indicated with asterisks and harmonic frequencies indicated with circles). It is further evident from these examples that the magnitude of the first two natural frequencies decreases with increasing drill depth, and this affect does not change with different auger speeds.

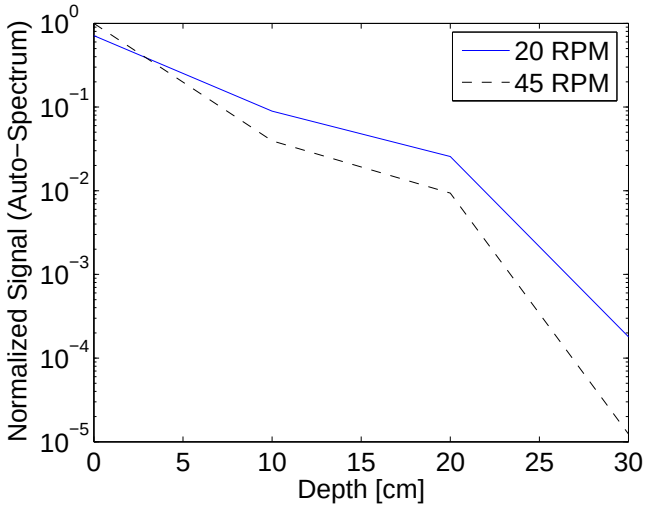

Figure 51: Maximum Rotating Amplitude of First Natural Frequency (1m Auger).

To analyze the extent of the diminishing signal with increasing depth, exponential curve fits were completed for the maximum amplitudes of the first natural frequencies

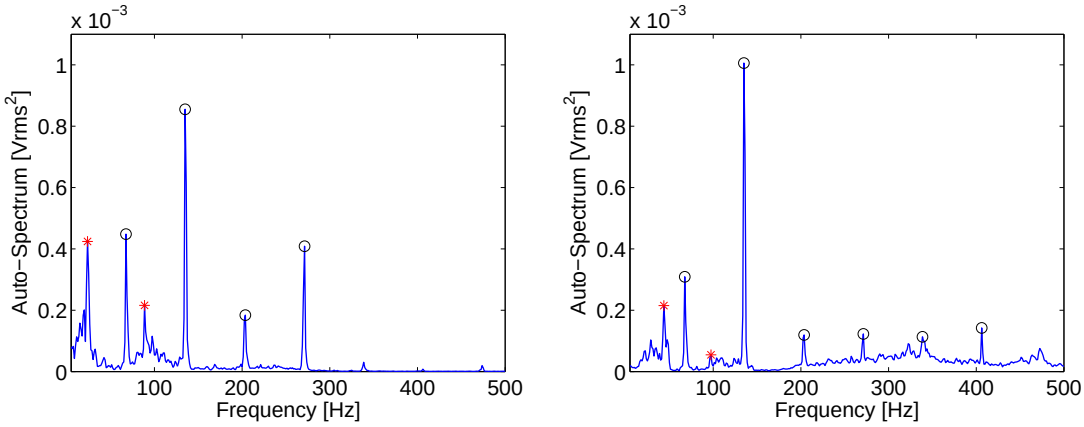

(a) 50cm Depth (b) 70cm Depth

Figure 52: Rotating Dynamic Response of Drill Auger Tube (2m, 45 RPM).

presented in Fig. 50. The exponential curve fits, as a function of the embedded auger (drill depth to total auger length ratio), are provided in Fig. 53. From these curve fits, it is seen that the maximum amplitudes, and the corresponding signal strength, converge toward zero as the auger tube becomes more embedded in the limestone. Assuming a similar trend for different auger lengths, it is also evident that the signal strength is greater for longer auger tube lengths but the rate of the diminishing signal increases with increasing length.

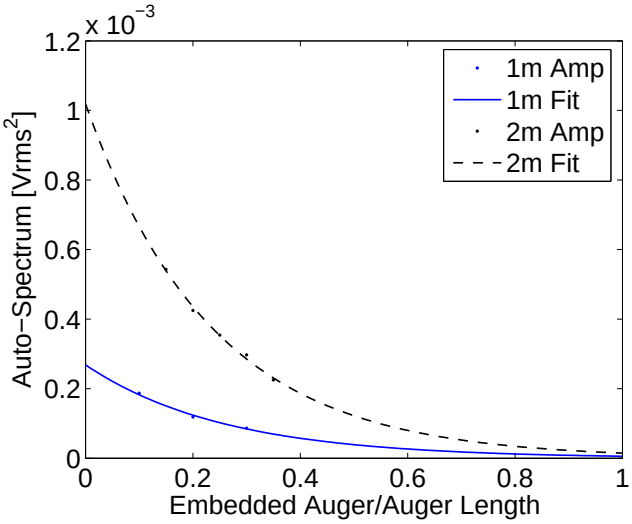

Figure 53: Exponential Curve Fit for Maximum Amplitudes of First Natural Frequency.

From these results, it is clear that the signal strength of surface measurements diminishes with increasing drill depth, which presents limitations for LDV sensors. The maximum depth for accurate surface measurements, however, greatly depends on the properties and measurement capabilities of the sensor. Without further information and data (larger depths and longer auger tubes), it is difficult to conclude a maximum depth limit for these particular LDV sensors.

To examine a possible depth limitation, let's now assume surface measurements by the PDV-100 LDV sensors provide adequate information for the embedded auger up to 80%. The drill system of interest is atop a 33 cm high platform and, with safety and other design tolerances, approximately 40 cm of the auger tube is always above the surface. The drill column allows for the drill head to translate (up and down, z-axis) 1.2 m, which gives a total length of 1.6 m from the surface to the maximum height of the drill head (Fig. 54). This indicates that each additional 1 m drill string is added when less than 60 cm of the current auger tube is above the surface. Therefore, the achievable depths for various auger tube lengths are in Table 9.

Table 9: Depth Limitations for Different Auger Lengths and Accurate Surface Measurements

Auger Length (m)	Max Depth (m)	Additional String Depth (m)	80% Embedded Length (m)
1	0.6	0.4	0.8
2	1.6	1.4	1.6
3	2.6	2.4	2.4
4	3.6	3.4	3.2
5	4.6	4.4	4.0
6	5.6	5.4	4.8
7	6.6	6.4	5.6
8	7.6	7.4	6.4
9	8.6	8.4	7.2
10	9.6	9.4	8.0

Analyzing the depth limits in Table 9, the limit for accurate surface measurements of this drill system is a 3.2 m drill depth with a 4 m auger tube length. Beyond this

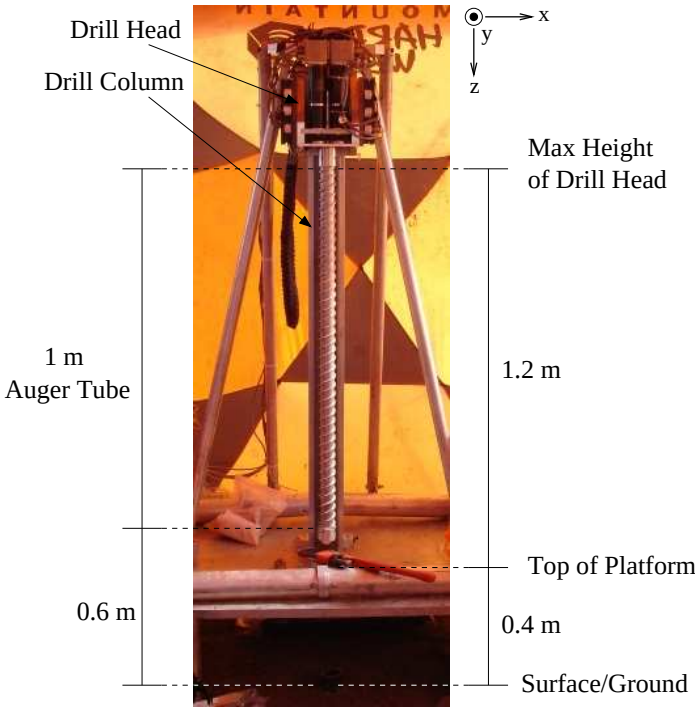

Figure 54: Drill System Dimensions Along z-Axis.

depth, the subsurface auger tube length will be beyond the 80% embedded length threshold. If smaller drill strings, however, are used (such as the 87.5 cm drill strings available with this drill system), the limit can be extended to 3.9 m drill depth with a 4.875 m auger tube length.

This estimated drill depth is very dependent on a number of varying factors. The exact location of the measurement along the auger is important for the magnitude of the individual frequencies and nodal positions. As discussed in Section 4.2 for the drilling experiments, the mode shapes and nodal positions also vary with drill depth and will affect these measurements and frequency magnitudes. Finally, a different drill design or mounting platform or smaller drill strings can alter this depth limit estimate. If more of the auger tube is above the surface, accurate surface measurements can be obtained for greater drill depths.

CHAPTER V

STRUCTURAL DYNAMIC MODELS

The formulation of theoretical models, with and without damage or defects, is an essential part of the SHM field to understand and analyze the health of structural dynamic systems. It provides a basis for using theory to accurately predict the behavior of structures under different types of damage and defects.

The drill auger tube is visualized as a moving and rotating beam supported by the drill head and platform. The auger tube is a hollow, stainless steel tube with helical flutes that wind along the length of the auger and enable the removal of the cuttings to the surface during the drilling process. In operation, the auger tube has a compressive tip load due to the force experienced at the drill bit by the bottom of the drilled hole, and the total length changes with time as the drill depth increases and more auger tube strings are added. A photograph and sketch of the subsurface exploration drill investigated in this research work is in Fig. 55.

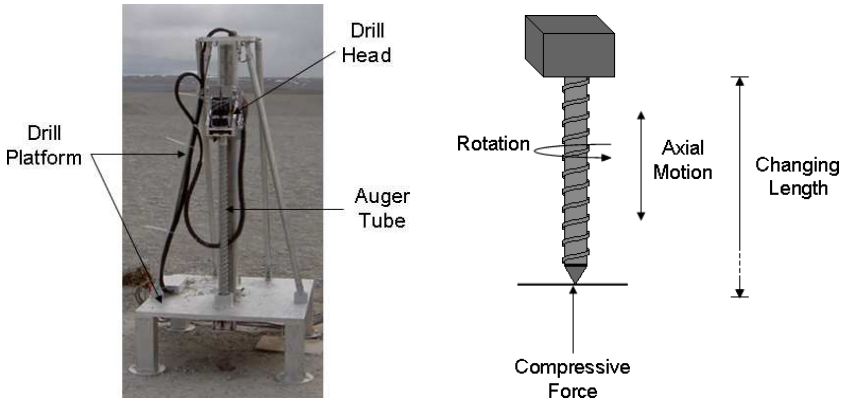

Figure 55: Photograph and Sketch of DAME Drill.

Assuming no coupling between the two orthogonal lateral motions and the torsional and axial motions, the model for the drill auger tube is a two-dimensional continuum fixed-free beam with length $L(t)$, axial velocity $\upsilon(t)$, angular velocity $\Omega(t)$, compressive tip load P, flute twist Θ, and lateral displacements, $u_1(z,t)$ and $u_2(z,t)$, in the x and y directions, respectively (Fig. 56). An engineering drawing of the auger tube and additional photos of the this drill prototype is in Appendix B (Fig. 123), and the material and geometric properties are provided in Table 10.

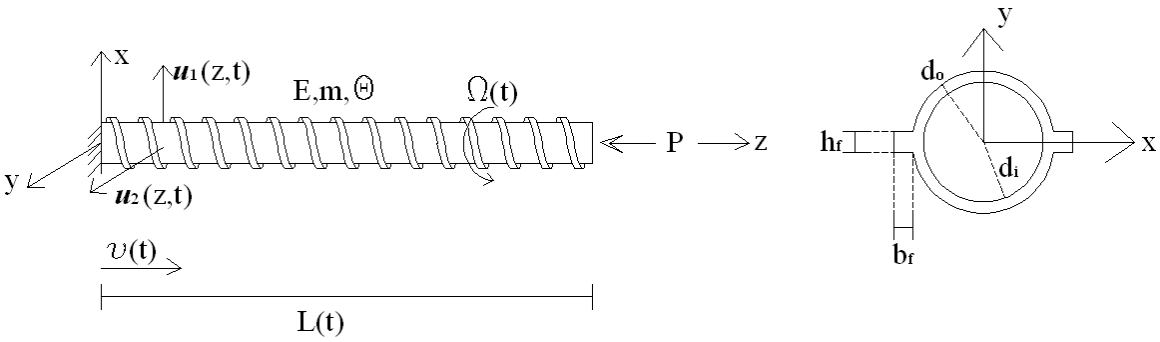

Figure 56: Original Model for Drill Auger Tube.

Table 10: Geometric and Material Properties of Drill Auger Tube

Property	Symbol	Value	Units
Cross-section:			
Inner Diameter	d_i	1.25	in
Outer Diameter	d_o	1.46	in
Length of Flanges	b_f	0.2	in
Height of Flanges	h_f	0.3	in
Length	L	1.0	m
Flute Twist	Θ	20	rev/m
Mass per unit length	m	8.5	lb/m
Modulus of Elasticity	E	197e9	Pa
Poisson's Ratio	ν	0.272	

The following sections present the detailed analysis of the formulated theoretical models for the drill auger tube. The effects of the drilling parameters on the drill auger tube dynamics (without damage and faults) are first analyzed to determine if any parameters are negligible to simplify the formulated models. A base model for the

stationary drill auger tube is then identified and compared with the stationary modal analysis experiments and results. Lastly, models to best represent the auger tube under nominal and drilling fault conditions are formulated, analyzed, and compared with experimental results.

5.1 Drilling Parameter Effects on Dynamic Characteristics of Drill Auger Tube

This section formulates a theoretical model for the drill auger tube to understand the effects of each drilling parameter on the overall dynamic characteristics of the auger tube and determine which parameters are negligible for this specific application. The underlying assumptions for these models are that each drilling parameter (axial velocity, υ; angular velocity, Ω; axial tip load, P; flute twist,Θ; and length, L) is constant (i.e. all time derivatives are zero) and the auger tube material is homogenous, isotropic, and linearly elastic, and the derivations assume Euler-Bernoulli beam theory with rotary inertial affects (i.e. Rayleigh Beam).

The displacement field for an elastic beam in bending is expressed as

$$\begin{aligned} U_x &= u_1(z,t), \\ U_y &= u_2(z,t), \\ U_z &= -x\frac{\partial u_1}{\partial z} - y\frac{\partial u_2}{\partial z}. \end{aligned}$$

The velocity field, including the axial and angular velocities [8, 98, 161], is therefore

$$\begin{aligned} \dot{U}_x &= \frac{\partial u_1}{\partial t} + \upsilon\frac{\partial u_1}{\partial z} - \Omega(u_2 + y), \\ \dot{U}_y &= \frac{\partial u_2}{\partial t} + \upsilon\frac{\partial u_2}{\partial z} + \Omega(u_1 + y), \\ \dot{U}_z &= -x\frac{\partial^2 u_1}{\partial z \partial t} - y\frac{\partial^2 u_2}{\partial z \partial t}. \end{aligned}$$

The equations of motion and boundary conditions for a beam in bending are found using variational analysis and the Extended Hamilton's Principle:

$$\int_{t_1}^{t_2} (\delta\hat{T} - \delta\hat{U} + \delta\hat{W})dt = 0 \tag{31}$$

where $\hat{T}$ is the kinetic energy, $\hat{U}$ is the strain energy, $\hat{W}$ is the external work, and $\delta u_1(z,t) = 0$ and $\delta u_2(z,t) = 0$ for $t = t_1, t_2$ [107]. For a beam in bending, the expression for kinetic energy is

$$\hat{T} = \frac{1}{2}\int \rho \left(\dot{U}_y^2 + \dot{U}_x^2 + \dot{U}_z^2\right) dV. \tag{32}$$

Applying the vector field into Eq. 32 and integrating over the cross-sectional area, the kinetic energy becomes

$$\begin{aligned}\hat{T} = \frac{1}{2}\int_0^L \Bigg\{ & \rho I_{xx}\left(\frac{\partial^2 u_2}{\partial z \partial t}\right)^2 + \rho I_{xy}\frac{\partial^2 u_1}{\partial z \partial t}\frac{\partial^2 u_2}{\partial z \partial t} + \rho I_{yy}\left(\frac{\partial^2 u_1}{\partial z \partial t}\right)^2 \\ & + m\left[\left(\frac{\partial u_1}{\partial t}\right)^2 + \left(\frac{\partial u_2}{\partial t}\right)^2\right] + m\upsilon^2\left[\left(\frac{\partial u_1}{\partial z}\right)^2 + \left(\frac{\partial u_2}{\partial z}\right)^2\right] \\ & + m\Omega^2\left[u_1^2 + u_2^2\right] + 2m\upsilon\left[\frac{\partial u_1}{\partial z}\frac{\partial u_1}{\partial t} + \frac{\partial u_2}{\partial z}\frac{\partial u_2}{\partial t}\right] \\ & + 2m\Omega\left[u_1\frac{\partial u_2}{\partial t} - u_2\frac{\partial u_1}{\partial t}\right] + 2m\Omega\upsilon\left[u_1\frac{\partial u_2}{\partial z} - u_2\frac{\partial u_1}{\partial z}\right]\Bigg\} dz\end{aligned} \tag{33}$$

where

$$\begin{aligned} I_{xx} &= I_{XX}\cos^2(\Theta z) + I_{YY}\sin^2(\Theta z), \\ I_{yy} &= I_{XX}\sin^2(\Theta z) + I_{YY}\cos^2(\Theta z), \\ I_{xy} &= (I_{YY} - I_{XX})\cos(\Theta z)\sin(\Theta z), \end{aligned}$$

and (I_{XX}, I_{YY}) are the principal cross-sectional area moments of inertia [81, 98]. For the auger tube and the designated coordinate system,

$$I_{XX} = \frac{\pi}{64}\left(d_o^4 - d_i^4\right) + 2\frac{b_f h_f^3}{12}, \tag{34}$$

$$I_{YY} = \frac{\pi}{64}\left(d_o^4 - d_i^4\right) + 2\frac{h_f b_f^3}{12} + 2b_f h_f\left(\frac{d_o + b_f}{2}\right)^2. \tag{35}$$

Evaluating $\delta\hat{T}$, we find

$$\begin{aligned}\delta\hat{T} = \int_0^L \Bigg\{ & \rho I_{xx}\frac{\partial^2 u_2}{\partial z\partial t}\frac{\partial^2}{\partial z\partial t}\delta u_2 + \rho I_{xy}\left(\frac{\partial^2 u_2}{\partial z\partial t}\frac{\partial^2}{\partial z\partial t}\delta u_1 + \frac{\partial^2 u_1}{\partial z\partial t}\frac{\partial^2}{\partial z\partial t}\delta u_2\right) \\ & + \rho I_{yy}\frac{\partial^2 u_1}{\partial z\partial t}\frac{\partial^2}{\partial z\partial t}\delta u_1 + m\left[\frac{\partial u_1}{\partial t}\frac{\partial}{\partial t}\delta u_1 + \frac{\partial u_2}{\partial t}\frac{\partial}{\partial t}\delta u_2\right] \\ & + mv^2\left[\frac{\partial u_1}{\partial z}\frac{\partial}{\partial z}\delta u_1 + \frac{\partial u_2}{\partial z}\frac{\partial}{\partial z}\delta u_2\right] + m\Omega^2\left[u_1\delta u_1 + u_2\delta u_2\right] \\ & + 2mv\left[\frac{\partial u_1}{\partial z}\frac{\partial}{\partial t}\delta u_1 + \frac{\partial u_2}{\partial z}\frac{\partial}{\partial t}\delta u_2\right] + 2m\Omega\left[\frac{\partial u_2}{\partial t}\delta u_1 - \frac{\partial u_1}{\partial t}\delta u_2\right] \\ & + 2m\Omega v\left[u_1\frac{\partial}{\partial z}\delta u_2 - u_2\frac{\partial}{\partial z}\delta u_1\right]\Bigg\}dz. \end{aligned} \tag{36}$$

Integrating by parts, the first term for Eq. 31 then becomes

$$\begin{aligned}\int_{t_1}^{t_2}\delta\hat{T} = \int_{t_1}^{t_2}\Bigg\{ & \Bigg[- \rho I_{xx}\frac{\partial^3 u_2}{\partial z\partial t^2}\delta u_2 - \rho I_{xy}\left(\frac{\partial^3 u_2}{\partial z\partial t^2}\delta u_1 + \frac{\partial^3 u_1}{\partial z\partial t^2}\delta u_2\right) - \rho I_{yy}\frac{\partial^3 u_1}{\partial z\partial t^2}\delta u_1 \\ & + mv^2\left(\frac{\partial u_1}{\partial z}\delta u_1 + \frac{\partial u_2}{\partial z}\delta u_2\right) + 2m\Omega v\left(u_1\delta u_2 - u_2\delta u_1\right)\Bigg]\Bigg|_0^L \\ & + \int_0^L\Bigg[\frac{\partial}{\partial z}\left(\rho I_{xx}\frac{\partial^3 u_2}{\partial z\partial t^2}\right)\delta u_2 + \frac{\partial}{\partial z}\left(\rho I_{xy}\frac{\partial^3 u_2}{\partial z\partial t^2}\right)\delta u_1 \\ & + \frac{\partial}{\partial z}\left(\rho I_{xy}\frac{\partial^3 u_1}{\partial z\partial t^2}\right)\delta u_2 + \frac{\partial}{\partial z}\left(\rho I_{yy}\frac{\partial^3 u_1}{\partial z\partial t^2}\right)\delta u_1 \\ & - m\left(\frac{\partial^2 u_1}{\partial t^2}\delta u_1 + \frac{\partial^2 u_2}{\partial t^2}\delta u_2\right) - mv^2\left(\frac{\partial^2 u_1}{\partial z^2}\delta u_1 + \frac{\partial^2 u_2}{\partial z^2}\delta u_2\right) \\ & + m\Omega^2\left(u_1\delta u_1 + u_2\delta u_2\right) - 2mv\left(\frac{\partial^2 u_1}{\partial z\partial t}\delta u_1 + \frac{\partial^2 u_2}{\partial z\partial t}\delta u_2\right) \\ & + 2m\Omega\left(\frac{\partial u_2}{\partial t}\delta u_1 - \frac{\partial u_1}{\partial t}\delta u_2\right) + 2m\Omega v\left(\frac{\partial u_2}{\partial z}\delta u_1 - \frac{\partial u_1}{\partial z}\delta u_2\right)\Bigg]dx\Bigg\}dt. \end{aligned} \tag{37}$$

The expression for the strain energy is

$$\begin{aligned}\hat{U} &= \frac{1}{2}\int_0^L\left(\sigma_x\epsilon_x + \sigma_y\epsilon_y + \sigma_z\epsilon_z + \sigma_{xy}\epsilon_{xy} + \sigma_{xz}\epsilon_{xz} + \sigma_{yz}\epsilon_{yz}\right)dV \\ &= \frac{1}{2}\int_0^L E\left(\epsilon_x^2 + \epsilon_y^2 + \epsilon_z^2 + \epsilon_{xy}^2 + \epsilon_{xz}^2 + \epsilon_{yz}^2\right)dV\,. \end{aligned} \tag{38}$$

Assuming small displacement gradients, the strain field is as follows:

$$\begin{aligned}
\epsilon_x &= \frac{\partial U_x}{\partial x} = 0, \\
\epsilon_y &= \frac{\partial U_y}{\partial y} = 0, \\
\epsilon_z &= \frac{\partial U_z}{\partial z} = -x\frac{\partial^2 u_1}{\partial z^2} - y\frac{\partial^2 u_2}{\partial z^2}, \\
\epsilon_{xy} &= \frac{1}{2}\left[\frac{\partial U_x}{\partial y} + \frac{\partial U_y}{\partial x}\right] = \frac{1}{2}\left[0+0\right] = 0, \\
\epsilon_{xz} &= \frac{1}{2}\left[\frac{\partial U_x}{\partial z} + \frac{\partial U_z}{\partial x}\right] = \frac{1}{2}\left[\frac{\partial u_1}{\partial z} - \frac{\partial u_1}{\partial z}\right] = 0, \\
\epsilon_{yz} &= \frac{1}{2}\left[\frac{\partial U_y}{\partial z} + \frac{\partial U_z}{\partial y}\right] = \frac{1}{2}\left[\frac{\partial u_2}{\partial z} - \frac{\partial u_2}{\partial z}\right] = 0.
\end{aligned}$$

Therefore, Eq. 39 becomes

$$\begin{aligned}
\hat{U} &= \frac{1}{2}\int_0^L E\left(-x\frac{\partial^2 u_1}{\partial z^2} - y\frac{\partial^2 u_2}{\partial z^2}\right)^2 dV \\
&= \frac{1}{2}\int_0^L \left[EI_{xx}\left(\frac{\partial^2 u_2}{\partial z^2}\right)^2 + 2EI_{xy}\frac{\partial^2 u_1}{\partial z^2}\frac{\partial^2 u_2}{\partial z^2} + EI_{yy}\left(\frac{\partial^2 u_1}{\partial z^2}\right)^2\right] dz. \qquad (39)
\end{aligned}$$

Evaluating $\delta\hat{U}$ and simplifying, the expression for $\delta\hat{U}$ becomes

$$\begin{aligned}
\delta\hat{U} &= \int_0^L \left[EI_{xx}\frac{\partial^2 u_2}{\partial z^2}\frac{\partial^2}{\partial z^2}\delta u_2 + EI_{xy}\left(\frac{\partial^2 u_1}{\partial z^2}\frac{\partial^2}{\partial z^2}\delta u_2 + \frac{\partial^2 u_2}{\partial z^2}\frac{\partial^2}{\partial z^2}\delta u_1\right) + EI_{yy}\frac{\partial^2 u_1}{\partial z^2}\frac{\partial^2}{\partial z^2}\delta u_1\right] dz \\
&= \Bigg[EI_{xx}\frac{\partial^2 u_2}{\partial z^2}\frac{\partial}{\partial z}\delta u_2 + EI_{xy}\left(\frac{\partial^2 u_1}{\partial z^2}\frac{\partial}{\partial z}\delta u_2 + \frac{\partial^2 u_2}{\partial z^2}\frac{\partial}{\partial z}\delta u_1\right) + EI_{yy}\frac{\partial^2 u_1}{\partial z^2}\frac{\partial}{\partial z}\delta u_1 \\
&- \frac{\partial}{\partial z}\left(EI_{xx}\frac{\partial^2 u_2}{\partial z^2}\right)\delta u_2 - \frac{\partial}{\partial z}\left(EI_{xy}\frac{\partial^2 u_1}{\partial z^2}\right)\delta u_2 - \frac{\partial}{\partial z}\left(EI_{xy}\frac{\partial^2 u_2}{\partial z^2}\right)\delta u_1 \\
&- \frac{\partial}{\partial z}\left(EI_{yy}\frac{\partial^2 u_1}{\partial z^2}\right)\delta u_1\Bigg]\Bigg|_0^L + \int_0^L \Bigg[\frac{\partial^2}{\partial z^2}\left(EI_{xx}\frac{\partial^2 u_2}{\partial z^2}\right)\delta u_2 + \frac{\partial^2}{\partial z^2}\left(EI_{xy}\frac{\partial^2 u_1}{\partial z^2}\right)\delta u_2 \\
&+ \frac{\partial^2}{\partial z^2}\left(EI_{xy}\frac{\partial^2 u_2}{\partial z^2}\right)\delta u_1 + \frac{\partial^2}{\partial z^2}\left(EI_{yy}\frac{\partial^2 u_1}{\partial z^2}\right)\delta u_1\Bigg] dz\,. \qquad (40)
\end{aligned}$$

The virtual work term in Eq. 31 includes the work done by the compressive tip load P and the gyroscopic moment effects due to the spinning beam:

$$\delta\hat{W} = \delta\hat{W}_P + \delta\hat{W}_G.$$

The virtual work due to the compressive tip load is expressed as

$$\begin{aligned}\delta\hat{W}_P &= \delta\left\{\frac{1}{2}\int_0^L\left[P\left(\frac{\partial u_1}{\partial z}\right)^2 + P\left(\frac{\partial u_2}{\partial z}\right)^2\right]dz\right\}\\ &= \int_0^L\left(P\frac{\partial u_1}{\partial z}\frac{\partial}{\partial z}\delta u_1 + P\frac{\partial u_2}{\partial z}\frac{\partial}{\partial z}\delta u_2\right)dz\\ &= P\frac{\partial u_1}{\partial z}\delta u_1\Big|_0^L + P\frac{\partial u_2}{\partial z}\delta u_2\Big|_0^L - \int_0^L\left(P\frac{\partial^2 u_1}{\partial z^2}\delta u_1 + P\frac{\partial^2 u_2}{\partial z^2}\delta u_2\right)dz, \qquad (41)\end{aligned}$$

and the virtual work due to the gyroscopic moment is

$$\delta\hat{W}_G = \int_0^L\left[\frac{\partial}{\partial z}\left(J_p\Omega\frac{\partial^2 u_2}{\partial z\partial t}\delta u_1\right) - \frac{\partial}{\partial z}\left(J_p\Omega\frac{\partial^2 u_1}{\partial z\partial t}\right)\delta u_2\right]dz \qquad (42)$$

where J_p is the polar mass moment of inertia per unit beam length [44].

Applying Eqs. 37, 40, 41, 42 with Eq. 31 and separating the terms by δu_1 and δu_2, we find

$$
\begin{aligned}
-\int_{t_1}^{t_2}\Bigg\{ & \left(EI_{xx}\frac{\partial^2 u_2}{\partial z^2}+EI_{xy}\frac{\partial^2 u_1}{\partial z^2}\right)\frac{\partial}{\partial z}\delta u_2\Bigg|_0^L+\left(EI_{yy}\frac{\partial^2 u_1}{\partial z^2}+EI_{xy}\frac{\partial^2 u_2}{\partial z^2}\right)\frac{\partial}{\partial z}\delta u_1\Bigg|_0^L \\
& +\Bigg[-\frac{\partial}{\partial z}\left(EI_{xx}\frac{\partial^2 u_2}{\partial z^2}+EI_{xy}\frac{\partial^2 u_1}{\partial z^2}\right)+\rho I_{xx}\frac{\partial^3 u_2}{\partial z\partial t^2}+\rho I_{xy}\frac{\partial^3 u_1}{\partial z\partial t^2} \\
& \quad -P\frac{\partial u_2}{\partial z}-m\left(\upsilon^2\frac{\partial u_2}{\partial z}+2\Omega\upsilon u_1\right)\Bigg]\delta u_2\Bigg|_0^L \\
& +\Bigg[-\frac{\partial}{\partial z}\left(EI_{yy}\frac{\partial^2 u_1}{\partial z^2}+EI_{xy}\frac{\partial^2 u_2}{\partial z^2}\right)+\rho I_{yy}\frac{\partial^3 u_1}{\partial z\partial t^2}+\rho I_{xy}\frac{\partial^3 u_2}{\partial z\partial t^2} \\
& \quad -P\frac{\partial u_1}{\partial z}-m\left(\upsilon^2\frac{\partial u_1}{\partial z}-2\Omega\upsilon u_2\right)\Bigg]\delta u_1\Bigg|_0^L \\
& +\int_0^L\Bigg[\Bigg[\frac{\partial^2}{\partial z^2}\left(EI_{xx}\frac{\partial^2 u_2}{\partial z^2}+EI_{xy}\frac{\partial^2 u_1}{\partial z^2}\right)-\frac{\partial}{\partial z}\left(\rho I_{xx}\frac{\partial^3 u_2}{\partial z\partial t^2}+\rho I_{xy}\frac{\partial^3 u_1}{\partial z\partial t^2}\right) \\
& \quad +\frac{\partial}{\partial z}\left(J_p\Omega\frac{\partial^2 u_1}{\partial z\partial t}\right)+P\frac{\partial^2 u_2}{\partial z^2}+m\Bigg(\frac{\partial^2 u_2}{\partial t^2}+\upsilon^2\frac{\partial^2 u_2}{\partial z^2}-\Omega^2 u_2 \\
& \quad +2\upsilon\frac{\partial^2 u_2}{\partial z\partial t}+2\Omega\frac{\partial u_1}{\partial t}+2\Omega\upsilon\frac{\partial u_1}{\partial z}\Bigg)\Bigg]\delta u_2 \\
& +\Bigg[\frac{\partial^2}{\partial z^2}\left(EI_{yy}\frac{\partial^2 u_1}{\partial z^2}+EI_{xy}\frac{\partial^2 u_2}{\partial z^2}\right)-\frac{\partial}{\partial z}\left(\rho I_{yy}\frac{\partial^3 u_1}{\partial z\partial t^2}+\rho I_{xy}\frac{\partial^3 u_2}{\partial z\partial t^2}\right) \\
& \quad -\frac{\partial}{\partial z}\left(J_p\Omega\frac{\partial^2 u_2}{\partial z\partial t}\right)+P\frac{\partial^2 u_1}{\partial z^2}+m\Bigg(\frac{\partial^2 u_1}{\partial t^2}+\upsilon^2\frac{\partial^2 u_1}{\partial z^2}-\Omega^2 u_1 \\
& \quad +2\upsilon\frac{\partial^2 u_1}{\partial z\partial t}-2\Omega\frac{\partial u_2}{\partial t}-2\Omega\upsilon\frac{\partial u_2}{\partial z}\Bigg)\Bigg]\delta u_1\Bigg]dz\Bigg\}dt=0. \qquad (43)
\end{aligned}
$$

Applying the fundamental lemma in the calculus of variations, the equations of motion are therefore

$$
\begin{aligned}
& \frac{\partial^2}{\partial z^2}\left(EI_{yy}\frac{\partial^2 u_1}{\partial z^2}+EI_{xy}\frac{\partial^2 u_2}{\partial z^2}\right)-\frac{\partial}{\partial z}\left(\rho I_{yy}\frac{\partial^3 u_1}{\partial z\partial t^2}+\rho I_{xy}\frac{\partial^3 u_2}{\partial z\partial t^2}\right)-\frac{\partial}{\partial z}\left(J_p\Omega\frac{\partial^2 u_2}{\partial z\partial t}\right) \\
& \quad +P\frac{\partial^2 u_1}{\partial z^2}+m\left(\frac{\partial^2 u_1}{\partial t^2}+\upsilon^2\frac{\partial^2 u_1}{\partial z^2}-\Omega^2 u_1+2\upsilon\frac{\partial^2 u_1}{\partial z\partial t}-2\Omega\frac{\partial u_2}{\partial t}-2\Omega\upsilon\frac{\partial u_2}{\partial z}\right)=0, \qquad (44)
\end{aligned}
$$

$$\frac{\partial^2}{\partial z^2}\left(EI_{xx}\frac{\partial^2 u_2}{\partial z^2}+EI_{xy}\frac{\partial^2 u_1}{\partial z^2}\right)-\frac{\partial}{\partial z}\left(\rho I_{xx}\frac{\partial^3 u_2}{\partial z\partial t^2}+\rho I_{xy}\frac{\partial^3 u_1}{\partial z\partial t^2}\right)+\frac{\partial}{\partial z}\left(J_p\Omega\frac{\partial^2 u_1}{\partial z\partial t}\right)$$
$$+P\frac{\partial^2 u_2}{\partial z^2}+m\left(\frac{\partial^2 u_2}{\partial t^2}+\upsilon^2\frac{\partial^2 u_2}{\partial z^2}-\Omega^2 u_2+2\upsilon\frac{\partial^2 u_2}{\partial z\partial t}+2\Omega\frac{\partial u_1}{\partial t}+2\Omega\upsilon\frac{\partial u_1}{\partial z}\right)=0, \tag{45}$$

for $0<z<L$, and the boundary conditions at $z=0,\ L$ are

$$u_1=0 \quad \text{or} \quad \left[-\frac{\partial}{\partial z}\left(EI_{yy}\frac{\partial^2 u_1}{\partial z^2}+EI_{xy}\frac{\partial^2 u_2}{\partial z^2}\right)+\rho I_{yy}\frac{\partial^3 u_1}{\partial z\partial t^2}+\rho I_{xy}\frac{\partial^3 u_2}{\partial z\partial t^2}\right.$$
$$\left.-P\frac{\partial u_1}{\partial z}-m\left(\upsilon^2\frac{\partial u_1}{\partial z}-2\Omega\upsilon u_2\right)\right]=0, \tag{46}$$

$$u_2=0 \quad \text{or} \quad \left[-\frac{\partial}{\partial z}\left(EI_{xx}\frac{\partial^2 u_2}{\partial z^2}+EI_{xy}\frac{\partial^2 u_1}{\partial z^2}\right)+\rho I_{xx}\frac{\partial^3 u_2}{\partial z\partial t^2}+\rho I_{xy}\frac{\partial^3 u_1}{\partial z\partial t^2}\right.$$
$$\left.-P\frac{\partial u_2}{\partial z}-m\left(\upsilon^2\frac{\partial u_2}{\partial z}+2\Omega\upsilon u_1\right)\right]=0, \tag{47}$$

$$\frac{\partial u_1}{\partial z}=0 \quad \text{or} \quad \left(EI_{yy}\frac{\partial^2 u_1}{\partial z^2}+EI_{xy}\frac{\partial^2 u_2}{\partial z^2}\right)=0, \tag{48}$$

$$\frac{\partial u_2}{\partial z}=0 \quad \text{or} \quad \left(EI_{xx}\frac{\partial^2 u_2}{\partial z^2}+EI_{xy}\frac{\partial^2 u_1}{\partial z^2}\right)=0\,. \tag{49}$$

These equations are compared with those found for other studies on drill dynamics. O. Tekinalp [155], C. L. Liao [98], and B. W. Huang [81] have all conducted studies on drill dynamics. These studies include complex geometries, compressive tip loads, and angular velocities (excluding the gyroscopic moment terms). D. M. Rincon's [125] study includes the gyroscopic terms. Each of these studies does not include an axial velocity component.

The following sections dissect the derived equations of motion and boundary conditions to evaluate the importance of the drilling parameters. Discussions of the results explain and indicate which parameters have negligible effects on the dynamic characteristics of the drill auger tube and are neglected in the present work.

5.1.1 Axial Motion Effects

To examine the effects due to the axial motion, the equations of motion are evaluated with $\nu \neq 0$ and $\Omega = P = \Theta = 0$, and the rotary inertia effects are neglected. Non-dimensionalizing the equations of motion by L, Eqs. 44 and 45 become

$$\frac{EI_{YY}}{mL^4}u_1^{IV} + v_*^2 u_1'' + 2v_* \dot{u_1}' + \ddot{u_1} = 0, \quad 0 < \eta < 1 \tag{50}$$

$$\frac{EI_{XX}}{mL^4}u_2^{IV} + v_*^2 u_2'' + 2v_* \dot{u_2}' + \ddot{u_2} = 0, \quad 0 < \eta < 1 \tag{51}$$

where

$$()' = \frac{\partial}{\partial \eta}, \ \dot{()} = \frac{\partial}{\partial t}, \ \eta = \frac{z}{L}, \ v_* = \frac{v}{L}.$$

These (uncoupled) equations match those found for several other studies involving axially moving beams [8,17,30,112]. For simplification, the solution to the remainder of this problem uses u for both lateral displacements and I for both principal cross-sectional area moments of inertia.

Substituting the solution form

$$u(\eta, t) = U(\eta)e^{i\omega t} = Be^{\lambda \eta}e^{i\omega t},$$

the equations of motion become

$$\lambda^4 + \hat{v}^2\lambda^2 + 2i\hat{v}\alpha^2\lambda - \alpha^4 = 0, \tag{52}$$

where

$$\hat{v}^2 = v_*^2\frac{mL^4}{EI} = v^2\frac{mL^2}{EI}, \quad \alpha^4 = \omega^2\frac{mL^4}{EI}.$$

Solving for λ [8,30], we find

$$\lambda_{1,2} = -i\frac{\hat{v}}{2} \pm \sqrt{\alpha^2 - \frac{\hat{v}^2}{4}} = -i\frac{\hat{v}}{2} \pm \gamma,$$

$$\lambda_{3,4} = i\frac{\hat{v}}{2} \pm i\sqrt{\alpha^2 + \frac{\hat{v}^2}{4}} = i\frac{\hat{v}}{2} \pm i\psi.$$

Therefore, the spatial solution for the lateral displacements is

$$U(\eta) = e^{-i\frac{1}{2}\hat{v}\eta}[B_1\cosh(\gamma\eta) + B_2\sinh(\gamma\eta)] + e^{i\frac{1}{2}\hat{v}\eta}[B_3\cos(\psi\eta) + B_4\sin(\psi\eta)], \quad (53)$$

and the boundary conditions for a fixed-free beam are

$$\begin{aligned} \eta = 0: \quad & U = 0,\ U' = 0, \\ \eta = 1: \quad & U'' = 0,\ -\left(U''' + \hat{v}^2 U'\right) = 0. \end{aligned} \quad (54)$$

Substituting Eq. 53 into Eq. 54, the characteristic equation is obtained and the natural frequencies are found. Figure 57 demonstrates the axial velocity effects on the first four drill modes, and Fig. 58 demonstrates the axial velocity effects on the first drill mode for various auger lengths. The y-axis for these plots is the percent error compared to the model that considers $v = 0$, which is evaluated as

$$\%\,\text{Error} = \frac{\omega\big|_{v=v} - \omega\big|_{v=0}}{\omega\big|_{v=v}} \cdot 100\,\%\,.$$

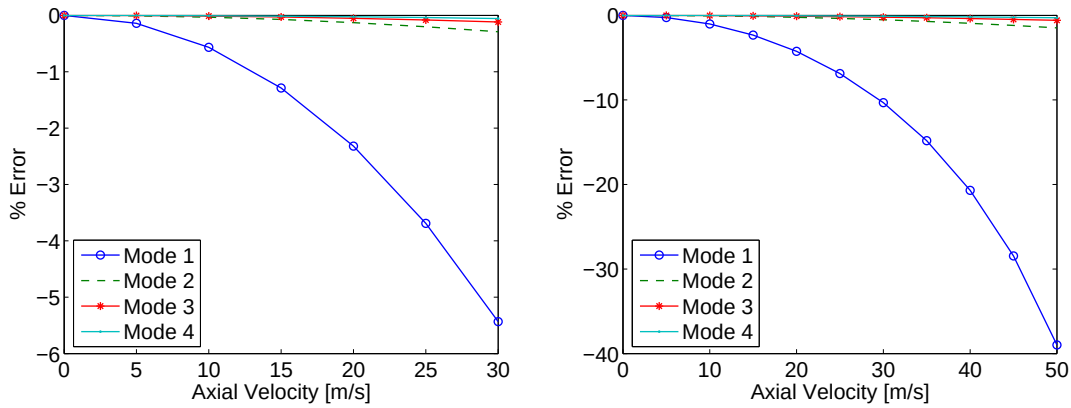

(a) $u_1(z,t)$ (b) $u_2(z,t)$

Figure 57: Effects of Axial Velocity on Drill Modes.

From these results, only the first mode considerably changes due to the axial velocity and this influence increases with increasing auger length. Furthermore, the

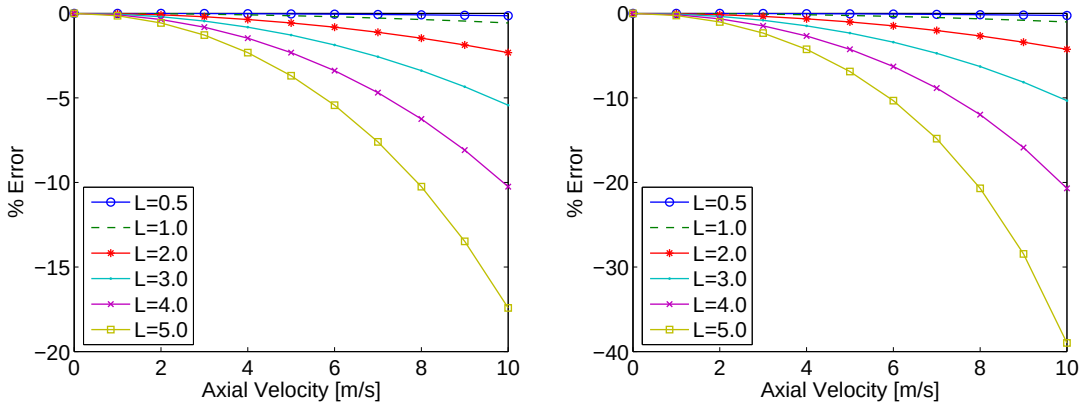

(a) $u_1(z,t)$ (b) $u_2(z,t)$

Figure 58: Effects of Axial Velocity on First Drill Mode for Various Auger Lengths.

frequencies for u_2 are more sensitive (i.e. the percent error is considerably greater than u_1) to the axial velocity parameter. This is due to the smaller cross-sectional area moment of inertia (I_{XX}).

Determining the critical velocity is also of interest. The critical velocity is the velocity at which the first bending natural frequency becomes zero and the system becomes unstable. To determine this velocity, Eq. 51 is evaluated for $\omega = 0$ (i.e. all time-derivative terms become zero). The spatial solution [76] therefore becomes

$$U(\eta) = B_1\cos(\hat{v}\eta) + B_2\sin(\hat{v}\eta) + B_3\eta + B_4. \tag{55}$$

Applying the boundary conditions to the static spatial solution, the characteristic equation is

$$\cos(\hat{v}) = 0.$$

Solving for $\hat{v}$, the critical velocity for a fixed-free beam is

$$\begin{aligned} \hat{v} =& v_{CR}\sqrt{\frac{mL^2}{EI}} = \frac{\pi}{2}, \\ v_{CR} =& \frac{\pi}{2}\sqrt{\frac{EI}{mL^2}}. \end{aligned} \tag{56}$$

5.1.2 Axial Force Effects

To examine the effects due to the compressive tip load P, we return to Eqs. 44 and 45 and all other drilling parameters $(\upsilon, \Omega, \Theta)$ and the rotary inertia components are set to zero. Non-dimensionalizing by L, the equations of motion become

$$\frac{EI_{YY}}{mL^4}u_1^{IV} + \frac{P}{mL^2}u_1'' + \ddot{u}_1 = 0, \quad 0 < \eta < 1 \tag{57}$$

$$\frac{EI_{XX}}{mL^4}u_2^{IV} + \frac{P}{mL^2}u_2'' + \ddot{u}_2 = 0, \quad 0 < \eta < 1 \tag{58}$$

These equations match exactly for a beam in bending with a compressive tip load [107, 144]. For simplicity, the solution to the remainder of this problem again uses u for both lateral displacements and I for both cross-sectional area moments of inertia. Substituting the solution form

$$u(\eta, t) = U(\eta)e^{i\omega t} = Be^{\lambda\eta}e^{i\omega t},$$

the equation of motion becomes

$$\lambda^4 + \hat{p}\lambda^2 - \alpha^4 = 0, \tag{59}$$

where

$$\hat{p} = \frac{PL^2}{EI}.$$

Solving for λ, we find

$$\lambda_{1,2} = \pm\sqrt{\frac{-\hat{p} + \sqrt{\hat{p}^2 + 4\alpha^4}}{2}} = \pm\gamma,$$

$$\lambda_{3,4} = \pm i\sqrt{\frac{\hat{p} + \sqrt{\hat{p}^2 + 4\alpha^4}}{2}} = \pm i\psi.$$

The spatial solution for the lateral displacements is then

$$U(\eta) = B_1\cosh(\gamma\eta) + B_2\sinh(\gamma\eta) + B_3\cos(\psi\eta) + B_4\sin(\psi\eta), \tag{60}$$

and the boundary conditions for a fixed-free beam with a compressive tip load are

$$\begin{aligned} \eta = 0: &\quad U = 0,\ U' = 0, \\ \eta = 1: &\quad U'' = 0,\ -(U''' + \hat{p}U') = 0\,. \end{aligned} \tag{61}$$

Applying Eq. 60 into Eq. 61, the characteristic equation is obtained and the natural frequencies are found. The compressive tip load effects on the first four drill modes are demonstrated in Fig. 59, and these effects on the first drill mode for various auger lengths is provided in Fig. 60.

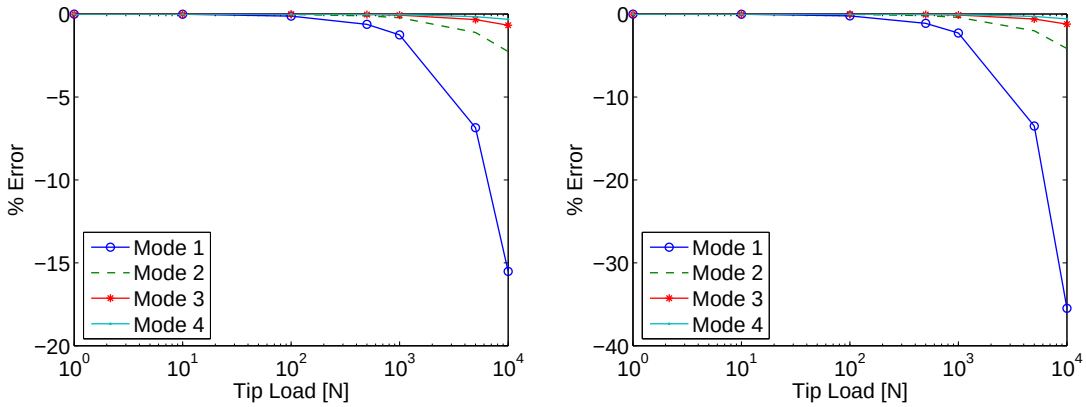

(a) $u_1(z,t)$ (b) $u_2(z,t)$

Figure 59: Effects of Compressive Tip Load on Drill Modes.

Similar to the axial velocity results, only the first mode changes considerably with the tip compressive load and this influence increases with increasing auger length. The frequencies for u_2 are also more sensitive than for u_1.

Determining the critical tip load is also of interest. Similar to the critical velocity, the critical tip load is the load at which the first bending natural frequency becomes zero and the system becomes unstable [138, 144]. To determine this load, Eq. 57 is evaluated for $\omega = 0$. The spatial solution therefore becomes

$$U(\eta) = C_1 \cos(\sqrt{\hat{p}}\eta) + C_2 \sin(\sqrt{\hat{p}}\eta) + C_3\eta + C_4, \tag{62}$$

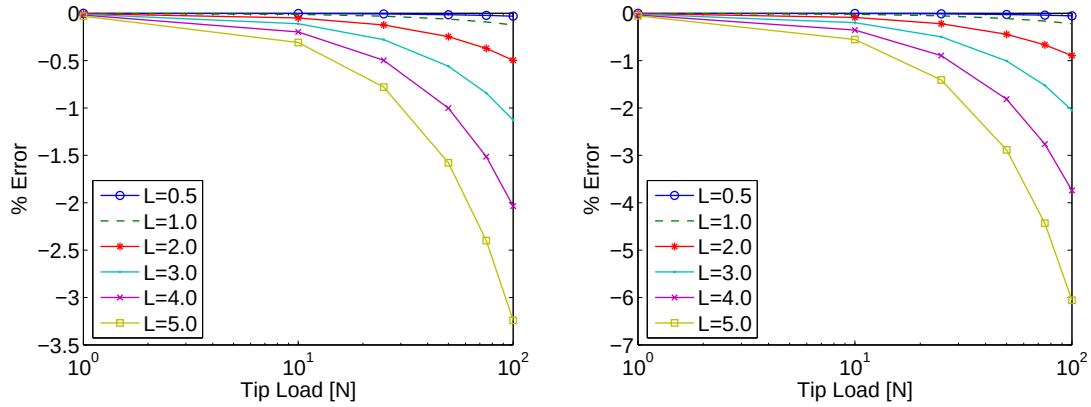

(a) $u_1(z,t)$ (b) $u_2(z,t)$

Figure 60: Effects of Compressive Tip Load on First Drill Mode for Various Auger Lengths.

Applying the boundary conditions, the characteristic equation is

$$\cos(\sqrt{\hat{p}}) = 0.$$

Solving for $\hat{p}$, the critical tip load for a fixed-free beam is

$$\begin{aligned} \hat{p} =& \frac{P_{CR}L^2}{EI} = \frac{\pi^2}{4}, \\ P_{CR} =& \frac{\pi^2}{4}\frac{EI}{L^2}. \end{aligned} \tag{63}$$

5.1.3 Angular Motion Effects

Returning to Eqs. 44 and 45, the dynamic effects due to the rotating auger tube are evaluated with all drilling parameters set to zero (υ, P, Θ) with the exception of the angular velocity Ω. Non-dimensionalizing by L, the equations of motion become

$$EI_{YY}\frac{\partial^4 u_1}{\partial z^4} - J\frac{\partial^4 u_1}{\partial z^2 \partial t^2} - J_P\Omega\frac{\partial^3 u_2}{\partial z^2 \partial t} + m\left(\frac{\partial^2 u_1}{\partial t^2} - \Omega^2 u_1 - 2\Omega\frac{\partial u_2}{\partial t}\right) = 0, \tag{64}$$

$$EI_{XX}\frac{\partial^4 u_2}{\partial z^4} - J\frac{\partial^4 u_2}{\partial z^2 \partial t^2} + J_P\Omega\frac{\partial^3 u_1}{\partial z^2 \partial t} + m\left(\frac{\partial^2 u_2}{\partial t^2} - \Omega^2 u_2 + 2\Omega\frac{\partial u_1}{\partial t}\right) = 0. \tag{65}$$

Using a similar approach found in literature [50,91,99], Eqs. 64 and 65 are simplified by multiplying Eq. 65 by i and assuming the displacement field $\bar{u} = u_1 + iu_2$. For

further simplification, the cross-sectional area moments of inertia are assumed equal (i.e. $I_{XX} = I_{YY} = I$ and $J_P = \rho(I_{xx} + I_{yy}) = \rho(I_{XX} + I_{YY}) = 2\rho I$). Therefore, the single equation of motion is

$$\frac{EI}{mL^4}\bar{u}^{IV} - \frac{\rho I}{mL^2}\left(\ddot{\bar{u}}'' - 2i\Omega\dot{\bar{u}}''\right) + \ddot{\bar{u}} + 2i\Omega\dot{\bar{u}} - \Omega^2\bar{u} = 0, \quad 0 < \eta < 1\,. \tag{66}$$

Again substituting the solution form

$$\bar{u}(\eta, t) = \bar{U}(\eta)e^{i\omega t} = Be^{\lambda\eta}e^{i\omega t},$$

the equation of motion becomes

$$\lambda^4 + \left(\alpha^4 - 2\hat{\Omega}\alpha^2\right)R^2\lambda^2 - \left(\alpha^4 + 2\hat{\Omega}\alpha^2 + \hat{\Omega}^2\right) = 0, \tag{67}$$

where

$$\hat{\Omega}^2 = \Omega^2\frac{mL^4}{EI},\ R^2 = \frac{\rho I}{mL^2}.$$

Solving for κ we find

$$\lambda_{1,2} = \pm\sqrt{\frac{-\left(\alpha^4 - 2\hat{\Omega}\alpha^2\right)R^2 + \sqrt{\left(\alpha^4 - 2\hat{\Omega}\alpha^2\right)^2 R^4 + 4\left(\alpha^4 + 2\hat{\Omega}\alpha^2 + \hat{\Omega}^2\right)}}{2}} = \pm\gamma,$$

$$\lambda_{3,4} = \pm i\sqrt{\frac{\left(\alpha^4 - 2\hat{\Omega}\alpha^2\right)R^2 + \sqrt{\left(\alpha^4 - 2\hat{\Omega}\alpha^2\right)^2 R^4 + 4\left(\alpha^4 + 2\hat{\Omega}\alpha^2 + \hat{\Omega}^2\right)}}{2}} = \pm i\psi.$$

Therefore, the spatial solution for the lateral displacements is

$$\bar{U}(\eta) = B_1\cosh(\gamma\eta) + B_2\sinh(\gamma\eta) + B_3\cos(\psi\eta) + B_4\sin(\psi\eta), \tag{68}$$

and the boundary conditions for a fixed-free beam are

$$\begin{aligned} \eta = 0: &\quad \bar{U} = 0,\ \bar{U}' = 0, \\ \eta = 1: &\quad \bar{U}'' = 0,\ -\left(\bar{U}''' + \alpha^4 R^2\bar{U}'\right) = 0. \end{aligned} \tag{69}$$

Applying Eq. 68 to the boundary conditions, the characteristic equation is obtained and the natural frequencies are found. The angular velocity effects on the first four

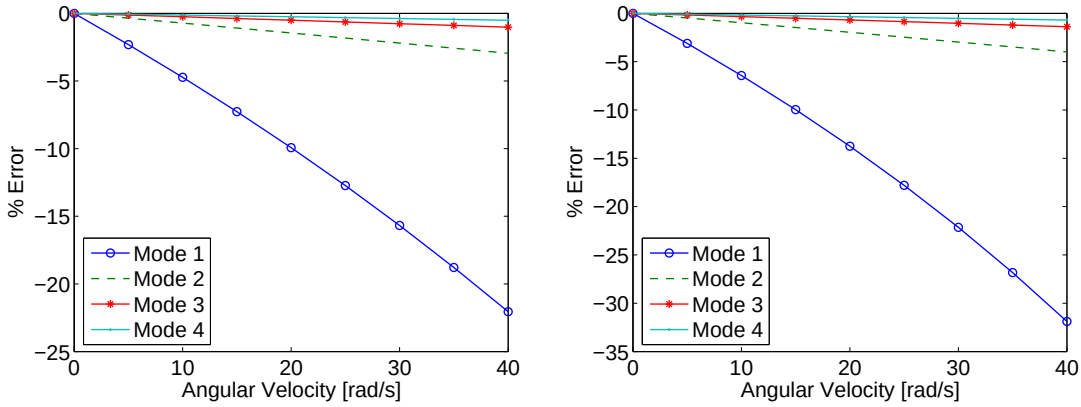

(a) $I = I_{YY}$ (b) $I = I_{XX}$

Figure 61: Effects of Angular Velocity on Drill Modes.

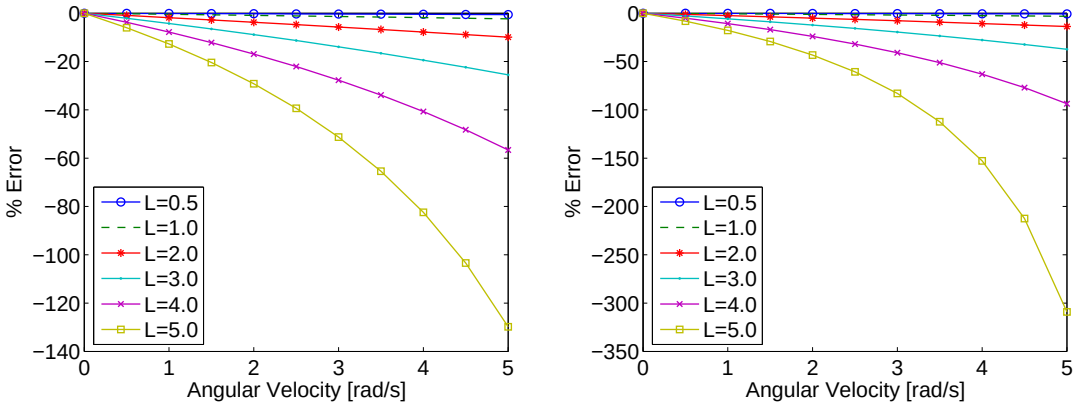

(a) $I = I_{YY}$ (b) $I = I_{XX}$

Figure 62: Effects of Angular Velocity on First Drill Mode for Various Auger Lengths.

drill modes is provided in Fig. 61, and the angular velocity effects on the first drill mode for various auger lengths is provided in Fig. 62.

Similar to the previous results, only the first mode significantly changes due to the axial velocity and this influence increases with increasing auger length. The frequencies when $I = I_{XX}$ are also more sensitive than when $I = I_{YY}$.

Determining the critical angular velocity is also of interest. The critical velocity occurs when $\Omega = \omega_1$ [50]. To determine this velocity, Eq. 66 is evaluated for $\omega = \Omega$

($\alpha^2 = \hat{\Omega}$). Therefore, γ and ψ are rewritten as

$$\gamma = \sqrt{\frac{\hat{\Omega}^2 R^2 + \sqrt{\hat{\Omega}^4 R^4 + 16\hat{\Omega}^2}}{2}},$$
$$\psi = \sqrt{\frac{-\hat{\Omega}^2 R^2 + \sqrt{\hat{\Omega}^4 R^4 + 16\hat{\Omega}^2}}{2}},$$

and the boundary conditions become

$$\eta = 0: \quad \bar{U} = 0,\ \bar{U}' = 0,$$
$$\eta = 1: \quad \bar{U}'' = 0,\ -\left(\bar{U}''' + \hat{\Omega}^2 R^2 \bar{U}'\right) = 0.$$

Applying the boundary conditions to the spatial solution, the characteristic equation is

$$2\hat{\Omega}^4 R^4 + 8\hat{\Omega}^2 + \left(8\hat{\Omega}^2 - \hat{\Omega}^4 R^4\right)\cosh(\gamma)\cos(\psi) - 3\hat{\Omega}^2 R^2 \psi\gamma \sinh(\gamma)\sin(\psi) = 0. \quad (70)$$

Unlike the critical values for the axial velocity and axial tip load, the characteristic equation for the critical angular velocity is not simple and the solution is solved numerically. From Eq. 70, however, the eigenvalue $\hat{\Omega}$ approaches the eigenvalue of a fixed-free Euler-Bernoulli beam as the beam length increases (i.e. $R^2 \cong 0$). Therefore, the approximate critical angular velocity is

$$\begin{aligned} \hat{\Omega} =& \Omega_{CR}\sqrt{\frac{mL^4}{EI}} \cong (1.875)^2 \\ \Omega_{CR} &\cong (1.875)^2\sqrt{\frac{EI}{mL^4}}. \end{aligned} \quad (71)$$

5.1.4 Full Model Analysis using Galerkin's Method

Finding a closed-form solution with two or more of the drilling parameters is very cumbersome if at all possible. Therefore, to evaluate the auger tube frequencies with all drilling parameters, a full model analysis is completed using Galerkin's Method.

We first assume the trial and test functions

$$u_1(z,t) = \sum_{i=1}^{N} p_i(t)\phi_i(z)\,, \tag{72}$$

$$u_2(z,t) = \sum_{i=1}^{N} q_i(t)\phi_i(z)\,, \tag{73}$$

where $\phi_i(z)$ are the admissible functions and $p_i(t)$ and $q_i(t)$ are weighting functions that have yet to be determined [80]. Applying Galerkin's method to Eqs. 44 and 45, the equations of motion are expressed in matrix form as

$$[\mathbf{M}]\begin{Bmatrix}\ddot{p}\\ \ddot{q}\end{Bmatrix} + [\mathbf{C}]\begin{Bmatrix}\dot{p}\\ \dot{q}\end{Bmatrix} + [\mathbf{K}]\begin{Bmatrix}p\\ q\end{Bmatrix} = \begin{Bmatrix}0\\ 0\end{Bmatrix}\,, \tag{74}$$

where

$$[\mathbf{M}] = \begin{bmatrix} m[\mathbf{M}]^1 + \rho[\mathbf{M}]^2 & \rho[\mathbf{M}]^3 \\ \rho[\mathbf{M}]^3 & m[\mathbf{M}]^1 + \rho[\mathbf{M}]^4 \end{bmatrix}\,, \tag{75}$$

$$[\mathbf{C}] = \begin{bmatrix} 2m\upsilon[\mathbf{M}]^5 & \Omega[\mathbf{M}]^6 - 2m\Omega[\mathbf{M}]^1 \\ 2m\Omega[\mathbf{M}]^1 - \Omega[\mathbf{M}]^6 & 2m\upsilon[\mathbf{M}]^5 \end{bmatrix}\,, \tag{76}$$

$$[\mathbf{K}] = \begin{bmatrix} [\mathbf{K}]^1 - (P + m\upsilon^2)[\mathbf{M}]^7 - m\Omega^2[\mathbf{M}]^1 & [\mathbf{K}]^2 - 2m\upsilon\Omega[\mathbf{M}]^5 \\ [\mathbf{K}]^2 + 2m\upsilon\Omega[\mathbf{M}]^5 & [\mathbf{K}]^3 - (P + m\upsilon^2)[\mathbf{M}]^7 - m\Omega^2[\mathbf{M}]^1 \end{bmatrix}\,, \tag{77}$$

and the individual matrix elements are

$$\mathbf{M}^1_{ij} = \int_0^1 \phi_i(\eta)\phi_j(\eta)\,d\eta\,, \qquad \mathbf{M}^2_{ij} = \frac{1}{L^2}\int_0^1 I_{yy}\frac{d\phi_i(\eta)}{d\eta}\frac{d\phi_j(\eta)}{d\eta}\,d\eta\,,$$

$$\mathbf{M}^3_{ij} = \frac{1}{L^2}\int_0^1 I_{xy}\frac{d\phi_i(\eta)}{d\eta}\frac{d\phi_j(\eta)}{d\eta}\,d\eta\,, \qquad \mathbf{M}^4_{ij} = \frac{1}{L^2}\int_0^1 I_{xx}\frac{d\phi_i(\eta)}{d\eta}\frac{d\phi_j(\eta)}{d\eta}\,d\eta\,,$$

$$\mathbf{M}^5_{ij} = \frac{1}{L}\int_0^1 \phi_i(\eta)\frac{d\phi_j(\eta)}{d\eta}\,d\eta\,, \qquad \mathbf{M}^6_{ij} = \frac{1}{L^2}\int_0^1 J_p\frac{d\phi_i(\eta)}{d\eta}\frac{d\phi_j(\eta)}{d\eta}\,d\eta\,,$$

$$\mathbf{M}^7_{ij} = \frac{1}{L^2}\int_0^1 \frac{d\phi_i(\eta)}{d\eta}\frac{d\phi_j(\eta)}{d\eta}\,d\eta\,, \qquad \mathbf{K}^1_{ij} = \frac{E}{L^4}\int_0^1 I_{yy}\frac{d^2\phi_i(\eta)}{d\eta^2}\frac{d^2\phi_j(\eta)}{d\eta^2}\,d\eta\,,$$

$$\mathbf{K}^2_{ij} = \frac{E}{L^4}\int_0^1 I_{xy}\frac{d^2\phi_i(\eta)}{d\eta^2}\frac{d^2\phi_j(\eta)}{d\eta^2}\,d\eta\,, \qquad \mathbf{K}^3_{ij} = \frac{E}{L^4}\int_0^1 I_{xx}\frac{d^2\phi_i(\eta)}{d\eta^2}\frac{d^2\phi_j(\eta)}{d\eta^2}\,d\eta\,.$$

A complete derivation of Eqs. 74 through 77 is in Appendix E.

To solve Eq. 74, it is rewritten as

$$\begin{bmatrix} [\mathbf{M}] & [\mathbf{0}] \\ [\mathbf{0}] & [\mathbf{K}] \end{bmatrix} \begin{Bmatrix} \ddot{p} \\ \ddot{q} \\ \dot{p} \\ \dot{q} \end{Bmatrix} + \begin{bmatrix} [\mathbf{C}] & [\mathbf{K}] \\ [-\mathbf{K}] & [\mathbf{0}] \end{bmatrix} \begin{Bmatrix} \dot{p} \\ \dot{q} \\ p \\ q \end{Bmatrix} = \begin{Bmatrix} 0 \end{Bmatrix} ,$$

$$[\mathbf{A}] \left\{ \dot{\mathbf{V}} \right\} + [\mathbf{B}] \left\{ \mathbf{V} \right\} = \left\{ 0 \right\} . \tag{78}$$

Solving the eigenvalue problem (Eq. 78), the natural frequencies for the two lateral motions are found. The mode shapes of a clamped-free beam up to eight modes are used for the admissible functions (Eq. 79).

$$\phi_i = \sinh(\alpha_i \eta) - \sin(\alpha_i \eta) - \frac{\sinh(\alpha_i) + \sin(\alpha_i)}{\cosh(\alpha_i) + \cos(\alpha_i)} \left[\cosh(\alpha_i \eta) - \cos(\alpha_i \eta) \right] , \quad i = 1, 2, .., 8 . \tag{79}$$

A first step is to analyze the effects of various cross-sectional geometries with all other drilling parameters (υ, P, Ω) set to zero. Figure 63 demonstrates the effects for various values of Θ (flute twist) on the first four drill modes, and Fig. 64 compares the change in the first drill mode for the two lateral displacements. These results show that the fluted auger tube geometry has considerable effects on all drill modes. Comparing the change in the two lateral frequencies (Fig. 64), the natural frequencies converge to a value that is between the two lateral frequencies without any twist.

To evaluate the effects of the simultaneous drilling parameters, four cases have been formulated and studied. Table 11 provides the nominal operating range for the various drilling parameters of the drill prototype, and Table 12 provides the values used in the four cases. Case 3 best represents the nominal operating conditions.

Figures 65 through 68 demonstrate the differences between the four cases studied. For each graph, four of the drilling parameters are kept constant while the fifth drilling parameter varies over a given range. From these results, we see close similarities

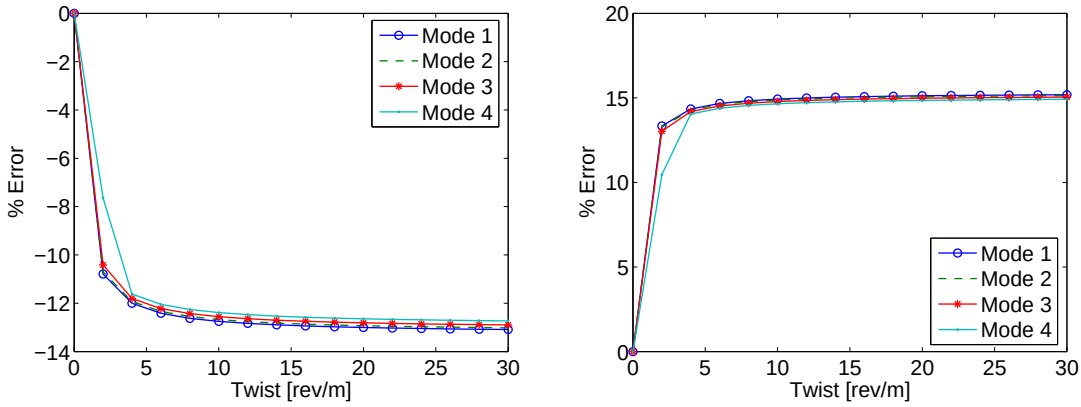

(a) $u_1(z,t)$ (b) $u_2(z,t)$

Figure 63: Effects of Flute Twists on Drill Modes.

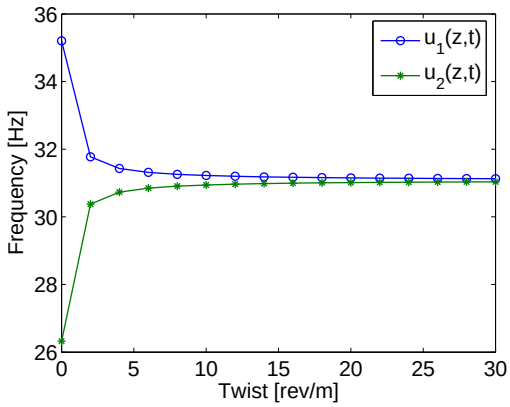

Figure 64: Comparison of First Drill Mode for Various Flute Twists.

Table 11: Nominal Operating Range for Drill Parameters

Property	Symbol	Range	Units
Axial Velocity	v	$0-0.5$	cm/min
Angular Velocity	Ω	$5-45$	RPM
Compressive Tip Load	P	$0-4500$	N
Flute Twist	Θ	20	rev/m
Auger Length	L	$1-5$	m

with those using the closed-form solutions (Figs. 57-62). The effects of each drilling parameter increases considerably with increasing length, and the frequencies for the lateral deflections about the y-axis ($u_2(z,t)$) are more sensitive than those for the

Table 12: Drill Parameters for Four Cases Studied

Parameter	Case 1	Case 2	Case 3	Case 4
Axial Velocity (cm/min)	0	10	0.5	50
Angular Velocity (RPM)	0	10	45	60
Compressive Tip Load (N)	0	500	1000	2000
Flute Twist (rev/min)	0	10	20	30
Auger Length (m)	1	2	2	3

lateral deflection about the x-axis ($u_1(z,t)$). These results also compare well with those in previous studies [81, 156].

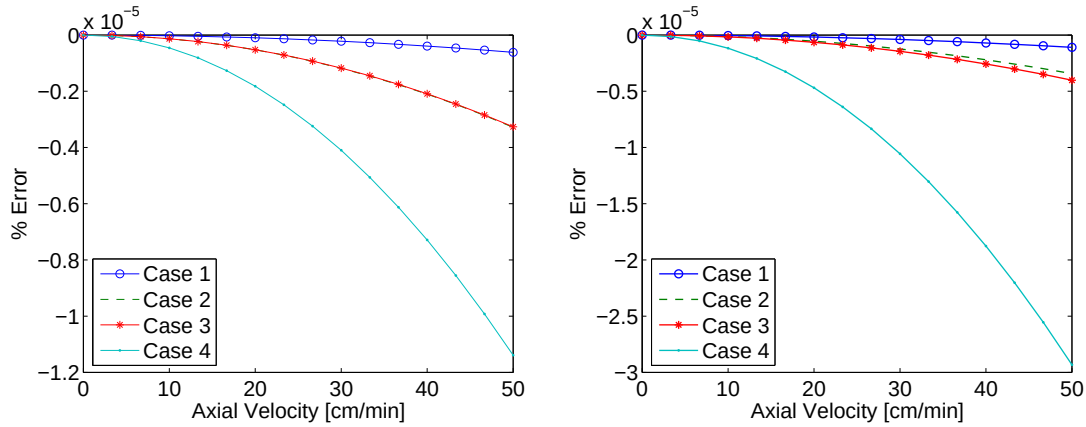

(a) $u_1(z,t)$ (b) $u_2(z,t)$

Figure 65: Four Drill Parameter Cases with Varying Axial Velocity.

Evaluating Case 3 (the most representative of the nominal drilling conditions) and the preliminary findings, it is decided that all drilling parameters within the nominal operating range ($v \leq 0.5$ cm/min, $\Omega \leq 45$ RPM, and $P \leq 4500$ N) are negligible. This significantly simplifies the theoretical models and analysis.

5.1.5 Finite Element Analysis

A finite element analysis (FEA) is conducted on the drill auger tube to obtain a clearer understanding of the dynamic characteristics of the auger and compare results found using the closed-form solutions and Galerkin's Method. To complete this analysis, the finite element program ABAQUS is used. ABAQUS is a commercially available

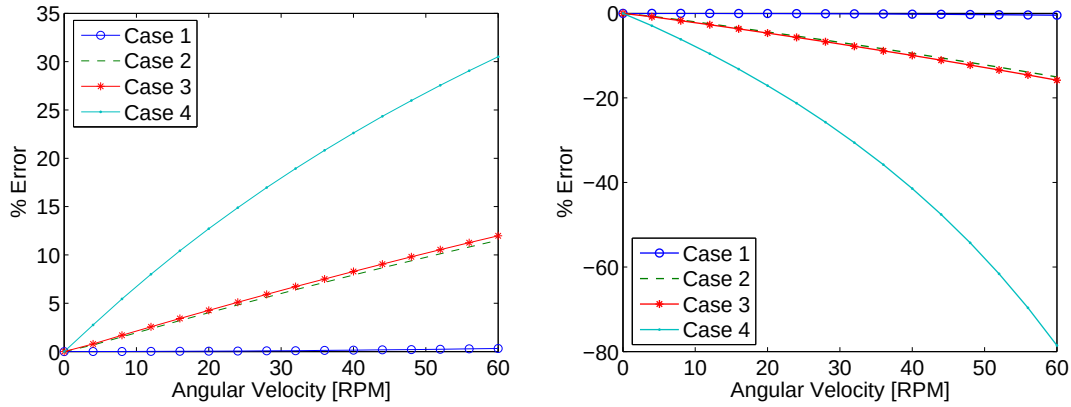

(a) $u_1(z,t)$ (b) $u_2(z,t)$

Figure 66: Four Drill Parameter Cases with Varying Angular Velocity.

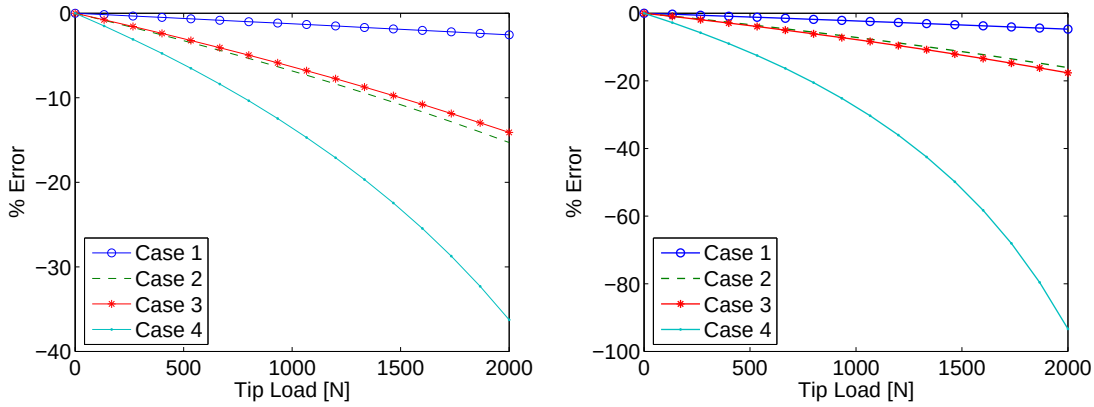

(a) $u_1(z,t)$ (b) $u_2(z,t)$

Figure 67: Four Drill Parameter Cases with Varying Compressive Tip Load.

general purpose finite element program, designed primarily to model the behavior of solids and structures under externally applied loading conditions [1].

To begin, a 3D flexible finite element model (FEM) is created with the geometry of the drill without the flute twist and clamped-free boundary conditions to compare with the closed-form solutions. This model is completed for 1 to 2 m auger tube lengths. A 3D FEM is then created with the exact geometry of the drill flutes and analyzed for the same auger lengths. These results are compared with the results

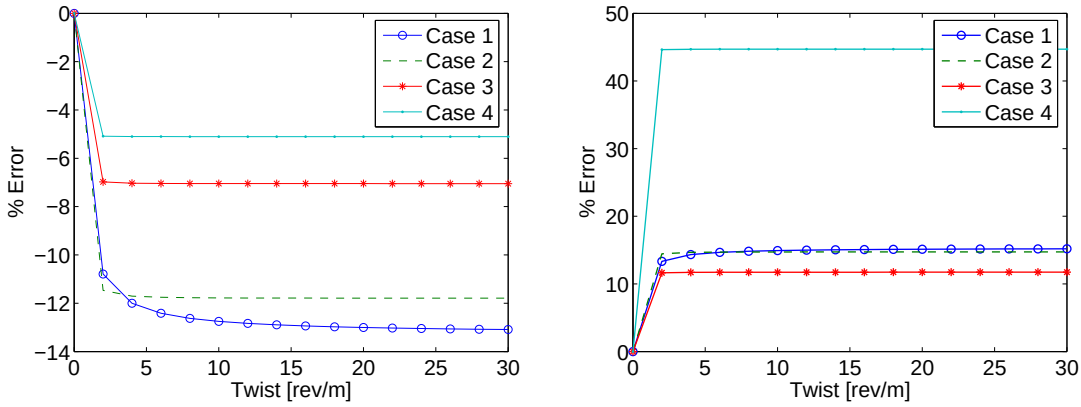

(a) $u_1(z,t)$ (b) $u_2(z,t)$

Figure 68: Four Drill Parameter Cases with Varying Flute Twist.

found using Galerkin's Method. The element type for these finite element models was a 3D stress hexahedral (8-node linear brick, reduced integration, hourglass control), and the mesh size for the 1 m auger was 17,600 elements for the simple geometry and 11,952 elements for the fluted geometry. A snapshot of these finite element models and the corresponding meshes are provided in Fig. 69, and a comparison of the natural frequencies found from the different methods is provided in Table 13. The percent error is calculated as

$$\%\,\text{error} = \frac{\omega_{FEM} - \omega_{CF}}{\omega_{FEM}} \cdot 100\%.$$

These results show that the natural frequencies for the simple geometry (i.e. no flute twist) match very well between the closed-form and finite element solutions. The results of the fluted beam do not match as well as the simple geometry; however, interesting observations and conclusions from these results are as follows. Similar to the Galerkin's Method results, the two lateral frequencies are almost identical for a flute twist of 20 rev/m. The difference is both lateral frequencies using Galerkin's Method converge toward a value in between the two lateral frequencies without a flute twist where the finite element models converge to a value slightly lower than the

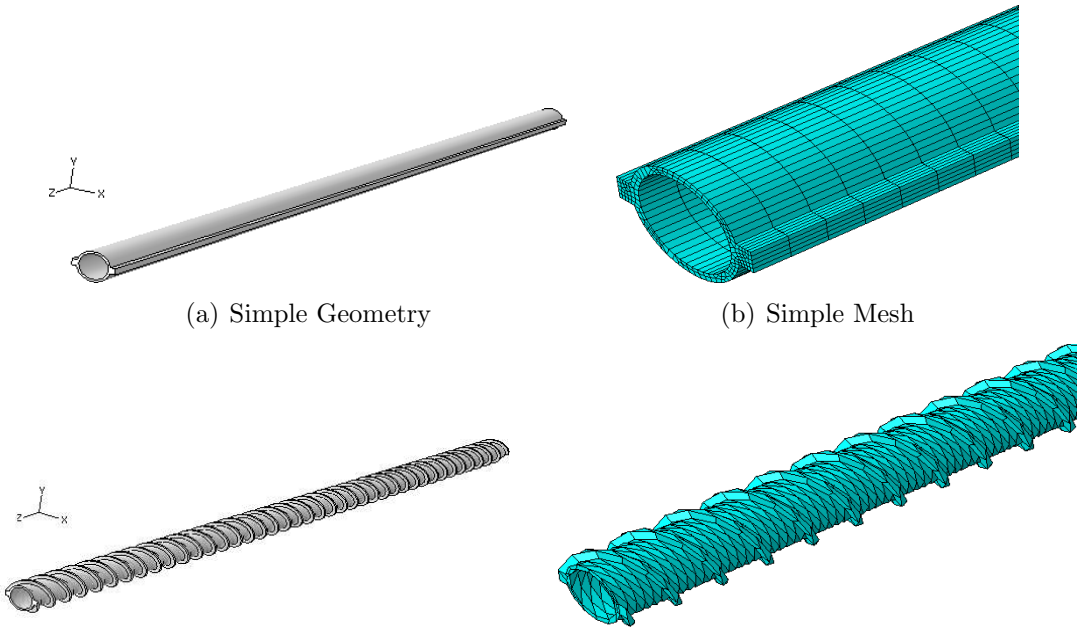

(a) Simple Geometry (b) Simple Mesh

(c) Exact Drill Geometry (d) Exact Drill Mesh

Figure 69: Finite Element Models of Drill Auger Tube.

first lateral frequency without a flute twist. For example, the first lateral frequencies of a 1 m auger tube using Galerkin's Method are $\omega_{1,2} = 26.32$ Hz and $\omega_{1,1} = 35.20$ Hz without a flute twist ($\omega_{i,j}$: natural frequency of mode i for lateral deflection u_j) and $\omega_{1,2} = 31.01$ Hz and $\omega_{1,1} = 31.15$ Hz with a 20 rev/m flute twist. The same frequencies using the finite element models are $\omega_{1,2} = 26.38$ Hz and $\omega_{1,1} = 34.70$ Hz without a flute twist and $\omega_{1,2} = 25.70$ Hz and $\omega_{1,1} = 25.71$ Hz with a 20 rev/m flute twist. A further observation is the natural frequencies from the finite element analysis for the fluted beam are more comparable to the closed-form frequencies found for $u_2(z,t)$ (lateral deflection in the y-direction) using the simple geometry. It is therefore concluded that the simple geometry (i.e. no flute twist) is a good approximation and represents the cross-sectional geometry given I_{XX} for both cross-sectional area moments of inertia (i.e. $I_{YY} = I_{XX}$, $u_1(z,t) = u_2(z,t)$).

To further evaluate the comparison between the fluted beam mesh and closed-form solution using the simple geometry, these two methods are analyzed for auger

Table 13: Frequencies of Drill Auger Tube using Numerical and FEM Analysis

Cross-Section Geometry	Length (m)	Mode*	Frequencies (Hz) Numerical†	FEM	Error (%)
Simple	1	1,2	26.32	26.38	0.20
	1	1,1	35.20	34.70	-1.46
	1	2,2	164.69	163.57	-0.68
	1	2,1	219.97	213.65	-2.96
Simple	2	1,2	6.58	6.55	-0.47
	2	1,1	8.80	8.65	-1.80
	2	2,2	41.23	40.50	-1.81
	2	2,1	55.13	53.96	-2.18
Flute Twist (20 rev/m)	1	1,2	31.01	25.49	-21.67
	1	1,1	31.15	25.50	-22.18
	1	2,2	193.91	157.93	-22.78
	1	2,1	194.78	158.01	-23.27
Flute Twist (20 rev/m)	2	1,2	7.76	6.43	-20.81
	2	1,1	7.78	6.43	-21.04
	2	2,2	48.63	40.16	-21.08
	2	2,1	48.74	40.18	-21.31

*Mode i, j = Natural frequency of mode i for lateral deflection $u_j(z,t)$
†Closed-form solution for simple beam, Galerkin's Method for fluted beam

tube lengths up to 3 m with fixed-free and fixed-fixed boundary conditions. Figure 70 provides the comparisons (percent error) from these results. These plots show that the closed-form solution (using $I = I_{XX}$, $u = u_2(z,t)$) matches very well with the finite element models and becomes more comparable with increasing beam lengths.

An additional observation between the numerical and finite element analyses was the difference (i.e. percent error) in the natural frequencies found (Table 13 and Fig. 70). Other than the lowest frequency value for the simple geometry case of the 1 m auger tube, the frequency values found from the finite element analysis are lower than those found from the numerical analysis. This was due to the higher-order elements used in this FEA. When using elements of the same order as a numerical analysis (e.g. two-node beam element versus Euler-Bernoulli analysis), the FEA frequencies are generally higher than the numerically evaluated frequencies, and they converge to the

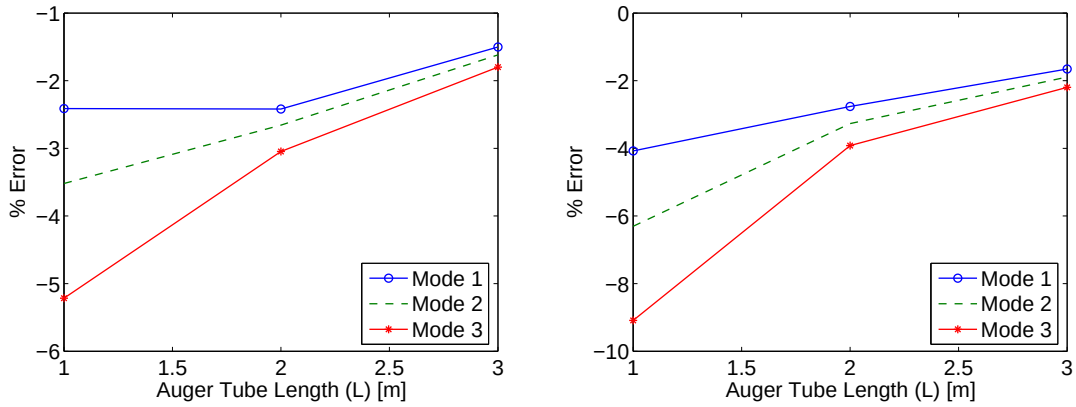

(a) Fixed-Free (b) Fixed-Fixed

Figure 70: Natural Frequency Comparison of Finite Element Models and Closed-Form Solution.

numerical solution with an increasing number of elements [100]. The frequency values using higher-order theories (e.g. Rayleigh and Timoshenko beam theories), however, are generally lower than those found using Euler-Bernoulli beam theory [76]. Thus, the finite element analysis using higher-order 3D solid elements most often resulted in lower frequency values compared with those found using Euler-Bernoulli beam theory [87, 100].

5.2 Drill Structural Dynamic Models

As accurate, reliable, and rapid-response "real-time" diagnosis of the drilling condition is needed, simple and reliable dynamic models are more useful and efficient than complex models for this specific application. From the preliminary field tests and the analysis conducted in Section 5.1, the angular velocity, axial velocity, compressive tip load, and flute twist are not considered. As the auger tube strings are added and removed when needed, the length of the current auger tube is fixed for a set amount of time t. Finally, when comparing the laboratory results with the fixed-free beam model, a fixed connection between the auger tube and drill head does not accurately represent the drill system. Therefore, the fixed end is replaced with spring constraints.

The modified model is in Fig. 71.

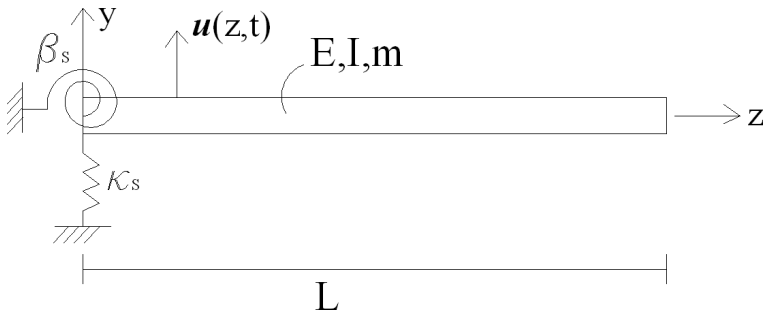

Figure 71: Simplified Base Model of Drill Auger Tube.

As the equations of motion are decoupled and most of the experimental results involve the lateral deflection in the y-direction, the remaining models focus on the lateral deflection $u_2(z,t)$. For simplicity, unless specified otherwise, $u = u_2(z,t)$ (the lateral deflection in the y-direction) and $I = I_{XX}$. Therefore, the equation of motion and boundary conditions become

$$EI\frac{\partial^4 u(z,t)}{\partial z^4} + m\frac{\partial^2 u(z,t)}{\partial t^2} = 0\,, \tag{80}$$

$$\begin{aligned} z = 0: \quad & EI\frac{d^3u(z)}{dz^3} + \kappa_s u(z) = 0, \quad EI\frac{d^2u(z)}{dz^2} - \beta_s\frac{du(z)}{dz} = 0, \\ z = L: \quad & EI\frac{d^3u(z)}{dz^3} = 0, \quad EI\frac{d^2u(z)}{dz^2} = 0, \end{aligned} \tag{81}$$

where κ_s and β_s are the translational and rotational spring constants representing the support conditions between the auger tube and drill head. Non-dimensionalizing by L ($\eta = z/L$) and using the solution form

$$u(\eta,t) = U(\eta)e^{i\omega t} = Be^{\lambda\eta}e^{i\omega t},$$

the spatial solution becomes

$$U(\eta) = B_1\cosh(\alpha\eta) + B_2\sinh(\alpha\eta) + B_3\cos(\alpha\eta) + B_4\sin(\alpha\eta), \quad 0 < \eta < 1\,. \tag{82}$$

Applying the boundary conditions, the characteristic equation for the drill model

is

$$\alpha^4 - (\alpha^4 - S_K S_B)\cosh(\alpha)\cos(\alpha) + (\alpha S_K - \alpha^3 S_B)\sinh(\alpha)\cos(\alpha)$$
$$-(\alpha S_K + \alpha^3 S_B)\cosh(\alpha)\sin(\alpha) + S_K S_B = 0 \qquad (83)$$

where

$$S_K = \frac{\kappa_s L^3}{EI}, \quad S_B = \frac{\beta_s L}{EI}.$$

The natural frequencies for various values of κ_s and β_s are first evaluated. These frequencies, evaluated using classic Euler-Bernoulli theory, are also compared with Rayleigh Beam and Timoshenko Beam theories [76]. Table 14 provides a list of frequencies for the three theories with various spring constant values. It is seen from these results that using the classic, simplified Euler-Bernoulli theory is reasonably accurate for this application involving long slender beams.

Table 14: Natural Frequencies of Drill Model for Various Spring Constant Values

Spring Constant	Modes	$L = 1$m			$L = 2$m		
		EB	Ray	Timo	EB	Ray	Timo
$\kappa_s, \beta_s = 10^4$	1	7.0	7.0	7.0	3.4	3.4	3.4
	2	26.9	26.9	26.9	11.8	11.8	11.8
	3	181.5	181.0	180.2	48.6	48.5	48.5
$\kappa_s, \beta_s = 10^6$	1	25.1	25.1	25.0	6.5	6.5	6.5
	2	112.0	112.0	111.5	38.9	38.9	38.8
	3	258.8	258.1	256.7	98.1	98.0	97.7
Clamped	1	26.33	26.32	26.29	6.58	6.58	6.58
	2	165.0	164.7	163.2	41.3	41.2	41.1
	3	426.0	459.9	450.3	115.5	115.4	114.8

The values for κ_s and β_s are evaluated by substituting the first two natural frequencies found from the modal analysis experiments of the stationary auger tube (9 and 95 Hz) into Eq. 83 and solving for S_K and S_B. The values for κ_s and β_s are found to be 712 kN/m and 4706 Nm/rad, respectively. Using these spring constants, the analytical mode shapes and natural frequencies are compared with the experimental results from the stationary auger tests. Table 15 provides comparisons of the analytical and experimental frequencies and Figure 72 provides the first two analytical

mode shapes. These results show great comparison between the analytical models and experimental results.

Table 15: Natural Frequencies of Drill Model for Various Spring Constant Values

Mode	Analytical	Experimental	% Error
1	9	9	0.00
2	95	95	0.00
3	230	225	-1.99
4	491	486	-1.05
5	924	920	-0.42

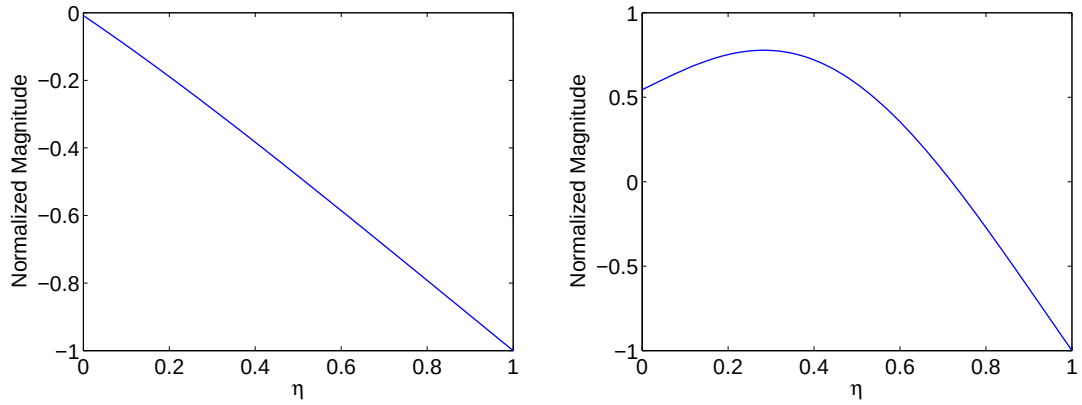

(a) Mode 1 (b) Mode 2

Figure 72: Analytical Mode Shapes of Base Model.

5.2.1 Drilling Model

The next step is to select a model for the nominal drilling condition. Many drilling studies either use clamped or pinned conditions for the end/embedded boundary condition [125, 155]. These boundary conditions are reasonable for considerably smaller drill dimensions. However, as evident from the results in Table 3, the natural frequencies of the auger tube increase with increasing depths. Thus, a constant boundary condition to represent the embedded drilling auger is not appropriate for this application.

B. W. Huang [81] uses a moving Winkler-type elastic foundation to model the embedded auger. Applying this to the base model, the drilling model is illustrated in Fig. 73. Including the Winkler-type elastic foundation, the non-dimensionalized

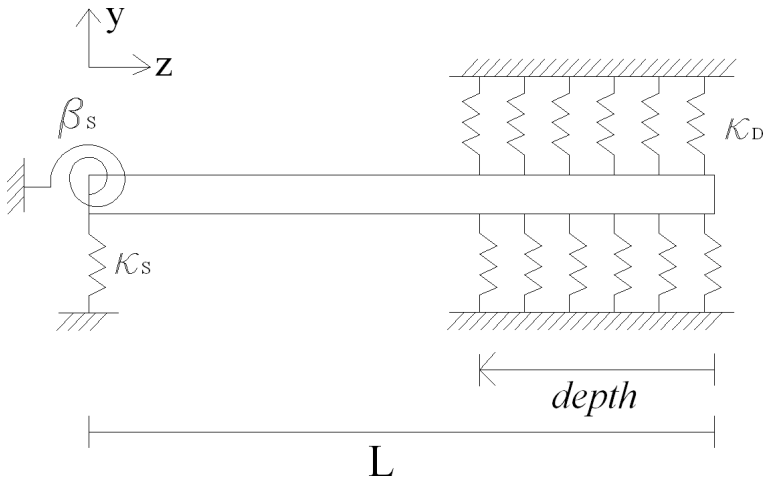

Figure 73: Nominal Drilling Model.

equation of motion becomes

$$\begin{aligned} u^{IV} + \frac{mL^4}{EI}\ddot{u} = 0, \quad 0 < \eta < \delta \\ u^{IV} + \frac{\kappa_D L^4}{EI}u + \frac{mL^4}{EI}\ddot{u} = 0, \quad \delta \leq \eta < 1 \end{aligned} \tag{84}$$

where

$$\delta = 1 - \frac{\text{depth}}{L}$$

is a non-dimensionalized length representing the length of the beam without an elastic foundation. The spatial solution is therefore

$$0 < \eta < \delta : U_L(\eta) = B_1\cosh(\alpha\eta) + B_2\sinh(\alpha\eta) + B_3\cos(\alpha\eta) + B_4\sin(\alpha\eta)\,,$$

$$\delta \leq \eta < 1 : U_R(\eta) = \begin{cases} B_5\cosh(\gamma\eta) + B_6\sinh(\gamma\eta) + B_7\cos(\gamma\eta) + B_8\sin(\gamma\eta), & \alpha^4 > D \\ [B_5\cosh(\gamma\eta)\cos(\gamma\eta) + B_6\sinh(\gamma\eta)\cos(\gamma\eta) & \\ \quad + B_7\cosh(\gamma\eta)\sin(\gamma\eta) + B_8\sinh(\gamma\eta)\sin(\gamma\eta)]\,, & \alpha^4 < D \end{cases} \tag{85}$$

where

$$\alpha^4 = \omega \frac{mL^4}{EI}, \quad D = \frac{\kappa_D L^4}{EI},$$

$$\gamma = \begin{cases} \left(\alpha^4 - D\right)^{1/4}, & \alpha^4 > D \\ \left(\left(D - \alpha^4\right)/4\right)^{1/4}, & \alpha^4 < D\,, \end{cases}$$

and the boundary conditions become

$$\begin{aligned} \eta = 0: \quad & U_L''' + S_K U_L = 0, \quad U_L'' - S_B U_L' = 0, \\ \eta = 1: \quad & U_R'' = 0, \quad U_R''' = 0\,. \end{aligned} \tag{86}$$

Finally, for continuity, the following must be true at $\eta = \delta$:

$$\frac{d^i U_L}{d\eta^i} = \frac{d^i U_R}{d\eta^i}, i = 1, 2, 3\,. \tag{87}$$

Figures 74 and 75 demonstrate the changes in natural frequencies with drill depths for various κ_D values. It is seen from these results that significant but gradual change occurs as a function of the drill depth. These also show better correlation with the experimental results in comparison to those results using a clamped or pinned boundary condition for the embedded auger tube.

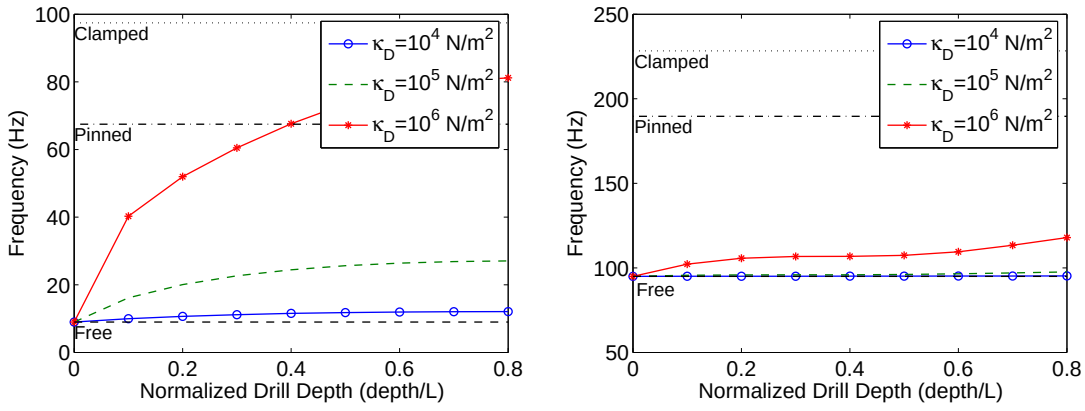

(a) Mode 1 (b) Mode 2

Figure 74: Changes in Natural Frequency with Drill Depth (1m Auger).

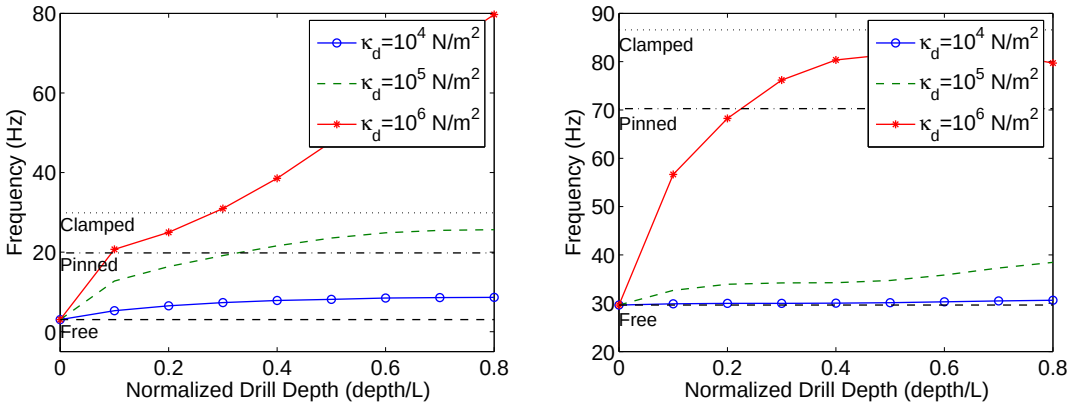

(a) Mode 1 (b) Mode 2

Figure 75: Changes in Natural Frequency with Drill Depth (2m Auger).

The value for κ_D is evaluated using the experimental frequencies from the stationary embedded auger. For each sample, the first natural frequency and drill depth are used to find κ_D. As the experimental frequencies are known for nine scenarios (1 m auger tube for 10 cm increments from 0 to 30 cm depth and 2 m auger tube for 10 cm increments from 30 to 70 cm depths), nine values for κ_D are found. The mean value of the nine κ_D values is then used and the frequencies are compared. Table 16 lists the analytical and experimental frequencies, and Figs. 76 and 77 provide the first two analytical mode shapes, with the sensor data, for a 2 m auger at 30 cm depth and 70 cm depth.

The analytical results for the drill model using an elastic foundation match well with those found from the laboratory experiments. Discrepancies in the results are most likely due to estimations of the experimental drill depths and the exact positions along the auger where data was collected. For example, the mode shapes for the experimental and analytical augers match well but appear to be slightly offset. Approximations in the drill depth and the sensor positions along the auger can both account for this small misalignment. Thus, the final model for the nominal drilling mode is determined, and the value for κ_D is 1333 kN/m^2.

Table 16: Auger Tube Natural Frequencies

Auger Length (m)	Drill Depth (cm)	Analytical		Experimental	
		1st Mode (Hz)	2nd Mode (Hz)	1st Mode (Hz)	2nd Mode (Hz)
1	0	9	95	9	95
1	10	44	105	41	111
1	20	57	110	58	119
1	30	67	112	71	131
2	30	23	68	17	60
2	40	26	74	20	61
2	50	29	79	23	62
2	60	32	84	36	81
2	70	36	88	42	94

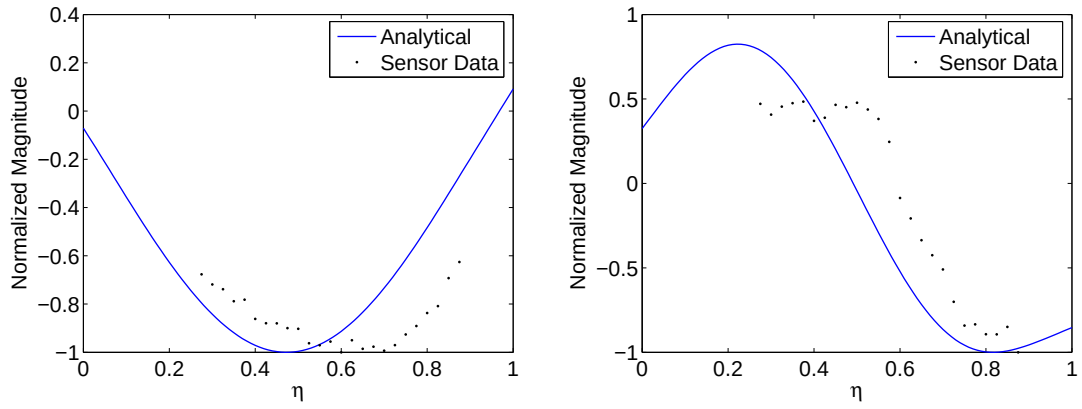

(a) Mode 1 (b) Mode 2

Figure 76: Comparison of Mode Shapes for Experimental Drill Frequencies and Drill Model ($L = 2$m, depth=30cm).

Finally, the natural frequencies of the drilling model with a compressive tip load are evaluated. This analysis determines the difference between a drilling model with and without a compressive ground force. Figure 78 demonstrates the changes in the first two natural frequencies for various depths over a range of loads. The frequencies are normalized by the natural frequencies found without a compressive tip load. From these results, it is possible to conclude that the effects of a compressive tip load (within the nominal operating range of this drill system) are minimal and even decrease with

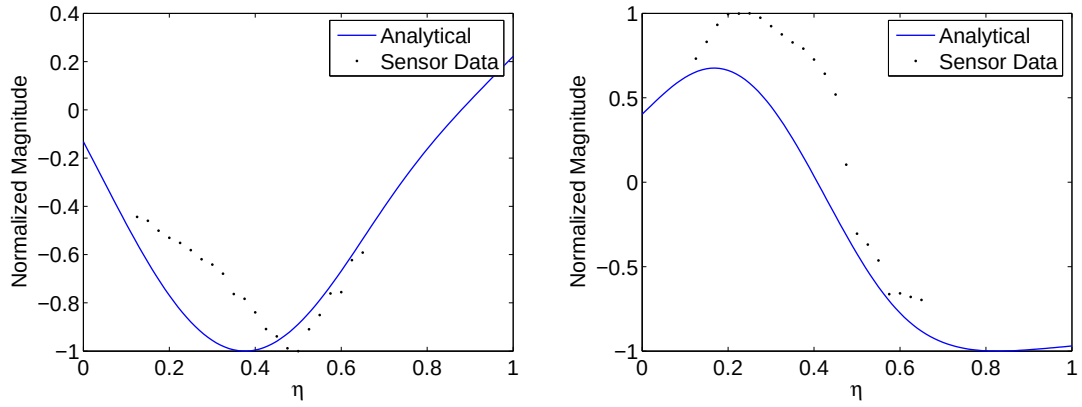

(a) Mode 1 (b) Mode 2

Figure 77: Comparison of Mode Shapes for Experimental Drill Frequencies and Drill Model ($L = 2$m, depth=70cm).

increasing depth.

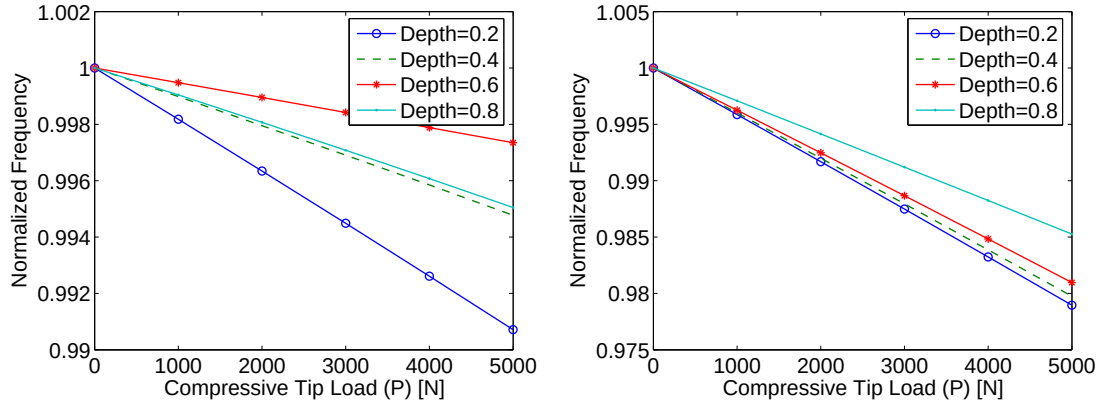

(a) Mode 1 (b) Mode 2

Figure 78: Effects of Compressive Tip Load on Nominal Drilling Model ($L = 1$m).

5.2.2 Models and Analysis of Drilling Fault Conditions

In this section, each drilling fault condition is modeled to analyze and determine changes in the dynamic characteristics of the drill system. These changes, along with changes in the drill operating parameters (rotation speed, rate of penetration, etc.), are useful in fault identification. From the preliminary field tests, six unique drilling

faults were identified: binding, choking, bit inclusion, jamming, hard material, and corkscrewing [63]. Sketches of the drilling faults are provided in Fig. 79 and the classification of each drilling fault is as follows:

1. Binding - a rock protrudes from the bore-hole wall causing the auger to catch on the rock each time it rotates. This fault is associated with increasing or spiking torque on the auger tube because the protruding rock interferes with the rotating motion of the drilling operation. Increasing or spiking auger torques can limit the progress of the drilling operation and, if the auger torque exceeds the design limits of the auger tube materials and/or the drill motors, a catastrophic event for the drill system can occur.

2. Choking - the cuttings from the drilled subsurface build up in the auger flutes causing an increase in pressure between the bore-hole wall and auger tube. This fault is associated with a torque increase at the bit (because the increased cuttings interfere with the rotating motion at the drill bit) while the torque on the auger tube remains nominal. Although this fault is not associated with a catastrophic failure of the drill system, it can cause a catastrophic event for the mission objectives. For example, as the cuttings build-up increases, the drilling progress is greatly diminished (axial velocity becomes zero) and subsurface samples can not be collected.

3. Jamming - a condition where the auger tube completely stops rotating most likely due to a large pebble or rock lodged between the bore-hole wall and bit or auger flutes. This fault is seen as an extreme case of binding, bit inclusion, or corkscrewing, and it is associated with a sudden halt in the rotational (angular) speed of the drill. If the auger tube seizes to rotate during the drilling operation, several catastrophic events are possible. Stresses in the drill motors can exceed design limits trying to clear the jam and continue rotating the auger tube. If the

axial velocity is non-zero, axial loads can increase beyond design limits. Finally, if the auger tube remains immobile in the [frozen] subsurface, the auger tube can freeze in place and become a permanent anchor for the drill system.

4. Hard Material - the drill encounters an ice layer or hard rock in the ground and the drilling operation cannot proceed with the normal cutting bit. This fault is associated with a low or zero rate of penetration (ROP, axial velocity). With low to zero ROP, energy resources will be wasted on limited drilling progress due to an inefficient drill bit. Although this fault is not associated with a catastrophic failure of the drill system, the overall drilling mission for a specified depth or other mission objective are not accomplishable unless a different drill bit is available.

5. Corkscrewing - the auger flutes catch on protruding material at the bore-hole wall and apply reverse screw tension from the ground. This fault is most commonly associated with large tensile forces on the auger tube. Large tensile forces are catastrophic to the auger tube and drilling system if design limits are exceeded.

6. Bit Inclusion - the drill bit encounters pebbles or a rock at the bottom of the hole causing the bit's cutting edge to catch and slip over the rock each time it rotates and resulting in periodic displacements along the auger. This fault is associated with torque spikes at the bit and [periodic] axial displacements of the auger tube. This fault is dangerous to the drilling operation because it has the potential to wear down and/or break the drill bit. Strong axial displacements also cause high compressive loads along the auger tube that can exceed the design limits of the auger tube and/or drill system.

To model the six expected drilling faults, the nominal drilling model (Fig. 73) is modified for the various drilling fault conditions. It is assumed that each fault

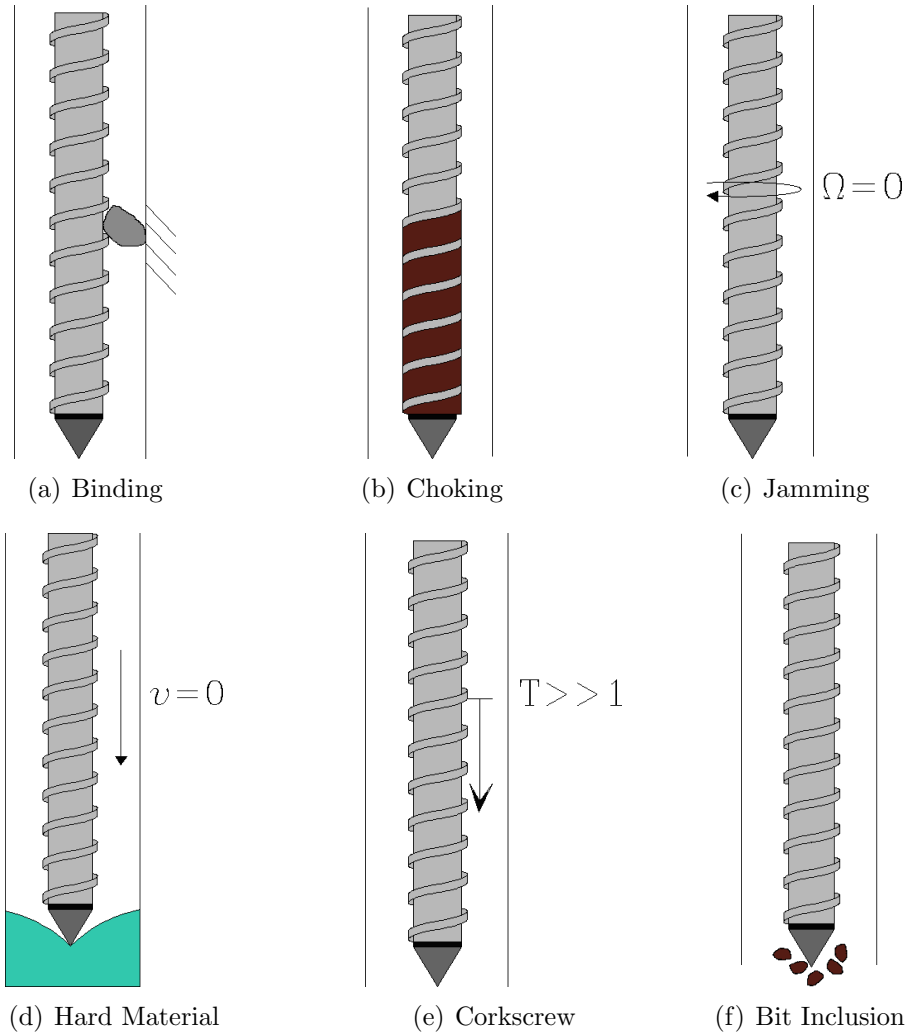

(a) Binding (b) Choking (c) Jamming

(d) Hard Material (e) Corkscrew (f) Bit Inclusion

Figure 79: Sketches of Identified Drilling Faults.

condition uniquely alters the dynamic characteristics of the drill system, specifically the boundary conditions. As the lower frequencies are most sensitive to changes in boundary conditions, changes in the natural frequencies of the drill system are used to predict any changes in the boundary conditions and thus the condition of the drilling operation. Each drilling fault is therefore carefully analyzed to determine what dynamic changes are occurring and how to appropriately model these changes.

5.2.2.1 Binding Fault Model

In a binding fault, a rock at the side of the auger tube (Fig. 79(a)) restricts the lateral displacement of the auger tube in the bore-hole and results in a constant transverse force at the point, or points, of contact. A translational spring (κ_z) models the protruding rock, and the position along the embedded auger (L') and intensity (i.e. spring constant) of the binding fault are varying parameters. Figure 80 provides the model for the binding fault.

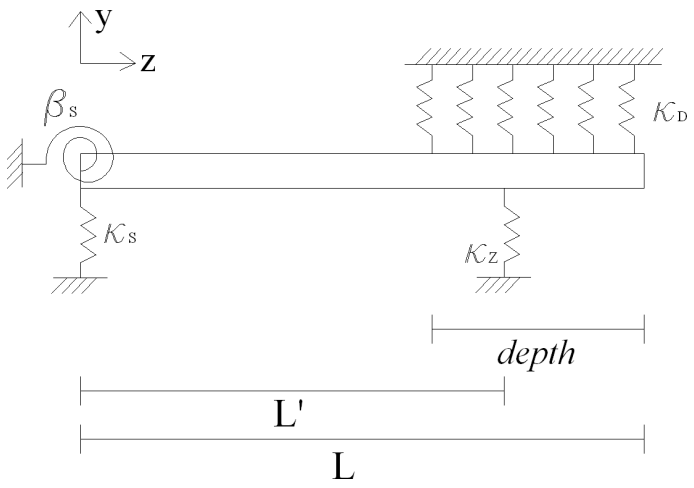

Figure 80: Structural Model of Binding Drill Fault.

The spatial solution for the binding fault is

$$
\begin{aligned}
&0 < \eta < \delta : U_L(\eta) = B_1\cosh(\alpha\eta) + B_2\sinh(\alpha\eta) + B_3\cos(\alpha\eta) + B_4\sin(\alpha\eta)\,, \\
&\delta \le \eta < \zeta : \\
&\qquad U_M(\eta) = \begin{cases} B_5\cosh(\gamma\eta) + B_6\sinh(\gamma\eta) + B_7\cos(\gamma\eta) + B_8\sin(\gamma\eta), & \alpha^4 > D \\ [B_5\cosh(\gamma\eta)\cos(\gamma\eta) + B_6\sinh(\gamma\eta)\cos(\gamma\eta) & \\ \quad + B_7\cosh(\gamma\eta)\sin(\gamma\eta) + B_8\sinh(\gamma\eta)\sin(\gamma\eta)]\,, & \alpha^4 < D \end{cases} \\
&\zeta \le \eta < 1 : \\
&\qquad U_R(\eta) = \begin{cases} B_9\cosh(\gamma\eta) + B_{10}\sinh(\gamma\eta) + B_{11}\cos(\gamma\eta) + B_{12}\sin(\gamma\eta), & \alpha^4 > D \\ [B_9\cosh(\gamma\eta)\cos(\gamma\eta) + B_{10}\sinh(\gamma\eta)\cos(\gamma\eta) & \\ \quad + B_{11}\cosh(\gamma\eta)\sin(\gamma\eta) + B_{12}\sinh(\gamma\eta)\sin(\gamma\eta)]\,, & \alpha^4 < D \end{cases}
\end{aligned}
\tag{88}
$$

where

$$
\begin{aligned}
\zeta &= \frac{L'}{L}, \\
\gamma &= \begin{cases} \left(\alpha^4 - D\right)^{1/4}\,, \alpha^4 > D \\ \left(\left(D - \alpha^4\right)/4\right)^{1/4}\,, \alpha^4 < D\,, \end{cases}
\end{aligned}
$$

and the boundary conditions become

$$
\begin{aligned}
&\eta = 0 : \quad U_L''' + S_K U_L = 0, \quad U_L'' - S_B U_L' = 0, \\
&\eta = 1 : \quad U_R'' = 0, \quad U_R''' = 0\,.
\end{aligned}
\tag{89}
$$

Finally, the continuity conditions are:

$$
\begin{array}{ll}
\underline{\eta = \delta} & \underline{\eta = \zeta} \\
U_L = U_M & U_M = U_R \\
U_L' = U_M' & U_M' = U_R' \\
U_L'' = U_M'' & U_M'' = U_R'' \\
U_L''' = U_M''' & U_M''' = Z_K U_M + U_R'''
\end{array}
\tag{90}
$$

where

$$Z_K = \frac{\kappa_z L^3}{EI}\,.$$

The next step is to determine the frequencies corresponding to this drilling fault for various values of the binding spring constant κ_z, normalized binding location ζ, and drill depth. Furthermore, as κ_z approaches infinity, the auger tube displacement becomes zero at ζ. Therefore, the binding fault is valid for any bind location $\zeta \geq \delta$ and any intensity factor between 0% and 100%, where 0% represents no binding and 100% represents the clamped condition (i.e. the most severe case for this fault). Figure 81 shows the overall effects of the binding condition on the natural frequencies. The sharp corners in these plots are due to a limited number of fault parameter values in this analysis.

5.2.2.2 Choking Fault Model

Choking is most commonly identified by a gradual increase in the bit and auger torque values as the cuttings build up and more pressure is experienced at the drill bit. A rotational spring (β_C) models the gradual increase in bit torque at the drill bit ($z = L$). A tip mass (M) is also added to account for the build up in cuttings at the bit. The value of the added mass and rotational spring constant are varying parameters. Figure 82 provides the developed model for the choking fault.

The spatial solution, boundary conditions, and continuity conditions for the choking model are the same as the nominal drilling model (Eqs. 85-87) with the exception of the boundary conditions at $\eta = 1$, which become

$$U_R'' + \left(C_B - \frac{\mu}{4}\frac{d_o^2}{L^2}\alpha^4\right) U_R' = 0, \quad U_R''' + \mu\alpha^4 U_R = 0$$

where

$$C_B = \frac{\beta_C L}{EI}\,, \quad \mu = \frac{M}{mL}\,.$$

Frequencies for the choking fault model using various values for M and β_C have been evaluated. The limit for the spring constant is again infinity (resulting in zero

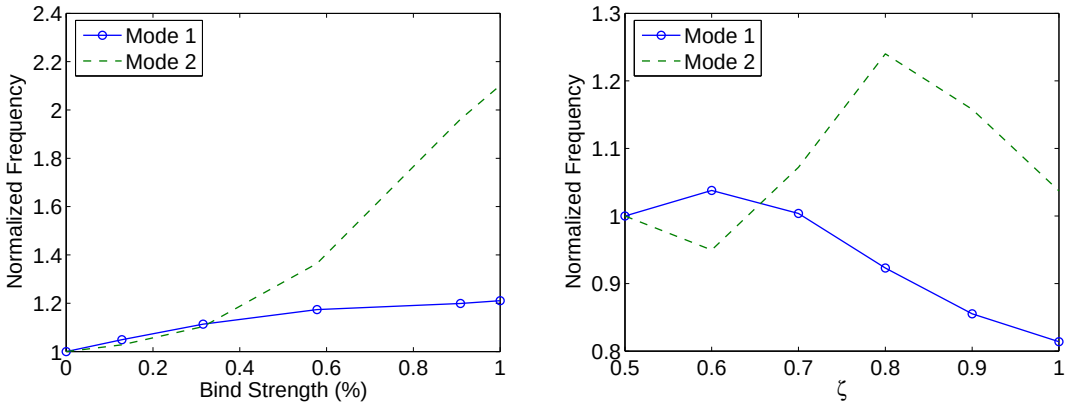

(a) $\delta = 0.5, \zeta = 0.8$ (b) $\delta = 0.5, \kappa_Z = \infty$

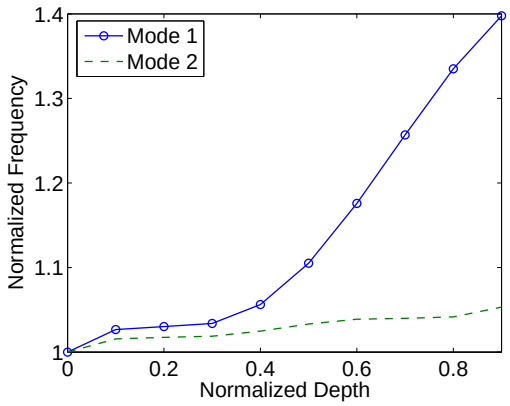

(c) $\zeta = 0.8, \kappa_Z = \infty$

Figure 81: Effects of Binding Condition on Natural Frequencies (L=1m).

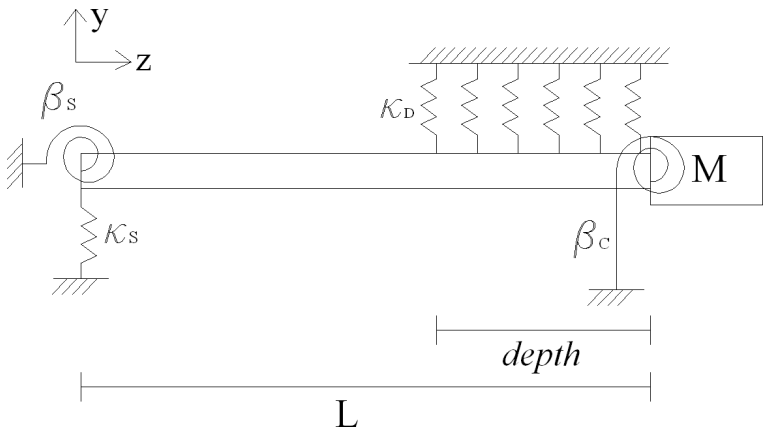

Figure 82: Structural Model of Choking Drill Fault.

rotation/slope at $\eta = 1$) and the limit for the added mass is the total mass of the auger tube (i.e. $\mu = 1$). As drilling environments vary, the severity and mass of the cuttings build-up will also vary. It can be assumed, however, that larger masses correlate with heavier cutting build-ups and, therefore, a more severe case of choking. Figure 83 demonstrates the change in natural frequencies for various values of M, β_C, and drill depth.

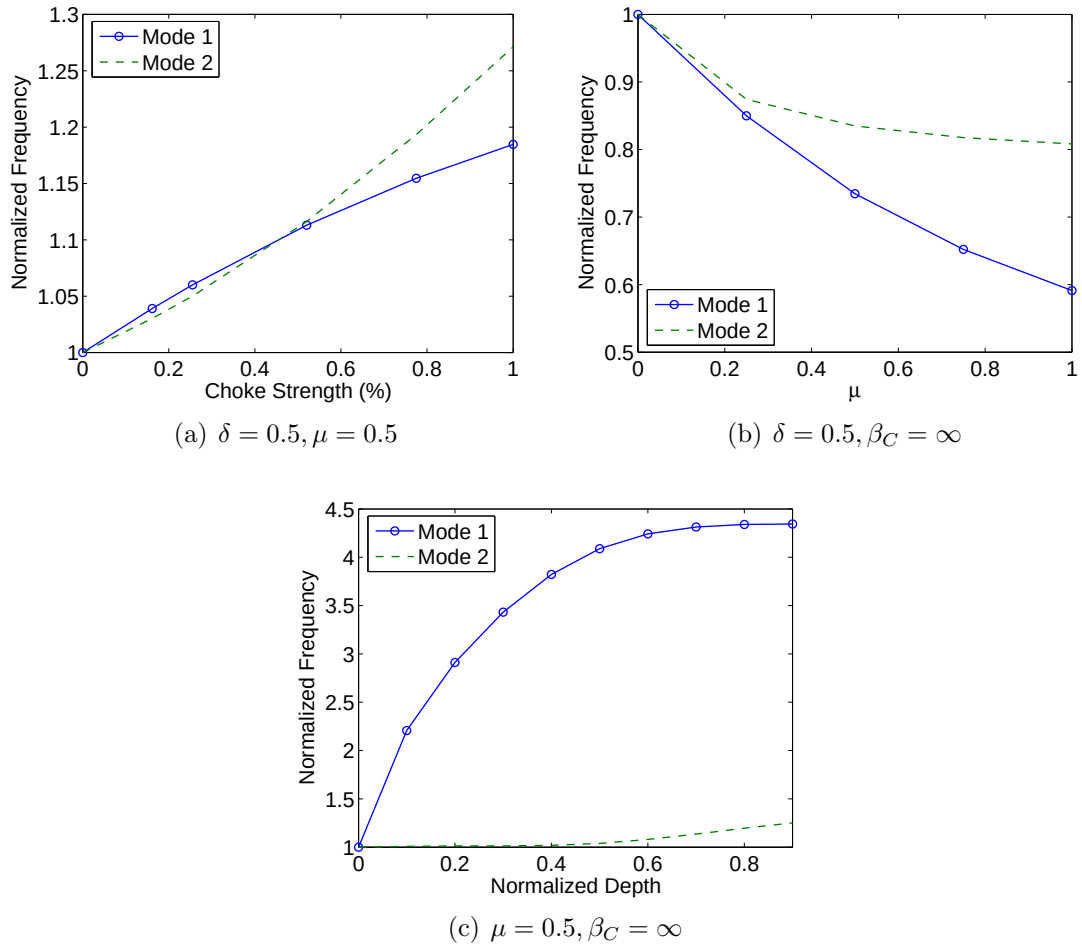

(a) $\delta = 0.5, \mu = 0.5$

(b) $\delta = 0.5, \beta_C = \infty$

(c) $\mu = 0.5, \beta_C = \infty$

Figure 83: Effects of Binding Condition on Natural Frequencies (L=1m).

5.2.2.3 Jamming Fault Model

Jamming, which is identified by a sudden decrease or halt in the angular velocity, is visualized as a fixed condition at some location along the embedded auger (L').

A translational (κ_Z) and rotational spring (β_Z) models the jamming fault, and the most severe case is when the auger tube becomes fixed. Figure 84 is a sketch of the jamming fault model.

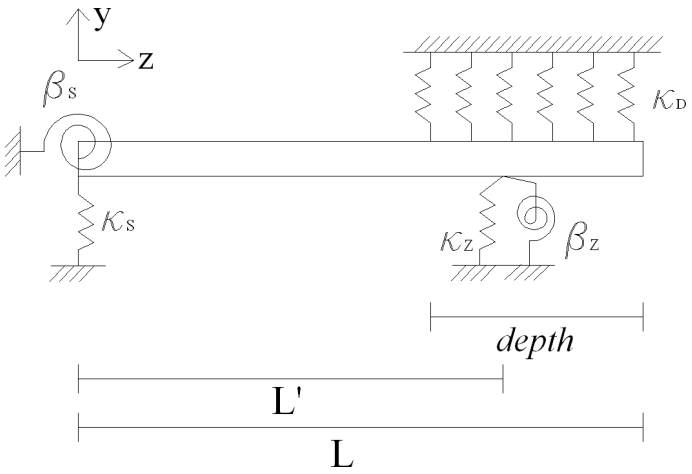

Figure 84: Structural Model of Jamming Drill Fault.

The spatial solution, boundary conditions, and continuity conditions for the jamming model are the same as the binding model (Eqs. 88-90) with the exception of the moment continuity at $\eta = \zeta$, which becomes

$$U_M'' + Z_B U_M' = U_R'' \tag{91}$$

where

$$Z_B = \frac{\beta_Z L}{EI}\,.$$

We determine the frequencies for the jamming fault for various values of κ_Z, β_Z, ζ, and drill depth. Similar to binding, the intensity of jamming is between 0 and 1, where 0 represents no jamming condition and 1 represents a fixed condition (i.e. most severe jam). Figure 85 demonstrates the change in natural frequencies for various values of jamming intensity, ζ, and drill depth. The sharp corners in these plots are due to a limited number of fault parameter values in this analysis.

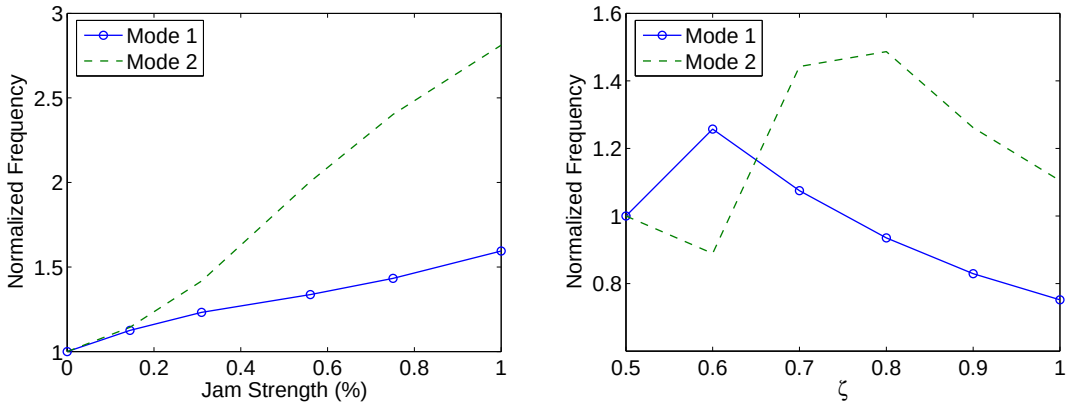

(a) $\delta = 0.5, \zeta = 0.8$ (b) $\delta = 0.5$, Fixed

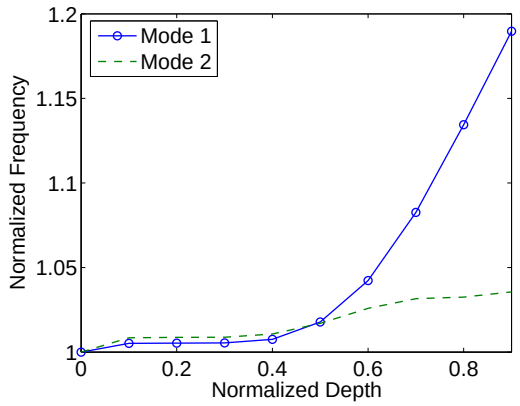

(c) $\zeta = 0.8$, Fixed

Figure 85: Effects of Jamming Condition on Natural Frequencies (L=1m).

5.2.2.4 Hard Material Fault Model

The [encounter of] hard material fault is identified by a decrease in the rate of penetration (ROP), or axial velocity, when all other telemetry values are nominal. This fault is visualized as a complete limit to the tip deflection. Given that the drill is still rotating in place and the tip slope is assumed non-zero, this fault is modeled with a pin support and high compressive load at the tip. Figure 86 provides a sketch and model of the hard material fault.

As the compressive tip load is a major factor in this drilling fault (e.g. if operating at large down-hole forces but making little to no progress, this is a major indicator

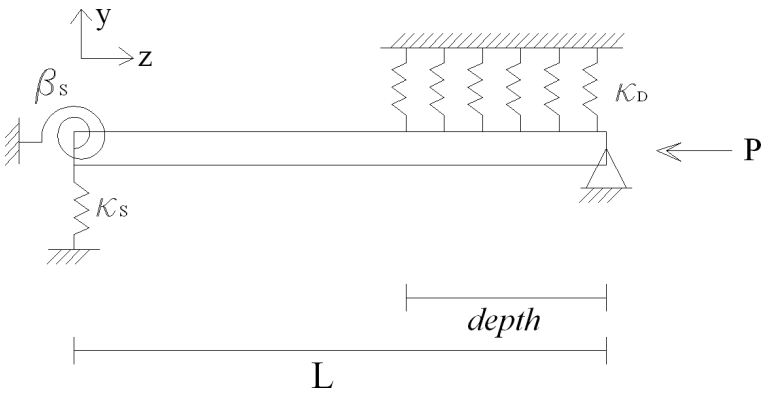

Figure 86: Structural Model of Hard Material Drill Fault.

of a hard material fault), it is included in this fault model. Therefore, the spatial solution becomes

$0 < \eta < \delta$:

$$U_L(\eta) = B_1\cosh(\gamma_1\eta) + B_2\sinh(\gamma_1\eta) + B_3\cos(\psi_1\eta) + B_4\sin(\psi_1\eta)\,,$$

$\delta \leq \eta < 1$:

$$U_R(\eta) = \begin{cases} B_5\cosh(\gamma_2\eta) + B_6\sinh(\gamma_2\eta) + B_7\cos(\psi_2\eta) + B_8\sin(\psi_2\eta), & (\star) \geq \hat{p} \\ B_5\cos(\gamma_2\eta) + B_6\sin(\gamma_2\eta) + B_7\cos(\psi_2\eta) + B_8\sin(\psi_2\eta), & 0 \leq (\star) < \hat{p} \\ [B_5\cosh(\gamma_2\eta)\cos(\psi_2\eta) + B_6\sinh(\gamma_2\eta)\cos(\psi_2\eta) & \\ \quad + B_7\cosh(\gamma_2\eta)\sin(\psi_2\eta) + B_8\sinh(\gamma_2\eta)\sin(\psi_2\eta)]\,, & (\star) < 0 \end{cases} \tag{92}$$

where

$$(\star) = \hat{p}^2 + 4\left(\alpha^4 - D\right),$$

$$\gamma_1 = \sqrt{\frac{-\hat{p} + \sqrt{\hat{p}^2 + 4\alpha^4}}{2}}\,, \quad \psi_1 = \sqrt{\frac{\hat{p} + \sqrt{\hat{p}^2 + 4\alpha^4}}{2}}\,,$$

$$\gamma_2 = \begin{cases} \sqrt{\left(-\hat{p} + \sqrt{\hat{p}^2 + 4\left(\alpha^4 - D\right)}\right)/2}\,, & \hat{p}^2 + 4\left(\alpha^4 - D\right) \geq \hat{p} \\ \sqrt{\left(\hat{p} - \sqrt{\hat{p}^2 + 4\left(\alpha^4 - D\right)}\right)/2}\,, & 0 \leq \hat{p}^2 + 4\left(\alpha^4 - D\right) < \hat{p} \\ Re\left|\sqrt{\left(-\hat{p} + \sqrt{\hat{p}^2 + 4\left(\alpha^4 - D\right)}\right)/2}\right|\,, & \hat{p}^2 + 4\left(\alpha^4 - D\right) < 0\,, \end{cases}$$

$$\psi_2 = \begin{cases} \sqrt{\left(\hat{p} + \sqrt{\hat{p}^2 + 4\left(\alpha^4 - D\right)}\right)/2}\,, & \hat{p}^2 + 4\left(\alpha^4 - D\right) \geq 0 \\ Im\left|\sqrt{\left(-\hat{p} + \sqrt{\hat{p}^2 + 4\left(\alpha^4 - D\right)}\right)/2}\right|\,, & \hat{p}^2 + 4\left(\alpha^4 - D\right) < 0\,, \end{cases}$$

and the boundary conditions become

$$\begin{aligned} \eta = 0: \quad & U_L''' + S_K U_L = 0, \quad U_L'' - S_B U_L' = 0, \\ \eta = 1: \quad & U_R = 0, \quad U_R'' = 0\,. \end{aligned} \tag{93}$$

The continuity conditions for $\eta = \delta$ remain the same as the nominal drilling model (Eq. 87). We determine the frequencies of the hard material fault for various compressive tip loads and depths. The compressive force limit for these models is 4500 N (the maximum value provided by the manufacturer for safe operations of the drill system). Therefore, the intensity of the hard material drilling fault again ranges from 0 to 1, where 0 reflects a zero compressive tip force and 1 reflects a compressive tip force of 4500 N. Figure 87 demonstrates the change in frequencies for this model as a function of the compressive tip load.

5.2.2.5 Corkscrewing Fault Model

The corkscrewing fault results from a large tensile force on the auger tube as the auger flutes create a corkscrewing effect with the bore-hole wall. Similar to other faults, this occurs anywhere along the embedded auger. Therefore, the corkscrewing fault contains a tensile force T at a location L'. Figure 88 provides a sketch of the corkscrewing fault model.

The spatial solution for this model, similar to the binding and jamming fault models, is broken into three pieces: auger tube out of the hole, auger tube in the

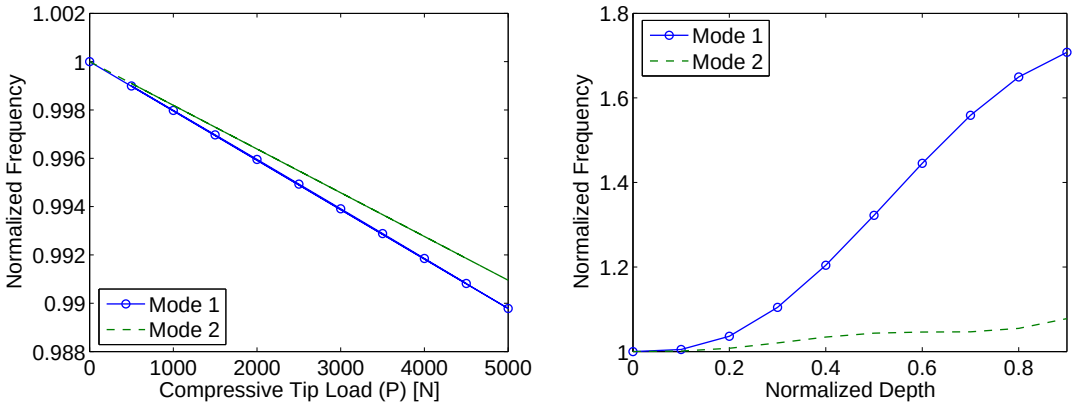

(a) $\delta = 0.5$ (b) $P = 4500$

Figure 87: Effects of Hard Material Condition on Natural Frequencies (L=1m).

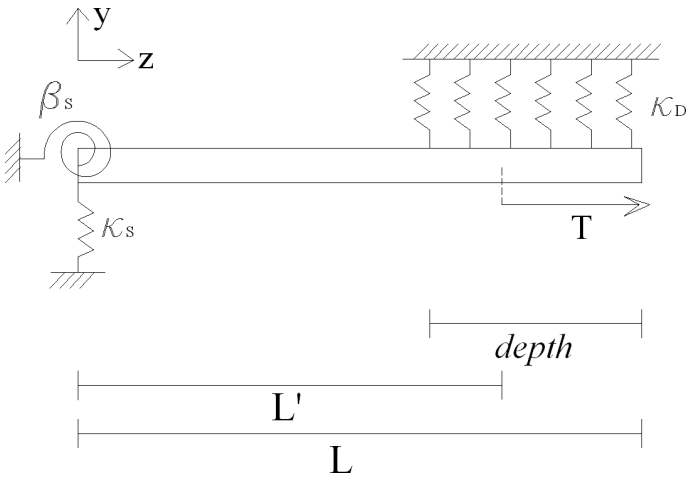

Figure 88: Structural Model of Corkscrewing Drill Fault.

hole before the corkscrew location, and auger tube in the hole after the corkscrew location. As the solutions have already been derived in previous models, the following description is provided:

1. $0 < \eta < \delta$: $U_L(\eta)$ is the same as the hard material model for this same range of η (Eq. 92). The variable $\hat{p}$, however, is changed to $-\tau$ where

$$\tau = \frac{TL^2}{EI} .$$

2. $\delta \leq \eta < \zeta$: $U_M(\eta)$ is the same as the hard material model for the range $\delta \leq \eta < 1$

(Eq. 92), and the variable $\hat{p}$ will again be replaced with $-\tau$.

3. $\zeta \leq \eta < 1$: $U_R(\eta)$ is the same as the binding model for this same range of η (Eq. 88).

4. γ and ψ are different for each spatial solution. Therefore, γ_i and ψ_i are used for the three spatial solutions, where $i = 1, 2, 3$.

5. The boundary conditions are the same as the binding fault model.

6. The continuity conditions for $\eta = \delta$ are the same as the nominal drilling fault model (Eq. 87), and the continuity conditions for $\eta = \zeta$ become

$$
\begin{aligned}
U_M &= U_R \\
U'_M &= U'_R \\
U''_M &= U''_R \\
U'''_M &= \tau U'_M + U'''_R \,.
\end{aligned}
$$

The frequencies for various corkscrew locations and forces and drill depths have been evaluated. The maximum tensile load is limited to 2000 N, which represents the maximum severity of a corkscrew condition. A lower load limit is given for the tensile force than the compressive force (4500 N) on the drill auger because of the nature of this fault mode. Compressive tip loads are expected during nominal drilling conditions and can be less than or equal to the weight of the drill system and any attachments (e.g. rover or lander, etc.). Tensile loads, however, are not expected during nominal drilling and can lead to critical problems with the drilling operation. Figure 89 demonstrates the changes in natural frequencies for various values of corkscrew force, corkscrew location, and drill depth. The sharp corners in these plots are due to a limited number of fault parameter values in this analysis.

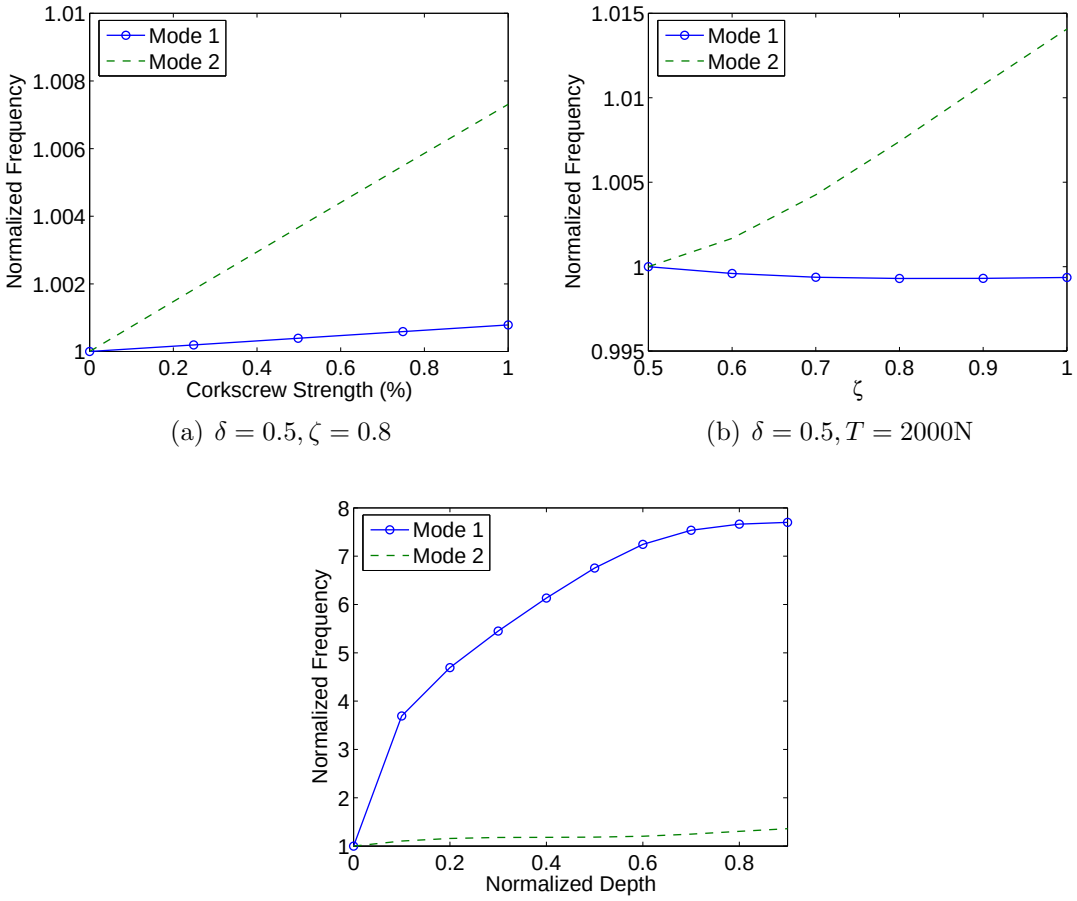

(a) $\delta = 0.5, \zeta = 0.8$

(b) $\delta = 0.5, T = 2000\text{N}$

(c) $\zeta = 0.8, T = 2000\text{N}$

Figure 89: Effects of Corkscrewing Condition on Natural Frequencies (L=1m).

5.2.2.6 Bit Inclusion Fault Model

Finally, the bit inclusion fault is identifiable by periodic spikes in the bit torque and axial displacements in the auger tube. This is due to the bit catching on a rock or jagged surface at the bottom of the hole (similar to the binding fault but limited to the drill bit). As the bit rotates, the auger tube will experience a continuous catch and release effect from the ground, which resembles a percussive motion in the axial direction. Therefore, a translational spring (κ_z) at $\eta = 1$ models the bit inclusion fault, and larger spring constants represent a more severe bit inclusion fault. Also, a strong rhythmic percussive motion is evident in the signal response of the auger

tube as incremental frequencies related to the rotational speed (angular velocity). Therefore, the model for the bit inclusion fault is in Fig. 90.

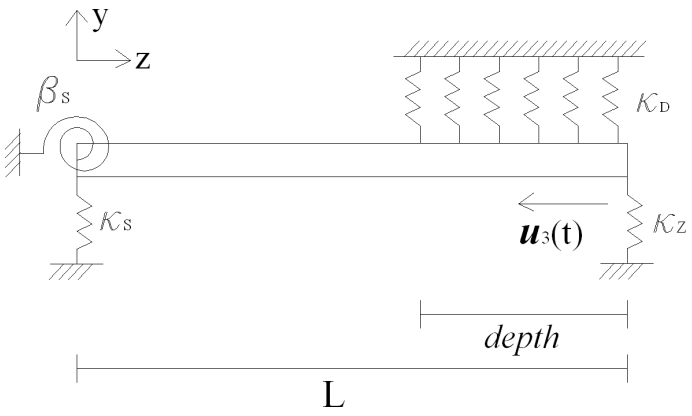

Figure 90: Structural Model of Bit Inclusion Drill Fault.

The frequencies for the bit inclusion model are evaluated for various depths and spring constants. Similar to the binding fault, the severity of the fault ranges from 0 to 1, where 0 reflects no translational spring and 1 reflects a zero displacement at the $\eta = 1$. To distinguish this fault from a binding fault at $\eta = 1$, the signal response is further analyzed to determine the presence of incremental spikes. For example, if the drill bit has two cutting edges and is rotating at 45 RPM (0.75 Hz), incremental frequencies will appear every 1.5 Hz. Figure 91 demonstrates the changes in natural frequencies due to a bit inclusion.

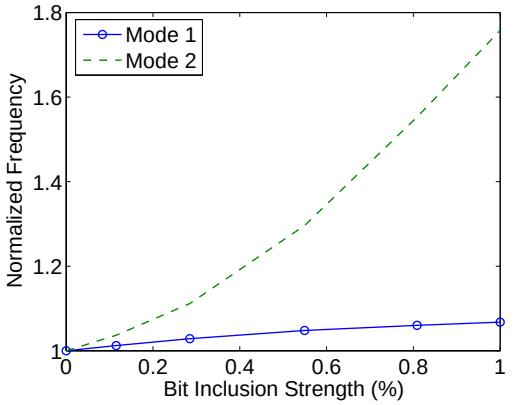

(a) $\delta = 0.5$

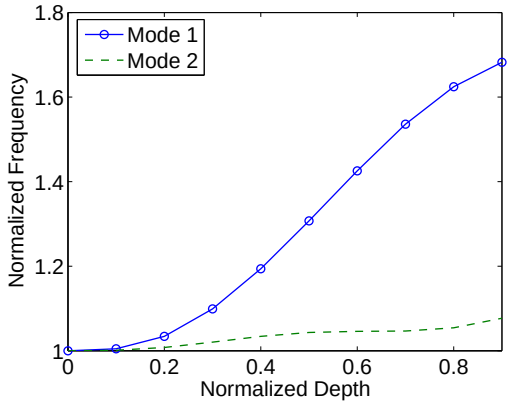

(b) $\kappa_z = \infty$

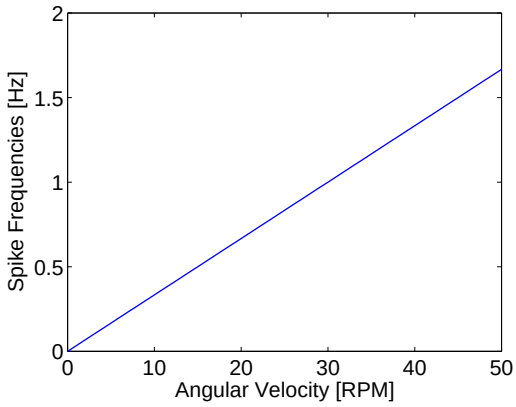

(c) Two Cutting Edge Bit

Figure 91: Effects of Bit Inclusion Condition on Natural Frequencies (L=1m).

CHAPTER VI

AUTONOMOUS SIGNAL ANALYSIS & HEALTH MONITORING

Automation in SHM, although advantageous for many techniques, is not common practice. According to Sohn, et al. [146], which provides a thorough review of SHM literature between 1996 and 2001, the state-of-the-art in damage detection techniques require user-interaction to make a final decision regarding the damage state of the structure, and much work is needed to automate system identification and damage diagnosis algorithms to remove the uncertainty involved by user interfaces.

Due to communication delays and the complexity of subsurface drilling on other planets and celestial objects, the drilling operation and all on-board diagnostic systems for an interplanetary exploration drill must be completely autonomous. When conducting dynamic response experiments, however, there are many hands-on activities from initializing equipment to capturing data to analysis. Therefore, an automation procedure and the corresponding software have been developed to control and operate these activities and network with the drill Executive computer to relay all diagnostics, ensuring full autonomous operations of the SHM technique. A flowchart of the automation procedure is provided in Fig. 92. The diagnostic module program is comprised of the harmonic frequency filter, a signal analysis algorithm, and trained Neural Networks for predicting the condition of the drill operation based on the six identified drilling faults. Details of the signal analysis algorithm, trained Neural Networks, automation procedure, and the network interface with the drill Executive computer are provided in the following sections.

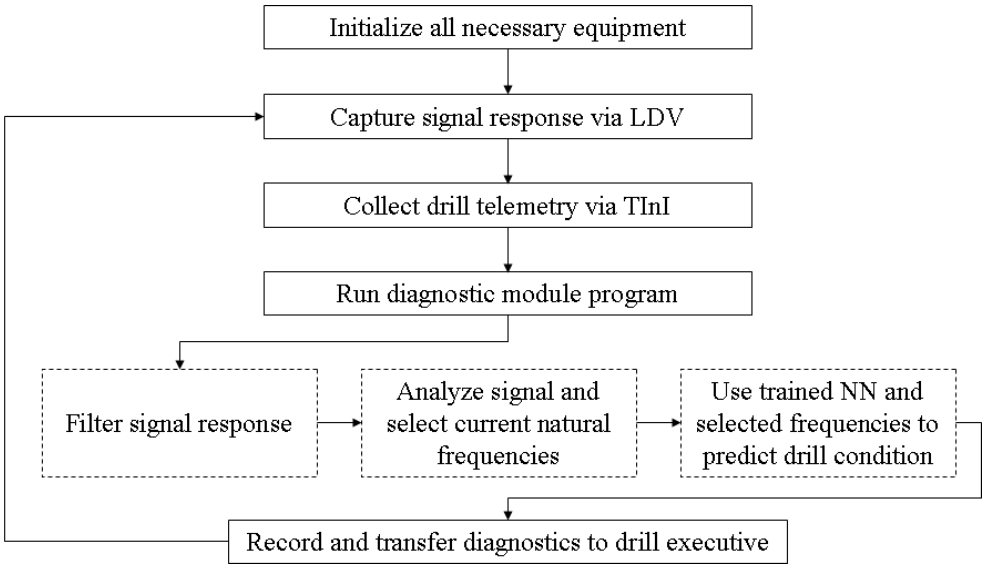

Figure 92: Automation Procedure for Dynamics-Based SHM.

6.1 Automated Signal Analysis

To analyze the filtered drill signal and define the current auger tube frequencies, a signal analysis algorithm has been developed. The first step of this algorithm is to define a frequency domain for the first two natural frequencies at the current drill depth. The minimum possible frequency is provided by the choking fault model and the maximum possible frequency is provided by the jamming fault model. These frequency limits for various drill depths have been recorded using a trained Neural Network (full description provided in the following section). Thus, a possible frequency domain is defined using the current drill depth ($\pm$ 5 cm to account for uncertainties in the depth measurement) and the trained frequency range NN. The frequency domain for nominal drilling at the current depth is also defined. An example of this is provided in Fig. 93.

Overlaps between the frequency domains for the first and second (and so on) auger frequencies often occur. This leads to four possible scenarios shown in Fig. 94. Therefore, the frequency domain is further broken down into three regions: lower domain, upper domain, and overlap domain.

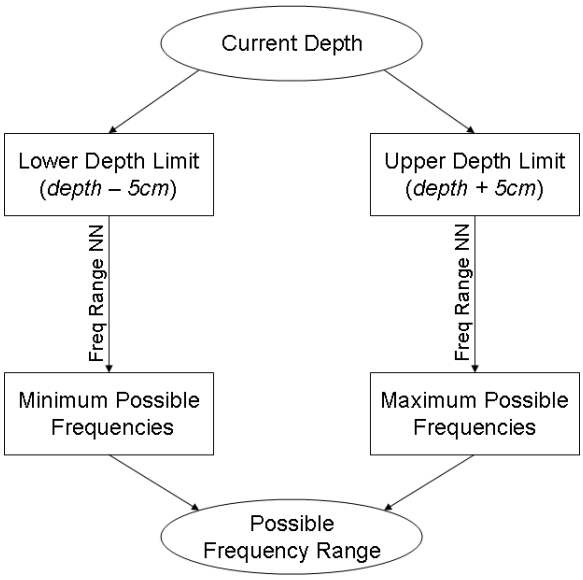

Figure 93: Defining Frequency Domain in Signal Analysis Algorithm.

These three regions are used to examine the signal and collect the highest peak in the lower region, the highest peak in the upper region, and the two highest peaks in the overlap region. A peak is defined as any point that satisfies the criteria

$$AS(\omega - 2df) < AS(\omega - df) < AS(\omega) > AS(\omega + df) > AS(\omega + 2df),$$

where AS is the auto-spectrum of the signal, ω is the frequency of the peak, and df is the signal resolution (distance between each data point). Therefore, a data point in the signal is defined as a peak if at least two points on each side (forward and aft) have declining magnitudes. It is important to note that signal noise and residues from the filtered harmonic gear mesh frequencies may also be defined as peaks with this algorithm. Assuming, however, that the magnitude of these peaks are small compared with the auger frequencies, these will be eliminated when only the highest amplitudes are considered.

The auger frequencies are finally resolved by examining the magnitude and frequency of the four remaining peaks and applying the four possible scenarios (Fig. 94). Specifically, the lowest two frequencies corresponding to significant peak magnitudes (at least 30% of the maximum amplitude in the signal) and within the appropriate

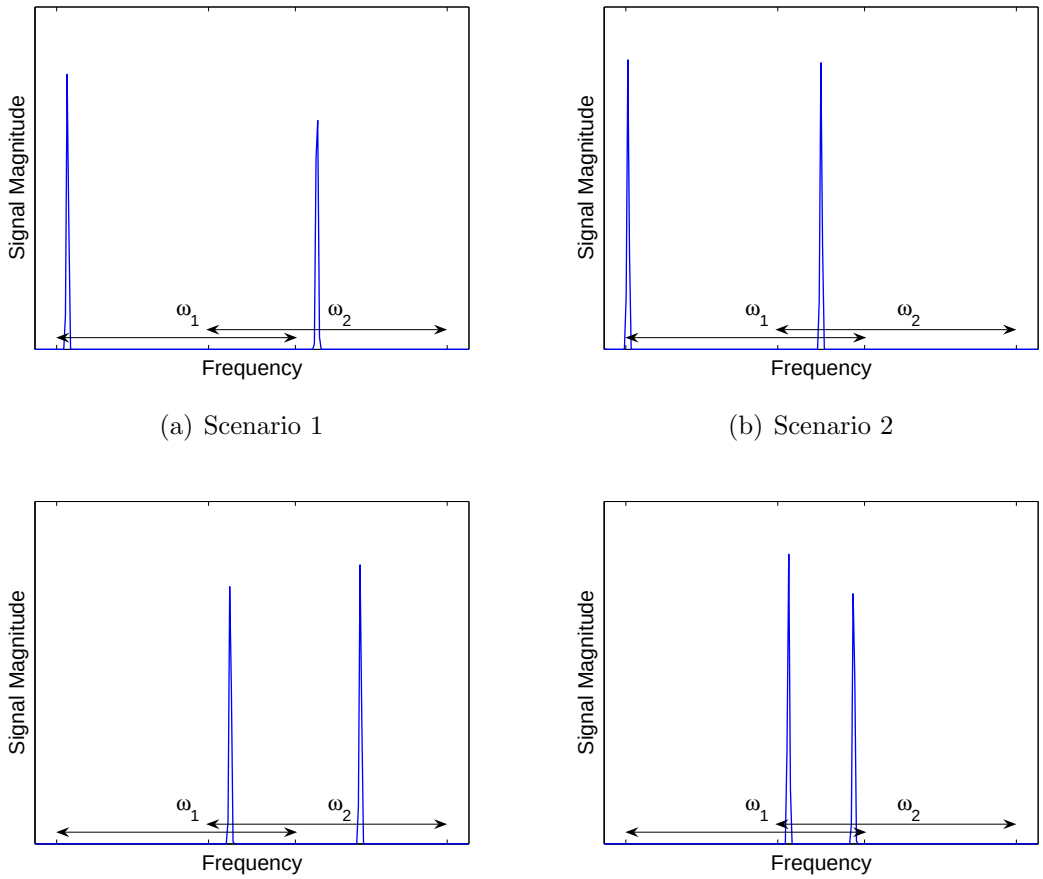

(a) Scenario 1

(b) Scenario 2

(c) Scenario 3

(d) Scenario 4

Figure 94: Four Signal Possibilities with Overlapping Frequency Domain.

frequency domains are defined as the first two auger tube frequencies.

Lastly, as discussed in Section 4.3.2, it is possible to unintentionally filter the auger frequencies if they occur near the harmonic frequencies. Therefore, a final check is implemented in the signal analysis algorithm for this reason. If two distinct auger frequencies are not found or if the magnitude of the signal at one of the defined frequencies is less than 30% of the maximum amplitude in the signal (i.e. a peak from signal noise is selected), it is assumed that the actual auger frequency was unintentionally filtered. Therefore, the designated auger frequency is set equal to the harmonic gear mesh frequency.

Figures 95 through 97 provide examples of the signal analysis algorithm results.

Figure 95 includes simulated frequency response signals with (ideal) and without simulated signal noise, Fig. 96 provides analysis of simulated frequency response signals with harmonic gear mesh frequencies (case 2 represents a possible scenario where the auger frequencies are unintentionally filtered with the harmonic frequencies), and Fig. 97 provides an example of this algorithm applied to an actual auger tube signal from the drilling experiments (Fig. 16). All determined auger frequencies are indicated with asterisks.

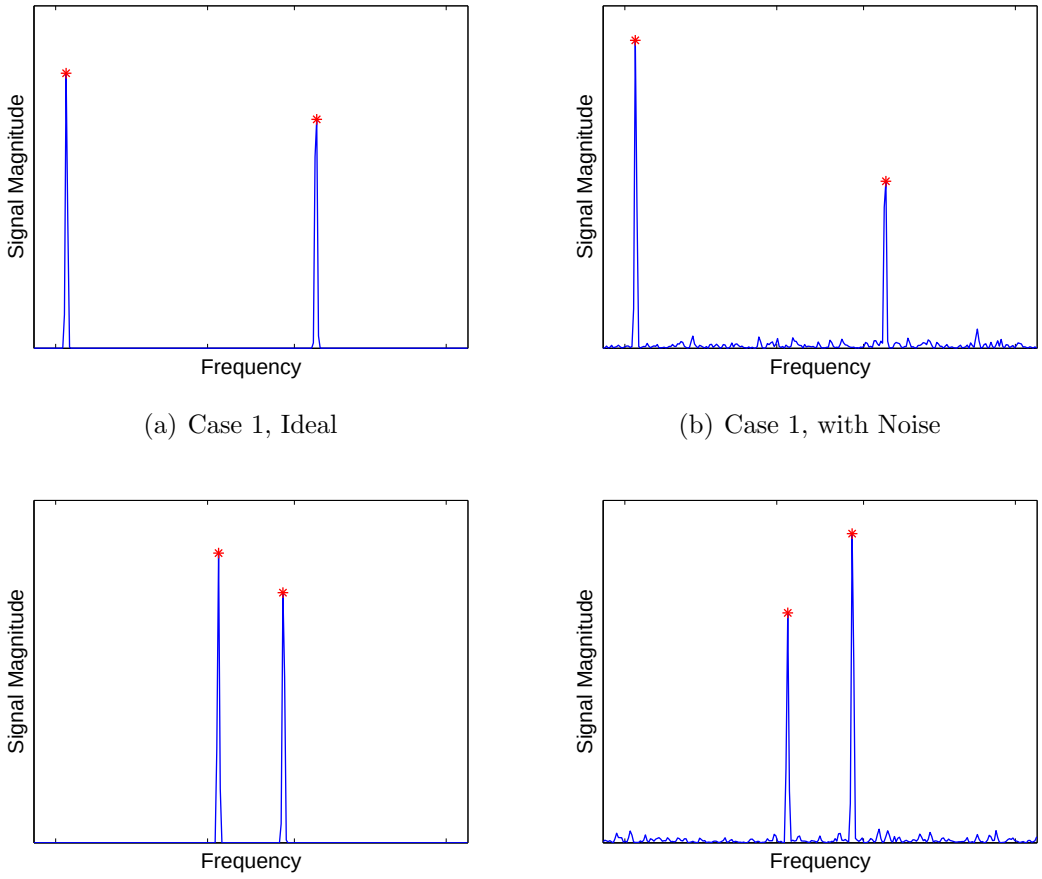

(a) Case 1, Ideal

(b) Case 1, with Noise

(c) Case 2, Ideal

(d) Case 2, with Noise

Figure 95: Signal Analysis Algorithm applied to Simulated Signals.

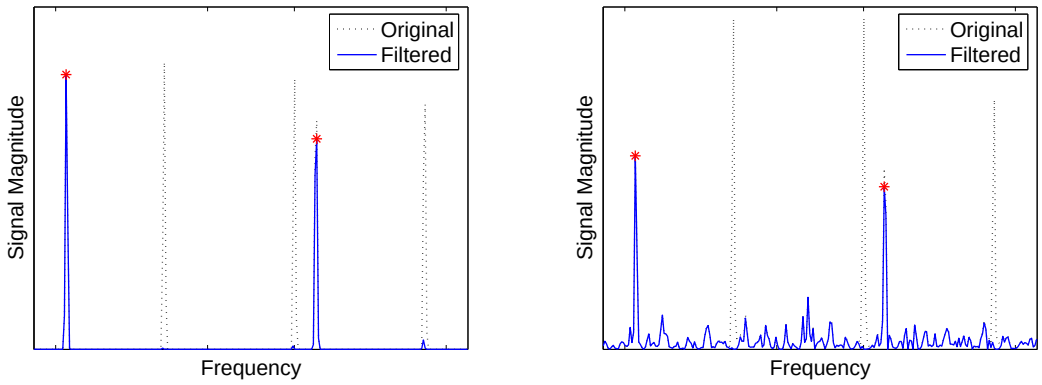

(a) Case 1, Ideal

(b) Case 1, with Noise

(c) Case 2, Ideal

(d) Case 2, with Noise

Figure 96: Signal Analysis Algorithm applied to Simulated Signals with Harmonic Frequencies.

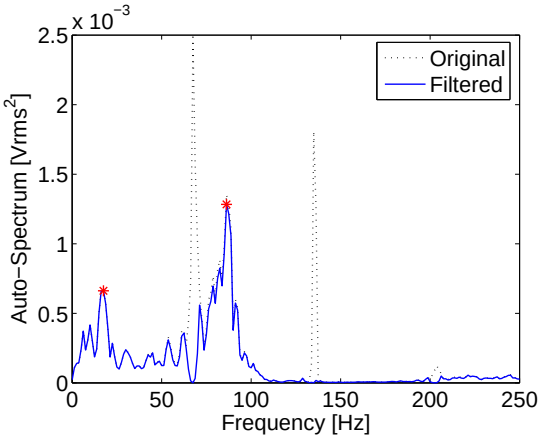

Figure 97: Signal Analysis Algorithm applied to Drilling Auger Tube Signal.

6.2 Neural Network Implementation

The requirement for a rapid-response system is addressed with Neural Networks. Each structural dynamic model has a complicated characteristic equation and an infinite number of possibilities for each parameter (e.g. depth, binding location, cork screw tensile force, etc.). Using these characteristic equations directly to solve the model parameters and fault probabilities (similar to the procedure used to quantify the spring constants for the drill supports and nominal drilling model) would be very cumbersome and time consuming, which are both problematic when a rapid-response diagnostics system is required. This is resolved by creating an adequate database of various model parameters and their corresponding frequencies off-line and implementing a function approximation algorithm (i.e. Neural Networks [11]) that can be easily accessed on-line.

A feed-forward, backpropagation Neural Network available through the MATLAB Neural Network Toolbox (*newff* [48]) is used in this research work. A database with various values for the model parameters (e.g. binding strength and location) and the corresponding natural frequencies is created for each drilling mode (nominal drilling and six drilling faults). These databases are then used to train a Neural Network for each modeled drilling condition.

In training Neural Networks, the accuracy and computing time are proportional (i.e. more accurate training requires more computing time), and there is usually a trade-off between accuracy and time/computing cost restraints. Larger databases and better training parameters yield more accurate results from the trained Neural Networks. This, however, goes hand in hand with higher time and/or computing cost requirements. Therefore, several settings for training the Neural Networks have been investigated. Table 17 provides the results for this investigation on the binding fault. The following definitions and settings are useful for understanding the training process of these Neural Networks:

- Training Data: The Neural Networks are trained with the databases created for each drilling mode using certain values for the input vectors and certain values for the output vectors, depending on the specific model. For binding, the input values are the first two natural frequencies and drill depth, and the output values are the binding fault strength and location. For training, these values are normalized by the maximum value within each parameter group (i.e. the first natural frequencies are normalized by the largest first natural frequency, etc.), giving values only between 0 and 1. Although this is not a necessary step, it was found in this research work to produce better results and also fit well with providing probabilistic output values.

- NN Layers: Each trained NN contains up to two hidden layers and one input and output layer. The hidden layers are trained using the hyperbolic tangent sigmoid (*tansig*) transfer function, and the output layer is trained using the linear (*purlin*) transfer function.

- Size of Layers: The input/output layers are always equal to the number of input/output parameters desired. For most of the trained NNs, this value is 3 for the input layer and 2 for the output layer. The size of the hidden layers is adjusted to determine what size is appropriate. Larger hidden layer sizes produce more accurate results but also require more training time.

- Training Algorithm: The Levenberg-Narquardt backpropagation (*trainlm*) algorithm is used for training these NNs. Although this backpropagation algorithm requires more computing memory and training time, it was by far the most accurate algorithm investigated. All MATLAB default parameters for this algorithm are used.

- Training Weights & Biases: The training weights and biases are initialized at zero and continuously updated by the backpropagation algorithm throughout

the training process.

- Epochs: An epoch is a single pass/iteration through the training set. After each epoch, the MSE is calculated and the training weights and biases are adjusted. The epoch setting is the maximum number of epochs to complete if the minimum MSE has not yet been obtained. The minimum MSE for each case was set to 1E-08.

- Training Time: The training time is the total time needed to train each NN. If the minimum MSE is obtained, this is the elapsed time to reach this limit. If the minimum MSE is not obtained, this is the elapsed time to complete the epoch limit.

Table 17: Binding Neural Network Training Results

Case	Number of Hidden Layers	Size of Hidden Layers	Max Epoch	MSE	Training Time (s)
1	1	10	500	9.40E-03	9.9
2	1	10	1000	8.20E-03	18.9
3	1	20	1000	5.60E-03	37.0
4	1	30	1000	6.10E-03	60.8
5	2	10	1000	2.00E-03	57.1
6	2	20	1000	8.43E-05	434.4
7	2	30	1000	4.21E-07	2181.5

It is evident from these results that increasing the complexity and size of the NN training parameters increases the overall accuracy but also greatly increases the training time. Figure 98 provides the target values versus the NN predictions of three of the investigated training settings. As the *purelin* transfer function is used for the output layer, a linear correlation between the target values and NN predictions is expected. From these graphs, it can be seen that very low correlation is achieved for case 1, and high correlation is achieved for cases 6 and 7.

Finding a compromise between accuracy and training time, the settings for case 6 have been used to train all the drilling mode Neural Networks. Figure 99 provides a

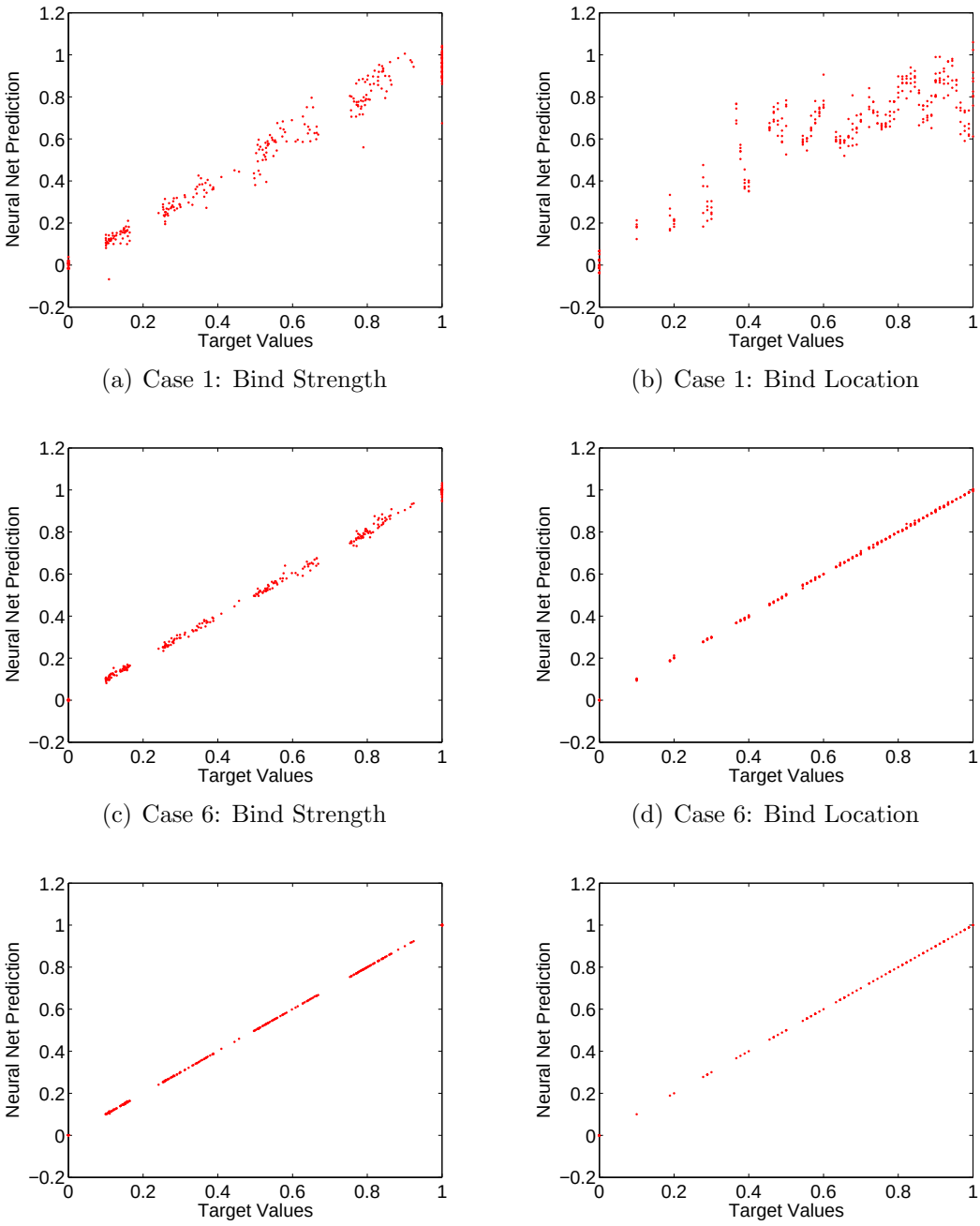

(a) Case 1: Bind Strength

(b) Case 1: Bind Location

(c) Case 6: Bind Strength

(d) Case 6: Bind Location

(e) Case 7: Bind Strength

(f) Case 7: Bind Location

Figure 98: Binding Neural Network Training Results - Target vs NN Values.

diagram of the trained Neural Network for the jamming fault, and Table 18 provides the training results from the seven identified and modeled drilling conditions. From Table 18, it is interesting to note that the binding, jamming, and corkscrewing faults

are more difficult to train compared to the other fault models. This is due to the complexity of these models and the similarity of frequency values for different values of ζ.

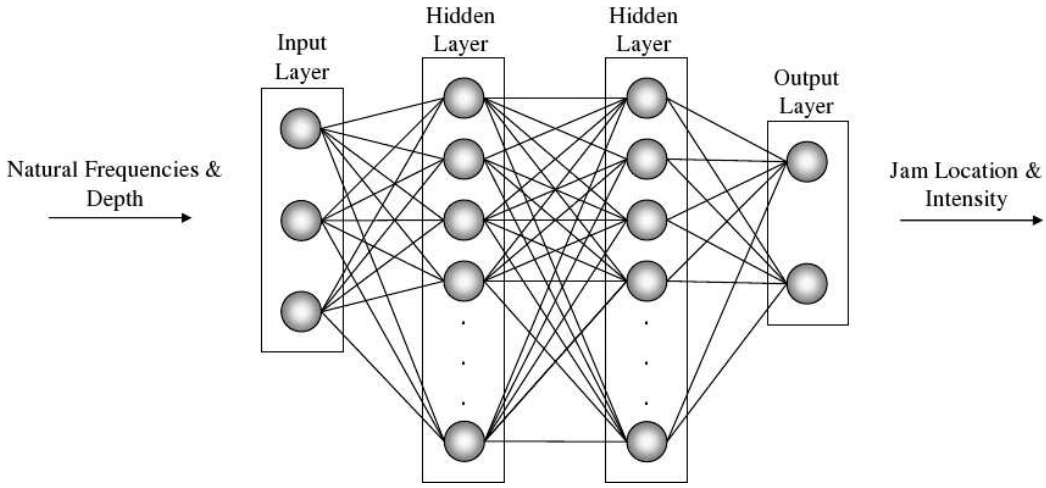

Figure 99: Neural Network Structure of Jam Drilling Fault.

Table 18: Neural Network Training Results for Seven Drilling Modes

Drill Mode	Input*	Output*	Database Size	MSE
Nominal	depth	ω_1, ω_2	51	1.00E-08
Binding	f_1, f_2, depth	bind strength, ζ	336	5.14E-05
Choking	f_1, f_2, depth	choke strength, μ	330	1.86E-07
Jamming	f_1, f_2, depth	jam strength, ζ	336	7.64E-05
Hard Material	f_1, f_2, depth	hm strength, P	561	1.00E-08
Cork Screw	f_1, f_2, depth	cork strength, ζ	392	2.43E-05
Bit Inclusion	f_1, f_2, depth	bitinc strength	306	1.00E-08

*ω_i =Theoretical Frequencies, f_i =Current Drill Frequencies

6.2.1 Heuristic Filter

Although the developed structural dynamic models are unique, it is easy to see that overlaps can occur for certain cases. For example, if a binding fault is occurring at the tip of the auger tube, this will most likely give a high probability from the bit inclusion NN as well, and a low to moderate probability from the jamming and hard material faults. Furthermore, even though the NNs are only trained with values

between 0 and 1, it is very possible for a NN to output values beyond this range when the given input values are beyond the training database. However, as each NN is trained with the maximum and minimum values possible for the corresponding model, it can be concluded that any output values beyond the 0 to 1 range correspond to input values that are not practical possibilities for the given model. Thus, it is critical to develop a heuristic filter to ensure the accuracy of the diagnostics and also reduce the occurrence of false positives.

The drill depth is the first and easiest parameter to use for filtering. The position of the drill head along the drill column is continuously monitored, and the drill depth is determined using the current drill head position, the drill head position at the surface of the ground, and the total number of drill strings (i.e. length of the auger tube). Thus, the drill depth can be negative (drill bit is out of the ground), positive (drill bit is in the ground), or zero (drill bit is right at the surface of the ground). Of these three possibilities, the positive drill depth is the only practical position for any drilling faults to occur. Therefore, if the drill depth is currently zero or negative, all drilling fault diagnostics are automatically set to 0% probability.

Other dynamic drilling parameters to consider are the auger speed (angular velocity), ROP (Rate of Penetration, axial velocity), WOB (Weight on Bit, compressive tip load), auger tube torque, and drill bit torque. These parameters are the backbone of rule-based diagnostic systems. The rule-based diagnostic system created for the DAME project uses only the current drilling parameter values (from the drill telemetry) and designated thresholds for each, defined by laboratory and field test observations, to provide diagnostic probabilities [63]. These values and similar thresholds can also be used to reduce false positives. It is important to note, however, that not all drill systems will be equipped with the same quantity or type of sensors. Therefore, the thresholds used for the DAME drill may need to be adjusted for other drill systems.

Any dramatic change to the auger speed during a drilling operation is a definite sign that a fault condition is occurring. As the jamming fault is associated with the rotation of the auger, the auger speed can be used as a filter for this fault model. Therefore, if the auger speed is nominal (operating at the user set speed), the diagnostic for jamming is set to zero. If the auger speed is considerably less than the user set speed, however, the NN produced diagnostics for jamming will be used.

The current drilling ROP indicates the progress being made down the hole. The nominal operating ROP is between 0.3 and 0.5 cm/min. If this value drops below 0.1 cm/min, this is a good indicator that the drill is most likely hitting an ice or other hard material layer. Therefore, if the ROP is above 0.1 cm/min (i.e. the drill is making head-way down the hole), the hard material diagnostic will be set to zero.

The corkscrewing fault is associated with a large tensile force along the auger tube. The WOB telemetry can therefore be used to filter this fault diagnostic. If the current WOB is greater than zero, the corkscrew diagnostic will be set to zero.

The torque along the auger tube (AugT) and at the bit (BitT) are also good indicators for the binding, choking, and bit inclusion faults. Binding is associated with an increasing AugT and nominal BitT, choking is associated with increasing AugT and BitT, and bit inclusion is associated with a harmonic spiking behavior in the BitT and nominal AugT. Therefore, if the AugT and BitT readings are constant (and within the nominal operating range, $\leq$ 30 Nm), the diagnostics for binding, choking, and bit inclusion will be set to zero.

As described in the bit inclusion model, harmonics proportional to the auger speed are expected to be present in the dynamic signal of the drill when this fault is occurring. Therefore, to distinguish between a binding fault near the bit and bit inclusion, harmonics in the current signal will be investigated. If harmonics are present, the bit inclusion diagnostic will be used and the binding diagnostic will be set to zero.

Lastly, if any of the NNs produce out of range results (i.e. less than 0 or greater than 1), it can be concluded that the current auger state is out of range for that particular drilling mode. Therefore, the fault diagnostics for that drilling mode is set to zero.

To evaluate the accuracy of the NN diagnostics, an *a priori* drilling simulation was created. Table 19 provides the drilling mode breakdown for this simulation, and Figs. 100 and 101 provide the diagnostic results. In these figures, the diagnostic results (NN) are compared with the preset simulation diagnostics (Model). Figure 100 provides the results without a heuristic filter for the current drill telemetry, and Fig. 101 includes the full heuristic filter. From these results, it can be concluded that the NN diagnostics, paired with a heuristic filter, are very accurate.

Table 19: Drilling Modes for Simulation Test

Data Set	Drilling Mode
1-5	Out of Hole (depth<0)
6-15	Nominal
16-25	Binding
26-35	Bit Inclusion
36-45	Jamming
46-50	Nominal
51-60	Choking
61-70	Hard Material
71-80	Nominal
81-90	Corkscrew
90-95	Nominal
96-98	Choking
99-100	Jamming

6.3 Automation Procedure & Drill Interface

To complete the automation process for the diagnostic module program and network with the drill Executive computer, a control program has been developed. This program, written in C++, interfaces the measurement equipment (LDV sensors and SigLab), diagnostic module program, and the drill Executive computer (Fig. 92).

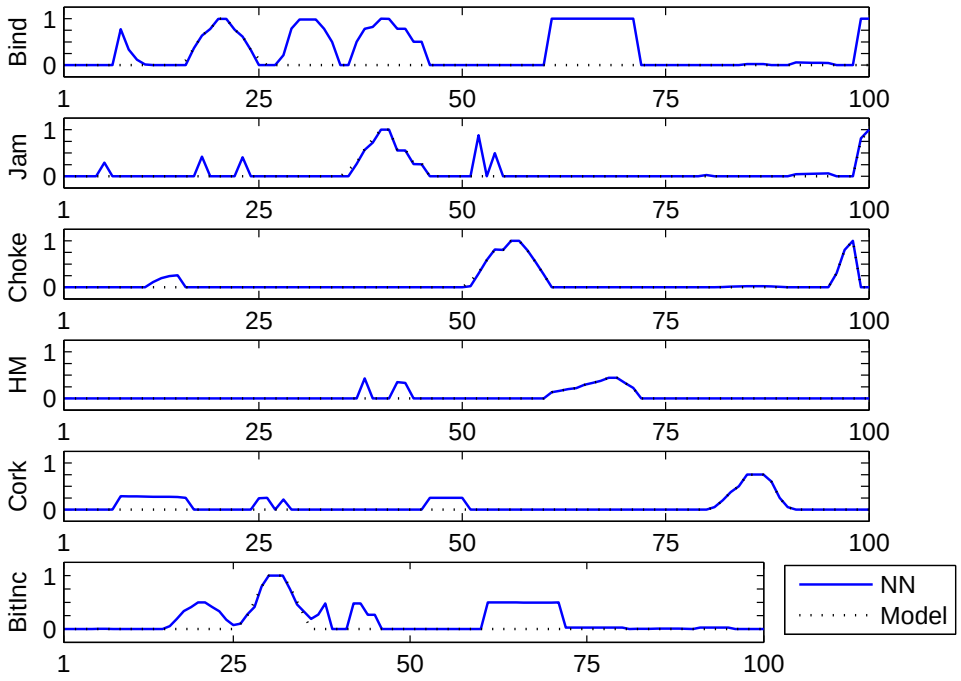

Figure 100: Neural Network Diagnostic Results of Drilling Simulation (No Heuristic Filter).

The MATLAB software and SigLab equipment are first initialized and the current auger tube signal is collected by SigLab via the LDV sensors. The auger tube signal is saved in a designated location that can later be opened and analyzed in the diagnostic module program.

The current dynamic drilling parameter values (from the drill telemetry) are then collected from the drill Executive computer. The DAME drill server outputs telemetry values every 0.25 seconds. Therefore, to obtain an accurate telemetry reading, the average telemetry for 2 seconds is recorded. These values are then defined in the global variable *dataVector*, which is accessed in the diagnostic module program.

With the current signal and telemetry values obtained, the diagnostic module program, which includes the signal filter, signal analysis algorithm, and trained Neural Networks, is executed and the diagnostic probabilities are output to the control

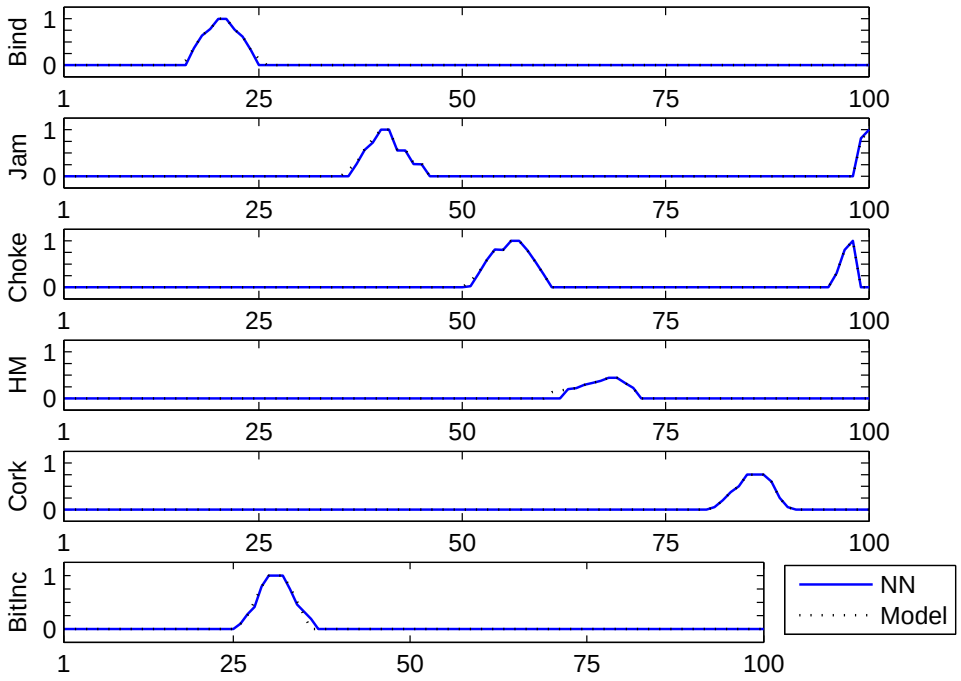

Figure 101: Neural Network Diagnostic Results of Drilling Simulation (With Heuristic Filter).

program. Lastly, the diagnostic results are relayed to the drill Executive computer. This process is repeated until the user terminates the executable.

The dynamics-based SHM system, comprised of LDV sensors, structural dynamic models and trained Neural Networks, a frequency filter, signal analysis algorithm, and automation procedure, has met all specified requirements. Field testing and validation of this system are presented in the following chapter.

CHAPTER VII

FIELD TESTING & VALIDATION

Three field tests have been conducted using the developed dynamics-based SHM system with the DAME drill prototype. These three field tests are described in more detail in the following sections.

7.1 Devon Island 2006

A field test was conducted at the Haughton Crater on Devon Island in July 2006. Devon Island is located in the Canadian Arctic and is the largest uninhabited island in the world. Devon Island is home to the Haughton impact crater (Fig. 102), which is located at 75°22′N, 89°41′W and is approximately 23 to 24 km in diameter [69]. The Haughton Crater was initially explored and geologically mapped in 1955 by H. R. Greiner as part of Operation Franklin, the first large scale reconnaissance mapping of the Arctic Islands [127]. Greiner named the region Haughton as a tribute to Reverend Samuel Haughton. During the 1970s and 1980s, teams of geologists studied the Haughton Crater to understand better the formation and erosion of impact structures. A brief history of these studies and the HISS (Haughton impact structure study) project are provided in Grieve [69] and Robertson [127]. From these studies, the Haughton Crater was formed approximately 23 million years ago. More recent studies, however, have suggested that the Haughton Crater was formed considerably earlier [142].

Much interest has been given to the Haughton Crater in the last 15 years by geologists and engineers because it offers a unique environment and presents operational challenges relevant to planetary exploration. The Haughton Crater, located in the

(a) Aerial View & Impact Insert [4]

(b) View from Inside Crater [4]

(c) Global Location [2]

Figure 102: Maps and Photographs of Haughton Crater, Devon Island, Canada.

polar desert, has experienced a predominantly cold and relatively dry climate throughout most of its history, which has left the region exceptionally well preserved [96]. Thus, understanding post-impact processes of the Haughton Crater will help geologists better understand Martian impact craters and Mars's climate evolution [96].

The surface and subsurface regions of the Haughton Crater are similar to what could be found in polar regions of Mars. These surface and subsurface characteristics

include impact breccia, ground ice and permafrost, intra-crater paleo-lacustrine deposits, hydrothermal deposits, and lack of any significant vegetation [95]. As Devon Island is uninhabited, scarcely vegetated, and resources are severely limited, the site also presents operational challenges that are analogous in fundamental ways to those expected in planetary surface and subsurface exploration [96]. Figure 103 provides radar images and shows similarities of the Haughton Crater of Earth and the Lunar Shackleton Crater. The Shackleton Crater is a prime candidate for human exploration and was initially one of the targets of the Ames LCROSS (Lunar Crater Observation and Sensing Satellite) mission [3]. Due to these unique and significant characteristics, the Haughton Crater and the surrounding area has been deemed a terrestrial analog for Mars and the Moon, which makes it an ideal location for testing and validating space exploration systems.

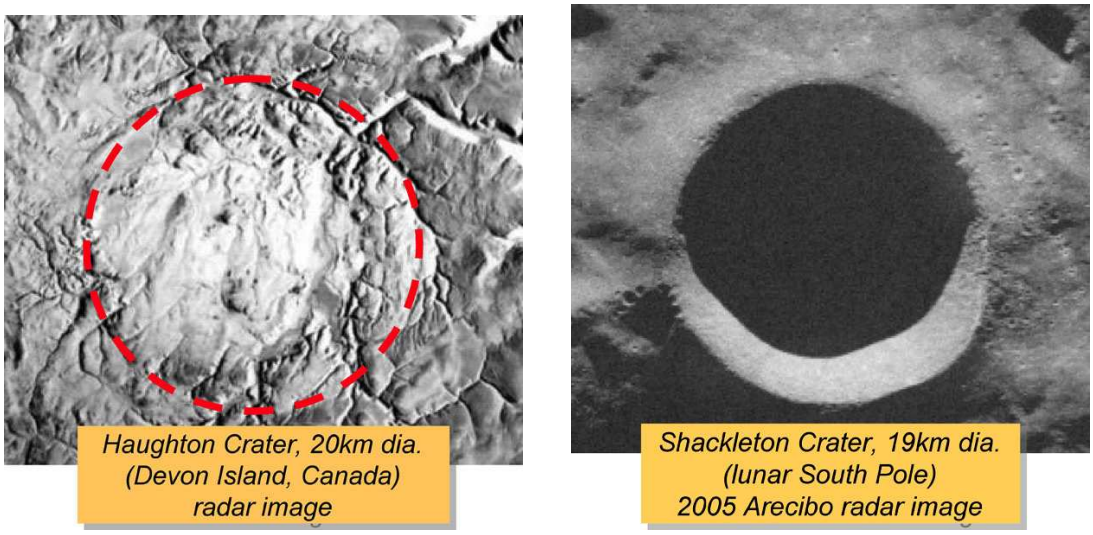

(a) Haughton Crater (b) Shackleton Crater

Figure 103: Radar Images of Haughton Crater and Lunar Shackleton Crater [3].

Since 1997, scientists and engineers alike have traveled to the Haughton-Mars Project (HMP) research station and other locations on Devon Island each year to study the crater and test space exploration systems at this unique, Mars-analog site. HMP is an international multidisciplinary planetary analog field research project

centered on the scientific study of the Haughton impact structure and surrounding terrains [96]. HMP is managed jointly by the Mars Institute and the SETI Institute with research funding support from NASA and the Canadian Space Agency. HMP supports both science and exploration programs and has provided research and basic living accommodations for all participants every summer since 1997. Figure 104 provides an aerial view of the HMP base camp, which serves as a modular Arctic base for all HMP participants.

Figure 104: Aerial View of Haughton-Mars Project Base Camp.

The drilling site for this field test was at a location known as *Drill Hill* (Fig. 105). Drill Hill is located inside Haughton Crater and has a deposit of impact breccia and bedrock matrixed with ground ice approximately 200 meters thick. This was also the site for the 2004 and 2005 preliminary field tests. Figure 106 is a photograph of the drill system set up on Drill Hill for this field test. The sand bags to the side of the drill system were used to simulate the additional weight of an attached rover or lander.

The project objectives for this field test were to operate hands-off for at least three hours, reach a drill depth of three meters, and successfully encounter and recover from three drilling faults. For this field season, the drill system was equipped for

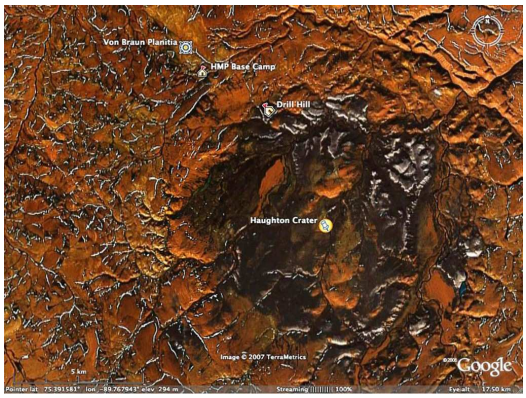

(a) Location in Crater [3]

(b) 2006 Drill Site on Drill Hill

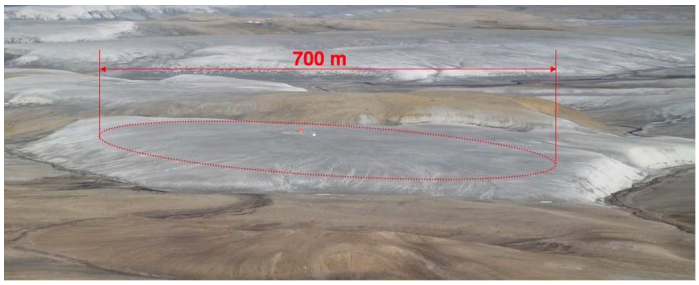

(c) Aerial View [3]

Figure 105: Drill Hill in Haughton Crater.

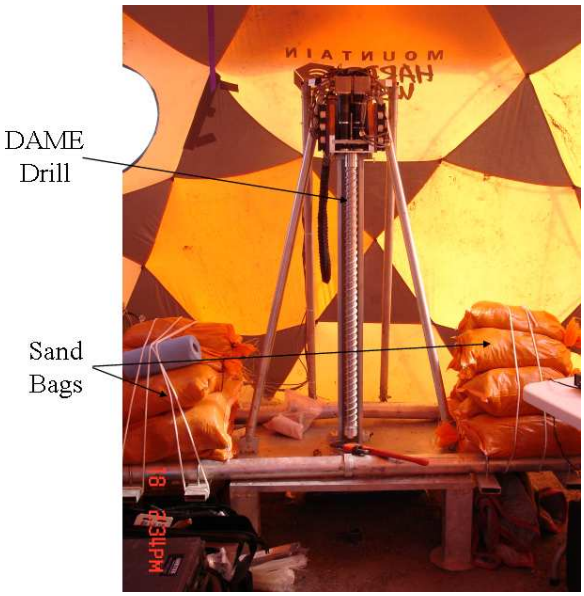

Figure 106: Drill System on Drill Hill, Devon Island, July 2006.

automated, hands-off drilling with automated diagnostic monitoring and recovery procedures.

The architecture for the automated drilling system is provided in Fig. 107 [62]. The *Contingent Executive* controls the drilling operation based on a drilling plan (most often set to achieve a specified drill depth). The Contingent Executive also collects and analyzes fault diagnostics from the three parallel diagnostic modules (Model-Based, Vibration Classification, and Rule-Based). If a fault mode is diagnosed by one or more of the diagnostic modules, the Contingent Executive (using pre-set weights and biases for each diagnostic module and fault mode) will continue with the drilling plan or pause the drilling plan and complete a recovery procedure for the specified drilling fault. Each drilling fault has a unique recovery procedure that has been identified and tested through numerous laboratory and field tests.

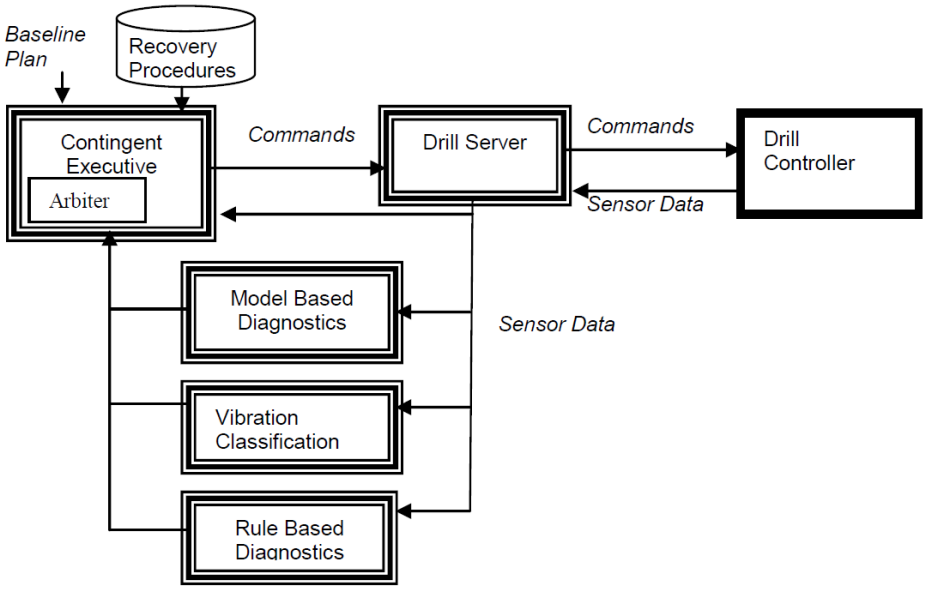

Figure 107: DAME Drill System Architecture [16].

The Contingent Executive executes the drilling plan and recovery procedures through a set of commands to the Drill Server that are transferred to the Drill Controller. The *Drill Controller* is the low level control system that controls the drill motors and retrieves and converts sensor data. The *Drill Server* collects the sensor data and broadcasts the information to the other modules. Sensor data for this drill

system is updated and broadcast every 0.25 seconds.

The communications backbone of the DAME drill system architecture (years 2006-2007) is known as Tiny Instrument Interface (TInI), which is responsible for transferring all of the data between the different modules [63]. TInI is a very small client/server string interface that supports multiple servers on independent machines and allows communications to various servers using telnet clients, which are available on any operating system [68]. TInI is faster than the MARTE Instrument Interface (MInI) developed for the MARTE drilling project, and it is more flexible than the K9Client developed for the K9 Rover. As of 2008, the Contingent Executive and TInI have been updated using PLEXIL and sockets, and more details of this update are provided in Section 7.3.

The three diagnostic modules work in parallel to provide continuous health monitoring of the drill system while in operation. The *Rule-Based* module is a simple diagnostic system that uses current and past sensor data (telemetry values) and simplistic thresholds and heuristics to determine the state of the drilling operation. The *Model-Based* module uses the Hybrid Diagnostic Engine (HyDE) developed at NASA Ames Research Center [16]. Throughout the drilling operation, HyDE tracks the evolution of the drill system state and compares the observed state to the one predicted by its model-based simulation [62]. If any discrepancies are detected, the model-based diagnostic system will flag the fault that best explains the abnormal drill system state. The *Vibration Classification* module is the dynamics-based SHM system presented in this thesis work.

The dynamics-based SHM system for this field test was equipped with two LDV sensors capturing the signal from the same position for redundancy (Fig. 108). The signal from each LDV sensor was captured and analyzed, and the diagnostics relayed to the drill Executive computer was the average found from the two signals. For this field test, the dynamics-based SHM was equipped to diagnose four of the six

drilling faults (binding, choking, jamming, and hard material) as the models and trained NNs for the corkscrewing and bit inclusion faults had not yet been developed. The dynamics-based SHM did however successfully diagnose these four fault modes, meeting the objective of correctly identifying at least three faults.

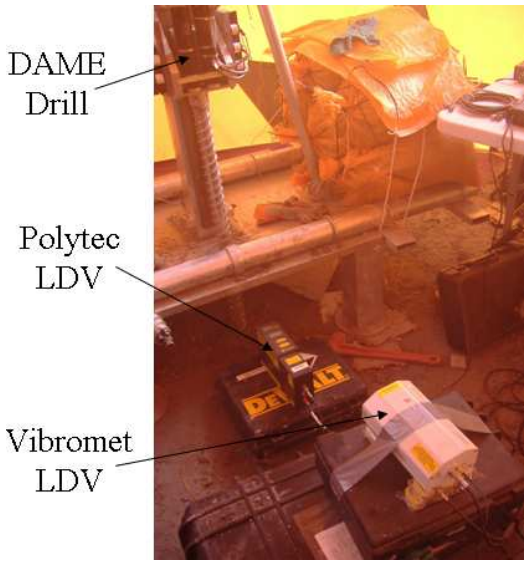

Figure 108: LDV Setup for Devon 2006 Field Test.

The original and filtered signal response of the drill auger tube during a jamming fault is provided in Fig. 109. The plots provided are just before (nominal diagnostics; 0% probability for all drilling faults) and at the jamming fault detection (60% probability). The determined natural frequencies are highlighted with asterisks. These plots show a clear shift in the natural frequencies of the auger tube, which was diagnosed as a jamming fault by the dynamics-based SHM system. For these measurements, the auger tube length was 3.75 m, the auger speed was 20 RPM, and the total drill depth was approximately 2.77 m.

An example of a signal response that triggered a binding fault by the dynamics-based SHM system is provided in Fig. 110 (the determined natural frequencies are highlighted with asterisks). The plots provided are the original and filtered signal response just before (nominal diagnostics; 0% probability for all drilling faults) and

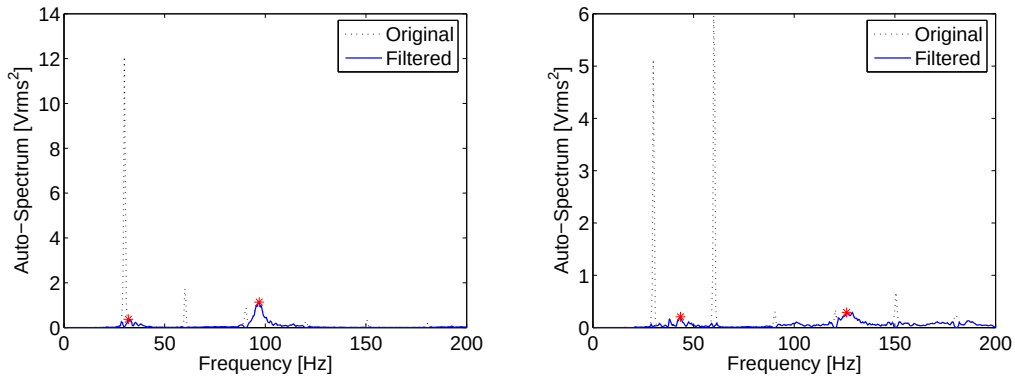

(a) Before Jamming Fault

(b) During Jamming Fault

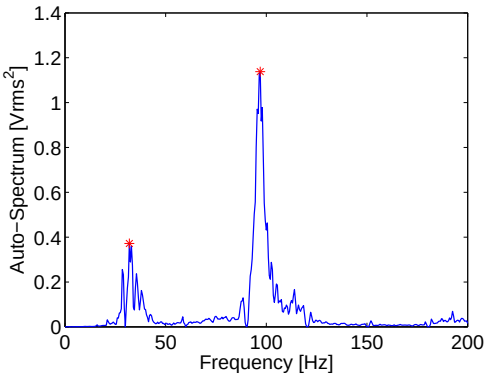

(c) Before Jamming Fault: Filtered

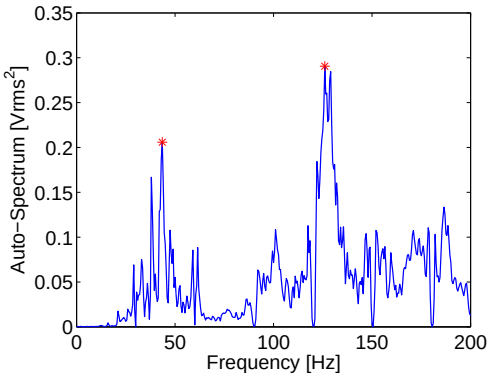

(d) During Jamming Fault: Filtered

Figure 109: Dynamic Response of Drill Auger Tube Through a Jamming Fault.

at the binding fault detection (71% probability). For these measurements, the auger tube length was 3.75 m, the auger speed was 20 RPM, and the total drill depth was approximately 3.07 m.

The 2006 field test to Devon Island was considered an overall success for the dynamics-based SHM system and the DAME system as a whole by the drilling team and NASA. This field test demonstrated automated drilling capabilities with reliable on-board diagnostic modules and recovery procedures. All the field test objectives were also met and exceeded. The drill system demonstrated detection and proper recovery from four drilling faults, 4.5 hours of consecutive hands-off drilling and a total of 44 autonomous drilling hours, and the final drill depth was 3.22 m.

This field test also validated the design approach for the dynamics-based SHM

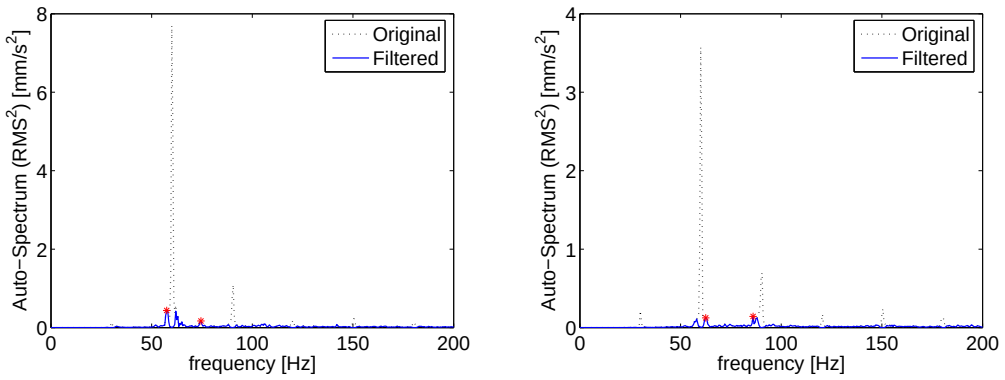

(a) Before Binding Fault (b) During Binding Fault

Figure 110: Dynamic Response of Drill Auger Tube Through a Binding Fault.

technique. An important note is the technique was not yet equipped with a heuristic filter for the NN probabilities. As seen from Section 6.2, this resulted in considerably higher false positives from the diagnostics. Therefore, future improvements for the technique were to update for all six drilling faults, implement a heuristic filter for the NN probabilities, and adapt for multi-dimensional LDV measurements.

7.2 Jet Propulsion Laboratory 2007

In October 2007, a blind test drilling demonstration at the Jet Propulsion Laboratory (JPL) in California was completed [67]. The objective of this demonstration was to complete hands-off blind drilling tests to further show the drill system's robust and adaptive capabilities. It was also important to show repeatability of the drilling procedure and fault-diagnostic accuracy, which is hard to accomplish during field tests on Devon Island given the unknown and unpredictable subsurface environment. The tests were considered *blind* as the contents and arrangements of the material test columns for drilling were unknown to the team.

The drilling tests and demonstrations were conducted at a new subsurface testbed facility in JPL building 141 (Fig. 111). Three one meter high specimen columns of various materials and structure were constructed by individuals outside of the drill team to ensure blind drilling tests. The contents of the specimen columns were not

revealed until post-test analysis. Figure 112 provides the material composition and structure of the three specimen columns. Each material section was chosen to simulate various conditions expected from drilling and hopefully simulate the six identified drilling faults. For example, the brick layers would simulate layers of permafrost that are relatively easy to drill (i.e. nominal drilling conditions), and the granite tiles would simulate ice layers that are harder to drill and could trigger a hard material fault.

Figure 111: Drill System at JPL Testbed, 2007.

Three independent LDV sensors were used to capture the signal response from three different directions for this demonstration (Fig. 113). Two LDV sensors were positioned directly to the back (Metro-500, labeled LDV #1) and side (PDV-100, labeled LDV #2) of the drill, and the third LDV sensor (second PDV-100, labeled LDV #3) was positioned between the side and back of the drill and a laser-quality mirror was used to offset the laser beam angle to capture axial vibrations. This setup provided more signal information for the drill, and it proved to increase the accuracy

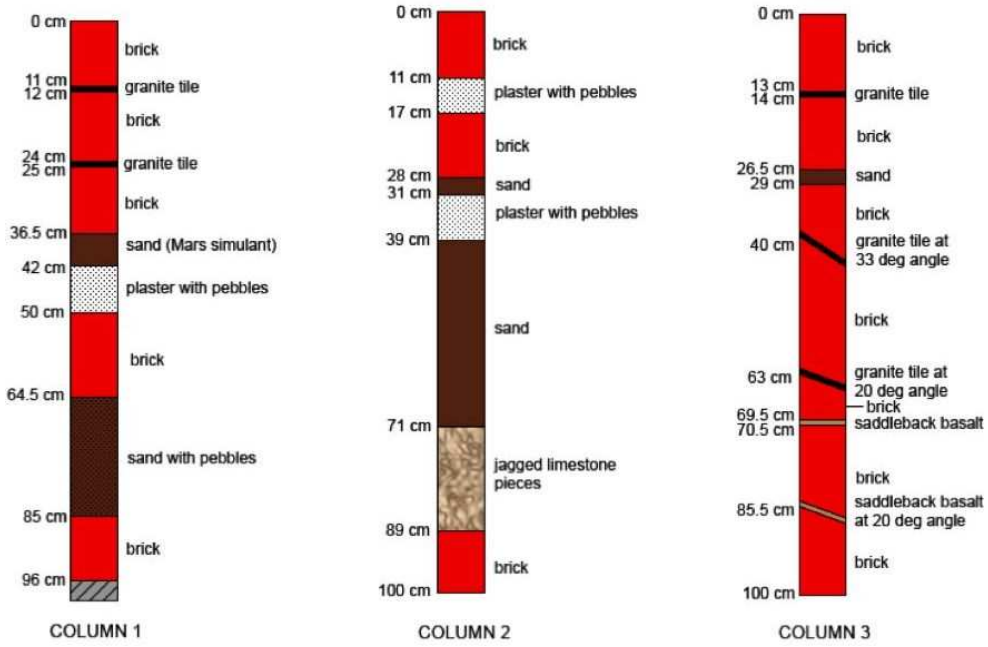

Figure 112: Specimen Column Composition for JPL Tests & Demonstration.

and capabilities of the dynamics-based SHM system.

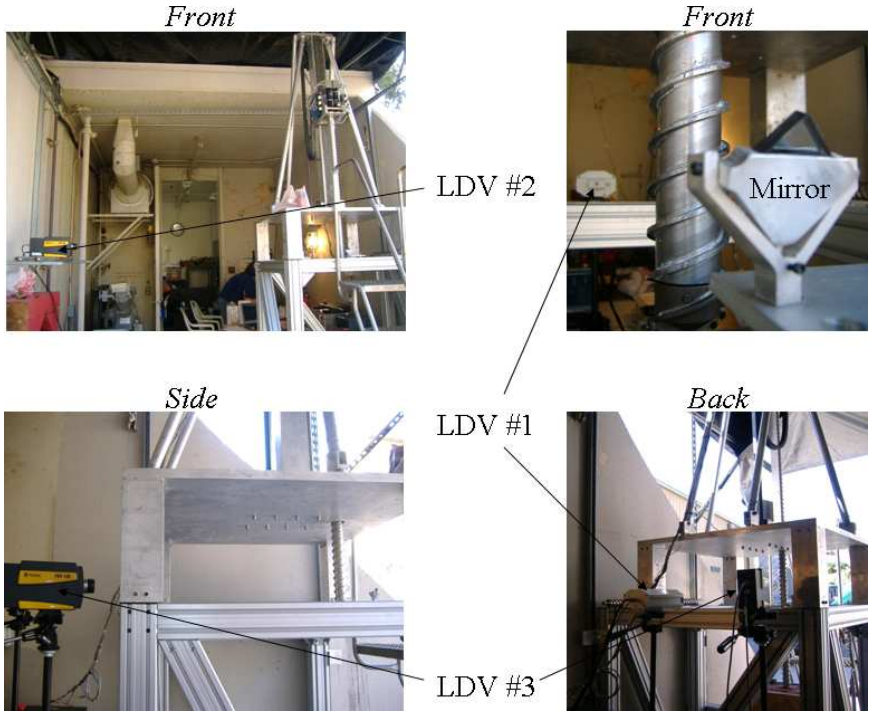

Figure 113: LDV Setup for JPL 2007 Field Test.

The dynamics-based SHM system for this field test was equipped to diagnose five of the six drilling faults (binding, jamming, choking, hard material, and bit inclusion). Figure 114 provides the dynamics-based SHM diagnostics for a drilling test in this field campaign. The hard material fault was encountered several times in this drilling test and a bit inclusion fault was detected immediately following a hard material fault toward the end (highlighted by the dotted circle in Fig. 114). Figure 115 provides (unfiltered) signal responses of the auger tube showing the transition from nominal drilling to a hard material fault (75% hard material probability) to a bit inclusion fault (100% bit inclusion probability). Each signal response is the auto-spectrum in units of $Vrms^2$. During this drilling test, the auger tube length was 2 m and the auger speed fluctuated from 20 to 25 RPM. The on-board sensors showed high auger and bit torque readings and low down-hole speed (ROP - rate of penetration). Based on the diagnostics and sensor data, it was hypothesized that the drill encountered a harder material, which triggered a hard material fault and successful recovery procedure. As the drill broke through the harder material, however, small chunks of the material remained at the bottom of the hole causing a bit inclusion fault.

This field test and demonstration was considered an overall success by the drilling team and NASA. All three specimen columns were successfully drilled for a cumulative drilling depth of 2.96 m. The drill system demonstrated 35 total hours of hands-off automated drilling, and five of the six drilling faults were detected and recovered successfully. Choking, which is commonly associated with wet cuttings not progressing up the auger flutes to the surface, was not detected. These blind and reproducible tests were a rigorous mean to demonstrate and verify the fully integrated autonomous drill system's capabilities. These tests also suggested that the SHM may be used to identify the geological composition of the subsurface region.

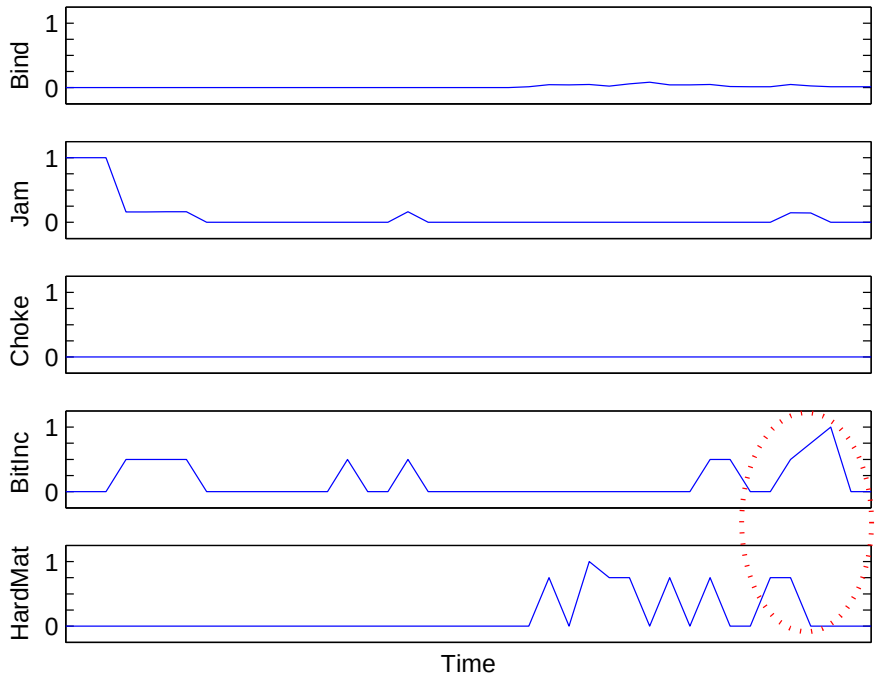

Figure 114: Dynamics-Based SHM Diagnostics for Drilling Test at JPL, 2007.

7.3 Devon Island 2008

The third field test was conducted at Devon Island, Canada, in July 2008. The drilling site, however, was changed to a location atop one of a group of paleo-hydrothermal chimneys believed to be along the original edge of the impact crater melt sheet [65]. A moderate- to low-temperature hydrothermal system was generated at Haughton by the interaction of groundwater with the hot impact melt breccia that filled the interior of the crater [114]. Hydrothermal systems are of significant interest because they may have provided habitats for the origin and evolution of early life on Earth and possibly other planets, and they have also played an important role in the formation of many different types of mineral and ore deposits. This field campaign joined drilling automation experiments and demonstration with subsurface sample acquisition at a Haughton Crater paleo-hydrothermal site, which were submitted for further analysis and studies by NASA and CSA geologists and scientists. Figure 116

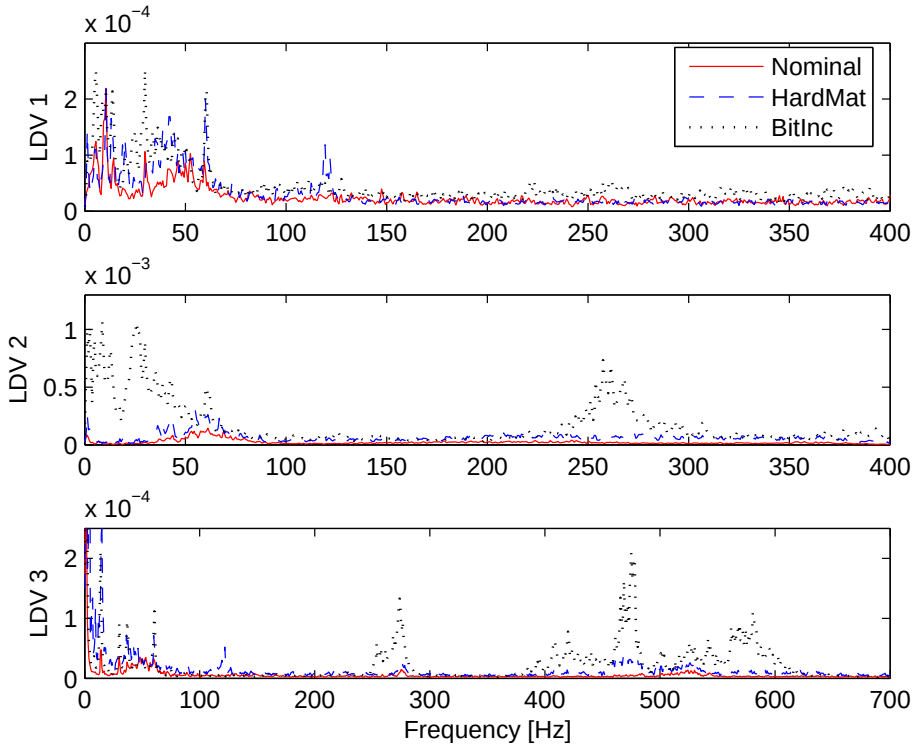

Figure 115: Dynamic Response of Drill Auger Tube through Nominal, Hard Material, and Bit Inclusion Drilling Conditions.

provides photographs of the hydrothermal drill site and the assembled drill system for this field test.

Figure 116: Drill Tent and System at Haughton Paleo-Hydrothermal Site, Devon Island, July 2008.

The objectives of this field test were to integrate and test the upgraded Contingent Executive, which had been redesigned in the new simple plan execution language for

autonomy applications, PLEXIL, drill at a location with hydrothermal vents to a depth of two meters, and collect subsurface samples at approximately every 25 to 50 cm for further geological analysis. Updates to the diagnostic modules based on the previous field tests and further laboratory tests were also implemented.

PLEXIL, which stands for Plan Execution Interchange Language, is designed specifically for flexible and reliable command execution and is more expressive than command sequencing languages currently used on space missions [159]. The previous Contingent Executive used the Contingent Rover Language (CRL), which was designed to serve as the communication medium between the ground operations team and a planetary rover [25].

Three LDV sensors were again used for this field test (Fig. 117). Similar to the JPL tests and demonstration, two lasers were placed directly to the front (Metro-500, labeled as LDV #1) and side (PDV-100, labeled as LDV #2) of the drill, and the third LDV sensor (second PDV-100, labeled as LDV #3) was positioned between the front and side of the drill and the laser beam was offset by a laser-quality mirror to capture the signal in the axial direction.

The dynamics-based SHM system for this field test was equipped to diagnose all six expected drilling faults. In addition to the Neural Network predictions based on the current drill signal and heuristic filters, a boundary condition (BC) based system was implemented to provide rapid-response diagnostics purely based on the current telemetry readings. To capture accurate measurements from the LDV sensors, the signal response is recorded and averaged, which produces diagnostics from the SHM system approximately every 20-25 seconds. As some drilling faults can occur instantaneously, in particular jamming, a parallel system was developed to analyze the drill telemetry for any sudden abnormal changes that breached or exceeded the drill system limitations.

An example of the diagnostics produced by the parallel BC-based and signal-based

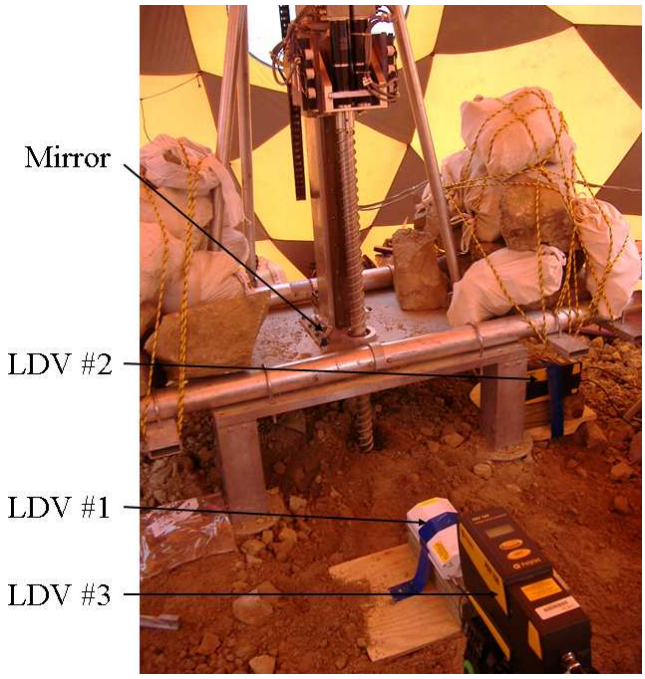

Figure 117: LDV Setup for Devon 2008 Field Test.

(NN) systems for a drilling operation during this field test is provided in Fig. 118. From this example, it was evident that the parallel systems were most often in agreement. However, due to the delay in the signal-based diagnostics, there were some delays in the signal-based diagnostics to detect a fault (false negatives) or to detect that a potential fault was alleviated through nominal drilling operations (false positives). The BC-based system provided an additional heuristic filter for the dynamics-based diagnostics and a means for triggering fault conditions immediately if a drilling parameter breached an unsafe operating threshold.

In Fig. 118, it is also evident that the hard material (HM) fault was triggered several times during this drilling operation. The first instance where the hard material fault was detected and a recovery procedure was completed is indicated in Fig. 118 and Fig. 119 (telemetry readings from drill sensors), and Fig. 120 provides the (unfiltered) signal response of the drill auger tube from LDV #2 just before and at the hard material fault detection. When the hard material fault was triggered, the Contingent

Executive paused the drilling plan and proceeded with the recovery procedure for hard material faults: auger speed was lowered from 40 RPM to 20 RPM, and the down-hole force was increased. This is evident in Fig. 118 where the hard material diagnostic probability decreases throughout the recovery procedure until the fault is no longer detected. The binding fault diagnostic throughout this recovery procedure is also notable. Due to the lower auger speeds and high down-hole force, binding, or binding-like, conditions can be experienced.

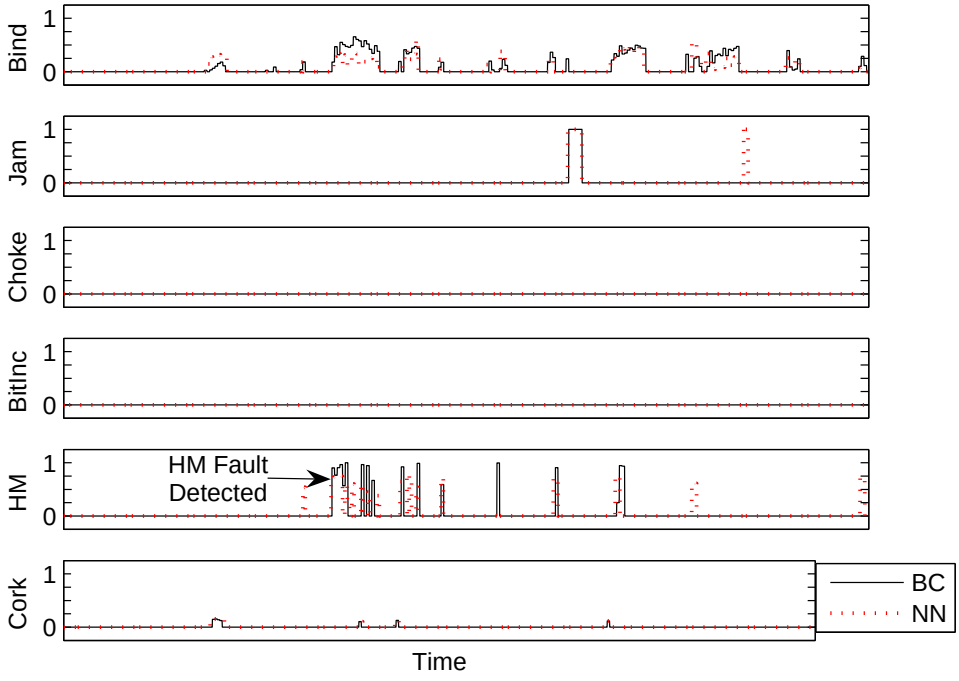

Figure 118: Example of Dynamics-Based SHM System Diagnostics.

This field test campaign was considered another success for the drilling team and the developed dynamics-based SHM system. A total of 32 hours of autonomous, hands-off drilling was accomplished over five days, and a total drill depth of 2.02 m was achieved. Two of the three diagnostic modules (rule-based and dynamics-based SHM) were used in parallel and demonstrated robust and reliable monitoring of the drilling operation, and five of the six drilling faults were encountered, detected, and

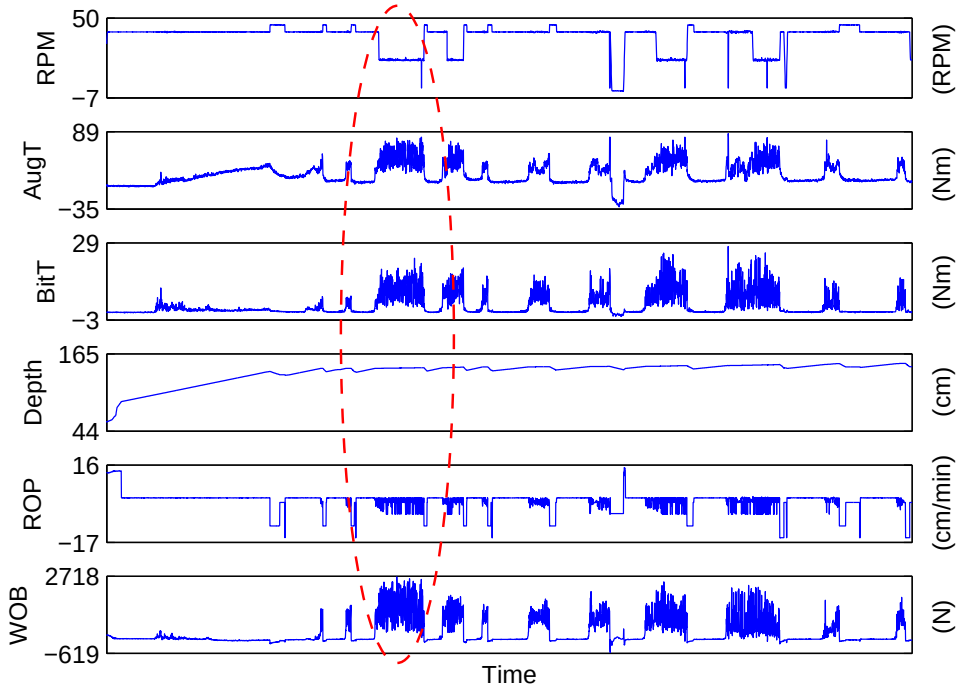

Figure 119: Example of Drill Telemetry Readings (corresponding to diagnostics in Figure 118).

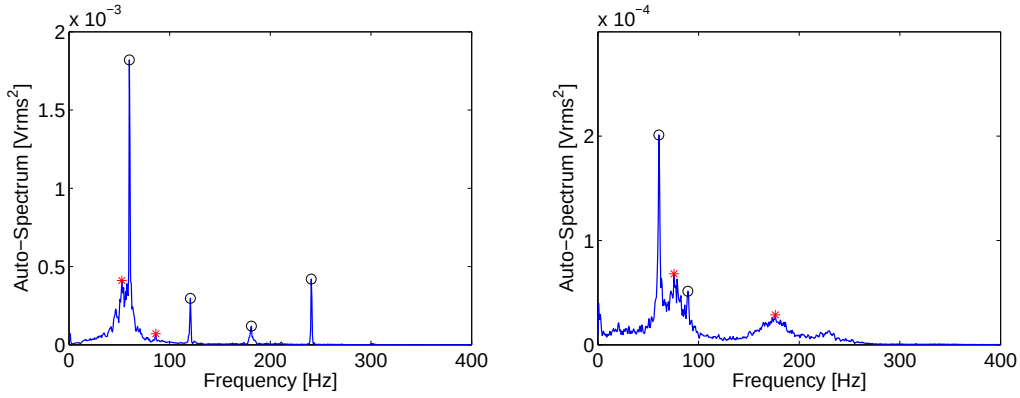

(a) Before HM Fault (b) During HM Fault

Figure 120: Dynamic Response of Drill Auger Tube Through a Hard Material Fault.

recovered successfully [65]. The BC-based system proved to be a reliable and beneficial addition to the dynamics-based SHM system, and the improved system was able to accurately predict all drilling fault conditions with even fewer false positives than previous field tests.

CHAPTER VIII

CONCLUSION & FUTURE WORK

An autonomous, real-time dynamics-based structural health monitoring system has been designed and developed in this thesis work. This system consists of:

1. *The drill motor system as an internal actuator for exciting the dynamic response of the drill.* This allows the dynamic response to be measured while the drill is in operation without the need for external actuators. Not requiring external actuators to excite the drill system saves on manufacturing time and costs and eliminates any mass-loading effects due to attached actuators.

2. *Fixed-point LDV sensors to capture the dynamic response of the drill system.* Using LDV sensors for this application has been very advantageous. Compared with more traditional contact-based sensors (such as accelerometers), LDV sensors have much position flexibility and can be isolated from the dynamic system to be measured, which eliminates any mass-loading affects and allows better comparison with theoretical models. They do not require any of the limited buslines in the drill auger tube, which saves on manufacturing cost and time as well. Multi-dimensional measurements using fixed-point LDV sensors has also been demonstrated in this thesis work, indicating the vast measurement capabilities of LDV sensors and great reduction costs compared with other measurement setups and sensor types to capture the same multi-dimensional measurements.

3. *Developed frequency filter to remove the harmonic gear mesh frequencies from the recorded signal.* This signal filter removes incremental frequencies (produced

by the drill's gear mesh system whenever the drill is rotating) that can interfere with the signal analysis and affect the results and diagnostics of the SHM technique. The developed filter procedure determines the location of these incremental frequencies based on the current rotating (angular) speed of the drill and uses a Chebyshev Type I filter to remove the frequencies from the collected signal before it is analyzed further.

4. *Developed structural dynamic models for all expected drilling conditions.* These models were designed and evaluated using variational methods and Euler-Bernoulli beam theory. Specific drilling parameters (axial velocity, angular velocity, compressive tip load, and complex geometry) were initially analyzed and determined to have negligible effects on the dynamic characteristics of the drill auger tube within the design operations of the drill system. The baseline model (non-operational drill) and nominal drilling model were also 'tweaked' using the results from modal analysis experiments on the drill auger tube to best match the theoretical models with the real system. Lastly, each drilling fault was carefully analyzed to determine what changes in boundary conditions would best represent each fault and the theoretical model was developed accordingly.

5. *Automated signal analysis algorithm to determine the current auger frequencies.* This algorithm uses a defined frequency domain and other specifications to examine the collected signal and determine the first two natural frequencies of the drill auger tube. The frequency domain is defined using the current drill depth and a NN that has been trained to compare drill depths with the minimum possible frequency (from choking fault model) and maximum possible frequency (from jamming fault model).

6. *Trained Neural Networks to compare the current natural frequencies of the drill auger tube with the recorded frequencies from the structural dynamic models.*

Neural Networks provide a rapid-response method for determining which drilling fault model (if any) best represents the current auger frequencies and to what extent. The output of the trained Neural Networks is the probability of each drilling fault, and a heuristic filter is used to compare the NN results with the current drill telemetry to eliminate false positives and more accurately predict the correct diagnostic (i.e. fault mode).

7. *An automation procedure and the corresponding software to create a complete autonomous dynamics-based SHM system.* From collecting the dynamic signal to producing the SHM diagnostics to relaying those diagnostics to the drill Executive computer, this procedure enables a complete hands-off operation and interfaces with the drill Executive.

The developed SHM system has met all formulated thesis objectives and the specified requirements for interplanetary exploration missions, and it has proven to be a valuable addition to the health monitoring procedure for the DAME prototype drill in three field tests.

8.1 Research Contributions

This thesis work provides research contributions that extend to a class of rotating flexible structures, including drill systems. The formulated SHM method also demonstrates advancements to the SHM industry that can be applied to drilling applications (both interplanetary and terrestrial) and future space missions. These contributions include the following:

1. *The design and development of an autonomous, real-time SHM method that has been demonstrated on a real structural system in its operating environment with minimal sensors.*

Many of the recommendations made by state-of-the-art reviews on SHM techniques [32, 53, 57, 146] have been addressed and met in this thesis work. The number and location of sensors have been limited due to the vast flexibility and capabilities of LDV technology and sensors and by using the natural frequencies (compared with mode shapes, mode shape curvatures, etc.) of the drill auger tube to determine the condition of the drilling operation. All modal analysis experiments have been completed on the actual drill system, and the successful field campaigns have validated the SHM technique to accurately monitor the health of the drill system in its operating environment. The SHM technique is autonomous, eliminating human involvement and error in the analysis of the drilling condition. Lastly, as the produced diagnostics are probabilities of each drilling fault, this SHM technique allows for preemptive action by the drill Executive computer before a fault occurs or before a fault significantly affects the drilling operation.

2. *The validation and advantages of LDV sensors in SHM methods have been demonstrated through modal analysis experiments, including multi-dimensional measurements.*

   Having much position flexibility and not requiring any of the limited bus-lines in the drill auger tube, LDV sensors are the ideal sensor type for collecting measurements from an interplanetary subsurface drill prototype compared with traditional contact-based sensors. Accurate measurements of the drill auger tube under various conditions have been captured by fixed-point LDV sensors, and these were the only sensor type used during the three field tests. Multi-dimensional measurements using one fixed-point LDV sensor has also been demonstrated. This has major implications for SHM techniques because it can greatly minimize costs of multi-dimensional measurements and provide additional information regarding the dynamic characteristics of a structural

system.

3. *The complete analysis of complex structural dynamic models.*

   The affects of various drilling parameters on the dynamic characteristics of the drill auger tube have been analyzed using complex structural dynamic models. Although the drilling parameters were neglected in the final models of the drill auger tube, limitations of these assumptions have been described.

4. *The demonstration of automated structural health monitoring for rotating flexible structures requiring real-time controls with focus on drilling applications.*

   The developed SHM technique is applicable for rotating flexible structures that require real-time controls and operation, and the formulated signal filter allows the analysis of the ambient response of rotating structures with harmonic excitation. The developed SHM is also applicable to any drilling system and operation, both terrestrial and interplanetary. The structural dynamic models can be easily modified for a different drill system, and the SHM technique can provide an automated and sophisticated health monitoring technique for the oil and other drilling industries.

5. *The demonstration of structural health monitoring for future space missions.*

   Adhering to the design requirements for an interplanetary subsurface drill system and validating the developed SHM technique in three separate field tests, structural health monitoring for interplanetary exploration systems has been demonstrated in this thesis work. This implies that SHM methods can be used for future space missions and will be a valuable addition to any on-board structural and mechanical components.

8.2 Recommendations for Future Work

The following recommendations are made for future research relevant to the thesis work presented.

1. *Extend the SHM technique to include other possible fault conditions and material characterization.* Although the six drilling faults described in this thesis work have been identified as the most common and expected fault conditions, other fault conditions can occur and should be included with the current SHM diagnostics. In particular, diagnostics of a bit failure would be a very valuable addition to the current fault modes. Failure of the drill bits will slow or prevent progress of the drilling operation, and can be a catastrophic event due to supply limitations of space missions. The signal response of the drill can also provide information regarding the health of the gear mesh system and material composition of the subsurface region.

2. *Extend the SHM technique to different interplanetary exploration systems.* As described as a major contribution of this thesis work, the SHM technique has met all of the formulated design requirements for interplanetary exploration missions and can be easily applied to other interplanetary exploration systems. Future research in this area can greatly increase the interest and use of SHM methods in space applications.

3. *Implement drill telemetry information for training fault-diagnostic Neural Networks.* The drill telemetry is currently being used with the formulated heuristic filter as a means for filtering the fault-diagnostic results from the trained Neural Networks (Section 6.2). This telemetry information and the defined thresholds, however, could be used as additional training data for the individual Neural Networks. Using the drill telemetry as additional inputs for the trained Neural Networks could increase the accuracy of the fault-diagnostics produced by the

individual Neural Networks and reduce or eliminate the need for a heuristic filter.

4. *Extend SHM technique for larger drill depths.* As explained in Chapter 5, there are depth limitations to surface-only measurements. For deep drilling missions, particularly oil and other terrestrial drilling operations, this issue of surface measurements and depth limitations needs to be resolved.

5. *More sophisticated techniques for 3D measurements and monitoring are needed.* The use of LDV sensors for multi-dimensional measurements has been demonstrated in this thesis work. However, with fixed mounting systems (such as tripods), these measurements can be time consuming and less practical for certain applications. Development of a mobile and remote user-controlled mounting system would be very valuable to provide easier and faster multi-dimensional measurements.

6. *Further development of laser technology and portability is needed.* Although the LDV sensors used in this research work are portable, they're size and weight is not adequate for spaceflight operations. Further research and development of laser technology and sensors is needed to provide a device that is compatible with interplanetary exploration missions.

7. *Extend SHM technique to include mode shape characteristics.* Although the mode shape characteristics of the drill auger tube were analyzed for the stationary experiments (Section 4.2), mode shapes have not been used in the formulated structural health monitoring technique due to the rapid-response requirement and sensor limitations. Advancements to the scanning LDV technology (specifically the portability of such sensors) and the formulation of more sophisticated measurement techniques using LDV sensors, however, could provide practical means for collecting the dynamic signal of multiple measurement

points along the auger tube in “real-time”. Thus, the mode shapes (and changes to the mode shape characteristics) could be measured and used to further determine the health of the auger tube and drilling operation.

APPENDIX A

LIST OF SYMBOLS

A = Cross-sectional area of elastic beam [m^2]

A^n_{jk} = n^{th} modal residue for system response at point j due to excitation at point k [1/kg]

$\mathbf{A}$ = Simplified matrix for Galerkin's Method $[\mathbf{A}] = \begin{bmatrix} [\mathbf{M}] & [\mathbf{0}] \\ [\mathbf{0}] & [\mathbf{K}] \end{bmatrix}$

$a(j)$ = Actual value of j^{th} Neural Network training data

$a_n(t)$ = n^{th} amplitude modulation of gear meshing vibration

B_i = Constants of state-space solution, $i = 1, 2, ...$ [m]

$\mathbf{B}$ = Simplified matrix for Galerkin's Method $[\mathbf{B}] = \begin{bmatrix} [\mathbf{C}] & [\mathbf{K}] \\ [-\mathbf{K}] & [\mathbf{0}] \end{bmatrix}$

b_f = Length of drill auger tube flanges (cross-section) [m]

$b_n(t)$ = n^{th} phase modulation of gear meshing vibration

$\mathbf{C}$ = Damping matrix [kg/s]

C_B = Non-dimensional rotational spring constant for choking fault model

c = Speed of light [m/s]

c_n = n^{th} component of diagonalized damping matrix using orthogonality property of mode shapes [kg/s]

D = Non-dimensional spring constant for elastic foundation

d = Diameter of added tip mass [m]

d_i = Inner diameter of drill auger tube [m]

d_o = Outer diameter of drill auger tube [m]

E = Modulus of elasticity [Pa]

$e(j)$ = Error of j^{th} Neural Network training data

f = Frequency of a wave source (sound, light, etc.) [Hz]

f' = Observed frequency of a moving wave source [Hz]

f_D = Frequency shift between two moving wave sources [Hz]

$\{F\}$ = Amplitude of external system excitation [N]

$\{f\}$ = Time history of external system excitation [N]

f_M = Frequency of measurement laser beam [Hz]

f_n = n^{th} harmonic frequency of gear meshing system [Hz]

f_R = Frequency of reference laser beam [Hz]

f_r = Gear rotation speed [Hz]

$H(w)$ = Frequency Response Function (FRF) [m/N]

(H_{jk} = FRF for system response at point j due to excitation at point k)

$H(z)$ = Frequency domain function of Chebyshev Type I filter

h_f = Height of drill auger tube flanges (cross-section) [m]

I = Cross-sectional area moment of inertia for simple geometry [m^4]

I_{AA} = Principle cross-sectional area moments of inertia (I_{XX}, I_{YY}) [m^4]

I_{aa} = Local cross-sectional area moments of inertia (I_{xx}, I_{yy}, I_{xy}) [m^4]

I_M = Mass moment of inertia of added tip mass [kg m^2]

J_p = Polar mass moment of inertia [kg m]

K_n = Constant for n^{th} harmonic of lateral deflection

$\mathbf{K}$ = Stiffness matrix [N/m]

k_n = n^{th} component of diagonalized stiffness matrix using orthogonality property of mode shapes [N/m]

L = Length of elastic beam, drill auger tube [m]

L' = Position of binding, jamming, and corkscrewing faults along z-axis [m]

$\mathbf{M}$ = Mass matrix [kg]

M = Added tip mass [kg]

m = Mass per unit length [kg/m]

m_n = n^{th} component of diagonalized mass matrix using orthogonality property of mode shapes [kg]

P = Compressive tip load [N]

$\hat{p}$ = Non-dimensional compressive tip load ($\hat{p} = PL^2/EI$)

$p_i(t)$ = i^{th} weighting functions of lateral displacement in x-direction (u_1) for Galerkin's Method analysis

Q = Number of teeth in gear meshing system

$q_i(t)$ = i^{th} weighting functions of lateral displacement in y-direction (u_2) for Galerkin's Method analysis

R = Non-dimensional rotational inertia variable ($R^2 = \rho I/mL^2$)

S_B = Non-dimensional rotational spring constant for drill supports

S_K = Non-dimensional translational spring constant for drill supports

T = Tensile force due to corkscrewing fault [N]

$\hat{T}$ = Kinetic Energy [N m]

t = Time [s]

$t(j)$ = Target value of j^{th} Neural Network training data

U = State-space solution for lateral deflection [m]

U_A = Lateral deflections along a split axis ($A = L$eft, Middle, Right) [m]

$\vec{U}$ = Displacement field of elastic beam ($\vec{U}(z,t) =< U_x, U_y, U_z >$) [m]

$\hat{U}$ = Strain Energy [N m]

$u_i(z,t)$ = Deflections of elastic beam, $i = 1, 2, 3$ for (x, y, z) axes [m]

$\bar{u}$ = Complex summation of lateral displacements for elastic beam [m] ($\bar{u} = u_1 + iu_2$)

V = Volume of three-dimensional body [m^3]

$\mathbf{V}$ = Simplified displacement vector for Galerkin's Method

$$\left\{\mathbf{V}\right\} = \left\{\dot{p} \quad \dot{q} \quad p \quad q\right\}^T$$

V_L = Magnitude of LDV velocity measurement along laser beam line-of-site

$\hat{W}$ = External Work [N m]

$w(t)$ = Noise in gear meshing vibration signal

$\{X\}$ = Amplitude of system displacement [m]

$\{x\}$ = Time history of system displacement [m]

(x, y, z) = Local coordinate system

Z_B = Non-dimensional rotational spring constant for jamming fault model ($Z_B = \beta_Z L/EI$)

Z_K = Non-dimensional translational spring constant for binding, jamming, and bit inclusion fault models ($Z_K = \kappa_Z L^3/EI$)

α = Eigenvalues of state-space solution (lateral, $\alpha^4 = \omega^2 mL^4/EI$)

β = Eigenvalues of state-space solution (axial , $\beta^2 = \omega_A^2 mL^2/EA$)

β_C = Rotational spring constant for choking fault model [Nm/rad]

β_S = Rotational spring constant for drill supports [Nm/rad]

β_Z = Rotational spring constant for jamming fault model [Nm/rad]

Γ_n = Linear operator for n^{th} eigenvector/mode shape [m]

γ = Real part of equation of motion roots ($\lambda = \gamma + i\psi$)

δ = Non-dimensional position of drilling model elastic foundation along z-axis ($\delta = 1 - \text{depth}/L$)

$\vec{\epsilon}$ = Strain Field ($\vec{\epsilon} =< \epsilon_x, \epsilon_y, \epsilon_z >$)

ζ = Non-dimensional position of binding, jamming, and corkscrewing faults along z-axis ($\zeta = L'/L$)

η = Non-dimensional variable for position along z-axis ($\eta = z/L$)

Θ = Flute twist of helical drill auger tube [rev/m]

θ_i = i^{th} angular position of LDV sensor (2D and 3D experiments)

κ_D = Spring constant for drilling model translational elastic foundation [N/m^2]

κ_S = Translational spring constant for drill supports [N/m]

κ_Z = Translational spring constant for jamming fault model [N/m]

λ = Roots of equation of motion for elastic beam ($\lambda = \gamma \pm i\psi$);
Wavelength of wave source [m]

μ = Non-dimensional added tip mass ($\mu = M/mL$)

ν = Poisson's Ratio

Ξ_n = Amplitude of n^{th} harmonic of gear meshing vibration

$\xi(t)$ = Gear meshing vibration

ρ = Density [kg/m^3]

$\vec{\sigma}$ = Stress Field ($\vec{\sigma} =< \sigma_x, \sigma_y, \sigma_z >$) [Pa]

ς = Viscous damping ratio

τ = Non-dimensional tensile force due to corkscrewing fault ($\tau = TL^2/EI$)

υ_O = Speed of moving object [m/s]

υ_S = Speed of wave source [m/s]

$\bar{\upsilon}$ = Velocity of moving object [m/s]

$\upsilon(t)$ = Axial velocity [m/s]

υ_* = Related to axial velocity of elastic beam ($\upsilon_* = \upsilon/L$) [1/s]

$\hat{\upsilon}$ = Non-dimensional axial velocity ($\hat{\upsilon}^2 = \upsilon_*^2 mL^4/EI$)

Φ_n = Phase angle of n^{th} harmonic of gear meshing vibration [rad]

ϕ_i = i^{th} Admissible functions of lateral displacements for
Galerkin's Method analysis

φ_i = i^{th} angular position of LDV sensor (3D experiments)

χ = Non-dimensional mass moment of inertia of added tip mass
($\chi = I_M/mL^2$)

Ψ_n = n^{th} eigenvector/mode shape of structural dynamic system

ψ = Imaginary part of equation of motion roots ($\lambda = \gamma + i\psi$)

$\Omega(t)$	=	Angular velocity [rad/s]
$\hat{\Omega}$	=	Non-dimensional angular velocity ($\hat{\Omega}^2 = \Omega^2 m L^4/EI$)
ω	=	Frequency (natural frequencies, mesh frequencies, etc.) [rad/s]
ω_n	=	Undamped natural frequency [rad/s]

APPENDIX B

ADDITIONAL THESIS FIGURES

This section provides additional figures of the Drilling Automation for Mars Exploration (DAME) and Mars Astrobiology Research and Technology Experiment (MARTE) drill systems, which were both designed and manufactured by Honeybee Robotics, Spacecraft Mechanisms Corporation.

Figure 121: Sister Drill Projects: MARTE (left) and DAME (right).

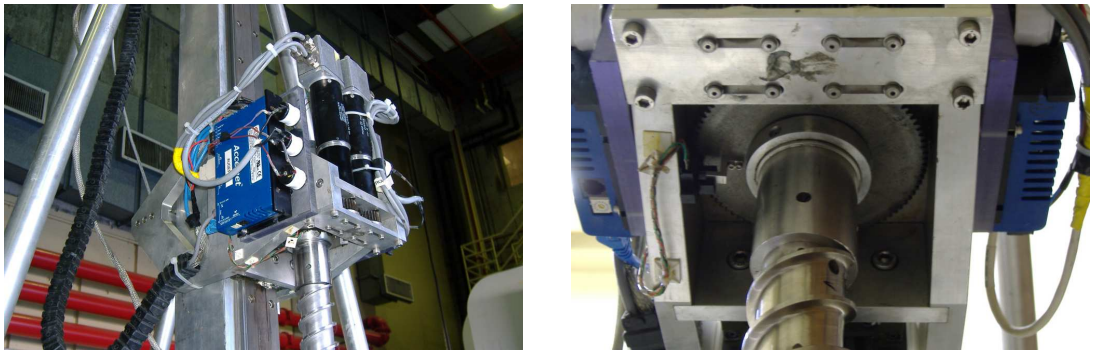

Figure 122: Close up view of DAME Drill Head and Auger Connection.

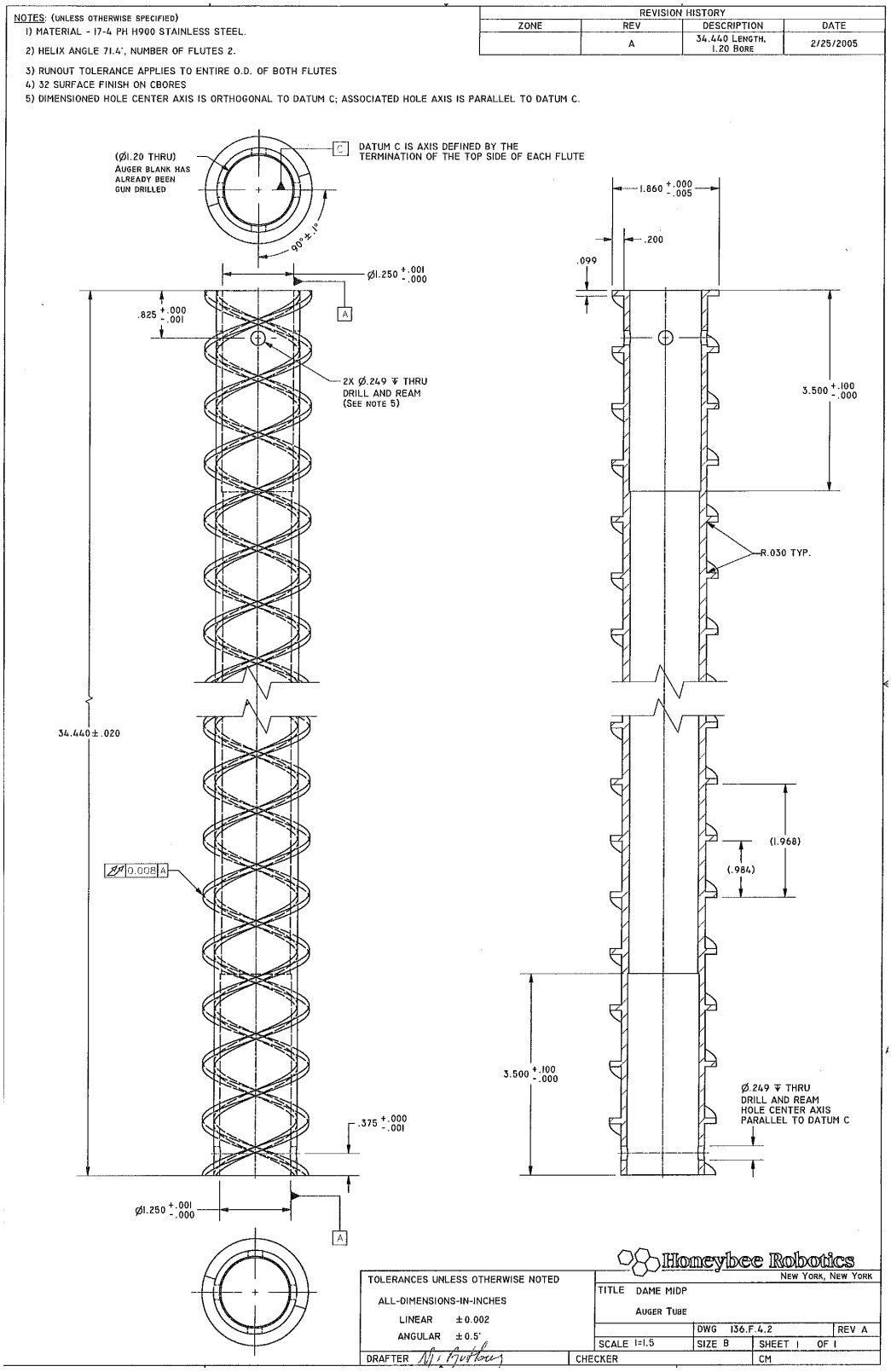

Figure 123: Engineering Drawing of DAME Drill Auger Tube.

APPENDIX C

THEORETICAL DERIVATION OF FREQUENCY RESPONSE FUNCTIONS AND MODAL PARAMETERS

The complete derivation of the Frequency Response Function (FRF) for a finite DOF system with viscous damping is presented in this section. The equation of motion for an N DOF viscously damped system is expressed as

$$[\mathbf{M}]\{\ddot{x}\} + [\mathbf{C}]\{\dot{x}\} + [\mathbf{K}]\{x\} = \{f\} \tag{94}$$

where [**M**], [**C**], and [**K**] are the mass, viscous damping, and stiffness matrices, respectively, $\{x\}$ is the time history of the system's displacement, and $\{f\}$ is the time history of the excitation to the system. To determine the steady-state response, let $f(t) = Fe^{i\omega t}$ and assume a solution of the form

$$x = Xe^{i\omega t}. \tag{95}$$

Equation 94 then becomes

$$-\omega^2[\mathbf{M}]\{X\} + i\omega[\mathbf{C}]\{X\} + [\mathbf{K}]\{X\} = \{F\}\ . \tag{96}$$

Rewriting Eq. 96, we find

$$\{X\} = \left[-\omega^2[\mathbf{M}] + i\omega[\mathbf{C}] + [\mathbf{K}]\right]^{-1}\{F\} \tag{97}$$

$$= H(\omega)\{F\} \tag{98}$$

where $H(\omega)$ is the FRF in terms of the spatial parameters (M, C, and K). To find the FRF in terms of the modal parameters (natural frequencies, damping ratio, and mode shapes), the homogeneous, non-damping solution for Eq. 96 is evaluated:

$$\left[-\omega^2[\mathbf{M}] + [\mathbf{K}]\right]\{X\} = \{0\}\ . \tag{99}$$

For a non-trivial solution, the determinant of the coefficient matrix must be zero, which yields a set of N eigenvalues (i.e. natural frequencies: $\omega_1, \omega_2, ..., \omega_N$) and a corresponding set of N eigenvectors (i.e. mode shapes: $\Psi_1, \Psi_2, ..., \Psi_N$). As the eigenvectors are linearly independent, $\{X\}$ can be rewritten as a linear combination of these N eigenvectors:

$$\{X\} = \sum_{n=1}^{N} \Gamma_n \{\Psi_n\}. \tag{100}$$

Applying this to Eq. 96, we find

$$-\omega^2[\mathbf{M}] \sum_{n=1}^{N} \Gamma_n \{\Psi_n\} + i\omega[\mathbf{C}] \sum_{n=1}^{N} \Gamma_n \{\Psi_n\} + [\mathbf{K}] \sum_{n=1}^{N} \Gamma_n \{\Psi_n\} = \{F\}. \tag{101}$$

Multiplying Eq. 101 by $\{\Psi_s\}^T$ $(s = 1, 2, ..., N)$ and using the orthogonality properties of the mode shapes:

$$\{\Psi_s\}^T [\mathbf{M}] \{\Psi_n\} = \begin{cases} m_n, & n = s \\ 0, & n \neq s \end{cases}, \tag{102}$$

$$\{\Psi_s\}^T [\mathbf{C}] \{\Psi_n\} = \begin{cases} c_n, & n = s \\ 0, & n \neq s \end{cases}, \tag{103}$$

$$\{\Psi_s\}^T [\mathbf{K}] \{\Psi_n\} = \begin{cases} k_n, & n = s \\ 0, & n \neq s \end{cases}, \tag{104}$$

Eq. 101 becomes

$$\left(-\omega^2 m_n + i\omega c_n + k_n\right) \Gamma_n = \{\Psi_n\}^T \{F\}, \tag{105}$$

and therefore

$$\Gamma_n = \frac{\{\Psi_n\}^T \{F\}}{-\omega^2 m_n + i\omega c_n + k_n}. \tag{106}$$

Applying Eq. 106 to Eq. 100, the solution for $\{X\}$ becomes

$$\{X\} = \sum_{n=1}^{N} \frac{\{\Psi_n\}^T \{F\} \{\Psi_n\}}{-\omega^2 m_n + i\omega c_n + k_n}. \tag{107}$$

Writing Eq. 107 for a single input at point k and a single output at point j, we have

$$X_j = \sum_{n=1}^{N} \frac{\Psi_j^n F_k \Psi_k^n}{-\omega^2 m_n + i\omega c_n + k_n}\,,$$

$$H_{jk} = \frac{X_j}{F_k} = \sum_{n=1}^{N} \frac{\Psi_j^n \Psi_k^n / m_n}{(-\omega^2 + i2\varsigma\omega\omega_n + \omega_n^2)}$$

$$= \sum_{n=1}^{N} \frac{A_{jk}^n}{(\omega_n^2 + i2\varsigma\omega\omega_n - \omega^2)}\,, \tag{108}$$

where H_{jk} is the FRF for an excitation at point k and the system response at point j, A_{jk}^n is the modal residue, ω_n is the undamped natural frequency, ς is the viscous damping ratio, and ω is the damped natural frequency. Equation 108 is the theoretical model used to evaluate the FRF data obtained in experiments and extract the modal properties of a structure.

Evaluating the free-response ($f = 0$) of a viscously damped system and assuming $N = 1$, Eq. 96 becomes

$$-\omega^2 + i2\varsigma\omega\omega_n + \omega_n^2 = 0, \tag{109}$$

where

$$\omega_n^2 = \frac{K}{M}\,, \quad 2\varsigma\omega_n = \frac{C}{M}\,.$$

Solving for ω and assuming an underdamped system ($0 < \varsigma < 1$), Eq. 95 becomes

$$x(t) = e^{-\varsigma\omega_n t}\left[X_1 \cos\left(\omega_n\sqrt{1-\varsigma^2}\,t\right) + X_2 \sin\left(\omega_n\sqrt{1-\varsigma^2}\,t\right)\right]. \tag{110}$$

The damped frequency (ω_d) is therefore

$$\omega_d = \omega_n\sqrt{1-\varsigma^2}. \tag{111}$$

From Eq. 111, it is seen that $\omega_d \approx \omega_n$ when $\varsigma \approx 0$. Thus, for simplicity, it is assumed in this thesis work that the damping coefficient of the auger tube is small, and the natural frequencies are therefore the peaks in the dynamic response of the drill auger tube.

APPENDIX D

THE DOPPLER EFFECT

The Doppler effect (or Doppler shift), named after the Austrian physicist Christian Johann Doppler (1803-1853), is the change in the frequency of a wave (light, sound, etc.) for an observer moving relative to the source of the wave [137] (Fig. 124).

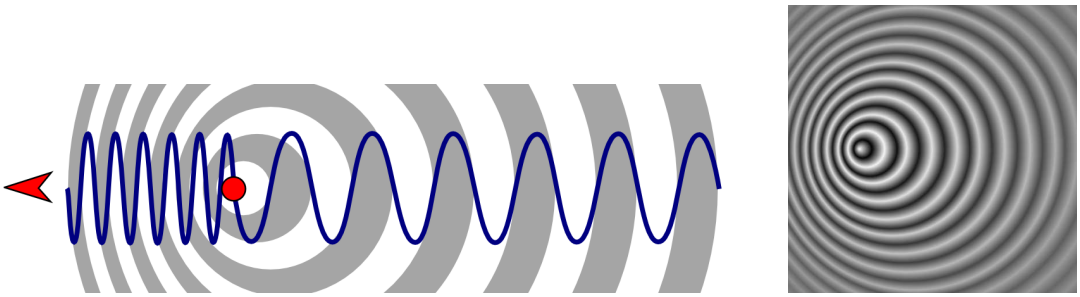

Figure 124: The Doppler Effect [6].

The frequency shift sensed by an observer at rest with respect to the light source and due to scattering by the moving object can be separated into two parts: the scattering object moving with respect to the source and the motion of the scattering object relative to the observer [148]. Assuming the object is moving away from a stationary source, the frequency observed by the object is

$$f' = \left(1 - \frac{v_O}{c}\right) f \tag{112}$$

where v_O is the speed of the moving object, c is the speed of light ($\lambda = c/f$), f and λ are the frequency and wavelength of the source, and the negative sign is used because the object is moving away from the source. Now let's assume the source is in motion relative to an observer at rest. As the source moves toward the observer, the wavelength is shortened by v_S/f where v_S is the speed of the source. The frequency

heard by the observer is therefore

$$f' = \frac{c}{\lambda'} = \frac{c}{\lambda - \frac{v_S}{f}} = \left(\frac{1}{1 - \frac{v_S}{c}}\right) f. \tag{113}$$

Combining the two cases (i.e. the object moving away from the source and the source moving toward the object), the observed frequency is

$$f' = \left(\frac{1 - \frac{v_O}{c}}{1 - \frac{v_S}{c}}\right) f. \tag{114}$$

Rewriting Eq. 114 and assuming $v_S << c$, the total frequency shift (Δf) is

$$\begin{aligned} \Delta f = f' - f &= \left(\frac{1 - \frac{v_O}{c}}{1 - \frac{v_S}{c}}\right) f - f \\ &= \frac{\left(1 - \frac{v_O}{c}\right) f - \left(1 - \frac{v_S}{c}\right) f}{\left(1 - \frac{v_S}{c}\right)} \\ &= \frac{v_S - v_O}{\lambda}. \end{aligned} \tag{115}$$

Laser Doppler Velocimeter (LDV) sensors are interferometer devices that measure the velocity of a moving object or surface using the Doppler effect principle [5, 141, 148]. LDV sensors use two laser beams (a reference beam and measurement beam), and the difference (or interference) between these laser beams yields the Doppler shift due to the motion of the moving object:

$$\begin{aligned} f_D &= f_M - f_R \\ &= \frac{2\bar{v}}{\lambda} \end{aligned} \tag{116}$$

where f_D is the measured frequency shift, f_M and f_R are the frequencies of the measurement and reference beams, λ is the wavelength of the emitted laser beam, and $\bar{v}$ is the velocity of the moving object/surface.

APPENDIX E

GALERKIN'S METHOD DERIVATION

The complete derivation of the equations of motion for a beam in bending with axial velocity, angular velocity, compressive tip load, and a complex geometry using Galerkin's Method is presented in this section. Beginning with the equation of motion for $u_1(z,t)$ (Eq. 44) and assuming the solution forms [80]

$$u_1(z,t) = \sum_{j=1}^{N} p_j(t)\phi_j(z)\,,$$
$$u_2(z,t) = \sum_{j=1}^{N} q_j(t)\phi_j(z)\,,$$

Eq. 44 becomes

$$\begin{aligned}
&\frac{d^2}{dz^2}\left(EI_{yy}\sum_{j=1}^{N} p_j\frac{d^2\phi_j}{dz^2} + EI_{xy}\sum_{j=1}^{N} q_j\frac{d^2\phi_j}{dz^2}\right) - \frac{d}{dz}\left(\rho I_{yy}\sum_{j=1}^{N}\frac{d^2p_j}{dt^2}\frac{d\phi_j}{dz}\right.\\
&\quad\left. + \rho I_{xy}\sum_{j=1}^{N}\frac{d^2q_j}{dt^2}\frac{d\phi_j}{dz}\right) - \frac{d}{dz}\left(J_p\Omega\sum_{j=1}^{N}\frac{dq_j}{dt}\frac{d\phi_j}{dz}\right) + P\sum_{j=1}^{N} p_j\frac{d^2\phi_j}{dz^2}\\
&\quad + m\left(\sum_{j=1}^{N}\frac{d^2p_j}{dt^2}\phi_j + \upsilon^2\sum_{j=1}^{N} p_j\frac{d^2\phi_j}{dz^2} - \Omega^2\sum_{j=1}^{N} p_j\phi_j\right.\\
&\quad\left. + 2\upsilon\sum_{j=1}^{N}\frac{dp_j}{dt}\frac{d\phi_j}{dz} - 2\Omega\sum_{j=1}^{N}\frac{dq_j}{dt}\phi_j - 2\Omega\upsilon\sum_{j=1}^{N} q_j\frac{d\phi_j}{dz}\right) = 0. \qquad (117)
\end{aligned}$$

Multiplying by $\phi_i(z)$ $(i = 1, 2, ..., N)$ and integrating over the length of the beam

$(0 < z < L)$, Eq. 117 becomes

$$\int_0^L \phi_i \Bigg\{ \frac{d^2}{dz^2}\left(EI_{yy}\sum_{j=1}^{N} p_j \frac{d^2\phi_j}{dz^2} + EI_{xy}\sum_{j=1}^{N} q_j \frac{d^2\phi_j}{dz^2}\right) - \frac{d}{dz}\left(\rho I_{yy}\sum_{j=1}^{N}\frac{d^2p_j}{dt^2}\frac{d\phi_j}{dz} + \rho I_{xy}\sum_{j=1}^{N}\frac{d^2q_j}{dt^2}\frac{d\phi_j}{dz}\right) - \frac{d}{dz}\left(J_p\Omega\sum_{j=1}^{N}\frac{dq_j}{dt}\frac{d\phi_j}{dz}\right) + P\sum_{j=1}^{N} p_j\frac{d^2\phi_j}{dz^2} + m\Bigg(\sum_{j=1}^{N}\frac{d^2p_j}{dt^2}\phi_j + \upsilon^2\sum_{j=1}^{N} p_j\frac{d^2\phi_j}{dz^2} - \Omega^2\sum_{j=1}^{N} p_j\phi_j + 2\upsilon\sum_{j=1}^{N}\frac{dp_j}{dt}\frac{d\phi_j}{dz} - 2\Omega\sum_{j=1}^{N}\frac{dq_j}{dt}\phi_j - 2\Omega\upsilon\sum_{j=1}^{N} q_j\frac{d\phi_j}{dz}\Bigg) = 0 \Bigg\} dz. \quad (118)$$

Reversing the order of integration and summation and non-dimensionalizing by the length of the beam, Eq. 118 is simplified to

$$\sum_{j=1}^{N}\int_0^\eta \Bigg\{ \frac{\phi_i}{L^4}\left(EI_{yy}p_j\phi_j'' + EI_{xy}q_j\phi_j''\right)'' - \frac{\phi_i}{L^2}\left(\rho I_{yy}\ddot{p}_j\phi_j' + \rho I_{xy}\ddot{q}_j\phi_j'\right)' - \frac{\phi_i}{L^2}\left(J_p\Omega\dot{q}_j\phi_j'\right)' + \frac{P}{L^2}p_j\phi_i\phi_j'' + m\Bigg(\ddot{p}_j\phi_i\phi_j + \frac{\upsilon^2}{L^2}p_j\phi_i\phi_j'' - \Omega^2 p_j\phi_i\phi_j + 2\frac{\upsilon}{L}\dot{p}_j\phi_i\phi_j' - 2\Omega\dot{q}_j\phi_i\phi_j - 2\Omega\frac{\upsilon}{L}q_j\phi_i\phi_j'\Bigg)\Bigg\} d\eta = 0 \quad (119)$$

where

$$(\ )' = \frac{d}{d\eta},\ (\dot{}) = \frac{d}{dt},\ \eta = \frac{z}{L},\ \phi = \phi(\eta).$$

Integrating the first four terms and υ^2 term by parts and bringing all time dependent variables out of the integral, the equation of motion becomes

$$\sum_{j=1}^{N}\Bigg\{ p_j\int_0^\eta \frac{EI_{yy}}{L^4}\phi_i''\phi_j''d\eta + q_j\int_0^\eta \frac{EI_{xy}}{L^4}\phi_i''\phi_j''d\eta + \ddot{p}_j\int_0^\eta \frac{\rho I_{yy}}{L^2}\phi_i'\phi_j'd\eta + \ddot{q}_j\int_0^\eta \frac{\rho I_{xy}}{L^2}\phi_i'\phi_j'd\eta + \dot{q}_j\int_0^\eta \frac{J_p\Omega}{L^2}\phi_i'\phi_j'd\eta - p_j\int_0^\eta \frac{P}{L^2}\phi_i'\phi_j'd\eta + \ddot{p}_j\int_0^\eta m\phi_i\phi_j d\eta - p_j\int_0^\eta \frac{m\upsilon^2}{L^2}\phi_i'\phi_j'd\eta - p_j\int_0^\eta m\Omega^2\phi_i\phi_j d\eta + \dot{p}_j\int_0^\eta 2\frac{m\upsilon}{L}\phi_i\phi_j'd\eta - \dot{q}_j\int_0^\eta 2m\Omega\phi_i\phi_j d\eta - q_j\int_0^\eta 2\frac{m\Omega\upsilon}{L}\phi_i\phi_j'd\eta\Bigg\} = 0\,. \quad (120)$$

Lastly, by grouping like terms and bringing all terms independent of η outside the integral, Eq. 120 can be simplified to

$$\sum_{j=1}^{N}\Bigg\{\ddot{p}_j\Big[mM_{ij}^1+\rho M_{ij}^2\Big]+\ddot{q}_j\Big[\rho M_{ij}^3\Big]+\dot{p}_j\Big[2m\upsilon M_{ij}^5\Big]+\dot{q}_j\Big[\Omega M_{ij}^6-2m\Omega M_{ij}^1\Big] + p_j\Big[K_{ij}^1-(P+m\upsilon^2)M_{ij}^7-m\Omega^2M_{ij}^1\Big]+q_j\Big[K_{ij}^2-2m\Omega\upsilon M_{ij}^5\Big]\Bigg\}=0, \quad (121)$$

where

$$\mathbf{M}_{ij}^1=\int_0^1\phi_i(\eta)\phi_j(\eta)\,d\eta\,, \qquad \mathbf{M}_{ij}^2=\frac{1}{L^2}\int_0^1 I_{yy}\frac{d\phi_i(\eta)}{d\eta}\frac{d\phi_j(\eta)}{d\eta}\,d\eta\,,$$
$$\mathbf{M}_{ij}^3=\frac{1}{L^2}\int_0^1 I_{xy}\frac{d\phi_i(\eta)}{d\eta}\frac{d\phi_j(\eta)}{d\eta}\,d\eta\,, \qquad \mathbf{M}_{ij}^4=\frac{1}{L^2}\int_0^1 I_{xx}\frac{d\phi_i(\eta)}{d\eta}\frac{d\phi_j(\eta)}{d\eta}\,d\eta\,,$$
$$\mathbf{M}_{ij}^5=\frac{1}{L}\int_0^1\phi_i(\eta)\frac{d\phi_j(\eta)}{d\eta}\,d\eta\,, \qquad \mathbf{M}_{ij}^6=\frac{1}{L^2}\int_0^1 J_p\frac{d\phi_i(\eta)}{d\eta}\frac{d\phi_j(\eta)}{d\eta}\,d\eta\,,$$
$$\mathbf{M}_{ij}^7=\frac{1}{L^2}\int_0^1\frac{d\phi_i(\eta)}{d\eta}\frac{d\phi_j(\eta)}{d\eta}\,d\eta\,, \qquad \mathbf{K}_{ij}^1=\frac{E}{L^4}\int_0^1 I_{yy}\frac{d^2\phi_i(\eta)}{d\eta^2}\frac{d^2\phi_j(\eta)}{d\eta^2}\,d\eta\,,$$
$$\mathbf{K}_{ij}^2=\frac{E}{L^4}\int_0^1 I_{xy}\frac{d^2\phi_i(\eta)}{d\eta^2}\frac{d^2\phi_j(\eta)}{d\eta^2}\,d\eta\,, \qquad \mathbf{K}_{ij}^3=\frac{E}{L^4}\int_0^1 I_{xx}\frac{d^2\phi_i(\eta)}{d\eta^2}\frac{d^2\phi_j(\eta)}{d\eta^2}\,d\eta\,.$$

The same procedure can be completed for Eq. 45, and the two discretized equations of motion can be written in matrix form as

$$[\mathbf{M}]\begin{Bmatrix}\ddot{p}\\ \ddot{q}\end{Bmatrix}+[\mathbf{C}]\begin{Bmatrix}\dot{p}\\ \dot{q}\end{Bmatrix}+[\mathbf{K}]\begin{Bmatrix}p\\ q\end{Bmatrix}=\begin{Bmatrix}0\\ 0\end{Bmatrix}, \quad (122)$$

where

$$[\mathbf{M}]=\begin{bmatrix}m[\mathbf{M}]^1+\rho[\mathbf{M}]^2 & \rho[\mathbf{M}]^3\\ \rho[\mathbf{M}]^3 & m[\mathbf{M}]^1+\rho[\mathbf{M}]^4\end{bmatrix}, \quad (123)$$

$$[\mathbf{C}]=\begin{bmatrix}2m\upsilon[\mathbf{M}]^5 & \Omega[\mathbf{M}]^6-2m\Omega[\mathbf{M}]^1\\ 2m\Omega[\mathbf{M}]^1-\Omega[\mathbf{M}]^6 & 2m\upsilon[\mathbf{M}]^5\end{bmatrix}, \quad (124)$$

$$[\mathbf{K}]=\begin{bmatrix}[\mathbf{K}]^1-(P+m\upsilon^2)[\mathbf{M}]^7-m\Omega^2[\mathbf{M}]^1 & [\mathbf{K}]^2-2m\upsilon\Omega[\mathbf{M}]^5\\ [\mathbf{K}]^2+2m\upsilon\Omega[\mathbf{M}]^5 & [\mathbf{K}]^3-(P+m\upsilon^2)[\mathbf{M}]^7-m\Omega^2[\mathbf{M}]^1\end{bmatrix}, \quad (125)$$

and each matrix ($[\mathbf{M}], [\mathbf{C}], [\mathbf{K}]$) is $2N \times 2N$.

REFERENCES

[1] "ABAQUS Tutorial." http://www.engin.brown.edu/courses/en175/abaqustut/abaqustut.htm, retrieved October 2010.

[2] "Haughton Global Location." http://nematode.unl.edu/crater02.jpg.

[3] "NASA Haughton Crater." http://ti.arc.nasa.gov/tech/asr/intelligent-robotics/haughton-field/.

[4] "National Geographic Photography." http://photography.nationalgeographic.com.

[5] "Polytec." www.polytec.com.

[6] "Your Dictionary." http://images.yourdictionary.com/doppler-effect.

[7] Adams, R. D., Cawley, P., Pye, C. J., and Stone, B. J., "A vibration technique for non-destructively assessing the integrity of structures," *Journal Mechanical Engineering Science*, vol. 20, pp. 93–100, 1978.

[8] Akulenko, L. and Nesterov, S., "Flexural vibrations of a moving rod," *Journal of Applied Mathematics and Mechanics*, vol. 72, pp. 550–560, 2008.

[9] Alam, M., Sedaghati, R., Soucy, Y., and Bhat, R. B., "Analytical and experimental study using output-only modal testing for on-orbit satellite appendages," *Advances in Acoustics and Vibration*, vol. 2009, pp. 1–10, 2009.

[10] Andersen, P., Brincker, R., Peeters, B., Roeck, G. D., Hermans, L., and Kramer, C., "Comparison of system identification methods using ambient bridge test data," in *Proc. of IMAC 17, the International Modal Analysis Conference*, (Kissimmee, FL), February 1999.

[11] Annema, A.-J., *Feed-Forward Neural Networks: Vector Decomposition Analysis, Modelling and Analog Implementation*. Kluwer Academic Publishers, Massachusetts, 1995.

[12] Apetre, N., Ruzzene, M., Hanagud, S., and Gopalakrishnan, S., "A wave-based damage index for the analysis of the filtered response of damaged beams," *Journal of Mechanics of Materials and Structures*, vol. 3, pp. 1605–1623, 2008.

[13] Ayers, J., Ruzzene, M., and Apetre, N., "A wave-filtering displacement-based damage measure," in *Proceedings of 6th IWSHM*, (Stanford University, CA), September 2007.

[14] Baher, H., *Analog and Digital Signal Processing.* John Wiley & Sons Ltd, New York, NY, 2001.

[15] Bai, H., Atiquzzaman, M., and Lilja, D., "Wireless sensor network for aircraft health monitoring," in *1st International Conference on Broadband Networks*, (San Jose, California), October 2004.

[16] Balaban, E., Cannon, H., Narasimhan, S., and Brownston, L. S., "Model-based fault detection and diagnosis system for nasa mars subsurface drill prototype," in *IEEE Aerospace Conference*, (Big Sky, MT), pp. 1–13, March 2007.

[17] Barakat, R., "Transverse vibrations of a moving thin rod," *The Journal of the Acoustical Society of America*, vol. 43, pp. 533–539, 1968.

[18] Basseville, M., Benveniste, A., Goursat, M., Hermans, L., Mevel, L., and der Auweraer, H. V., "Output-only subspace-based structural identification: From theory to industrial testing practice," *Journal of Dynamic Systems, Measurement, and Control*, vol. 123, pp. 668–676, 2001.

[19] Batel, M., Gade, S., Moller, N., and Herlufsen, H., "Ambient response modal analysis on a plate structure," in *Proc. of IMAC 21, the International Modal Analysis Conference*, 2003.

[20] Bauer, H. F., "Vibration of rotating uniform beam, part i: Orientation in the axis of rotation," *Journal of Sound and Vibration*, vol. 72, no. 2, pp. 177–189, 1980.

[21] Bell, J. R. and Rothberg, S. J., "Rotational vibration measurements using laser doppler vibrometry: Comprehensive theory and practical approach," *Journal of Sound and Vibration*, vol. 238, no. 4, pp. 673–690, 2000.

[22] Bendat, J. S. and Piersol, A. G., *Engineering Applications of Correlation and Spectral Analysis.* New York: Wiley, 1993.

[23] Bishop, C. M., *Neural Networks for Pattern Recognition.* New York: Clarendon Press, 1995.

[24] Blacic, J. D., Dreesen, D. S., and Mockler, T. T., "The 3rd dimension of planetary exploration - deep subsurface sampling," in *AIAA Space 2000 Conference and Exposition*, no. AIAA-2000-5301, (Long Beach, CA), September 2000.

[25] Bresina, J. and Washington, R., "Robustness via run-time adaptation of contingent plans," in *AAAI-2001 Spring Symposium: Robust Automony*, 2001.

[26] Brincker, R., Andersen, P., and Moller, N., "An indicator for separation of structural and harmonic modes in output-only modal testing," in *IMAC-XVIII: A Conference on Structural Dynamics*, (San Antonio, TX), February 2000.

[27] Brincker, R., Zhang, L., and Andersen, P., "Modal identification of output-only systems using frequency domain decomposition," *Smart Material and Structures*, vol. 10, pp. 441–445, 2001.

[28] Brown, R. G. and Hwang, P. Y. C., *Introduction to random signals and applied Kalman filtering: with MATLAB exercises and solutions.* Wiley, New York, 1997.

[29] Bucher, I. and Ewins, D. J., "Modal analysis and testing of rotating structures," in *Philosophical Transactions of The Royal Society A*, vol. 359, pp. 61–96, 2001.

[30] C. D. Mote, J., "A study of band saw vibrations," *Journal of The Franklin Institute*, vol. 279, pp. 430–444, June 1965.

[31] Cam, E., Luy, M., Kocaarslan, I., and Taplamacioglu, C., "Defect detection in a cantilever beam from vibration data," tech. rep., Kirikkale University, Dept. Electrical & Electronics, Kirikkale, Turkey, 2002.

[32] Carden, E. P. and Fanning, P., "Vibration based condition monitoring: A review," *Structural Health Monitoring*, vol. 3, no. 4, pp. 355–377, 2004.

[33] Carpenter, G. A., "Neural network models for pattern recognition and associative memory," *Neural Networks*, vol. 2, no. 4, pp. 243–257, 1989.

[34] Castellini, P., Martarelli, M., and Tomasini, E., "Laser Doppler Vibrometery: Development of advanced solutions answering to technology's needs," *Mechanical Systems and Signal Processing*, vol. 20, pp. 1265–1285, 2006.

[35] Castellini, P. and Paone, N., "Development of the tracking laser vibrometer: Performance and uncertainty analysis," *Review of Scientific Instruments*, vol. 71, pp. 4639–4647, December 2000.

[36] Castellini, P. and Revel, G. M., "Laser vibration measurements and data processing for structural diagnostic on composite material," *Review of Scientific Instruments*, vol. 71, no. 1, pp. 207–215, 2000.

[37] Cawley, P. and Adams, R. D., "The location of defects in structures from measurements of natural frequencies," *The Journal of Strain Analysis for Engineering Design*, vol. 14, no. 2, pp. 49–57, 1979.

[38] Chang, C. C., Chang, T. Y. P., Xu, Y. G., and Wang, M. L., "Structural damage detection using an iterative neural network," *Journal of Intelligent Material Systems and Structures*, vol. 11, pp. 32–42, 2000.

[39] Chen, J. C. and Garba, J. A., "Analytical model improvement using modal test results," *AIAA Journal*, vol. 18, no. 6, pp. 684–690, 1980.

[40] Chen, M. L. and Liao, Y. S., "Vibrations of pretwisted spinning beams under axial compressive loads with elastic constrains," *Journal of Sound and Vibration*, vol. 147, no. 3, pp. 497–513, 1991.

[41] Chen, S.-E., Venkatappa, S., Petro, S. H., and GangaRao, H. V., "Damage detection using scanning laser vibrometer," in *Proceedings in Third International Conference on Vibration Measurements by Laser Techniques: Advances and Applications* (Tomasini, E. P., ed.), pp. 473–484, 1998.

[42] Chirlian, P. M., *Signals and Filters*. Van Nostrand Reinhold, 1994.

[43] Choi, M. Y. and Kwon, I. B., "Damage detection system of a real steel truss bridge by neural networks," in *Smart Structures and Materials 2000: Smart Systems for Bridges, Structures and Highways*, (Newport Beach, CA), March 2000.

[44] Choi, S. H., Pierre, C., and Ulsoy, A. G., "Consistent modeling of rotating timoshenko shafts subject to axial loads," *Journal of Vibration and Acoustics*, vol. 114, pp. 249–259, April 1992.

[45] Chondros, T. G., Dimaragonas, A. D., and Yao, J., "Vibration of a beam with a breathing crack," *Journal of Sound and Vibration*, vol. 239, no. 1, pp. 57–67, 2001.

[46] Dalpiaz, G., Rivola, A., and Rubini, R., "Effectiveness and sensitivity of vibration processing techniques for local fault detection in gears," *Mechanical Systems and Signal Processing*, vol. 14, no. 3, pp. 387–412, 2000.

[47] de Noyer, M. P. B., *Tail Buffet Alleviation of High Performance Twin Tail Aircraft using Offset Piezoceramic Stack Actuators and Acceleration Feedback Control*. PhD thesis, Georgia Institute of Technology, 1999.

[48] Demuth, H. and Beale, M., *Neural Network Toolbox User's Guide*. The MathWorks, Inc., Natick, MA, 1992.

[49] Dimaragonas, A. D., "Vibration of cracked structures: A state of the art review," *Engineering Fracture Mechanics*, vol. 55, no. 5, pp. 831–857, 1996.

[50] Dimentberg, F. M., *Flexural Vibrations of Rotating Shafts*. Butterworth & Co., 1961.

[51] Doebling, S. W., Farrar, C. R., Prime, M. B., and Shevitz, D. W., "Damage identification and health monitoring of structural and mechanical systems from changes in their vibration characteristics: A literature review," Tech. Rep. LA-13070-MS, Los Alamos National Laboratory, 1996.

[52] Doebling, S. W. and Farrar, C. R., "Computation of structural flexibility for bridge health monitoring using ambient modal data," in *Proc. of 11th ASCE Engineering Mechanics Conference* (Lin, Y. and Su, T., eds.), (Ft. Lauderdale, FL), pp. 1114–1117, May 1996.

[53] Doebling, S. W., Farrar, C. R., and Prime, M. B., "A summary review of vibration-based damage identification methods," *The Shock and Vibration Digest Journal*, vol. 30, pp. 91–105, 1998.

[54] Drain, L., *The Laser Doppler Technique*. New York: Wiley, 1980.

[55] Drexel, M. V. and Ginsberg, J. H., "Modal overlap and dissipation effects of a cantilever beam with multiple attached oscillators," *Journal of Vibration and Acoustics*, vol. 123, pp. 181–187, 2001.

[56] Duda, R. O., Hart, P. E., and Stock, D. G., *Pattern Classification*. Canada: John Wiley & Sons, Inc., 2001.

[57] Farrar, C. R. and Doebling, S. W., "An overview of modal-based damage identification methods," in *Proceedings of DAMAS Conference*, (Sheffield, UK), June 1997.

[58] Farrar, C. R. and Worden, K., "An introduction to structural health monitoring," in *Philosophical Transactions of The Royal Society A*, 2007.

[59] Fujino, Y., Kaito, K., and Abe, M., "Detection of structural damage by ambient vibration measurements using laser doppler vibrometer," in *Proceedings of the Sixth Annual International Symposium on NDE for Health Monitoring and Diagnostics*, (Newport Beach, USA), 2001.

[60] Gladwell, G. M. L. and Bishop, R. E. D., "The vibration of rotating shafts supported in flexible bearings," *Journal Mechanical Engineering Science*, vol. 1, no. 3, pp. 195–206, 1959.

[61] Glaser, D., Paulsen, G., Zacny, K., Davis, K., Mumm, E., and Glass, B., "Autonomous drills for planetary subsurface access," in *LPI Space Resources Roundtable VIII*, November 2006.

[62] Glass, B., Cannon, H., Hanagud, S., Lee, P., and Paulsen, G., "Drilling automation tests at a Lunar/Mars analog site," in *37th Lunar and Planetary Science Conference*, no. 2300, March 2006.

[63] Glass, B., Cannon, H., Hanagud, S., and Paulsen, G., "Dame: Planetary-prototype drilling automation for subsurface access," *Astrobiology*, vol. 8, pp. 653–664, 2008.

[64] Glass, B., Cannon, H., Stoker, C., and Davis, K., "Robotic and human-tended collaborative drilling automation for subsurface exploration," in *Proc. International Astronautical Congress*, no. IAC-05-A5.2.01, October 2005.

[65] Glass, B., Thompson, S., Hanagud, S., Statham, S., Cohen, J., Lee, P., Osinksi, G., and Huffman, S., "Planetary drill prototype testing at an impact structure palaeo-hydrothermal site," in *40th Lunar and Planetary Science Conference*, 2009.

[66] Glass, B. J. and Hanagud, S., "An ai-based approach to structural damage identification by modal analysis," in *31st AIAA SSDM Conference*, (Long Beach, CA), April 1990.

[67] Glass, B., Christa, S., Hanagud, S., Statham, S., Mukherjee, S., Shirashi, L., and *et al.*, "Planetary drilling automation blind tests," in *39th Lunar and Planetary Science Conference*, March 2008.

[68] Glass, B., Cannon, H., Christa, S., Johnson, J., and Huffman, S., "Executive modular control of heterogeneous spacecraft components and agents," tech. rep., International Astronautical Federation, 2006.

[69] Grieve, R. A. F., "The haughton impact structure: Summary and synthesis of the results of the hiss project," *Meteoritics*, vol. 23, pp. 249–254, 1988.

[70] Groover, C. L., Trethewey, M. W., Maynard, K. P., and Lebold, M. S., "Removal of order domain content in rotating equipment signals by double resampling," *Mechanical Systems and Signal Processing*, vol. 19, pp. 483–500, 2005.

[71] Gudmundson, P., "Eigenfrequency changes of structures due to cracks, notches or other geometrical changes," *Journal of the Mechanics and Physics of Solids*, vol. 30, no. 5, pp. 339–353, 1982.

[72] Gurgoze, M., Dogruoglu, A., and Zeren, S., "On the eigencharacteristics of a cantilevered visco-elastic beam carrying a tip mass and its representation by a spring-damper-mass system," *Journal of Sound and Vibration*, vol. 301, pp. 420–426, 2007.

[73] Gurgoze, M. and Zeren, S., "On the eigencharacteristics of an axially vibrating viscoelastic rod carrying a tip mass and its representation by a single degree-of-freedom system," *Journal of Sound and Vibration*, vol. 294, pp. 388–396, 2006.

[74] Halliwell, N. A., "The laser torsional vibrometer: A step forward in rotating machinery diagnostics," *Journal of Sound and Vibration*, vol. 190, no. 3, pp. 399–418, 1996.

[75] Han, R. P. S. and Zu, J. W.-Z., "Modal analysis of rotating shafts: A body-fixed axis formulation approach," *Journal of Sound and Vibration*, vol. 156, no. 1, pp. 1–16, 1992.

[76] Han, S. M., Benaroya, H., and Wei, T., "Dynamics of transversely vibrating beams using four engineering theories," *Journal of Sound and Vibration*, vol. 225, pp. 935–988, 1999.

[77] Hariharan, P., "Optical interferometry," *Reports on Progress in Physics*, vol. 54, no. 3, pp. 339–390, 1991.

[78] Hasselman, T. K., "Modal coupling in lightly damped structures," *AIAA Journal*, vol. 14, pp. 1627–1628, November 1976.

[79] Hermans, L. and Auweraer, H. V. D., "Modal testing and analysis of structures under operational conditions: Industrial applications," *Mechanical Systems and Signal Processing*, vol. 13, no. 2, pp. 193–216, 1999.

[80] Hodges, D. H. and Pierce, G. A., *Introduction to Structural Dynamics and Aeroelasticity*. Cambridge, UK: Cambridge University Press, 2002.

[81] Huang, B. W., "Dynamic characteristics of a drill in the drilling process," *Proceedings of the Institution of Mechanical Engineers, Part B: Journal of Engineering Manufacture*, vol. 217, no. 2, pp. 161–167, 2003.

[82] Huang, C. S., "Structural identification from ambient vibration measurement using the multivariate ar model," *Journal of Sound and Vibration*, vol. 241, no. 3, pp. 337–359, 2001.

[83] Ibrahim, S. R. and Milkulcik, E. C., "A time domain modal vibration test technique," *Shock and Vibration Bulletin*, vol. 43, no. 4, pp. 21–37, 1973.

[84] Ibrahim, S. R. and Milkulcik, E. C., "A method for the direct identification of vibration parameters from the response," *Shock and Vibration Bulletin*, vol. 47, no. 4, pp. 183–198, 1977.

[85] Jacobsen, N.-J., Andersen, P., and Brincker, R., "Eliminating the influence of harmonic components in operational modal analysis," in *IMAC XXV: A Conference on Structural Dynamics*, 2007.

[86] Jaishi, B. and Ren, W.-X., "Structural finite element model updating using ambient vibration test results," *Journal of Structural Engineering*, vol. 131, pp. 617–628, April 2005.

[87] Jaworski, J. W. and Dowell, E. H., "Free vibration of a cantilevered beam with multiple steps: Comparison of several theoretical methods with experiment," *Journal of Sound and Vibration*, vol. 312, pp. 713–725, 2008.

[88] Jenq, S. T. and Lee, W. D., "Identification of hole defect for gfrp woven laminates using neural network scheme," in *Structural Health Monitoring, Current Status and Perspectives*, (Palo Alto, CA), 1997.

[89] Juang, J. N. and Pappa, R. S., "An eigensystem realization algorithm for modal parameter identification and model reduction," *Journal of Guidance, Control, and Dynamics*, vol. 8, no. 5, pp. 620–627, 1985.

[90] Kam, T. Y. and Lee, T. Y., "Detection of cracks in structures using modal test data," *Engineering Fracture Mechanics*, vol. 42, no. 2, pp. 381–387, 1992.

[91] Katz, R., Lee, C. W., Ulsoy, A. G., and Scott, R. A., "The dynamic response of a rotating shaft subject to a moving load," *Journal of Sound and Vibration*, vol. 122, no. 1, pp. 131–148, 1988.

[92] Kim, J.-T., Ryu, Y.-S., Cho, H.-M., and Stubbs, N., "Damage identification in beam-type structures: Frequency-based method vs mose-shape-based method," *Engineering Structures*, vol. 25, pp. 57–67, 2003.

[93] Kim, S., Pakzad, S., Culler, D., Demmel, J., Fenves, G., Glaser, S., and Turon, M., "Health monitoring of civial infrastructures using wirless sensor networks," in *6th IPSN Conference*, 2007.

[94] Lee, H. P., "Dynamic stability of spinning pre-twisted beams," *International Journal of Solids and Structures*, vol. 31, no. 18, pp. 2509–2517, 1994.

[95] Lee, P., Bunch, T. E., Cabrol, N., Cockell, C. S., Grieve, R. A. F., McKay, C. P., Jr., J. W. R., Schutt, J. W., and Zent, A. P., "Haughton-mars 97 - i: Overview of observations at the haughton impact crater, a unique mars analog site in the canadian high arctic," in *24th Lunar and Planetary Science Conference*, 1998.

[96] Lee, P. and Osinksi, G. R., "The haughton-mars project: Overview of science investigations at the haughton impact structure and surrounding terrains, and relevance to planetary studies," *Meteoritics & Planetary Science*, vol. 40, no. 12, pp. 1755–1758, 2005.

[97] Leong, W. H., Staszewski, W. J., Lee, B. C., and Scarpa, F., "Structural health monitoring using scanning laser vibrometry: Iii. lamb waves for fatigue crack detection," *Smart Materials and Structures*, vol. 14, pp. 1387–1395, 2005.

[98] Liao, C. L. and Dang, Y. H., "Structural characteristics of spinning pretwisted orthotropic beams," *Computers & Structures*, vol. 45, no. 4, pp. 715–731, 1992.

[99] Likins, P. W., Barbera, F. J., and Baddeley, V., "Mathematical modeling of spinning elastic bodies for modal analysis," *AIAA Journal*, vol. 11, no. 9, pp. 1251–1258, 1973.

[100] Liu, G. R. and Quek, S. S., *The Finite Element Method: A practical course*. Burlington, MA: Elsevier Science Ltd., 2003.

[101] Losada, R. A., "Digital filters with matlab," tech. rep., The MathWorks, Inc., May 2008.

[102] Luo, H. and Hanagud, S., "Dynamic learning rate neural network training and composite structural damage detection," *AIAA Journal*, vol. 35, pp. 1522–1527, September 1997.

[103] Lynch, J. P. and Loh, K. J., "A summary review of wireless sensors and sensor networks for structural health monitoring," *The Shock and Vibration Digest*, vol. 38, pp. 91–128, March 2006.

[104] Martarelli, M., *Exploiting the Laser Scanning Facility for Vibration Measurements*. PhD thesis, Imperial College of Science, Technology & Medicine, University of London, May 2001.

[105] The MathWorks, Inc., *Signal Processing Toolbox User's Guide 6.13*.

[106] McFadden, P., "Examination of a technique for the early detection of failure in gears by signal processing of the time domain average of the meshing vibration," *Mechanical Systems and Signal Processing*, vol. 1, pp. 173–183, 1987.

[107] Meirovitch, L., *Principles and Techniques of Vibrations*. Upper Saddle River, NJ: Prentice Hall, Inc., 1997.

[108] Miles, T. J., Lucas, M., Halliwell, N. A., and Rothberg, S. J., "Torsional and bending vibration measurements on rotors using laser technology," *Journal of Sound and Vibration*, vol. 226, pp. 441–467, 1999.

[109] Miyashita, T. and Fujino, Y., "Development of three dimensional vibration measurement system using laser doppler vibrometers," in *International Conference on Advances in Experimental Structural Engineering* (Y, I. and T, A., eds.), (Nagoya), pp. 649–656, 2005.

[110] Mohanty, P. and Rixen, D. J., "Operational modal analysis in the presence of harmonic excitation," *Journal of Sound and Vibration*, vol. 270, pp. 93–109, 2004.

[111] Mukherjee, S., Bartlett, P., Glass, B., Guerrero, J., and Stanley, S., "Technologies for exploring the martian subsurface," in *Aerospace Conference, 2006 IEEE*, March 2006.

[112] Oh, H., Lee, U., and Park, D.-H., "Dynamics of an axially moving bernoulli-euler beam: spectral element modeling and analysis," *KSME International Journal*, vol. 18, no. 3, pp. 395–406, 2004.

[113] Orfanidis, S. J., *Introduction to Signal Processing*. Prentice-Hall, Inc., 1996.

[114] Osinksi, G. R., Lee, P., Parnell, J., Spray, J. G., and Baron, M., "A case study of impact-induced hydrothermal activity: The haughton impact structure, devon island, canadian high arctic," *Meteoritics & Planetary Science*, vol. 40, no. 12, pp. 1859–1877, 2005.

[115] Pahk, H. J., Lee, D. S., and Park, J. H., "Ultra precision positioning system for servo motor-piezo actuator using the dual servo loop and digital filter implementation," *International Journal of Machine Tools & Manufacture*, vol. 41, pp. 51–63, 2001.

[116] Pakzad, S. N., Kim, S., Fenves, G. L., Glaser, S. D., Culler, D. E., and Demmel, J. W., "Multi-purpose wireless accelerometers for civil infrastructure monitoring," in *5th International Workshop on Structural Health Monitoring (IWSHM)*, pp. 125–132, September 2005.

[117] Paulsen, G., Mumm, E., Kennedy, T., Chu, P., Davis, K., Frader-Thompson, S., Petrich, K., and Glass, B., "Development of autonomous drills for planetary exploration," in *37th Lunar and Planetary Science Conference*, no. 2358, 2006.

[118] Polytec, *Portable Digital Vibrometer, PDV 100, User Manuel*, man-vib-pdv100-1104-03e ed.

[119] Prakash, S., Upadhyay, S., and Shakher, C., "Real time out-of-plane vibration measurement/monitoring using talbot interferometry," *Optics and Lasers in Engineering*, vol. 34, pp. 251–259, 2000.

[120] Rantatalo, M., Tatar, K., and Norman, P., "Laser doppler vibrometry measurements of a rotating milling machine spindle," in *Proc. of Eighth International Conference on Vibrations in Rotating Machinery*, 2004.

[121] Ratcliffe, C. P., "A frequency and curvature experimental method for locating damage in structures," *Journal of Vibration and Acoustics*, vol. 122, pp. 324–329, July 2000.

[122] Reinhardt, A. K., Kadambi, J. R., and Quinn, R. D., "Laser vibrometry measurements of rotating blade vibrations," *Journal of Engineering for Gas Turbines and Power*, vol. 117, no. 3, 1995.

[123] Reynders, E., Teughels, A., and Roeck, G. D., "Finite element model updating and structural damage identification using omax data," *Mechanical Systems and Signal Processing*, vol. 24, pp. 1306–1323, 2010.

[124] Richardson, M. H. and Formenti, D. L., "Parameter estimation from frequency response measurements using rational fraction polynomials," in *1st IMAC Conference*, (Orlando, FL), November 1982.

[125] Rincon, D. M. and Ulsoy, A. G., "Complex geometry, rotary inertia and gyroscopic moment effects on drill vibrations," *Journal of Sound and Vibrations*, vol. 188, no. 5, pp. 701–715, 1995.

[126] Ripley, B. D., *Pattern Recognition and Neural Networks*. Cambridge, UK: Cambridge University Press, 1996.

[127] Robertson, P. B., "The haughton impact structure, devon island, canada: Setting and history of investigations," *Meteoritics*, vol. 23, pp. 181–184, 1988.

[128] Rothberg, S. and Bell, J., "On the application of laser vibrometry to translational and rotational vibration measurements on rotating shafts," *Measurement*, vol. 35, pp. 201–210, 2004.

[129] Ruzzene, M., "Frequency-wavenumber domain filtereing for improved damage visualization," *Smart Materials and Structures*, vol. 16, pp. 2116–2129, 2007.

[130] Salawu, O. S., "Detection of structural damage through changes in frequency: a review," *Engineering Structures*, vol. 19, no. 9, pp. 718–723, 1997.

[131] Samuel, P. D. and Pines, D. J., "A review of vibration-based techniques for helicopter transmission diagnostics," *Journal of Sound and Vibration*, vol. 282, pp. 475–508, 2005.

[132] Sanders, W., Akhavan, F., Watkins, S., and Chandrashekhara, K., "Fiber optic vibration sensing and neural networks methods for prediction of composite beam delamination," in *Smart Structures and Materials 1997: Smart Structure and Integrated Systems*, (San Diego, CA), March 1997.

[133] Schubert, L., Barth, M., Klesse, T., Kohler, B., and Frankenstein, B., "Guided elastic waves and their impact interaction in cfrp structures characterized by 3d laser scanning vibrometry," in *Proceedings of SPIE*, vol. 6935, 2008.

[134] Schwarz, B. J. and Richardson, M. H., "Experimental modal analysis," in *CSI Reliability Week*, (Orlando, FL), October 1999.

[135] Schwarz, B. J. and Richardson, M. H., "Introduction to operating deflection shapes," in *CSI Reliability Week*, (Orlando, FL), October 1999.

[136] Serviere, C. and Fabry, P., "Blind source separation of noisy harmonic signals for rotating machine diagnosis," *Journal of Sound and Vibration*, vol. 272, pp. 317–339, 2004.

[137] Serway, R. and Beichner, R. J., *Physics for Scientist and Engineers, Volume 1, 5th Edition*. Orlando, FL: Saunders College Publishing, 2000.

[138] Shaker, F. J., "Effect of axial load on mode shapes and frequencies of beams," Tech. Rep. NASA TN D-8109, National Aeronautics and Space Administration, December 1975.

[139] Sharma, V. K., Apetre, N., Ayers, J., Ruzzene, M., and Hanagud, S., "Dynamics-based nondestructive structural health monitoring techniques." In Progress.

[140] Sharma, V. K., Hanagud, S., and Ruzzene, M., "Damage index estimation in beams and plates using laser vibrometry," *AIAA Journal*, vol. 44, pp. 919–923, April 2006.

[141] Sharma, V. K., *Laser Doppler Vibrometer for Efficient Structural Health Monitoring*. PhD thesis, Georgia Institute of Technology, School of Aerospace Engineering, 2008.

[142] Sherlock, S. C., Kelley, S. P., Parnell, J., Green, P., Lee, P., Osinksi, G. R., and Cockell, C. S., "Re-evaluating the age of the haughton impact event," *Meteoritics & Planetary Science*, vol. 40, no. 12, pp. 1777–1787, 2005.

[143] Sheu, G. J. and Yang, S. M., "Dynamic analysis of a spinning rayleigh beam," *International Journal of Mechanical Sciences*, vol. 47, pp. 157–169, 2005.

[144] Simitses, G. J., *An Introduction to the Elastic Stability of Structures*. R. E. Kreiger Pub. Co., 1986.

[145] Sinou, J.-J. and Lees, A. W., "The influence of cracks in rotating shafts," *Journal of Sound and Vibration*, vol. 285, no. 4–5, pp. 1015–1037, 2005.

[146] Sohn, H., Farrar, C., Hemez, F., Shunk, D., Stinemates, D., and Nadler, B., "A review of structural health monitoring literature: 1996-2001," Tech. Rep. LA-13976-MS, Los Alamos National Laboratory, 2003.

[147] Spectral Dynamics, Inc., San Jose, California, *SIGLAB User Guide: S2022D1/A*, 2001.

[148] Sriram, P., *Whole Field Optical Methods for Structural Mechanics: Digital Speckle Correlation and Laser Doppler Velocimetery*. PhD thesis, Georgia Institute of Technology, 1988.

[149] Sriram, P., Hanagud, S., and Craig, J. I., "Mode shape measurement using a scanning laser doppler vibrometer," *The International Journal of Analytical and Experimental Modal Analysis*, vol. 7, pp. 169–178, July 1992.

[150] Staszewski, W. J., Lee, B. C., and Traynor, R., "Fatigue crack detection in metallic structures with lamb waves and 3d laser vibrometry," *Measurement Science and Technology*, vol. 18, pp. 727–739, 2007.

[151] Stergiou, C. and Siganos, D., "Neural networks," tech. rep., Imperial College of London, Department of Computing, Surprise 96, 1996.

[152] Stoker, C. R., Lemke, L. G., Cannon, H., Glass, B., Dunagan, S., Zavaleta, J., Miller, D., and Gomez-Elvira, J., "Field simulation of a drilling mission to Mars to search for subsurface life," in *36th Lunar and Planetary Science Conference*, no. 1537, 2005. Abstract.

[153] Stoker, C. R., Lemke, L. G., Cannon, H., Glass, B., Dunagan, S., Zavaleta, J., Miller, D., and Gomez-Elvira, J., "Drilling to search for subsurface life on Mars: Analog mission in Rio Tinto, Spain," in *37th Lunar and Planetary Science Conference*, 2006. PPT Presentation.

[154] Structural Dynamics Research Corporation, *User Manual for Modal Analysis*, 1983.

[155] Tekinalp, O. and Ulsoy, A. G., "Modeling and finite element analysis of drill bit vibrations," *Journal of Vibration, Acoustics, Stress, and Reliability in Design*, vol. 111, pp. 148–155, 1989.

[156] Tekinalp, O. and Ulsoy, A. G., "Effects of geometric and process parameters on drill transverse vibrations," *Journal of Engineering for Industry*, vol. 112, pp. 189–194, 1990.

[157] Theodoridis, S. and Koutroumbas, K., *Pattern Recognition*. Academic Press, Elsevier, 2006.

[158] Tsou, P. and Shen, M.-H. H., "Structural damage detection and identification using neural networks," *AIAA Journal*, vol. 32, pp. 176–183, January 1994.

[159] Verna, V., Estlin, T., Jonsson, A., Pasareanu, C., Simmons, R., and Tso, K., "Plan execution interchange language (PLEXIL) for executable plans and command sequences," in *Proc. ISAIRAS 2005 Conference*, (Munich, Germany), September 2005.

[160] Vold, H. and Rocklin, G. T., "The numerical implementation of a multi-input modal estimation method for mini-computers," in *Proc. of IMAC 1, the International Modal Analysis Conference*, (Orlando, FL), pp. 542–548, November 1982.

[161] Wickert, J. A. and C. D. Mote, J., "Classical analysis of axially moving continua," *Journal of Applied Mechanics*, vol. 57, pp. 738–744, September 1990.

[162] Widrow, B. and Lehr, M. A., "30 years of adaptive neural networks: Perceptron, madaline, and backpropagation," in *Proceedings of IEEE*, vol. 78, pp. 1415–1442, September 1990.

[163] Xu, N., Rangwala, S., Chintalapudi, K., Ganesan, D., Broad, A., Govindan, R., and Estrin, D., "A wireless sensor network for structural monitoring," in *ACM Conference on Embedded Networked Sensor Systems*, November 2004.

[164] Yeh, Y. and Cummins, H. Z., "Localized fluid flow measurements with a he-ne laser spectrometer," *Applied Physics Letter*, vol. 4, no. 10, pp. 176–178, 1964.

VITA

Shannon Marie Statham was born in Jacksonville, Florida in 1982. She received her Bachelor of Science in Aerospace Engineering with magna cum laude from the University of Central Florida in 2005. She has been working toward her Ph.D. in Aerospace Engineering at the Georgia Institute of Technology since 2005, and she became an Amelia Earhart Fellow in 2007. Her research interests include structures, structural dynamics, diagnostics and failure analysis, and structural health monitoring.